A seismic investigation of the lithosphere of the Gregory rift

Savage, John Edward Graham

A SEISMIC INVESTIGATION OF THE LITHOSPHERE OF THE GREGORY RIFT

by

John Edward Graham Savage

A thesis submitted for the degree of
Doctor of Philosophy at the University of Durham

Department of Geological Sciences December, 1979

To Vivien

DECLARATION

I declare that this thesis, with the exception of Appendix 1 which was researched and written in equal partnership with Mr. W.G. Rigden, is my own work. I further declare that this thesis, submitted for the degree of Doctor of Philosophy at the University of Durham, is not substantially the same as any which has previously been submitted to any University.

John E.G. Savage

John E.G. Savage
University of Durham
December, 1979

ABSTRACT

During 1976 and the first six months of 1977, the Department of Geological Sciences at Durham University maintained networks of temporary seismic stations over the southeast flank of the Kenya dome and in the central section of the Gregory rift. At each station, signals from local and teleseismic events were recorded from a three component set of seismometers onto magnetic tape. Recorder generated timecode, and B.B.C. G.M.T. pips recorded alongside, enable reproduced seismograms to be timed accurately.

Waveform matching of replayed teleseismic P-wave arrivals enabled relative onset times to be obtained with great accuracy. Delay times were obtained for each of the 24 stations, also with high relative accuracy.

It is shown that the significantly larger delay times obtained for stations near the culmination of the dome must be due to the presence of anomalously low P-wave velocity material in the upper mantle. A localised trough in the pattern of delay times over the rift and coincident with the positive axial Bouguer anomaly is shown to be due to the presence of anomalously high P-wave velocity material within the crust.

Preliminary interpretations assume horizontal layering beneath each station. Flat bottomed models, assuming a uniform anomalous zone velocity of 7.5 km/sec are derived

for profiles running southeast over the flank of the dome and across the rift. Interpretations for the flank show a sharply increasing thickening of the anomalous zone towards the rift, with a secondary thickening near or under Mt. Kilimanjaro. The rift profile shows that the anomalous zone penetrates the crust to within about 20 km of the surface. A depth of 120 km is deduced for the base of the anomalous zone, but this may be in error due to systematic error in the baseline of station delays.

To circumvent the significant errors associated with the assumption of horizontal layering, a three-dimensional ray tracing technique is devised. Flat bottomed models are derived assuming uniform anomalous zone velocities of 7.5 and 7.0 km/sec. The 7.0 km/sec model shows a thinner and shallower anomalous zone, but the overall shapes of these models are in good agreement with the preliminary models. Deficiences in the ray tracing technique are discussed and it is shown that the parameters characterising the three-dimensional models are not well controlled. Suggestions are made for improving the technique.

The models are all consistent with the theory that upward perturbation of the lithosphere-asthenosphere boundary, giving rise to magmatic activity, thinning of the lithosphere and domal uplift, is the primary cause of rifting.

ACKNOWLEDGEMENTS

I should like to thank Prof. M.H.P. Bott for permission to work in the Department of Geological Sciences, Durham, and Dr. R.E. Long for being my supervisor. I should also like to thank the Natural Environment Research Council for granting me a research studentship.

My very sincere thanks go to all those who my wife and I met in Kenya and who made our visits to East Africa so enjoyable. I should like to thank especially David Coe, Bill Arnold, Alistaire Pearce, Samuel Kimani, Nigel and Muffat Trent, Brendan Mulholland, Peter Magius and Jill Simpson who as enthusiastic amateur seismologists looked after recording stations for several months in 1977.

My thanks go to Rowland Burley for introducing me to Kenya, and for much encouragement throughout this project.

I am very gratefull to Bill Rigden for much constructive criticism of this work, and many suggestions for improvements.

I should also like to thank the staff of the computer unit at Durham for help with some knotty problems and for providing facilities for typing and printing this text.

Finally, I should like to thank my wife, Vivien, for typing and editing much of this thesis, and for unfailing encouragement and patience, especially during the final months of preparation.

CONTENTS

LIST OF FIGURES

LIST OF TABLES

We knocked the bastard off...

Edmund Hillary

...And so each venture

Is a new beginning, a raid on the inarticulate

With shabby equipment always deteriorating

T.S. Eliot

CHAPTER 1

THE GREGORY RIFT AND THE EAST AFRICAN RIFT SYSTEM

1.1 Introduction

The East African rift system, which incorporates the Gregory rift, is a unique feature on the earth's surface. No other continental rift system is as well developed, or as extensive. The system is connected to the Red Sea and Gulf of Aden spreading axes, and via the latter to the oceanic ridge-rift system, implying that it might represent the initial stage of continental rupture.

The region is being subjected to lithospheric processes which are on a par with those responsible for continental drift. It is important that these processes be understood within the framework of the theory of plate tectonics. Study of the system will give valuable information on the mechanism of continental break-up and the formation of new oceans, and might give insights into the subsequent behaviour of passive continental margins as well as active spreading centres.

1.2 The East African Rift System

The East African Rift system consists of a series of trough-like depressions formed by faulting and crustal flexure, which traverse two major regions of uplift.

The system extends nearly 3,500 km, from the Afar triple-junction in the north, to mid-Mozambique, where it dies out. The two broad regions of uplift which are associated with the system are the Afro-Arabian plateau and the East African plateau. Both regions are roughly elliptical in plan, measuring some 1,500 X 1,000 km in extent, their major axes having a NNE-SSW trend.

The rift valleys are divided into two quasi-continuous systems, the Western Rift and the Eastern Rift (Baker et al, 1972), as shown in Figure 1.1. The Western Rift is developed over most of its length as typical 50-60 km wide, fault-bounded graben. It extends from Uganda in the north, and follows the line of Lakes Albert, Edward, Kivu, and Tanganyika, skirting the western edge of the East African plateau, to continue, via Lake Malawi, into Mozambique.

The Eastern Rift consists of two sections, the Ethiopian Rift and the Gregory Rift.

Together with the Red Sea and the Gulf of Aden, the Ethiopian Rift trisects the Afro-Arabian plateau into the plateaux of Yemen, Somalia, and Ethiopia. The Ethiopian Rift is contiguous with the Afar depression, a complex, low lying, triangular shaped area which separates it from the junction of the Red Sea and Gulf of Aden. From its connection with the Afar depression, at latitude 9.5^{o}N, the Ethiopian rift extends south-southwestwards as a well developed, 55-80 km wide trough. Farther south the rift tends to die away, and its connection with the Gregory Rift is difficult to trace.

The Gregory Rift, trending meridionally overall, tends

FIGURE 1.1

THE RIFT ZONES OF EAST AFRICA

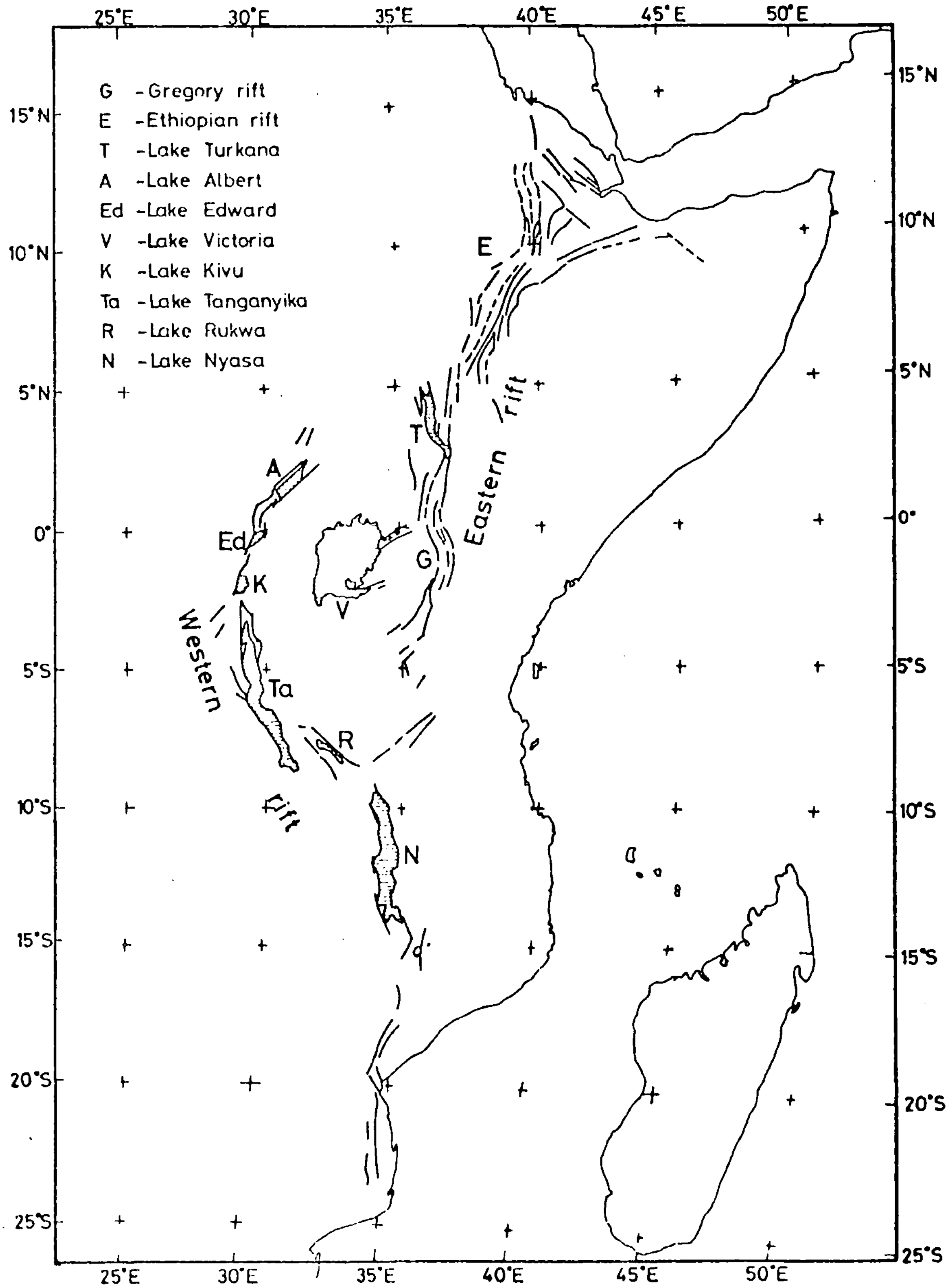

to skirt the eastern side of the East African plateau, although it transects its region of greatest elevation, the Kenya dome. The Gregory rift is best developed at the culmination of the Kenyan dome. Here it forms a complex trough-like depression, some 55-70 km wide, bounded by steep escarpments up to 2,000 m in height. The escarpments are typically step-like, consisting of series of normal faults arranged en echelon. This structure gives rise to platforms, typically a kilometer wide, which often form ramps between offset major faults. A few such steps are as much as 30 km wide, forming, for example, the Kamasia-Loriu platform and Kinangop "plateau".

Beyond about 2°S, the eastern marginal faulting gives way to predominantly monoclinal flexure, while the western fault scarps subdivide to give a series of westerly dipping blocks, bounded by east and south-east facing scarps. This zone of faulting broadens southwards and dies away beyond about 5°S. A broad series of faults connects the Eastern rift with the Western rift, at the north end of Lake Malawi.

The pattern of faulting to the south of the Gregory rift is closely mirrored in the north, where the symmetrical graben gives way, beyond about 2°N, to a predominantly block-faulted structure with east facing scarps. Further north, in the triangular shaped Turkana depression, faulting gives rise to a disconnected series of shallow depressions, offset succesively to the north east. These die away at about 5.5°N, and the main Ethiopian rift resumes some 50 km to the east (Baker et al, 1972).

Associated with the Gregory rift is the Kavirondo rift, which emerges from Lake Victoria to run in an ENE direction, joining the main rift at the latitude of the equator. Here it bisects the western plateau at its highest point. This rift is 15-25 km wide and bounded by faults with throws of up to 700 m, except in the central sector where monoclinal flexure forms the margins. In the east, near its connection with the main rift, the structure is largely obscured by central volcanoes.

The faulting of the Gregory rift, illustrated in Figure 1.2, and superimposed on the Kenya dome, has a striking symmetry, noted by Baker and Wohlenberg (1971). The main rift bisects the dome along its major axes, and the pattern of faulting is mirrored about its minor axis, which is coincident with the equator.

1.3 The Evolution of the Gregory Rift

The basement systems, on which the topographic features of the Eastern rift are impressed, are of Precambrian and lower Paleozoic age. During most of the Paleozoic, east Africa was occupied by fold mountains undergoing erosion. Continental sediments of the Karoo facies (upper Paleozoic), up to 15,000 m thick, are preserved in broad faulted troughs along the southern Kenyan coast and striking south-westwards across Tanzania to L. Malawi (Baker et al, 1972).

Throughout the Jurassic, marine transgressions

FIGURE 1.2

PATTERN OF FAULTING FOR THE GREGORY RIFT

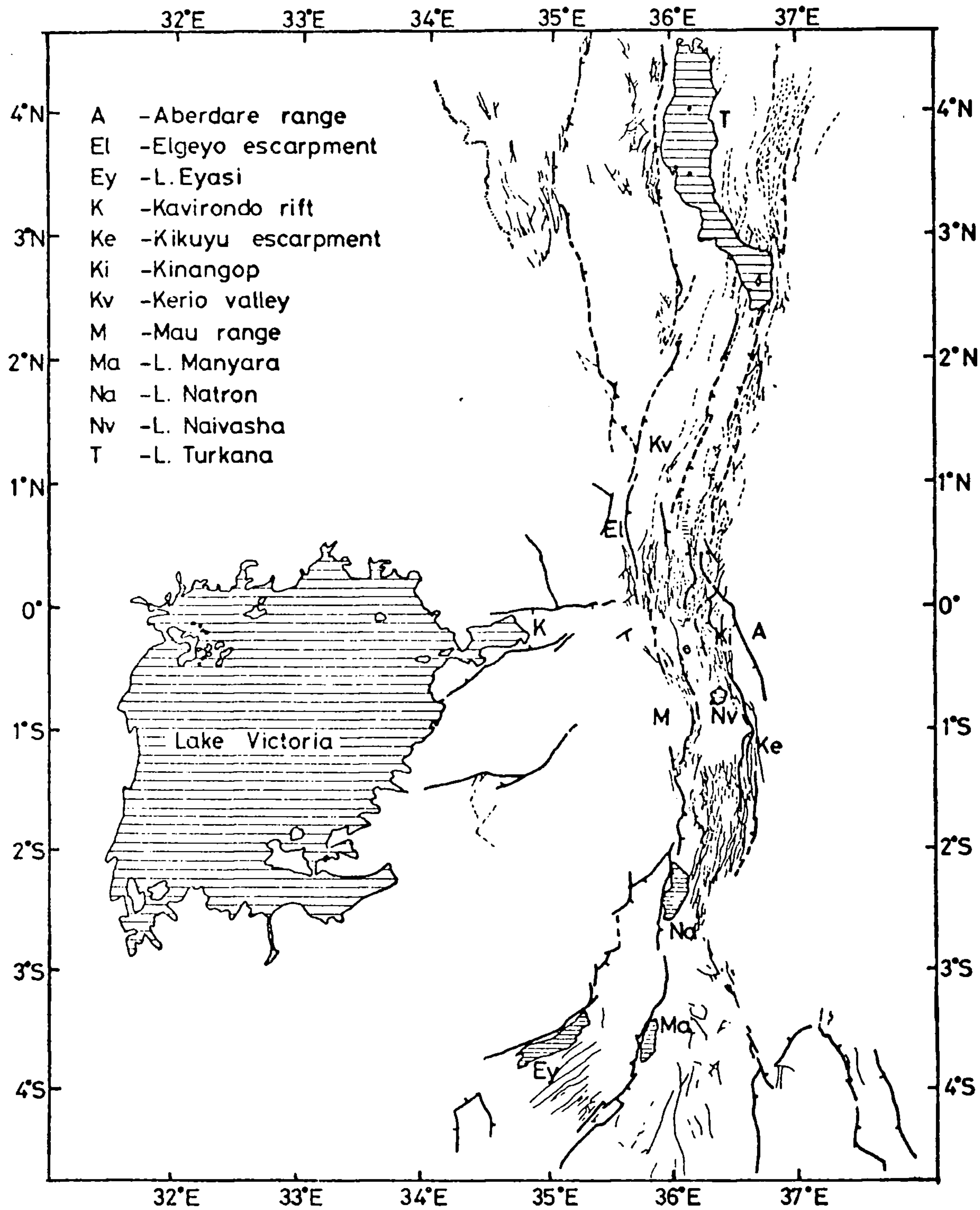

developed westwards from the Horn of Africa to cover south-western Arabia, Somalia, most of Ethiopia, and the north-east of Kenya. A subsiding trough may have existed along the future course of the Ethiopian rift in the Jurassic. Much of Ethiopia had re-emerged by the start of the Cretaceous and this process continued until the early Tertiary (Baker et al, 1972).

The end of the Mesozoic left central Kenya at an elevation of not less than 500 m, gradually falling away to the newly formed Atlantic and Indian oceans. Parts of a well planed late Mesozoic erosion surface are preserved in Kenya, at heights between 2,000 m and 3,500 m, testifying to Cainozoic movements (King, 1978).

Igneous activity associated with the Gregory rift was initiated at least 30 million years ago, with the eruption of basalts in southwest Ethiopia and northwest Kenya. (Baker et al, 1971). By 25 million years ago, much of Ethiopia had been covered by the extensive Trap series flood basalts which attain a thickness of over 2,500 m in Afar (Shackleton, 1978).

Trough formation along the future axis of the Gregory rift appears to have started in the lower Miocene with the subsidence of the Turkana depression, resulting in monoclinal flexure along the Kenya-Uganda border. This phase of activity was accompanied by continuing eruption of basalts from fissures in the depression and possibly to the north of Mt. Kenya, and by the formation of carbonatite volcanoes in eastern Uganda, and along the Kavirondo rift (Logatchev et al, 1972)

In the middle Miocene, from 13.5-11 million years ago, the centre of igneous activity shifted to sources within the Gregory rift with the eruption of some 25,000-50,000 km^3 of phonolites. These flood phonolites attained a thickness of about 700 m (McCall, 1967), overflowing the sides of the still shallow rift depression (Shackleton, 1978) to distances of 100 km or more (King, 1978).

There is some doubt as to whether these plateau phonolites were extruded from widely distributed dykes or a relatively few very low angle volcanoes. Whatever the mode of eruption, this phase of activity accounts for about a quarter of the total volume of the Gregory rift volcanics (King, 1978).

Late Miocene to early Pliocene (10-5 million years ago) activity in the Gregory rift was characterised by a further narrowing and southward development of igneous activity, which was predominantly from central volcanoes. The chemistry of the volcanics became more varied but retained a strongly alkaline nature, especially in the west and south. During this stage, the first major western boundary faults, for example the Elgeyo escarpment, were formed, the eastern margins retaining a flexural character (Logatchev et al, 1972). The Aberdare range, composed mainly of basalts, was built up between 6.5 and 5.0 million years ago (Shackleton, 1978).

After initial trough formation, massive basalt eruptions in the upper Pliocene, 5.0-2.0 million years ago, formed a continuous horizon across the rift floor. (Logatchev et al, 1972). Further north, in Turkana, sedimentation prevailed. Around the latitude of Nakuru, ignimbrite sheets covered a large area of the rift and the area to the east.

Towards the end of the Pliocene, the final phase of uplift raised the general level of the Kenya dome by about 1,500 m (Saggerson and Baker, 1965). The marginal faults were renewed and extended. At the same time the large volcanoes of Mount Kenya and Mount Kilimanjaro were initiated.

The volcanic activity of the Upper Pliocene continued into the Pleistocene with the eruption of alkaline and quartz trachytes, accompanied by large volumes of pyroclastics. The rift was deepened and extended at its northern and southern extremities. New faults formed inside the trough, forming the characteristic "ramp" and "gang-plank" structures. The formation of this "rift in rift" structure was, according to Logatchev et al (1972), due to subsurface devastation caused by the preceding and contemporaneous massive eruptions.

The importance of uplift in the formation of the elliptical elevated region, the Kenya dome, on which the Gregory rift is impressed, is disputed. By mapping and dating what are thought to be the remnants of peneplaned surfaces, Saggerson and Baker (1965) have inferred a total uplift of about 2,000 m for central Kenya. They believe the uplift to have occurred as short periods of activity, separated by long periods of quiescence, during which erosion took place. They infer three main phases. The first of these, occurring at the end of the Cretaceous, resulted in some 400 m of uplift in central Kenya, decreasing eastwards to give way to subsidence along the present coastline. A second phase of uplift occurred during the Miocene and resulted in some 300 m increase in elevation in central Kenya, with subsidence again dominant along the coast. The final and greatest phase of uplift occurred in the Pliocene, and seems to have been related to the major graben formation at this time. The isobases of a sub-Miocene erosion surface, as mapped by Saggerson and Baker, are illustrated in Figure 1.3

King (1978) considers the present elevation of the Kenya dome to result predominantly from the large accumulation of volcanics. Although it is admitted that traces of a well planed and lateritised surface of late Mesozoic age are preserved in parts of Kenya at heights of between 2,500 and 3,500 m, the elevation of these surfaces is ascribed partly to their position along an ancestral watershed between the Indian and Atlantic oceans and partly to pre-rifting movements. Considerable uplift of the rift shoulders during the Pliocene and Pleistocene is also admitted, but the top of the basement under the floor of the

FIGURE 1.3

MAP ILLUSTRATING DOMAL UPLIFT

(Saggerson and Baker, 1965)

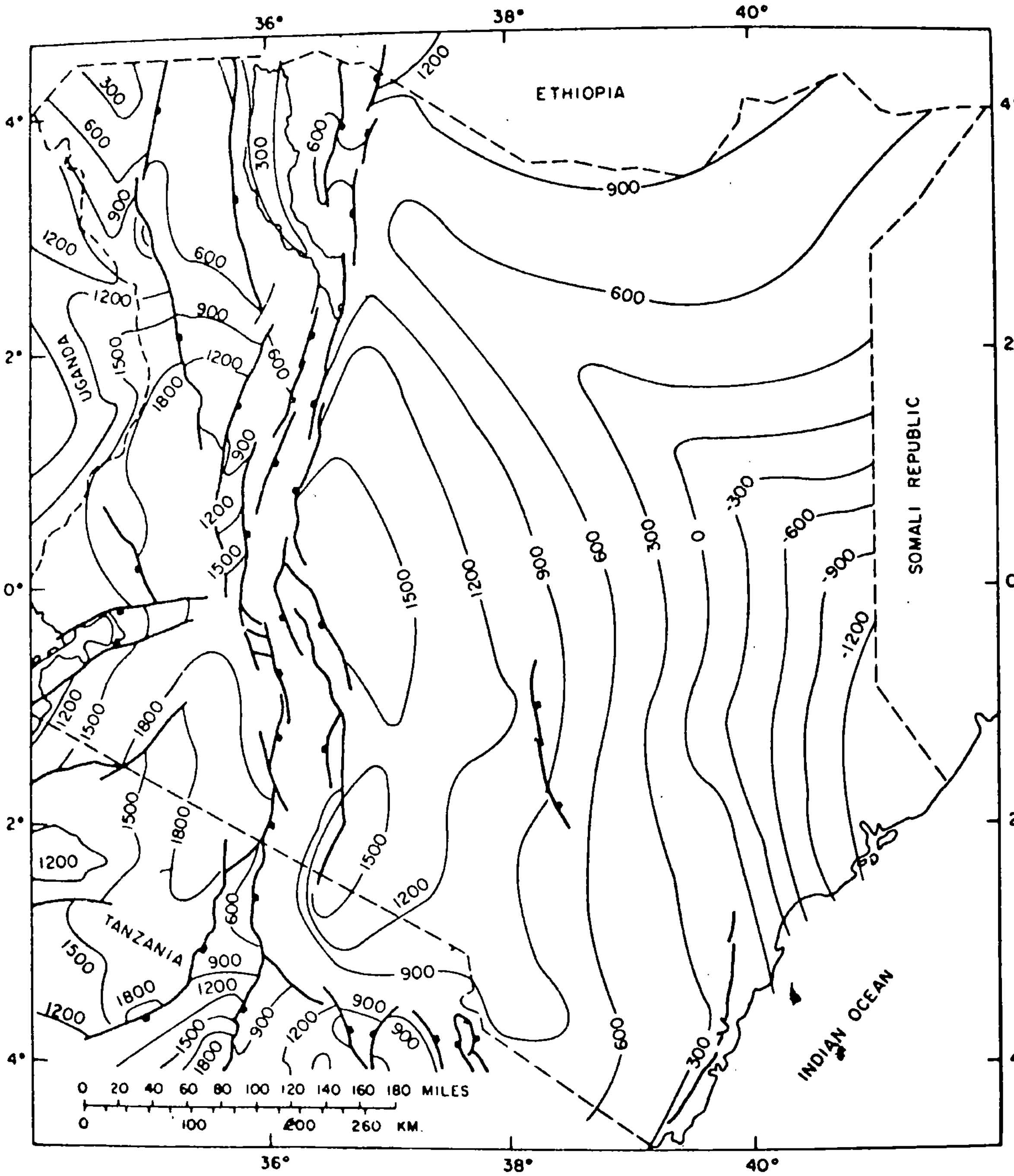

Isobases of the sub-Miocene erosion surface in Kenya. Present-day elevation of the surface given in meters.

rift, it is claimed, is depressed to a depth of as much as 2,500 m below sea-level, although the evidence for this assertion is not given.

Certainly, rift formation has been accompanied by considerable flexure, and basement is exposed in a few areas of the rift at considerable elevations. The degree to which the crust has been subject to overall uplift in central Kenya is of key importance for a full understanding of the development of the region and the above conflict must be resolved.

1.4 Petrochemistry

Although the petrochemistry of the Gregory rift volcanics is complicated and not well understood, certain broad features are clear. Two genetic series are observable, one strongly alkaline, and the other mildly so. Baker et al (1972) suggest that these derive from synchronous melting in parts of the mantle with different water contents, or variation in the degree of partial melting, or both. They also note that the basalt compositions, for both Kenya and Ethiopia, indicate shallower melting under the rifts than under the plateaux, with a generally deeper origin in Kenya.

Goles (1975) has studied two suits of basalt, one collected from the Chyulu range, about 300 km to the southeast of the culmination of the Kenya dome, and the other from Olorgesailie, in the southern part of the rift.

The Chyulu suite seems to have been derived from magma which equilibriated at a temperature of 1,450°C and pressures substantially less than 25 kbar (about 80 km depth). Goles infers unusually elevated temperatures within the upper mantle beneath the Chyulu range.

The Olorgesailie suite being more evolved, and having equilibriated at shallower depth (1200°C and 3-10 kbar pressure), is thought to be derived from a secondary magma chamber located within the crust. A series of such secondary magma chambers along the rift axis would give rise to the observed positive Bouguer anomaly (Searle, 1970).

Goles relates the range of volcanic types to the size of magma bubbles which are imagined to be drawn off from the mantle causing, or in response to, the rifting process. Larger bubbles, of greater vertical extent, would give rise to the extensive basaltic volcanism observed in the north while smaller bubbles would give rise to trachytic and phonolitic styles as seen farther south.

1.5 Previous Geophysical Studies

1.5.1 The African Lithosphere far from the Rift Zones

Surface wave dispersion studies are useful for obtaining average shear wave velocity models for the crust and upper mantle between seismic stations (Brune et al, 1960; Bloch et al, 1968), and the method has been applied successfully to various paths across Africa.

Models derived for southern Africa (Bloch et al, 1969), and the AFRIC model for the areas of Africa away from the major rift zones (Gumper and Pomeroy, 1970), indicate a normal shield type structure, characterized by high sub-Moho velocities. These models match closely the equivalent model for the Canadian Shield (Brune and Dorman, 1963). Figure 1.3 illustrates these models.

Whilst there is a fundamental limit to the resolving power of surface wave dispersion data (Der et al, 1970), and accurate determinations of crustal thicknesses are not to be expected, it should be pointed out that the above models and the results of earlier studies in Africa (Press et al, 1956; Oliver et al 1959) indicate normal continental crustal thicknesses of 35-40 km.

More accurate determinations of crustal structure, in Southern Africa, have come from the refraction studies of Willmore et al (1952), Gane et al (1956) and Hales and Sacks (1959). These studies all employed, as sources of energy, the frequent earth tremors which occur in the Witwatersrand gold-mining area. The hypocentres and origin times were determined from recordings at a local network of stations. Recordings made at temporary stations at various distances up to 500 km, along a number of profiles, enabled travel time tables to be constructed.

The results of the earlier two studies were interpreted in terms of a single layered crust, with a thickness of 35-36 km. Hales and Sacks obtained a more refined model

FIGURE 1.4

CANSD, AFRIC, AND SOUTHERN AFRICA SHEAR WAVE MODELS OF THE LITHOSPERE

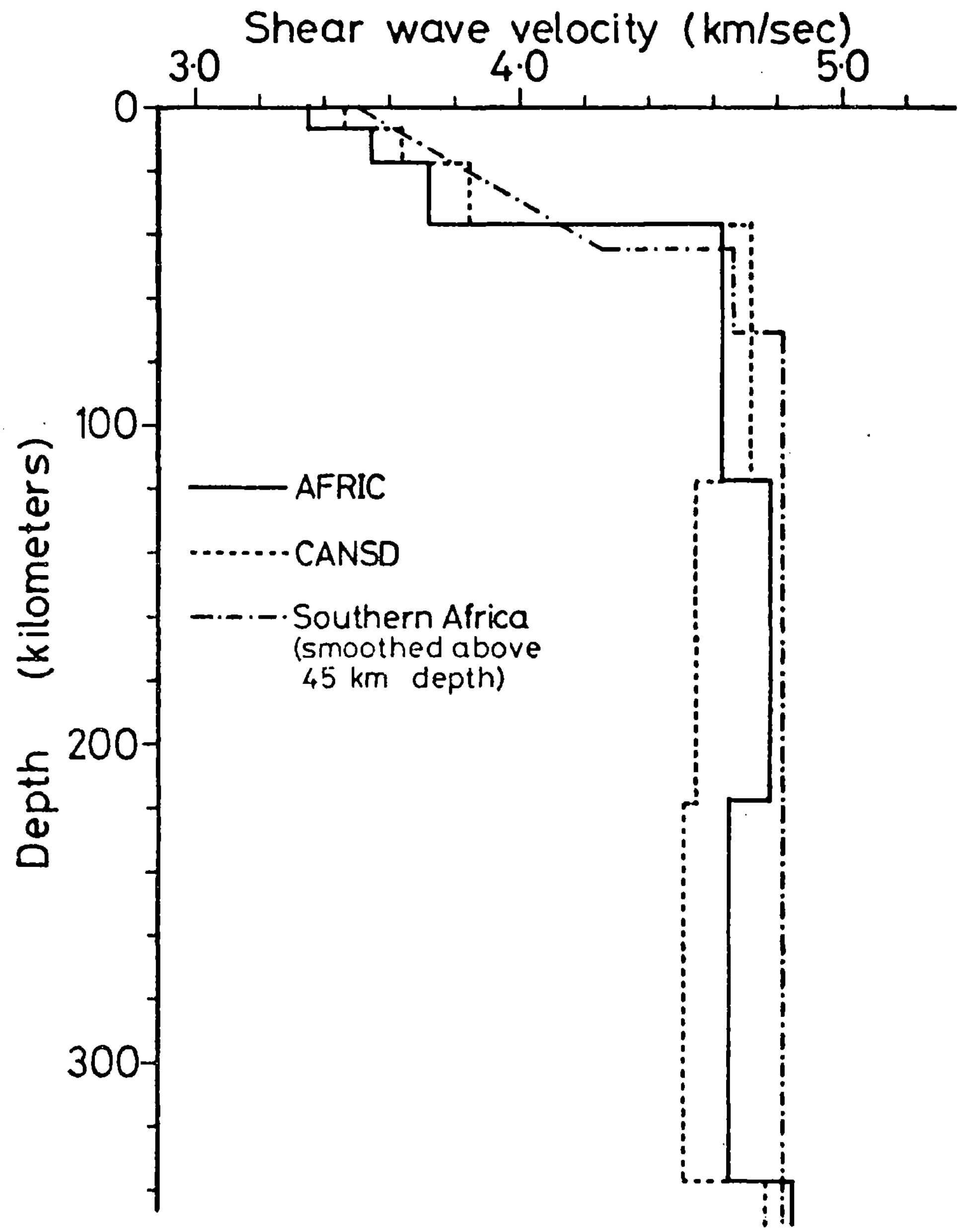

with the identification of an intermediate discontinuity which had been suspected from the earlier work. They inferred a crustal thickness of 36.1 km. They also showed that the Rayleigh wave dispersion curve obtained by Press et al could be better interpreted in terms of a two-layered crust. These models are illustrated in Figure 1.5

1.5.2 The Upper Mantle under the Rift Zones

Evidence that the upper mantle beneath the rift zones is anomolous comes from a variety of geophysical studies.

Bullard (1936) was the first to interpret gravity measurements in East Africa, using 56 of his own pendulum determinations together with 33 measurements made by Kohschuffer in 1899-1900. He showed that the uplifted regions are in approximate isostatic equilibrium, and that there is a mass deficiency under both the Gregory and the Western rifts. The latter he interpreted as being due to downward displacement of lighter crustal material into the mantle.

Since this early work, many more gravity readings have been made, and more detailed maps produced. The East African plateau as a whole is associated with a long (~1,000 km) wavelength negative Bouguer anomoly, which reaches a maximum intensity over the Kenya dome. Interpretations in terms of a thickened crust under the dome and plateau are untenable, as they cannot account for the observed Cainozoic uplift and volcanism. The preferred

FIGURE 1.5

SEISMIC CRUSTAL MODELS FOR SOUTHERN AFRICA

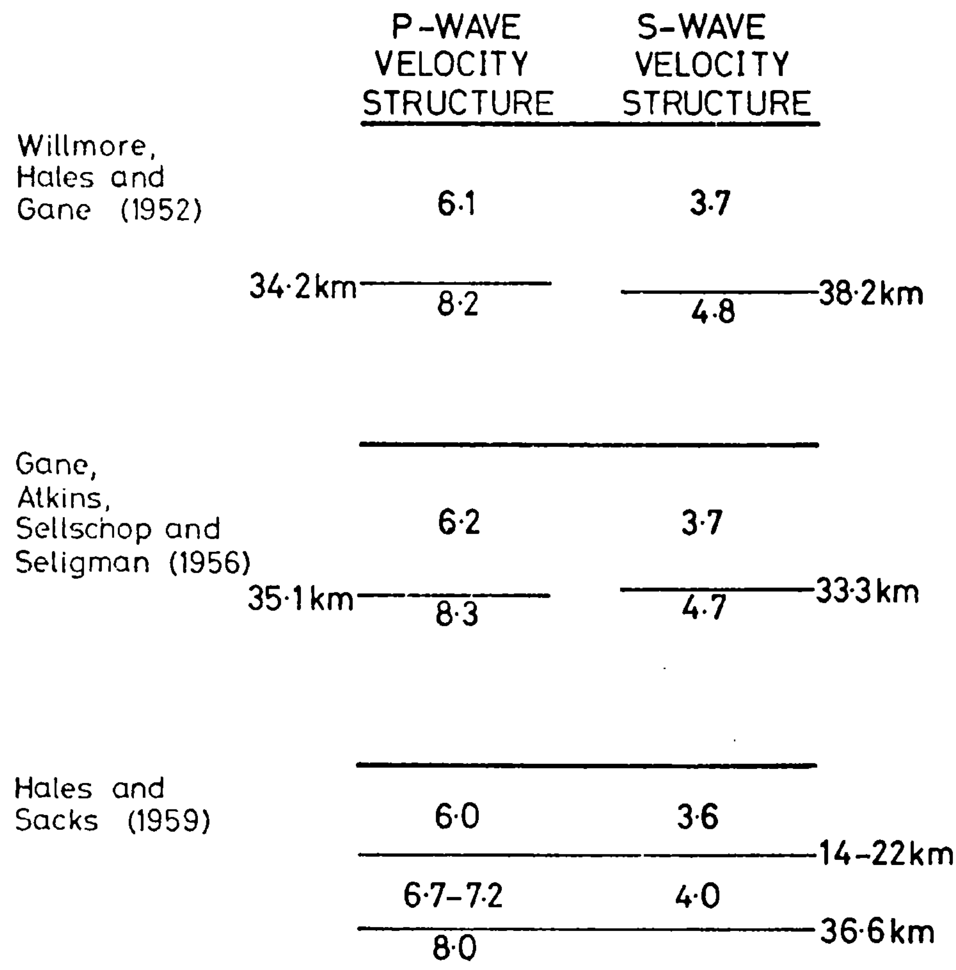

interpretations are in terms of anomolously light upper mantle material (Sowerbutts, 1969; Khan and Mansfield, 1971) (see Figure 1.8).

Sundaralingham (1971) used surface wave dispersion to investigate the average lithospheric shear wave structure along various paths between Addis Ababa (AAE), Nairobi (NAI), Lwiro, (LWI) and Bulawayo (BUL). Knopoff and Schlue (1972) also studied the path NAI-AAE. The short period phase velocities in each case were similar to those for the AFRIC model (Gumper and Pomeroy, 1970). At longer wavelengths, corresponding to significant penetration of the upper mantle, the velocities were slower. The effect is least pronounced for the path NAI-BUL, which is mostly to the south of the well-developed rift zones, and most pronounced for the path AAE-NAI, which is close to the Eastern rift over its entire length. Shear wave models derived by Sundaralingham are illustrated, alongside the AFRIC model, for the paths AAE-NAI, AAE-LWI and BUL-NAI, in Figure 1.6.

Gumper and Pomeroy (1970) noted abnormalities in the transmission of the upper mantle shear wave phase, S_n, across the rift zones. S_n is normally recorded as a high amplitude, high frequency, impulsive phase, but when the paths traversed the well developed rift zones, north of about 10°S, this phase was either absent from the seismograms, or present as a highly attenuated, emergent, low frequency phase. Similar poor propagation of S_n has

FIGURE 1.6

SHEAR WAVE SEISMIC MODELS FOR VARIOUS PATHS NEAR RIFT ZONES

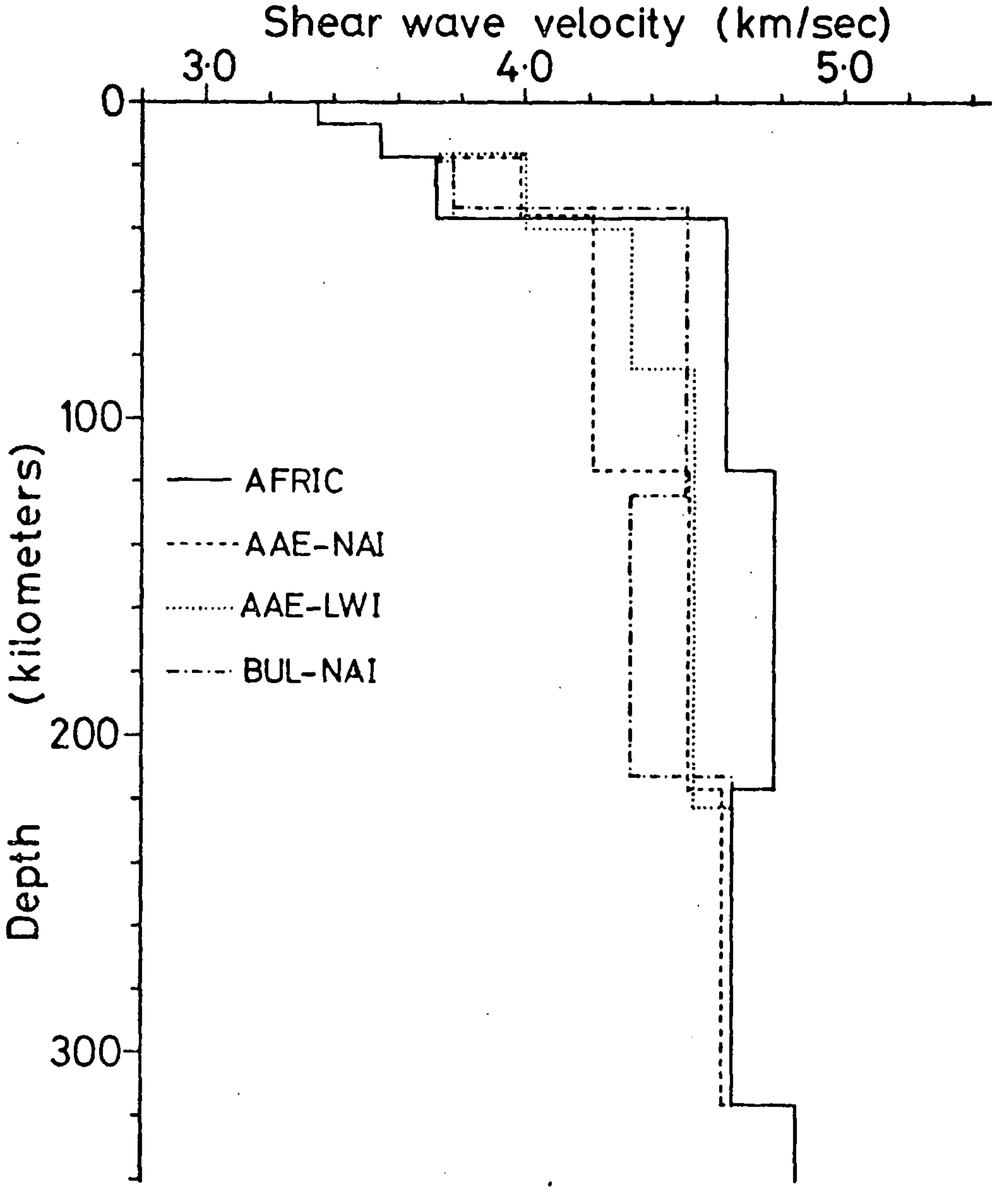

been observed across the oceanic ridges, and subduction zones (Molnar and Oliver, 1969). The high attenuation (low Q) results from low shear strength, and is taken to imply an upward deviation of the lithosphere-asthenosphere boundary beneath these regions.

Time residuals at African rift stations, derived during the construction of travel time tables (Cleary and Hales, 1966; Herrin and Taggart, 1968; Lilwall and Douglas, 1970), have large positive values, compared with other African stations, as illustrated in Table 1.1. These residuals and relative delay time measurements between NAI and BUL (Sundaralingham, 1971) and between Durham University's temporary array station at Kaptagat (KAP) and BUL (see Table 1.2), show that stations located near the Eastern rift lie on regions with anomolously low P-wave velocities. The magnitudes of the relative delays are such that they must be due, at least in part, to the existence of anomalous material in the upper mantle.

The Kaptagat array, which was located about 10 km west of the Elgeyo escarpment, has been used to determine the apparent slowness of teleseismic P-wave arrivals. The measured values differ considerably from those calculated from published hypocentral determinations and travel time tables. The slowness anomalies indicate a velocity structure with a dipping interface, or interfaces, beneath the array. Interpretations based on a dipping Moho, or mid-crustal discontinuity, were ruled out, as a horizontally

TABLE 1.1

DELAY TIMES AT AFRICAN STATIONS

SOURCE / STATION	Cleary and Hales (1966)	Herrin and Taggart (1968)	Lilwall and Douglas (1970)
AAE	1.5	1.12	2.20
NAI	-	-	1.88
LWI	-0.2	0.36	0.78
BUL	0.0	-0.45	-0.53
PRE	-0.2	-	-0.42
WIN	0.3	-0.99	0.87
ERROR	0.3	1.1	0.34
CONF. LIM.	65%	65%	95%

TABLE 1.2

DELAYS RELATIVE TO BULAWAYO

SOURCE / STATION	Sundaralingham (1971)	Backhouse (1972)
AAE	2.7	-
NAI	2.3	-
KAP	-	2.20
ERROR	0.3	2.0
CONF. LIM.	95%	95%

stratified crust had been deduced from studies of locally occurring earthquakes (see the section following). Backhouse (1972) interpreted the slowness anomalies in terms of a westery thinning, plane sided wedge of anomalously low velocity (7.5 km/sec) material embedded within normal (8.1 km/sec) meterial. Dips for the upper and lower surfaces of 50° and -25° respectively were suggested. Later work (Forth, 1975; Long and Backhouse, 1976) showed that the data could be better fitted if curved interfaces were introduced. A flat base to the anomalous zone was assumed, and the upper interface contoured. Figure 1.7 illustrates a model derived, assuming an anomalous velocity of 7.3 km/sec.

Further evidence for the existence of anomalous upper mantle material beneath the rift has been obtained from geomagnetic deep sounding. Banks and Ottey (1973) occupied six sites on a 300 km traverse, crossing the Gregory rift and region to the east. They detected a shallow concentration of current beneath the axis of the rift, together with a more complicated high conductivity zone beneath the eastern flank.

A more detailed study (Rooney and Hutton, 1977), using measurements from ten sites along a similar profile, confirmed and elaborated the previous work. The existence of a highly conductive region within the crust was inferred, along with a deeper region of high conductivity. Unfortunately, the near surface conductor hindered

FIGURE 1.7

CONTOURED MAP OF THE UPPER INTERFACE OF THE ANOMALOUS ZONE

(Long and Backhouse,1976)

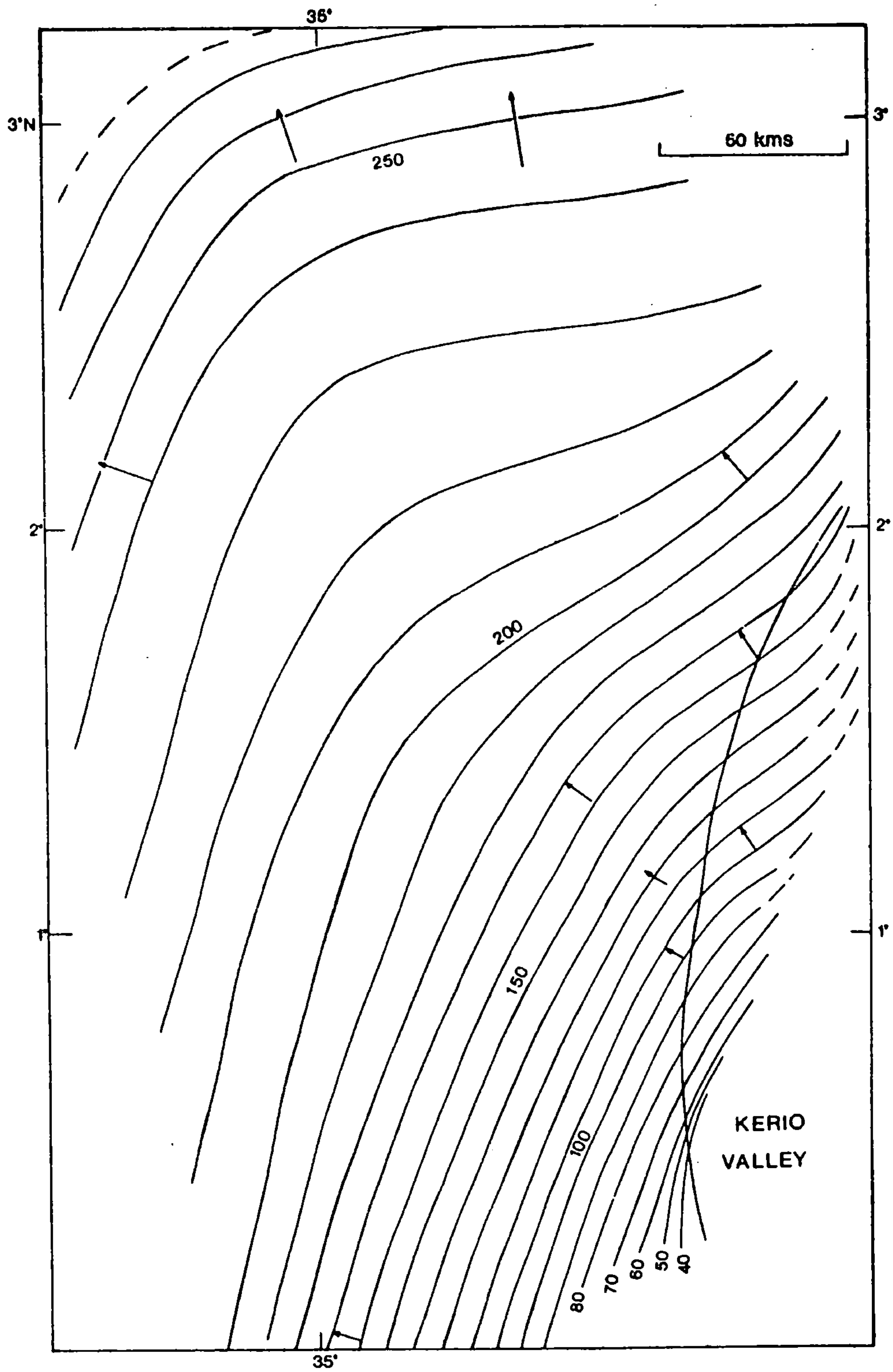

observation of the lower region, but a minimum depth of 30 km was obtained, associating it with the upper mantle, and implying a considerable degree of partial fusion.

1.5.3 The Crustal Structure near the Gregory Rift

Maguire (1974) determined apparent velocities and backbearings for first arrivals for local and regional earthquakes recorded by the Kaptagat array. The apparent velocities for events located to the west of the Gregory rift clustered around the values 5.9 (for S-P times less than 9 seconds), 6.5 and 8.0 km/sec. These velocities were interpreted as being due to an upper crustal P_g phase, and $P*$ and P_n refractions respectively. By considering possible focal depth distributions, and noting the distribution of apparent velocities with S-P time, Maguire and Long (1976) derived the crustal structure given in Figure 1.9. Despite a slightly greater overall crustal thickness than in southern Africa, the structure is typically continental to within 30 km, at least, of the rift axis (Maguire and Long, 1976).

Rykounov et al (1972) used recordings of microearthquakes in the southern part of the Gregory rift, in Northern Tanzania, to derive a two layered crustal model for this area. This model is also given in Figure 1.5, and shows that normal continental crust exists in this region.

Bonjer et al (1970) determined the spectral response ratios of long period body waves at AAE and NAI, from two earthquakes in the Hindu Kush region. Assuming upper and lower crustal velocities of 6.0 and 6.7 km/sec respectively, they inferred a total crustal thickness of 39 km for Addis Ababa and 43 km for Nairobi.

Thus the seismic evidence indicates the existence of normal continental crust to within a few kilometers at least of the Gregory rift margins.

1.5.4 Crustal Structure of the Rift Floor

Detailed gravity mapping has revealed the existence of a Bouguer anomaly ridge, along the axis of the Gregory rift, superimposed on the broad negative which is associated with the Kenya dome. The precise extent of this component of the total anomaly pattern is difficult to extract from the superimposed effects of the superficial volcanic deposits, and the "regional" due to the anomalous upper mantle. Nevertheless, this axial Bouguer high can be traced without interruption as a 30-50 mgal amplitude ridge, with a width of 50-100 km, from Lake Turkana in the North (Khan and Mansfield,1971) to about 2°S in Northern Tanzania, where it dies away (Darracott et al, 1972).

Searle (1970) has ruled out the possibility that surface volcanics give rise to the axial positive anomaly; the basalt and phonolite cover is neither dense enough nor thick enough. However, the gradients vary rapidly and a dense igneous intrusion within the crust, along the axis, is generally inferred from the data. Detailed interpretation is hampered by the unknown thickness of light volcanics, but several models have been proposed, with the top of the intrusion placed at between 2 km (Searle, 1970) and 20 km (Khan and Manfield, 1971) depth. Several gravity profiles for the crust and upper mantle across the rift at a range of latitudes are illustrated in Figure 1.8.

A major refraction experiment to derive a velocity structure for the crust of the rift floor was performed by Griffiths et al (1971). Large explosive charges were detonated in Lakes Turkana and Hannington, and recorded at ten linear array stations between them, thus sampling the material beneath the rift floor in the northern sector. Only the first P and first S arrivals were used in analysis as other phases could not be reliably identified, despite attempts at velocity filtering. Each phase in each direction yielded a single apparent velocity, but the velocities were considerably higher from the Lake Turkana shot point. Interpretations in terms of a single northward dipping interface were discarded, as end to end times, extrapolated from the travel time graphs, differed for the two directions. It was considered more likely that different refractions were being detected for the two directions. Assuming plane, horizontal interfaces, the composite model illustrated in Figure 1.9 was obtained.

Despite the problems associated with interpretation of effectively unreversed refraction data, this study demonstrates unambiguously the presence of anomalously high velocity material within the crust of the northern sector of

FIGURE 1.8

GRAVITY MODELS FOR THE KENYA DOME AND GREGORY RIFT

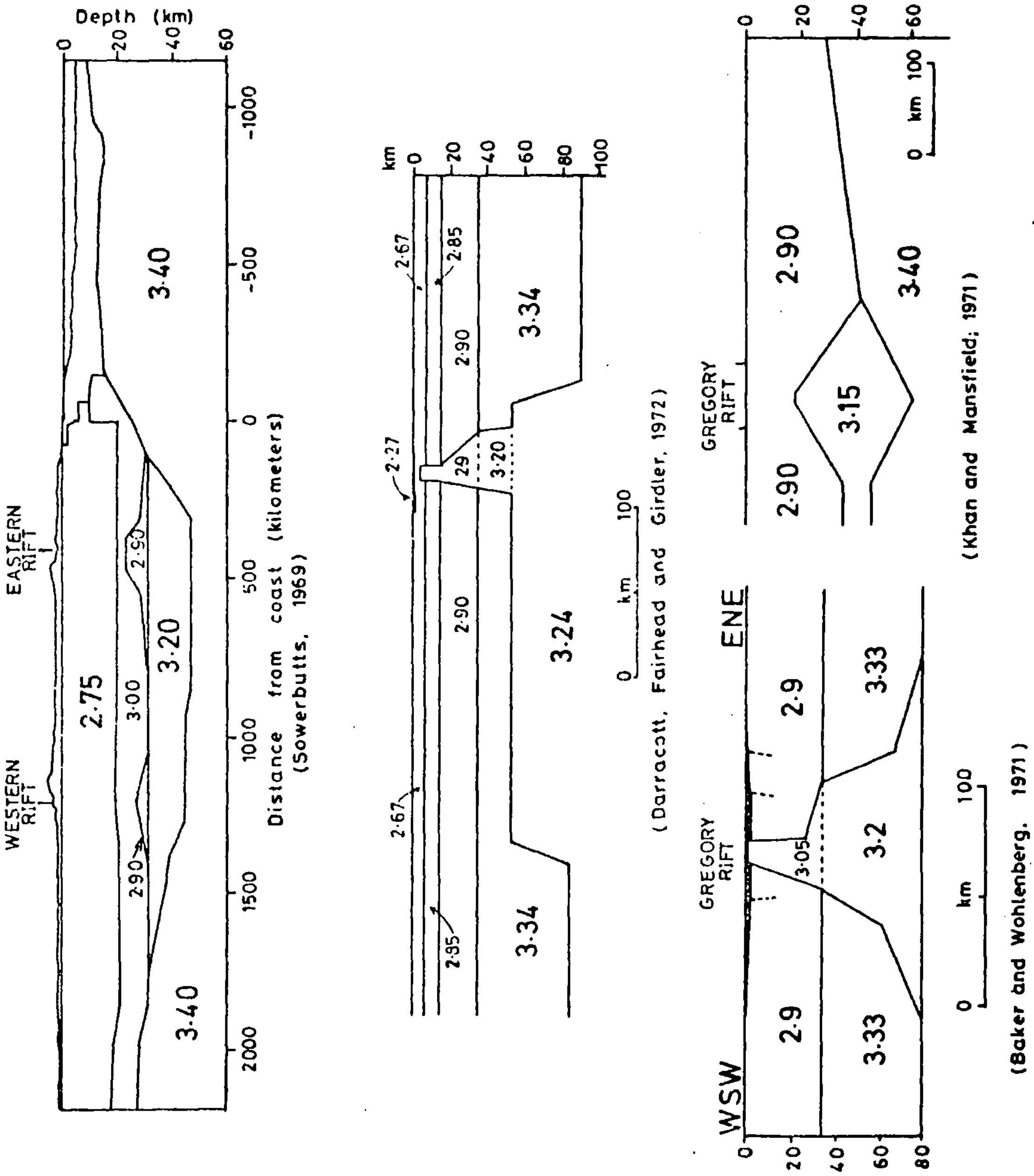

FIGURE 1.9

SEISMIC CRUSTAL STRUCTURES OBTAINED NEAR AND WITHIN THE GREGORY RIFT

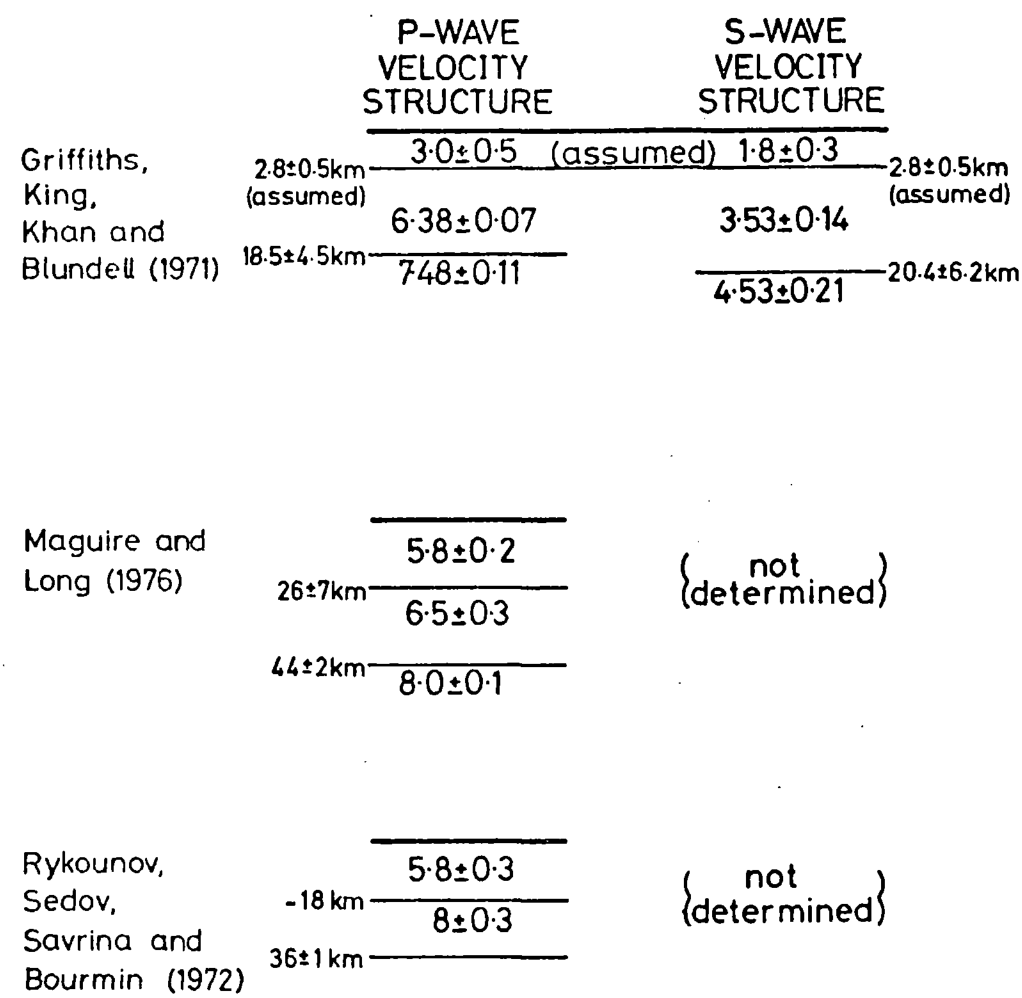

the Gregory rift.

The high conductivity (2-20Ωm) region within the crust, detected by geomagnetic sounding, is at least 5 km thick and situated at a depth of less than 8 km (Rooney and Hutton, 1977). Interpretation in terms of conductive infill of the rift trough is rejected on account of the thickness, and the preferred interpretation is in terms of high temperatures and water saturation of a highly fractured crust. This and the close association of hydrothermal activity and prominent central volcanoes (for example, Silali, Menengai, Suswa and Ol Doinyo Lengai) with the axis of the rift indicate a considerable degree of magmatic activity.

1.6 Theories of Rift Formation

Current theories of rift formation fall into two contrasting categories. The first, and probably more popular, holds that the primary cause of continental rifting is the development of anomalous upper mantle material. The second holds that continental rifting is induced by the build-up of lithospheric stresses large enough to cause fracture of the brittle upper crust, and that the development of anomalous upper mantle material is a secondary feature.

Gass has argued for a theory of the former type in a number of papers (eg. 1970, 1972). According to his theory, instability of the lithosphere-asthenosphere boundary is of key importance. Local heating causes an initial upward movement of this boundary, which gives rise to an increase in the liquid fraction of the asthenosphere. Upward migration of hot liquid by "penetrative convection" (Elder, 1970) raises farther the isotherms and thus the lithosphere - asthenosphere transition. The process is aided by the blanketing effect of the comparatively intense radioactivity within the crust.

Heating the asthenosphere deepens the main phase boundaries, resulting in transition of mineral types to less dense polymorphs. The resulting volume increase is most easily accommodated by vertical uplift, giving rise to domal arching of the crust. The resultant tension in and bending of the brittle upper crust results in fractures, the egress of basaltic magmas and rift formation.

An alternative theory, of the same type, holds that deep seated heat sources within the mantle are the primary cause of rifting. A world wide system of such convective plumes has been proposed to explain the existence of certain well known magmatic provinces, such as Iceland and the Hawaiian Island-seamount chain (Morgan,1971). According to Morgan, such plumes are the localised upwelling of hot material from deep within the mantle. Compensating downward flow of cooler material is relatively uniformly distributed throughout the rest of the mantle. Morgan argues that it is this type of convective motion which provides the primary driving force for plate tectonics. It is suggested that anomalous upper mantle material, such as is detected under the Eastern rift, results from heating by such a plume. This would give rise to expansion of upper mantle material, resulting in a localised thinning of the lithosphere and doming, as for the Gass model.

The latter category of theories is reprented by the "membrane tectonic" hypothesis of Turcotte and Oxburgh (1973). The essence of this theory is that variation in the radius of curvature of the geoid from the equator to the poles is sufficient to induce brittle fracture in the lithosphere of large plates as they change latitudes. The theory has been applied to the African plate (Oxburgh and Turcotte, 1974). They cite palaeomagnetic evidence as showing that Africa has move northwards at an average rate of about 0.25°/my, for the last 100 million years. The size of the African plate (taken to be 90° in diameter) is sufficient to have induced stresses of up to 135 bars, assuming a total northward movement of 23°. This is sufficient to cause brittle fracture in the upper 25 km or so of continental crust. (Beneath this depth viscous flow takes place over geological time scales.)

As the plate moved northwards, it is envisaged that a crack developed in its interior and propagated southwards. This accounts for the observed uniform progress of the onset of igneous activity southwards along the line of the eastern rift. The theory also explains the significant but finite degree of crustal extension observed for the Eastern rift.

However, the theory cannot, on its own, explain the much larger separations of the Red Sea and Gulf of Aden. Here some other process, perhaps similar to that proposed by Gass, must have taken over to induce the formation of oceanic crust. A similar process must have started beneath the Gregory rift to account for the presence of anomalous upper mantle material.

Whatever the primary cause of rifting, a regional tensional stress pattern must have been present to induce the fault structures observed.

Some early workers (Wayland, 1930; Bullard, 1936) interpreted the rift as a compressional feature, the central block supposedly being held down by the overthrusting flanks. This hypothesis is now discounted as the marginal faulting is overwhelmingly normal (Gregory, 1921; Baker et al, 1972). Also, gravity observations indicate a downward thinning rather than upward thinning central block (Girdler, 1964), and fault-plane solutions of earthquakes in the region indicate a tensional regime (Fairhead and Girdler, 1972).

Heiskanen and Vening Meinesz (1958) have shown how tensional stress within the crust can lead to the formation of a parallel sided fault trough. Figure 1.10 illustrates the process. A primary fault develops with a hade, typical of normal faults, of 50-75°. Bending of the crust on the downthrown side results in maximum bending stress being developed about 65 km from the primary fault and a second normal fault developing parallel to the first. The

FIGURE 1.10

CRUSTAL TENSION AND THE FORMATION OF GRABENS

(Heiskanen and Vening Meinesz, 1958)

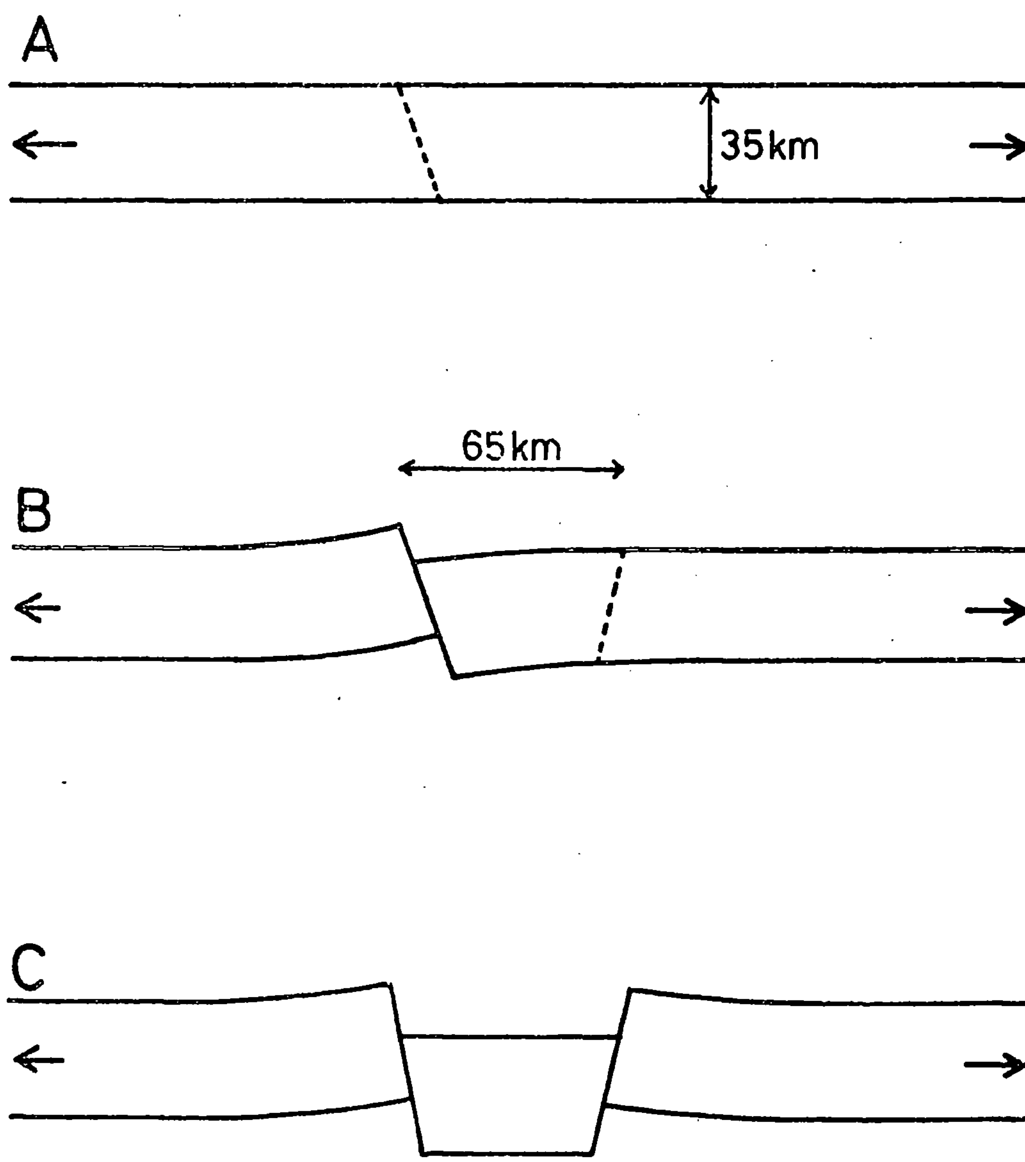

keystone-shaped central block then subsides under its own weight. The isostatic principle is not violated, since the central block narrows downwards, and has to sink farther before its weight is supported by hydrostatic upthrust. By the same principle, the shoulders are raised in relation to their surroundings.

1.7 Summary

The broad features of the crust and upper mantle have been deduced from a variety of geological and geophysical studies, which have been described above. The subtle interplay that exists between deep seated processes within the mantle and the crust has been touched upon, and these are discussed further in Chapter 7.

A full understanding of the underlying causes of the Gregory rift can only be expected when the anomalous zone within the upper mantle has been mapped in detail, and the nature of its connection with the zone of crustal intrusion precisely defined.

Although gravity has helped to map the lateral extent of these structures, the depths, especially of the anomalous zone within the upper mantle, are poorly known. Seismic investigations have helped to control these for the northern sector of the rift (Griffiths, 1972) and for the northwest flank of the dome (Long and Backhouse, 1976), but the picture is not yet complete. The present study is concerned to increase our knowledge of the seismic structures for the southeast flank of the Kenya dome, and the central part of the Gregory rift.

CHAPTER 2

DURHAM KENYA SEISMIC PROJECT : DATA AQUISITION

2.1 Introduction

The Durham Kenya Seismic Project (DKSP) was designed as a cheap method of obtaining seismic data within and to the east of the Gregory rift, where previous seismic work was scant or lacking. Data were to be collected over as wide an area as possible, so that variations in crustal and upper mantle structure might be determined, and to this end it was decided to use a network of independent, widely spaced temporary seismic stations, rather than an array as for the Kaptagat experiment.

Since the field-work was to be managed and largely performed single-handed, no local shots could be organized, as for a conventional refraction experiment. Thus naturally occurring earthquakes were to be the sole source of energy. Locally occurring earthquakes were to be used for crustal studies, whilst recordings of earthquakes at teleseismic distances (greater than 20 degrees) would give information on deeper structure. Recording was to last about 18 months altogether to ensure collection of sufficient data. One long-duration magnetic tape recorder was to be used at each site, recording signals from a three-component set of seismometers, so that complete ground motion could be continuously monitored at a number of stations simultaneously.

2.2 Site Equipment

The scientific equipment at each site comprised a three-component set of seismometers, a Durham MkIII seismic recorder and a NATIONAL PANASONIC transistorised short-wave radio receiver, together with the required interconnecting cables. The purpose of the radio receiver was to receive G.M.T. pips which are frequently transmitted over the B.B.C. World Service, and which were used as timing standard.

2.2.1 Seismometers

Willmore Mk II Seismometers (Hilger and Watts, 1964) were used throughout, although six Willmore MkIII seismometers were also available. The latter gave so much mechanical trouble that they were never actually installed. Several MkII seismometers were also unusable due to broken coils.

The seismometers were set to have a natural period of 2.0 seconds, which was checked by observing the undamped motion of the mass, either directly, or by displaying the resultant electrical signal on an oscilloscope, and by timing ten or more cycles using a stopwatch.

A suitable fixed resistor, Rd, was then connected in parallel with the coil, to give damped oscillations with about 10% overshoot when the mass was disturbed. The oscillations could be observed and measured either on a storage oscilloscope or oscillograph. This degree of overshoot gives an optimum damping factor of about 0.7. A value of 4,700 Ohms for Rd was generally found satisfactory. The damping resistor, together with a balance resistor, Rb, equal to the parallel resistance of the coil and damping resistor was mounted inside the seismometer case, and the whole connected to the recorder input via a twin screened cable, as shown in Figure 2.1.

The balance resistor serves two purposes. Firstly, it equalizes the resistance to ground of the two internal cable conductors, balancing out electrical pickup at the recorder's differential input. Secondly, it acts as part of the Wheatstone bridge input circuit for the application of a calibration current to the seismometer coil, as explained in Section 2.2.2.

It was found that once installed and adjusted the seismometers rarely needed further attention, except for those which were vertically orientated, for which the mass occassionally drifted out of position to "bottom" or "top" against one or other stop.

2.2.2 Seismic Recorders

The Durham MkIII Seismic recorders used for DKSP are an improved version of the MkII recorders described by Long (1974). The major differences between the MkIII and the MkII recorders are as follows:-

FIGURE 2.1

DIAGRAM OF SEIESMOMETER AND RECORER INPUT CIRCUITRY

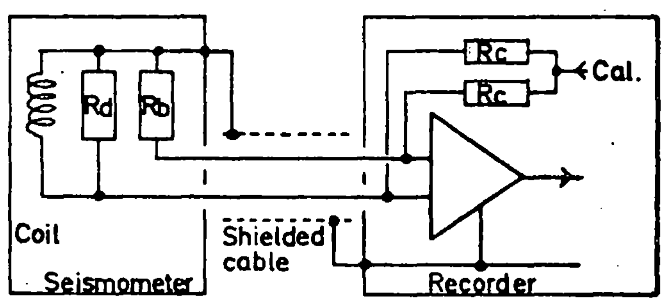

Schematic Diagram

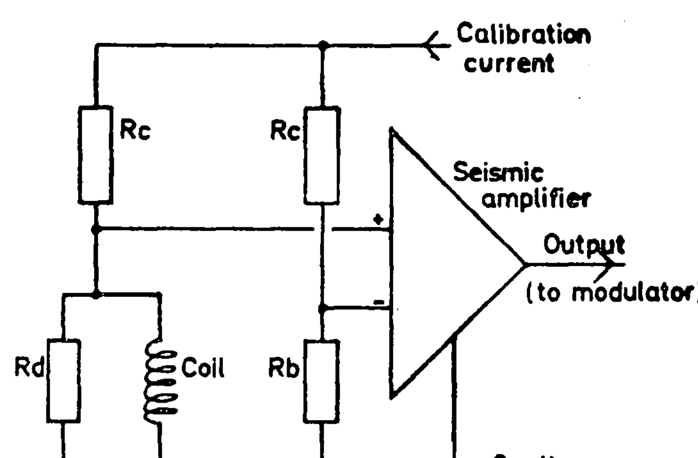

Circuit Diagram

i) The TANDBERG tape transport has been replaced by a NAGRA IV tapedeck, modified to receive two eight track heads and, by the incorporation of an additional small motor, to run at very low speeds.

ii) A simplified power arrangement is used, requiring only one battery bank. Total power requirement has been reduced to some 125 mW. In Kenya ,where battery life is somewhat prolonged by the generally warm temperatures, a set of six internally housed PP9 batteries will usually keep a recorder running continuously for at least three weeks.

iii) The whole equipment is housed in a single light-weight alloy case, dispensing with the need to interconnect three separate units as in the case of the MkII recorders. Thus, the inherent unreliability of cables and connectors is circumvented, and the whole arrangement is somewhat better protected against dust and moisture.

iv) The clock circuits have been redesigned and the controls are more easily understood. Display of clock time and status is continuous, and more intelligible, using liquid crystal display panels. The incandescent displays used in the MkII sets consumed much power and were switched on only for reading. More information is encoded into the MkIII timecode, a clock "year" of a hundred days being encoded along with additional information about the clock's status.

The recorder uses standard "Hi-Fi" quality 1/4 inch tape, nominally running at 0.07 inches per second. The recorder can accomodate spools of up to 7 inches in diameter. The tape used for DKSP was AGFA-GEVAERT triple play type, with 3,600 feet per reel. In theory a reel should last 7.14 days, but in practice it was necessary to wind an extra length of tape onto each new reel to give a full 7 days recording.

The tape is divided into eight tracks, recording in one direction only. Each track was used for a separate frequency modulated carrier, the frequency of which lies nominally between 50Hz and 100Hz.

Tracks 1,3 and 5 are used for recording the seismic signals, while 6,7 and 8 are devoted to recording a reference frequency, radio signals, and the clock generated timecode respectively. Tracks 2 and 4 were not used for DKSP, but are available for extra seismic channels if required.

The constant reference frequency of 100Hz recorded on track 6 is used during playback to maintain the correct average replay speed, and to help compensate for remaining speed variations ("flutter"), as explained in Chapter 3 and Appendix 1.

The signals applied to tracks 7 and 8 are essentially binary in character, being switched between 50Hz (binary "low") or 100Hz (binary "high"). The radio signal is derived from the short-wave receiver via a detector and trigger. Thus a binary high is recorded on track 7 only while the amplitude of the received audio signals is above a certain threshold. In this way the G.M.T. pips which consist of six bursts of a 1kHz tone are squared up, the objectives being to aid their subsequent recognition and measurement when they are played out, and to avoid bandwidth problems associated with recording such high frequencies using a low tape speed.

The timecode recorded on track 8 consists of binary high pulses whose leading edges occur at precise one second intervals. The durations of the pulses are 0.2, 0.4 or 0.8 seconds. The 0.8 second pulses occur every 60 seconds and mark the first second of each minute. The remaining pulses are grouped in six blocks of ten. The first eight pulses of each block correspond to a two digit binary coded decimal word. 0.4 second pulses correspond to binary ones, and 0.2 second pulses to binary zeros. The final two pulses in each block are of 0.2 and 0.4 seconds duration respectively.

The first four blocks of each minute of normal time code represent clock minutes, hours, days and "years" respectively. The fifth block records the site number, and the sixth the clock status and seismic amplifier gains. (A sample of timecode is illustrated in Figure 2.2.)

The clock counting and the 100Hz and 50Hz modulation frequencies for the reference, radio, and timecode are all derived from a single quartz crystal oscillator, and are

FIGURE 2.2

SAMPLE OF TIMECODE

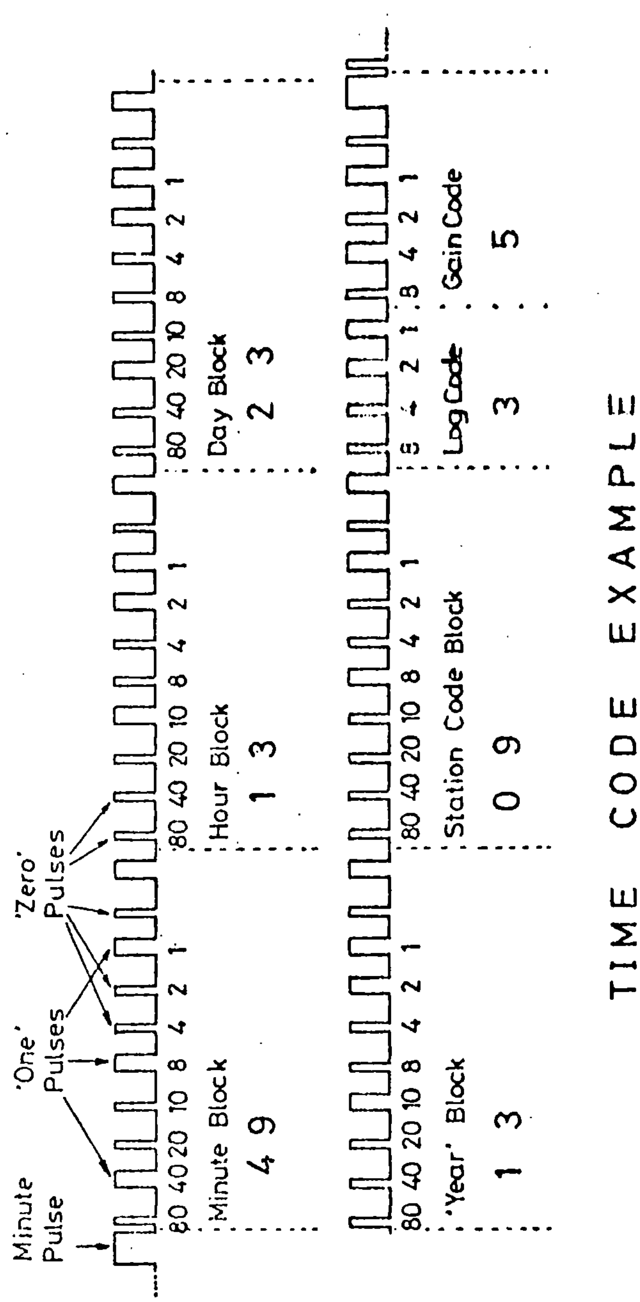

normally quite stable. Clock drift was of the order of one second a month, so that resetting was only necessary when installing the recorder initially, or after a malfunction had caused the clock to lose count ("jump").

Clock setting on initial installation was usually done by entering the appropriate information into each block while in a "hold" status, using the appropriate control switches. Normal counting status could then be initiated by depressing a switch as near as possible to an hour, while listening for G.M.T. pips on the radio. Clock jumps generally occurred as discontinuities of whole numbers of minutes or hours, in which case the relevant blocks were corrected while the clock was counting.

The resulting clock errors, which were usually not more than a few seconds, were of no consequence, as subsequent calibration against the recordings of G.M.T. pips gave complete information on their magnitudes and rates of change, providing jumps were not too frequent.

The signals from the seismometers were fed to the seismic amplifiers where they are amplified before being used to frequency modulate a 71Hz (nominal centre frequency) carrier. Maximum carrier deviation is 33% nominally, corresponding to saturation in the amplifier section. The amplifier gains can be switched by factors of two. Ten settings are available, numbered zero to nine. This allows selection of optimum gain corresponding to the expected signal level and ambient seismic noise, taking into account the dynamic range of the recorder.

The recorder incorporates test features to monitor all recorded signals, display being on three meters, referred to by the letters A, B and C. A mode switch selects one of two display modes. In the record mode the premodulation signal for any track can be selected and displayed on meter A, while meter C displays a peak level of the same signal, averaged over about three seconds. In this way signals which are varying too quickly for Meter A to follow, can be detected and their amplitude measured. Meter B indicates the amplitude of the carrier signal applied to the tape head for the track selected. Shorts in the head wiring and malfunction of the oscillator show up as a lower than normal reading, while an open circuit head is indicated by an abnormally high reading. When in the playback mode, meters A and C register the demodulated signal for the selected track, derived from a monitor head placed after the record head, in the same way as for record mode. Meter B displays the replayed carrier amplitude. In addition, the amplified carrier can be heard on an earpiece when plugged into the recorder. This is a useful facility as the ear can detect changes in the quality of the recorded signal which sometimes do not register on the meters.

There is no compensation for recorder flutter, which is detectable on meter A in the playback mode and audible in the earpiece as a distinct wavering in pitch of the reference track signal. Such flutter is estimated to be about 5% normally.

The input circuit of each seismic channel comprises a Wheatstone bridge, (as illustrated in Figure 2.2). A sequence of calibration current steps, going first positive, then to zero, and then negative can be applied through the bridge to move the seismometer mass. The bridge is balanced so that the current itself produces no differential voltage input to the amplifier, but the output voltage resulting from the motion of the seismometer mass is fed to the input. The current step produces a small displacement of the mass' equilibrium position, so that it executes damped oscillations. The resulting signal (Figure 2.3), when played back, is the impulse response of the seismometer-recorder-playback system, and can be analyzed to give frequency response and other information (for example Espinosa et al, 1962). The train of four pulses can be generated manually, and this is a good check of overall system function, since the signal can be monitored both before and after being recorded, and can be heard as a distinct variation in pitch. The amplitude of the calibration pulse is varied by factors of two (nominally) in step with the amplifier gain, so that the pulses are recorded with the same frequency deviation, irrespective of the gain setting. The recorder can be left in an automatic mode whereby a train of four pulses is recorded for each seismic channel soon after each clock midnight. This is useful as a daily check on seismometer response.

FIGURE 2.3

REPLAYED CALIBRATION SIGNAL

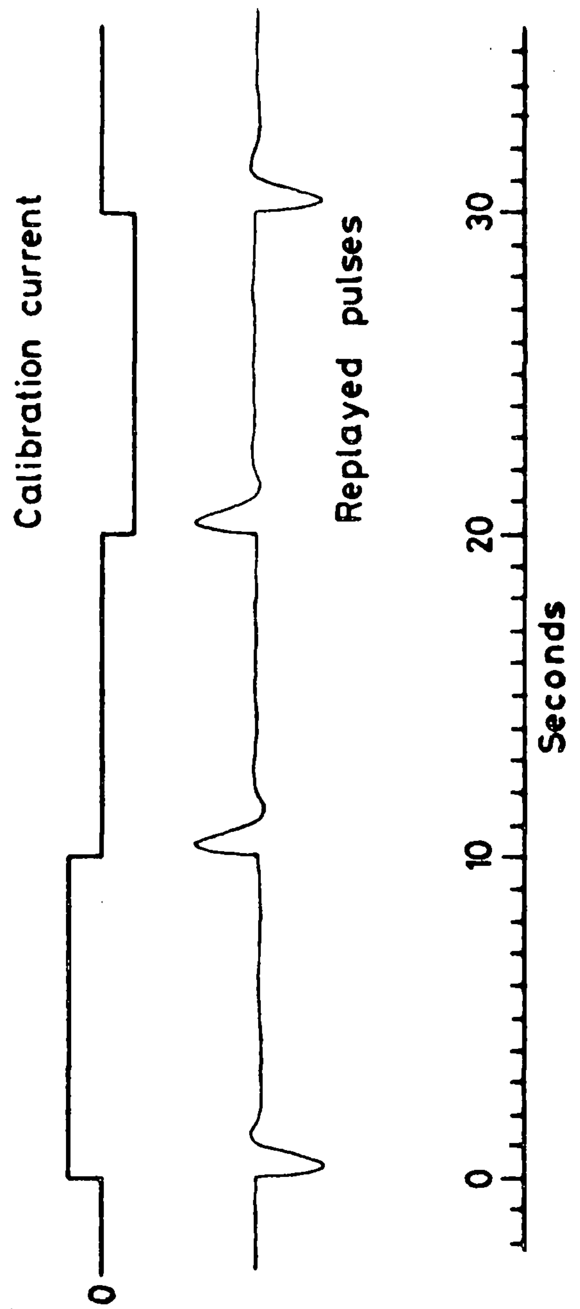

2.2.3 Radio Receivers

NATIONAL PANASONIC transistorised receivers, capable of reception of a.m. signals on the short wave broadcast bands, were used to receive G.M.T. pips transmitted by the World Service of the British Broadcasting Corporation. These pips were used as the primary standard for all timing. These sets were modified to use the tone switch to cut out the internal loud-speaker, thus reducing power consumption, and by the soldered connection of a 3 metre aerial wire to improve reception.

Reasonable reception could be obtained at different times of day on different wavebands, but in general the receivers were left tuned to the transmissions on 15.42 MHz, which provided the most consistently good reception, during daylight hours at least.

The output amplitude is varied by means of the receiver's volume control. This effectively alters the threshold level of the amplitude detector. This setting is quite critical: if the volume is set too high, noise triggers the detector, while if it is too low the G.M.T. pips are not recorded. Accurate tuning is also essential, and requires a delicate touch.

Propogation conditions on the short wave bands are notoriously variable, and these radios, being inductor-capacitor tuned, tend to drift off-frequency quite rapidly. The human ear can adjust to rapid changes in volume, and extract information against remarkably high levels of background noise. Readjustment of tuning every quarter of an hour or so is not a great burden to the domestic user, so these cheap sets are adequate for their intended purpose. However, for the continous reception of a single signal at an unsupervised site, under widely varying propagation conditions and ambient temperatives, they are far from ideal. Even when continuous readjustment of volume and tuning is made by an experienced operator, a set of pips can easily be lost, so that the satisfactory recording of G.M.T. pips at other times is a matter of good luck, although great care by operators to leave the sets well adjusted increases the chances of success.

It is recommended that future experiments of this sort employ crystal tuned receivers, with the excellent automatic gain control now available through integrated circuit technology. Such sets could be built as cheaply as the domestic sets used for DKSP.

2.3 Site Layout

All the seismic equipment was usually housed together in a Ø.9m diameter corrugated iron drum, set into a hole dug in the ground, or on to bedrock if exposed. The drum was about Ø.6m deep and provided with a lockable lid. The base of the hole and the bottom of the drum were filled with concrete to provide a stable, well coupled base for the seismometers. The arrangement was generally proof against both rain and seepage of ground water.

The radio and recorder were placed on a wooden table straddling the seismometers, as shown in Figure 2.4, with the aerial wire laid out on the ground away from the drum. The drums were usually surrounded by a circular thorn-bush fence of some 15 metres diameter, to guard against wild or stray animals and to deter would-be theives. A twenty-four hour guard was placed on many of the sites as an additional safeguard against theft, especially after equipment had been stolen from two sites, previously considered safe, early during the fieldwork.

The arrangement described above was modified at sites 31, 11 and 17. At site 31 a corrugated iron hut was used. At the latter two sites only the seismometers were housed in the drums, the recorder and radio being housed indoors and connected to the seismometers by means of buried cables.

The horizontal seismometers were aligned using the following method. A taut string was positioned over the drum and adjusted until it was aligned north-south, as checked by sighting using a prismatic compass, and taking account of local magnetic deviation. This direction was transferred to the concrete base by aligning one arm of a large, wooden try-square with the string, by eye, and ruling the two required lines at right angles with chalk. The horizontal seismometer stands could be lined up with these marks. It is estimated that the error in alignment was no more than three degrees.

Site positions were marked on to Survey of Kenya

FIGURE 2.4

ARRANGEMENT OF EQUIPMENT INSIDE DRUM

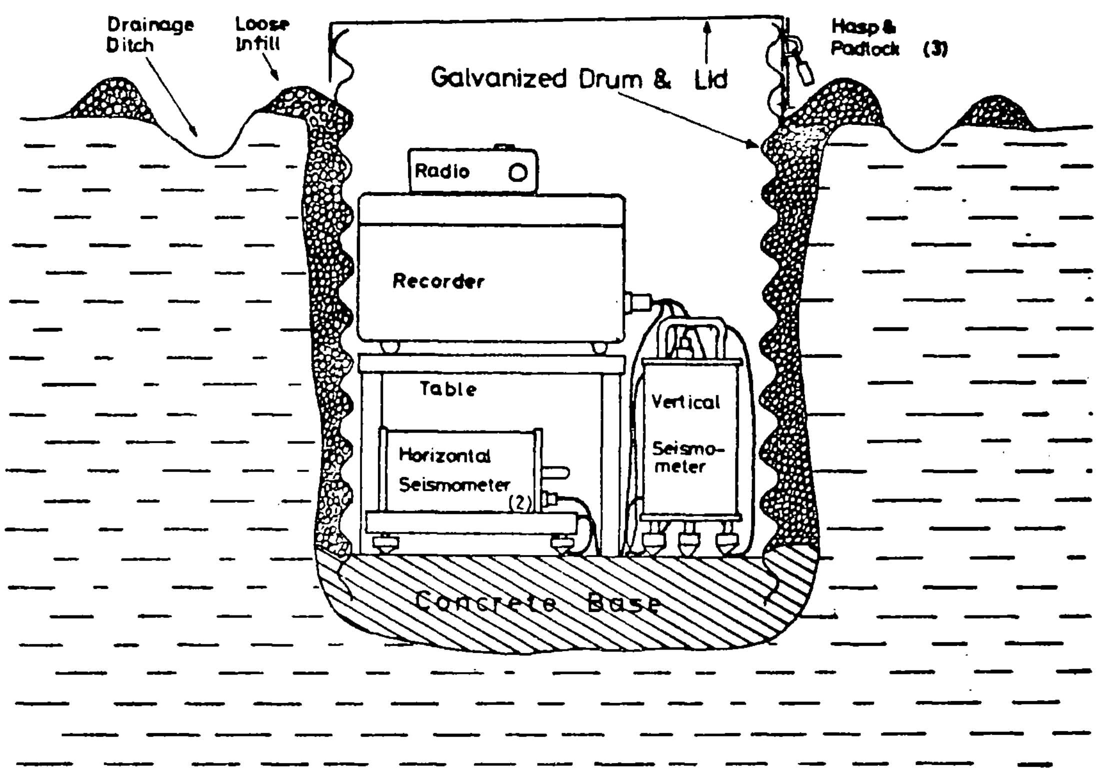

1:50,000 scale maps in relation to local features, using whatever combination of compass bearings and distance measurements were appropriate. Estimated error circles were also marked on the maps. The site coordinates were then measured from their plotted positions, and heights obtained by interpolating from contours.

The station coordinates are listed in Table 2.1, and Figures 2.5 and 2.6 show their positions.

2.4 Station Visits

The operating stations were visited routinely every six or seven days. During these visits the tapes were changed, the tapeheads cleaned and routine checks performed. At least one set of G.M.T. pips was recorded during each visit if at all possible, as there was no means of telling if pips had been successfully recorded at other times. Frequently this meant waiting an hour or two, and occasionally it was not possible to obtain a satisfactory recording of pips at all.

Not infrequently the recorders were found to be faulty. Minor repairs could be performed on site, but usually it was necessary to remove the recorder to work on it in easier surroundings. Repairs could often be made in a day or two and extra visits were often made to return recorders or swop them about.

Site 50 was visited by air, but all the others were easily accessible by landrover.

TABLE 2.1

DKSP STATION COORDINATES AND HEIGHTS

STN. NO.	STATION NAME	LATITUDE (DEG. NORTH)	LONGITUDE (DEG. EAST)	HEIGHT (METERS)	ERROR (METERS)
08	MOLO	-0.3118	35.6724	2745	200
09	LONDIANI	-0.1715	35.8185	1919	250
10	EGERTON	-0.3572	35.9210	2255	150
11	NAKURU	-0.2753	36.0885	1888	150
12	GREENSTEDS	-0.3415	36.1757	1922	100
13	OL KALOU	-0.3275	36.3625	2360	100
14	NJORO	-0.3313	35.9385	2168	100
15	ELMENTEITA	-0.5032	36.1160	1834	100
16	ILKEK	-0.5957	36.3642	1940	150
17	NAIVASHA	-0.7953	36.2778	1900	150
18	LONGONOT	-1.0175	36.4965	1695	250
19	KIJABE	-0.9310	36.5687	2188	100
21	UPLANDS	-1.0658	36.6850	2306	250
22	NAIROBI	-1.2740	36.8037	1691	40
23	ISINYA	-1.6763	36.8515	1640	100
24	ULU	-1.8210	37.1775	1660	200
25	KESIKAU	-1.9130	37.3590	1321	250
26	SULTAN HAMUD	-2.1738	37.4392	1178	150
27	MAKINDU	-2.2680	37.8035	978	150
28	KIBWEZI	-2.3458	38.0067	867	150
29	MTITO ANDEI	-2.6388	38.1333	797	150
30	TSAVO	-2.9255	38.3833	618	150
31	OLOITOKITOK	-2.8138	37.5288	399	150
50	LODWAR	3.1255	35.6173	564	250

FIGURE 2.5

MAP OF DKSP STATIONS THROUGHOUT KENYA

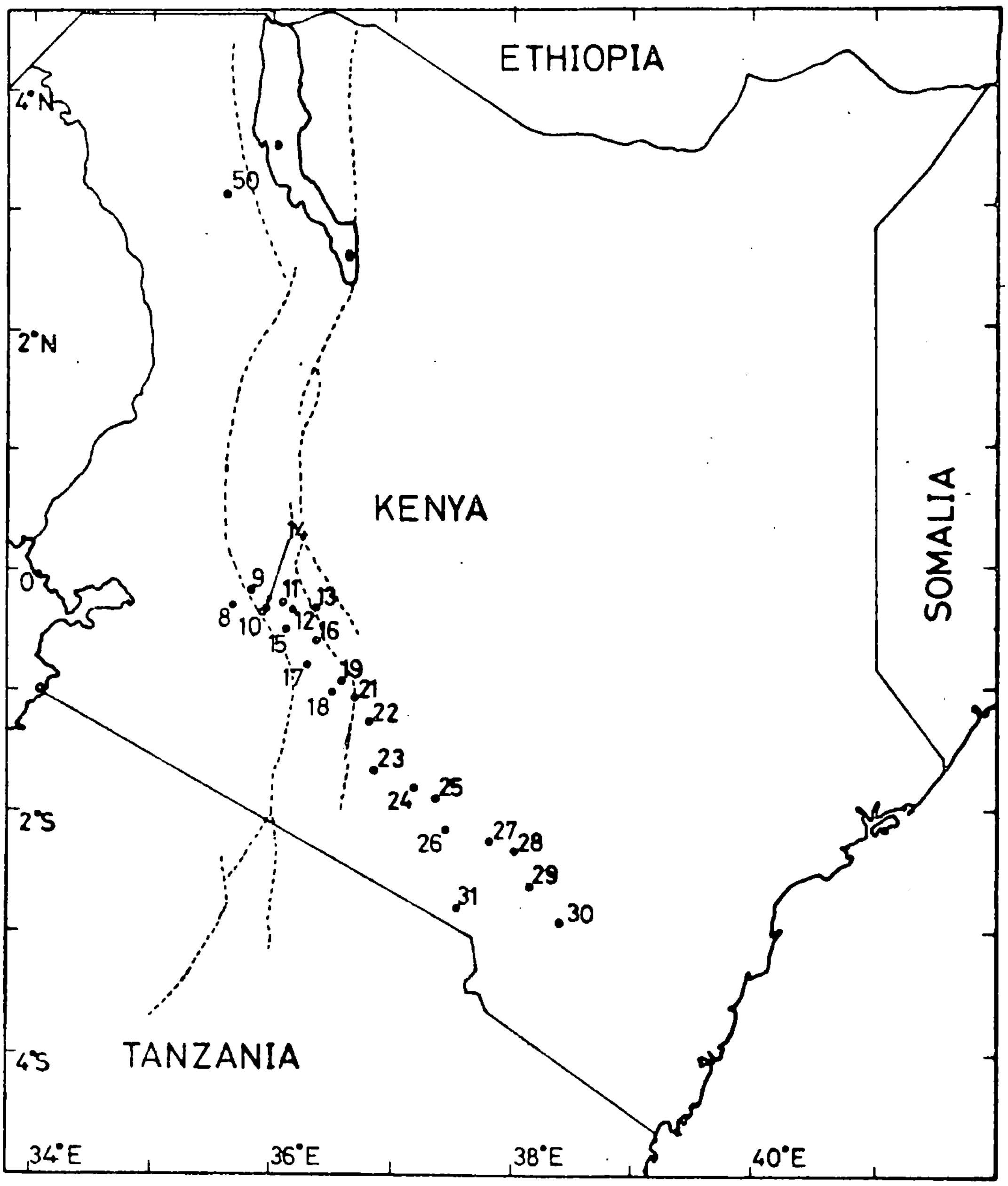

• D.K.S.P. Seismic Recording Stations
------ Gregory Rift Boundary Faults

FIGURE 2.6

MAP OF DKSP STATIONS WITHIN THE GREGORY RIFT

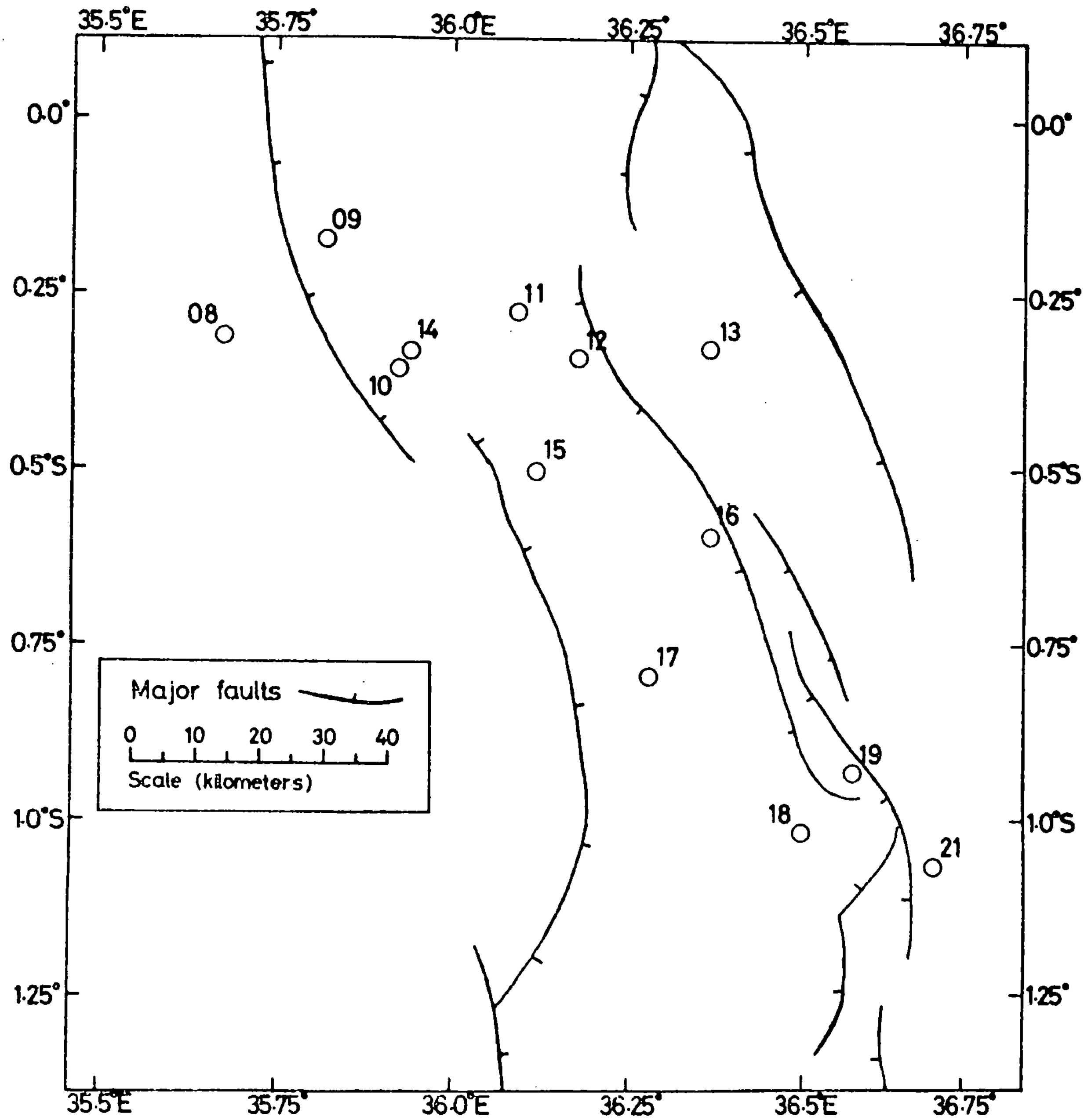

2.5 Management of Field Work

The DKSP field work comprised three main phases. Phase I was managed by Mr. R.A. Burley, then of Durham University. He arrived in Kenya in September 1975 and obtained the necessary research authority from the Kenya Ministry of Education, commissioned the long wheelbase landrover (Reg. No. KPK495) which was used throughout the project, and started the search for suitable sites.

The equipment, including nine recorders, was air freighted out to Kenya at the end of October and cleared through customs. November and December were spent checking, repairing and cleaning the equipment.

Recording was initiated on 3rd January 1976, and between then and September 1976 sites number 09,10, 11,12,18,19,21,22,23,24,25,26,27,28,29,30,31 and 50 were occupied, between three and six being used at any one time according to the serviceability of the recorders.

The primary purpose of this phase was to obtain suitable recordings of teleseismic events over the eastern flank of the Kenya dome for delay time analysis. Variation in delay would enable the structure of the upper mantle anomaly in this area to be mapped.

The profile running south-east from the highest point of the dome along the Nakuru-Nairobi-Mombasa road was chosen, primarily because of easy access. The profile runs perpendicular to the lines of the topograghic and Bouguer anomaly contours between stations 21 and 30, and is therefore presumably along the local dip of the upper mantle structure over the flank. However it has the disadvantage of meeting the Kikuyu escarpment, which marks the eastern boundary of the rift at this point, at a very acute angle, and at a point where the faulting trend turns from a N-S direction to a NW-SE direction. A line running across the Gregory rift and Kenya dome E-W or NE-SW might have been preferable. However such a line would have been difficult to maintain, as it would have crossed the Aberdare range and the flanks of Mt. Kenya. The unknown, but considerable, thicknesses of volcanics, would have made interpretation more difficult.

Phase II began when the author took over management of stations 09,10,11 and 12, left operational by Mr. Burley in late September 1976.

It was intended that this phase of recording should use a line of stations across the Gregory rift for a refraction-like study of local and regional earthquakes, especially from the east and west, to give information on crustal structure.

At the beginning of this phase, four stations within the Gregory rift had been installed by Mr. Burley. At the workshop in Nairobi there were three recorders which had broken down in the previous months, together with a serviceable recorder which had just arrived from England. (Two recorders had been stolen during Phase I and not recovered). During the next few weeks much time was spent attempting to repair the broken recorders, and occupy further sites with serviceable equipment. Site 13 was occupied on the 6th October, and 08 on the 30th October, thus forming an approximately straight line of six stations across the rift from Molo to Ol Kalou.

The recorders had been unreliable during Phase I, and they continued to give much trouble during Phase II.

Mechanical troubles which arose included worn heads, failing motors, and jerky tape motion caused by "stiction" (stickiness due to static friction being much greater than sliding friction) in the tape-tensioning/spool-breaking mechanism. At first the worn tapeheads were replaced by new units, but the stock of these soon ran out. Further units were not sent out from Durham, and so the author experimented with methods of restoring the correct shape by grinding. The best technique found, was to use abrasive grits of increasingly finer grades, mixed with water, on a glass plate. This admittedly drastic action gave surprisingly good results. Failing motors had to be replaced by new units. The "stiction" in the tape-tensioning mechanism was due to build-up of dust on the feed spool brake pads, which are made of felt. It is recommended in the recorder operating manual that these be lightly oiled, but the author found that the presence of oil increased the tendency of the pads to pick up and retain dust. He therefore embarked on a policy of cleaning the pads in isopropyl alcohol, to remove both dirt and oil. The oil-free pads seemed to need attention far less often, although the problem could not be entirely eliminated. The root of the trouble is that the deck is running at about a twentieth of its designed minimum speed, so that there is insufficient angular momentum in the feed spool and hub to overcome the small irregularities in the braking mechanism.

In many cases the Durham manufactured head mounting blocks set the heads asymmetrically on to the head and/or held the heads too low on the tape, exposing the lowest segment. Filing out the screw holes allowed the block to be rotated so that the tape passed each head symmetrically, and so that the gaps coincided with the point of greatest pressure. The head could be shimmed up to improve its position relative to the tape. Bent tape guides were discovered on many of the recorders which caused the tape to pass the heads at odd angles, introducing a skew component.

Among the numerous electronic faults that arose, clock failures were the most common and the most difficult to rectify. The author cannot agree with the assertion that the circuit consists of "a simple loop of some six packages" which is "ultra reliable" (Long,1974). The clock circuit in fact uses some 40 integrated circuits, and experience on DKSP (as well as other projects) has clearly demonstrated their inherent unreliability. Complete clock breakdowns were frequent on DKSP and even working clocks jumped often. Recorders' clocks will not keep time if transported, and even slight shock is enough to make them jump. This sensitivity to shock is undoubtedly due to the poorly designed mounting arrangement for the clock board, which allows it to move in its edge connector.

Integrated circuit failures were very common, despite their widely recognised inherent reliability. Quite possibly this was due to damage caused by static electricity during assembly, as recommended earthing procedures for these COSMOS circuits had not been followed.

It is shown in Appendix 1 that even under optimum conditions, the specifications for the Durham Seismic Recorders and the corresponding replay equipment fall far short of those which are claimed for it (Long 1974), and which are considered adequate for seismological investigations. This, together with their inherent unreliability, makes them far from ideal for studies of this nature where simultaneous recording at as many sites as possible is essential.

Phase II of DKSP recording finished in early January 1977, when the equipment at sites 10 and 13 was removed.

Phase III recording was to use a zig-zag network of stations offset alternately to the east and west of the inferred position of the axial intrusion, with the major axis of the network running down the centre of the Gregory rift. Local earthquakes, especially from southerly back-bearings, were expected to give rise to phases refracted along the relatively high velocity intrusion, and it was hoped that these would be detected.

The stations were to be left in the hands of Kenyan residents who could perform the routine tape changes and checks. Local residents were approached and asked if they would undertake the work, and it is greatly to their credit that all enthusiastically undertook the work, which was without remuneration.

Selection of sites for this phase was additionally constrained by the consideration of ease of access for the operators. Therefore, equipment tended to be located in gardens and near to buildings, and hence sources of seismic noise. Sites 15 and 17 were inconveniently near generator sheds and borehole pumps, but these were only operated for a few hours each day and alternative sites were not available.

The lack of ideal sites meant that three stations had to be located at previously occupied sites: these were 11,12 and 18. Moreover, site 14 was situated only about 3.5km from site 10. The final configuration consisted of sites 11,12,14,15,16,17,18, and all the equipment was installed and the operators trained by the end of January 1977. This allowed the writer to return to Durham on the 7th February to begin replaying the recorded tapes.

Mr. Burley returned to Kenya in June, and repaired the recorders at sites 12 and 15 which had broken down in March and May respectively. He supervised the remaining period of recording which lasted until the beginning of July.

The remaining stations were then dismantled and the equipment put into storage at the University of Nairobi.

The equipment was eventually shipped back to Durham in August 1978.

CHAPTER 3

DURHAM SEISMIC PROCESSING EQUIPMENT AND THE PRELIMINARY EXAMINATION OF DKSP TAPES

3.1 Introducion

This chapter describes the playback, filtering, computing and display equipment available at Durham and which was used to process the field tapes. The clock calibration method and measurements of filter delays are also described, and these allow the accurate, absolute timing of seismograms. Possible sources of timing errors are discussed and the magnitude of the overall error determined.

The equipment used in processing the DKSP tapes consists of the following items:

i) a quarter-inch playback deck and associated demodulating electronics,

ii) a set of wide-range variable frequency filters,

iii) a 16 channel jet pen oscillograph,

iv) a 12 channel medium persistence oscilloscope,

v) a timecode decoder/display,

vi) a single channel drum oscillograph, and

vii) a Modular 1 computer.

Interconnection between the various devices is made through a patch board. This consists of a row of forty-eight 58-way slide switches, which allow any input of a chosen device to be connected rapidly to the selected output of any device by appropriate positioning of the relevant peg.

3.2 The Quarter-inch Playback System

A block diagram of the basic system, designed by Dr. Long and built at Durham, is shown in Figure 3.1. A modified Nagra IV tape deck, fitted with an eight-track tape head similar to those used in the Durham Mk III recorders, reproduces the frequency modulated carrier signals which are fed to the demodulators.

The demodulators amplify the carrier signal and convert the instantaneous frequency to a corresponding voltage level. The system uses phase locked loop (PLL) circuits to perform the frequency to voltage conversions as they are less susceptible to superimposed noise than other types. However the PLL circuits only work properly within a certain "locking range" of frequencies. Outside this range the output voltage fluctuates randomly. For the seismic and reference tracks the output voltage is proportional to frequency, while for the timecode and radio tracks the circuits are wired up as frequency comparators. In the latter mode, the output voltage represents a binary high while the input frequency is above a certain value and binary low when it is below. The demodulated signal is passed through a 250 Hz low-pass filter to remove residual carrier before being outputted.

The replay speed is controlled by a servo-loop to run at ten times the recording speed. Correction signals which

FIGURE 3.1

BLOCK-DIAGRAM OF THE DURHAM PLAYBACK SYSTEM

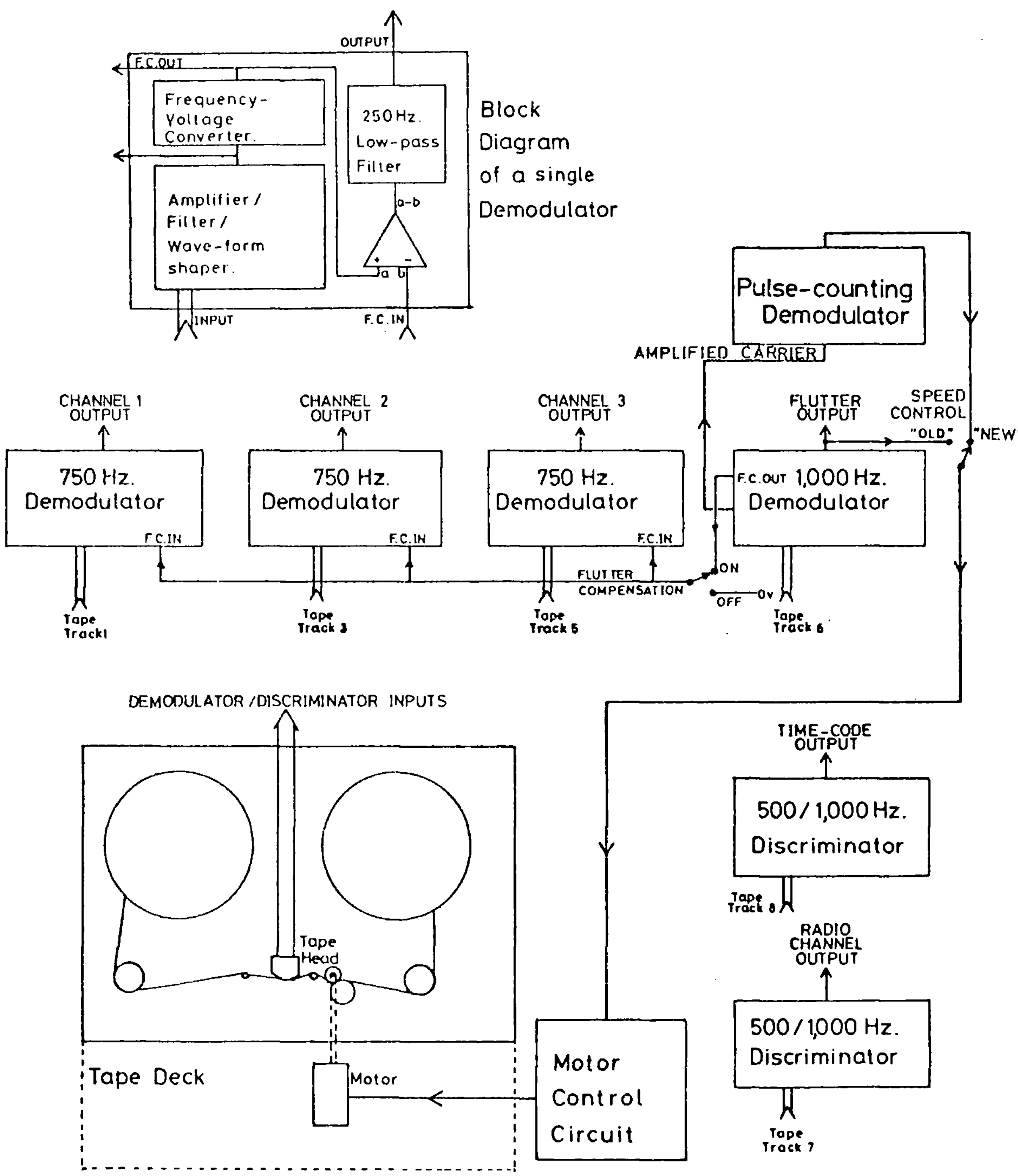

control the tape deck motor voltage are derived from the reference track.

Originally, the PLL demodulated signal was used to control the tape speed, but this was unsatisfactory as the speed control system would go "out of lock" on encountering poorly recorded or distorted segments of tape, which occur frequently. The tape would then continue to run at too high a speed for the demodulator to function. The author made various attempts to counteract this tendency by adding circuitry to limit the maximum motor voltage and so prevent the out of lock situation arising. These attempts were only partially successful, as setting of the limiting voltage was critical and resulted in a compromise between effective prevention of the out of lock condition and proper control of playback speed.

Eventually, the author added a pulse-counting demodulator, with a much wider input frequency range, to derive the speed control signal. This has proved entirely satisfactory in preventing the out of lock condition arising, and will cope with poorly recorded tapes better than the PLL based loop.

Although this method of speed control maintains the average replay speed at exactly ten times the record speed, despite variations in the latter, inertia in the moving parts of the tape deck introduces a degree of instability. Consequently additional flutter is introduced, superimposed on that produced by the recorder. The total flutter on playback has been measured by observing the demodulated reference track output signal on an oscilloscope, having calibrated the demodulator using a test oscillator and Avometer. Typical measurements, on well recorded tapes, indicate 15% speed variations, and these have been confirmed by observations of incomplete flutter compensation for near-saturating low frequency test signals (see Appendix 1).

Tape speed variations alter the frequencies of replayed carrier signals, and these variations must be compensated for if excessive noise is not to be introduced into the reproduced seismic signals. The method chosen in the Durham Playback System is to electronically subtract the demodulated reference signal from each of the demodulated seismic signals. For the method to work effectively, the reference demodulator and each of the seismic demodulators must have a matched amplitude and phase response, and there must be no time shift in the replayed signals due to tape-head misalignment. Subtraction is performed before 250 Hz filtering so that mismatch between filters, due to component variations in these sections, does not affect the compensation.

The sensitivity of the seismic demodulators can be matched to the reference demodulator by means of presettable "gain" controls. Also, the tape head may be realigned to minimise "skew" by means of a three point screw attachment on the tapedeck. Residual flutter is reduced to a minimum by making these adjustments, while observing the seismic signals on an oscilloscope.

Readjustment is necessary each time a tape from a different recorder is to be replayed, and frequently at other times. This is because of differences in head alignment between recorders and occasional weaving of the tape over the record heads, and because the centre frequencies of the seismic modulators often differ, and sometimes vary with ambient temperature.

Appendix 1 describes tests made on the recorder/Playback System to determine frequency response and dynamic range. Usually dynamic range is defined as the ratio (expressed in decibels) between a signal which just saturates a system and one which is just detectable in system noise. A second definition is intended to reflect the accuracy with which signals are reproduced, and accordingly it is defined as the ratio between signal size and the precision with which it is reproduced.

Appendix 1 measurements show that according to the first definition, dynamic range (with the seismic amplifier gains set as for DKSP) is only 35 dB. This compares very unfavourably with the figure of over 50 dB claimed for the equipment (Long, 1974) and which is usually regarded as acceptable for seismic work.

The subtraction method of flutter compensation is discussed in Appendix 1 and it is shown that this method cannot completely compensate for speed variations in the presence of recorded signals. It is shown that for the

Durham System, noise equal to 15% of the instantaneous value of the recorded signal is added and that this corresponds to a dynamic range, using the second definition, of only 23 dB.

Theoretically, complete flutter compensation in the presence of recorded signals may only be obtained by a process involving division of a function of the demodulated reference signal into a function of the seismic signal. Experiments using the Modular 1 computer to perform the division were tried, and although results demonstrated that the principle worked, reducing flutter at the peaks of test signals, the residual flutter in the absence of signals was greater than for electronic subtraction.

This might have been due to crossfeed which is known to occur between the input channels of the computer, or more probably to mismatch in the 250 Hz demodulator filters which had to be included before digitization to prevent aliasing of the residual carrier.

3.3 Variable Frequency Filters

During the early stages of playing out of seismograms, the three KROHN-HITE model 335 variable frequency filters originally in use gave much trouble and were replaced by three KEMO model VBK/8K filter units, kindly loaned by the Atomic Weapons Research Establishment's Seismological Unit at Blacknest.

According to the manufacturer's specifications, the characteristics of the two types of unit are similar, having a 24 dB/Octave roll-off.

The KEMO filter units each consist of two identical sections which may be switched into high- or low-pass modes. The corner frequencies are variable, being set by means of three decade switches and a range switch. The two sections may be used independently or switched in parallel, but invariably during this study the two sections were used in series, giving either a sharp 48 dB/Octave low-pass characteristic or a band-pass characteristic.

The KROHN-HITE filter units also have two sections each, one high-pass and one low-pass. The corner frequencies are variable by means of range switches and dials. Either section may be switched out giving a high-pass or low pass characteristic, or the two sections may be connected in series or parallel.

The necessity for and the effect of analogue fitering is discussed in Section 3.8.

3.4 Jet Pen Oscillograph

For the permanent display of multichannel seismic data, a 16 channel ELEMA-SCHONANDER Jet Pen oscillograph is available at Durham.

Paper is drawn past 16 capillary ink jets at a constant, selectable speed. Available speeds range from 0.25 to 100 cm/sec. The jets are directed towards the paper and are coupled to galvanometer movements which alter their directions in a plane perpendicular to the motion of the paper. While the paper is in motion, a constant stream of ink from each jet traces a curve which reproduces the electrical signal fed to the corresponding galvanometer. The galvanometers are mechanically damped to give a constant amplitude response to at least 250 Hz, the highest seismic frequency presented to them.

The input signals are amplified before being fed to the galvanometers, and the gain of each amplifier is variable. There is a switched coarse gain control and a continuously variable fine gain control, which may be returned to a presetable position.

Before each session of use, the oscillograph was checked, and if necessary recalibrated using the following method.

Timecode from the playback deck is displayed on each channel, this being a suitable rectangular signal of constant amplitude. With the coarse gains all at the same setting, the fine gains are adjusted to give the same trace amplitude on all channels. Relative displacement of the jets along the direction of the traces (skew) is checked for by drawing a best fitting straight line through the leading edge of a common pulse; any jet more than 0.2mm out of alignment is realigned by means of the corresponding screw adjustment provided for the purpose.

The timecode signal has sharp leading and trailing edges which are useful for indicating deficiencies in the damping. Underdamping shows up as damped oscillations superimposed on each step of the waveform, while overdamping is indicated by comparatively slowly rising and falling edges to the pulses. Such effects were often noticed, but their effect on the more slowly varying seismic signal was considered negligible.

When properly maintained, the oscillograph is reliable and produces very clean readable traces. However, the jets and galvanometer movements have a limited life, and tended to break down frequently. Replacement units were rarely to hand.

3.5 Twelve Channel Oscilloscope

The twelve channel oscilloscope uses a medium pesistence television tube to display multichannel information simultaneously. Sweep rate and individual channel gains and D.C. shifts are variable.

The unit is used to display all signals from the playback deck while performing skew and flutter compensation adjustments. The device is invaluable as a general purpose monitor in observing the quality of the replayed signals and in searching for the precise position of events recorded on tape. A practiced user can use the displayed timecode to read the recorded time and find his way about tapes. The oscilloscope was most useful for finding GMT pips recorded on the radio channel, and permitted rapid searches to be made without using exorbitant amounts of paper.

3.6 Time Decoder and Display

Originally, the recorded timecode had to be decoded by eye, which results in extravagent use of paper when the jet pen oscillograph is used, and is not particularly easy when displayed on the oscilloscope. At any rate, decoding by eye is tiring and error prone, resulting in considerable frustration to the user who wishes to play out seismograms rapidly.

Since Durham University was unwilling to provide a suitable decoder, the author designed and built his own device for analysing the timecode and displaying, in an easily readable decimal format, the timecode minutes, hours, days and years as replayed. This decoder is at present on loan to the University, and the author and other users have found it invaluable for finding their way through tapes.

Additionally, the decoder detects hours and produces a rectangular pulse, which can be superimposed on to the single channel trace drawn by the drum oscillograph, for subsequent timing of displayed events.

Although the decoder automatically compensates for small distortions in the timecode due to drops in recording quality, it cannot decode some very poorly recorded tapes.

3.7 Single Channel Drum Oscillograph

The HELICORDER single channel drum oscillograph consists of a cylindrical drum around which heat sensitive paper is attached by means of clamps. As the drum revolves, a hot wire scriber attached to a galvanometer movement traces a dark line across the paper. The galvanometer base moves synchronously with the drum and parallel to its axis, so that the line drawn is helical. Signals applied to the galvanometer through the unit's amplifiers are thus reproduced on the helical trace.

The unit is used for reproducing a single seismic track from tape in a suitably compact form for continuous monitoring of seismic activity. The drum revolves quite slowly, and about three and a half days continuous recording can be displayed on a single sheet. It takes about nine hours to reproduce this much information and the density is 9 mm per recorded minute.

3.8 The Modular 1 Computer

The Modular 1 computer accepts multichannel analogue signals as inputs, which it digitizes internally for subsequent computations. A digital-to-analogue converter can reconvert internal numbers to multichannel analogue form for display or further processing.

The computer is programmed using a Durham written compiler, SERAC. This specialized compiler enables pseudo-infinite length time series channels to be handled in much the same way as ordinary variables are in other compilers. Using single statements, actions ranging in complexity from addition and delaying to bandpass filtering may be performed on one or more time series channels.

The computer was used for experiments in an attempt to improve flutter compensation for the playback equipment, as described in Section 3.2. During these experiments, considerable crossfeed was discovered between analogue input channels. This was first noticed as a superposition of the high amplitude timecode signal on to other channels. Selection of a different computer input channel for the timecode reduced its effect on other channels, but the crossfeed which must also have existed between the seismic and reference signals might have affected the flutter compensation experiments.

The Modular 1 computer has a half inch tape drive and disk store. At one stage it was thought that it might be worthwhile rerecording events in digital format on tape for subsequent processing, either on the Modular 1 computer or on the Northern Universities Multiple Access Computer (NUMAC) system. The primary objective was to enable side by side display of seismograms for the same event recorded at different stations, which would enable comparison of waveforms, and for local events the tracing of corresponding phases.

Experiments showed that the first digital records were far from satisfactory. Apart from the crossfeed problem already described the sampling rate, referred to recorder time, varied from record to record and even significantly along the length of some records. Additionally, while writing digital tapes, the Modular 1 would occasionally detect parity errors and rewrite the misrecorded block: in the mean time samples would be lost, resulting in gaps in the digital record.

These problems were eventually overcome, and digital seismograms could be reproduced on the NUMAC graph plotters, corrected for differing sampling rates, clock errors, recorder gains and seismometer polarities. The process involves the use of two programs written in FORTRAN by the author for the NUMAC system. The digital tapes are first examined by the program TAPESEE which measures the sampling rate and the time of the first sample for each record by examining the digitized timecode, and measures the D.C. offset for each of the seismic channels. This information is written into a disk file. TAPESEE detects and ignores spurious pulses in the timecode and makes allowances for those that are sometimes missing. However, gross errors due to missing samples and severe variations in sampling rate, which are easily picked up by examination of the program's printed output, cannot be allowed for, and frequently necessitate redigitization of events.

Other information, such as station coordinates, recorder clock errors and gains and seismometer polarities are appended to the disk file information produced by TAPESEE. The disk file is then used by the main plotting program, EPLOT, to correct the selected traces read off magnetic tape, before they are drawn.

Digital recording of events, checking of the resultant digital records and subsequent plotting all take considerable time, both the computer's and the user's. Moreover, the use of tape drives and graph plotters on NUMAC involve delays, and it takes a minimum of a week to reproduce a seismogram from the original analogue tape through the system. The seismograms plotted on NUMAC are not as clear as those drawn on the jet pen oscillograph, and bearing in mind that the poor dynamic range of the original signals hardly allows for the satisfactory application of sophisticated digital waveform processing techniques, the routine digitizing of events was abandonned.

3.9 Clock Calibration

As explained in Chapter 2, the timecode recorded on tape, which is derived from the recorder's internal clock, is subject to an error which may amount to several seconds. To obtain accurate timing of seismograms, this clock error must be measured and allowed for. Measurement of the clock error is made by comparison of timecode with GMT pulses recorded alongside on the radio track, as described in Chapter 2.

The tapes are searched for GMT pips recorded on the radio track by examining the signal on the oscilloscope. When found, they are played out on to paper alongside the timecode, using the jet pen oscillograph, at a rate of 25 or 50 millimeters per recorded second. GMT pips known to be well recorded during visits to the stations are also played out.

Searching tapes for GMT pips is immensely tedious and time-consuming work, but the task can be shortened by not looking for more sets of pips than are necessary to define accurately the drift curves, and reliably detect irregularities in clock rates. One satisfactorily recorded set of pips for each day or two days is usually adequate for moderately well behaved clocks. Only the few seconds either side of each hour need be examined, as pips are not transmitted at other times. Effort is concentrated on the daylight hours, as night-time reception is very poor.

Often there is no activity on the radio track for long periods together, or activity follows a diurnal pattern. This may be due to weak radio batteries or to too low a setting of the volume control or to mistuning. An experienced observer can tell from the nature of the replayed radio signals whether the radio was properly receiving program material, which gives long duration semi-regular pulses or electrical noise, which either gives short irregular pulses or continuously saturates the radio channel. Diurnal variations in reception quality are very noticeable, and often well recorded GMT pulses are found at the same or nearby hours on successive days. No doubt this is due to diurnal drift in radio tuning with temperature, combined with similar variations in propagation conditions, which result in optimum reception conditions occurring once or twice each day at about the same time. Once long periods of quiet, or diurnal variations have been noted, the search can be concentrated on those sections of tape most likely to have satisfactory recordings of pips.

Frequently, however, reception was poor for periods ranging from several days to a few weeks. To obtain satisfactory clock calibration for these periods, there is no alternative but to search every hour and obtain playouts of the few, if any, poorly recorded pips which do exist.

Each set of GMT pips transmitted by the B.B.C. consists of six pulses, the leading edges of which are separated by precise one second intervals. The first five are shorter than the last, the leading edge of which indicates the instant of the hour.

Due to noise and variable reception conditions, these pulses are rarely received undistorted; extra pulses are added, and those transmitted are often absent. The first step in making measurements on a set of time pips is to recognize the pulses that are present, especially their leading edges. The whole number component of the clock error is read by noting the position of the final pulse against the timecode. Originally, the GMT pulses were played out on to a trace between two timecode traces. The decimal part of the clock error is then determined by the following method. Lines are ruled between the corresponding leading edges of the timecode pulses. For each GMT pulse, the following two measurements are made:- a, the distance between the preceeding ruled line and the leading edge of the pulse, and b, the distance between the preceeding and succeeding ruled lines. The ratios a/b then give estimates of the fractional part of the clock error. Later, the format of the paper records was changed to avoid the necessity of ruling lines. Using the second format, the radio trace is superimposed on the timecode trace, and the base lines are brought very near coincidence. The measurements of a's and b's can then be made accurately along the base lines. To aid identification of the two traces, the amplitude of the timecode is made larger. Figure 3.2 gives examples of both formats, along with typical measurements.

Each pulse gives an estimate of the fractional part of the clock error. The mean of these estimates is used in subsequent calculations, while the standard deviation gives an estimate of its accuracy. Normally a standard deviation of about 0.03 seconds is obtained. High standard deviations usually indicate mistiming of one or more pulses due to distortions. Examination of the residuals leads to rapid detection of the offending pulse, and the corresponding measurements are then omitted in recalculating the mean and standard deviation.

The clock errors thus obtained are smoothed using a computer program TERFIT written in FORTRAN for NUMAC. The program uses a NAG Mk IV library subroutine E04ABF to fit a polynomial in x, the time in days from an arbitrary origin, to the clock error measurements. The time origin chosen was

FIGURE 3.2

TYPICAL SETS OF GMT PIPS

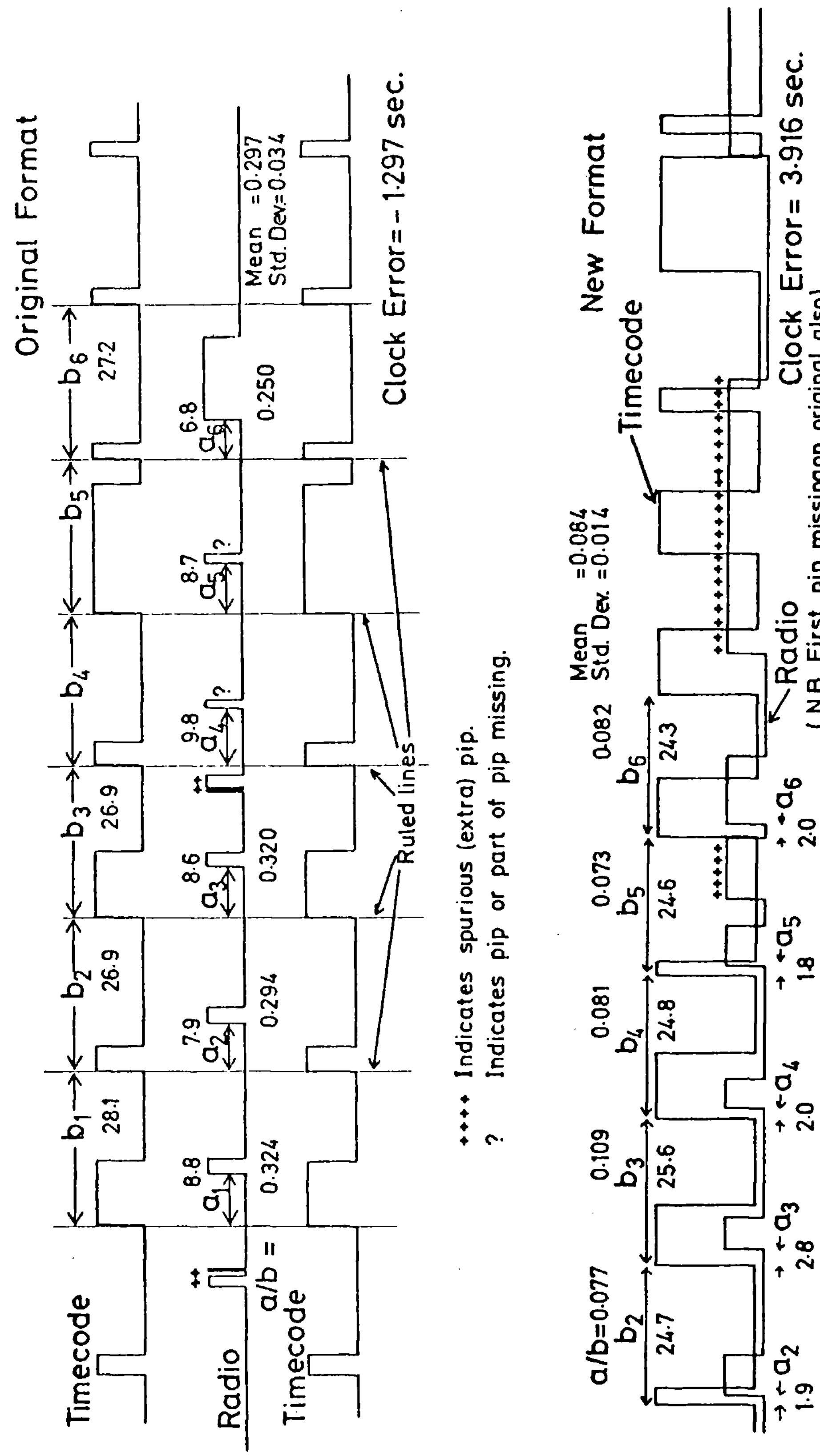

midnight on 31st December 1975. Each clock error measurement is assigned a weight dependent on the number of pips used and the calculated standard deviation according to the following formula

$$w = 100n/(s+0.01) \qquad (3.1)$$

where w is the assigned weight, n is the number of pips used and s is the standard deviation.

There is no rigorous statistical justification for this formula. It is, however, intuitively reasonable, giving added weight to those measurements with low standard deviations and which use more pips, but without letting the very low values of s, which sometimes occur by chance, take overriding importance.

Using the derived polynomial coefficients, a table of interpolated clock error values at three-hourly intervals is calculated. This table, together with inputted values, assigned weights, corresponding interpolated values and residuals, is printed.

For a constant clock rate, the clock error would drift linearly with time. In practice, quartz crystal oscillators, such as those used to control the clock rates, tend to age in such a way that their frequency varies slightly with time. This change is approximately linear, and gives rise to a parabolic drift curve. Thus quadratics are normally used to fit the measurements, although linear fits are sometimes used when only a few points are available. Higher order polynomials would tend to follow the random fluctuations in measurement, and cannot be justified.

Jumps in the drift curve are either obvious from a cursory glance at the clock error measurements, or show up in the pattern of residuals after curve fitting. In such cases the measurements are split up into blocks in such a way that drift within each block is thought to be continuous.

Some individual measurements also give large residuals, often traced to incorrect measurement or miscalculation. After rectification of such errors, the revised measurements are resubmitted to the computer. Sometimes the large residuals are due to the use of time signals from other transmissions. Radio Republic of South Africa transmits six equally spaced pulses to denote the hours and half hours, and these are easily misidentified as B.B.C. GMT pips. Even the time signals transmitted by the Voice of Kenya, which consist of various numbers of pips at various times, can sometimes be mistaken for GMT pips. These signals are not synchronized with GMT and must be discarded.

The interpolated curves gave good fits to the data. The R.M.S. residuals were often smaller than 0.02 seconds, and always less than 0.04 seconds.

3.10 The Effect of Filtering on Seismic Signals

Filtering is an invaluable technique for reducing the effect of noise on seismic signals, and thus aiding their identification and timing. In reflection seismology, various forms of filtering using digital techniques can be used to enhance the required signal relative to noise with the same spectral composition. Analagous techniques in earthquake seismology can be used with array station data to enhance signals arriving from a specific direction and with a specified velocity. For this study, the only filtering practicable is electronic, using the filters described in Section 3.3. This type of filtering can only reduce noise if it has a different spectral composition to the required seismic signal.

Teleseismic arrivals used in this study rarely have a significant frequency component above 2 Hz; usually the dominant frequency is 1 Hz or below. Superimposed noise, both instrumental and from local sources, has a dominant frequency of 3 Hz or above. Thus 2 Hz, 48 dB/Octave low-pass filtering was adopted as standard when playing out teleseismic arrivals on to paper.

For local earthquakes with dominant frequencies above 2 Hz, a higher cut-off frequency must be used. Interfering noise in the form of residual flutter, and local ground disturbances has a wide ranging frequency content, which often overlaps the frequency range of the desired signals. However, 10 Hz, 48 dB/Octave low-pass filtering usually gives the best compromise between noise rejection and signal retention and was adopted as standard when playing out local events on to paper.

These standard filter settings were used whenever practicable when playing events out on to paper, to preserve as constant a processing tecnique as possible. However, the variable nature of signals and noise often necessitated the use of alternative filter settings. For example, high amplitude very low frequency surface waves from large teleseismic events occasionally interfere with the required signals. Introducing a high-pass section with 0.05 Hz cut-off frequency removes this source of interference. Spikes are sometimes introduced on to the waveform when replaying poorly recorded tapes, or by jerky tape motion during recording. Low-pass filtering broadens these large amplitude spikes to give humps which are often more confusing to the eye than the original interference. In such cases no filtering, or a very high cut-off frequency, is preferable.

Electronic filtering inevitably leads to some distortion of the seismic signal due to phase shifting and differential attenuation of the various frequency components present. To determine in a qualitative way the effect of filtering on the shape of a waveform, and in a quantitative way the effect on timing, filtered and unfiltered calibration pulses were played out side by side. Calibration pulses were chosen as test signals as they are reproduceable and contain both rapidly varying and more sedate components of motion, representing the full bandwidth of the seismometer-recorder-playback system. In particular the effects of low-pass and high-pass filtering at

48 dB/Octave were examined. The effect of such filtering for a range of corner frequencies is demonstrated in Figure 3.3, where the time shifts are preserved.

From Figure 3.3 it can be seen that the effects of low-pass filtering are to round off the sharp corners of the signal, to broaden the pulse and to delay it. These effects increase with decreasing cut-off frequency, but marked distortion of the pulse shape only occurs below about 2 Hz. However, there is significant delay of the waveform for all frequency settings.

High-pass filtering does not alter the timing or sharpness of the initial onset, but reduces the width of the pulse and increases the amplitude of the "overshoot" following it. The effect is to advance the waveform in time overall, as indicated by the corresponding negative delay measurements, described later in this section. Distortion of the waveform is not marked until the cut-off frequency increases beyond 0.05 Hz; beyond this frequency the waveform is increasingly distorted and reduced in amplitude until 0.2 Hz, when the original shape is entirely lost.

To measure the delays introduced by filtering a waveform matching procedure, similar to that described in Chapter 4, is used. The unfiltered waveform is traced and an arbitrary point on the zero line preceding the waveform selected. This point is marked using a fine needle, making a small hole in the tracing paper and denting the underlying paper record.

FIGURE 3.3

THE EFFECT OF FILTERING ON CALIBRATION PULSES

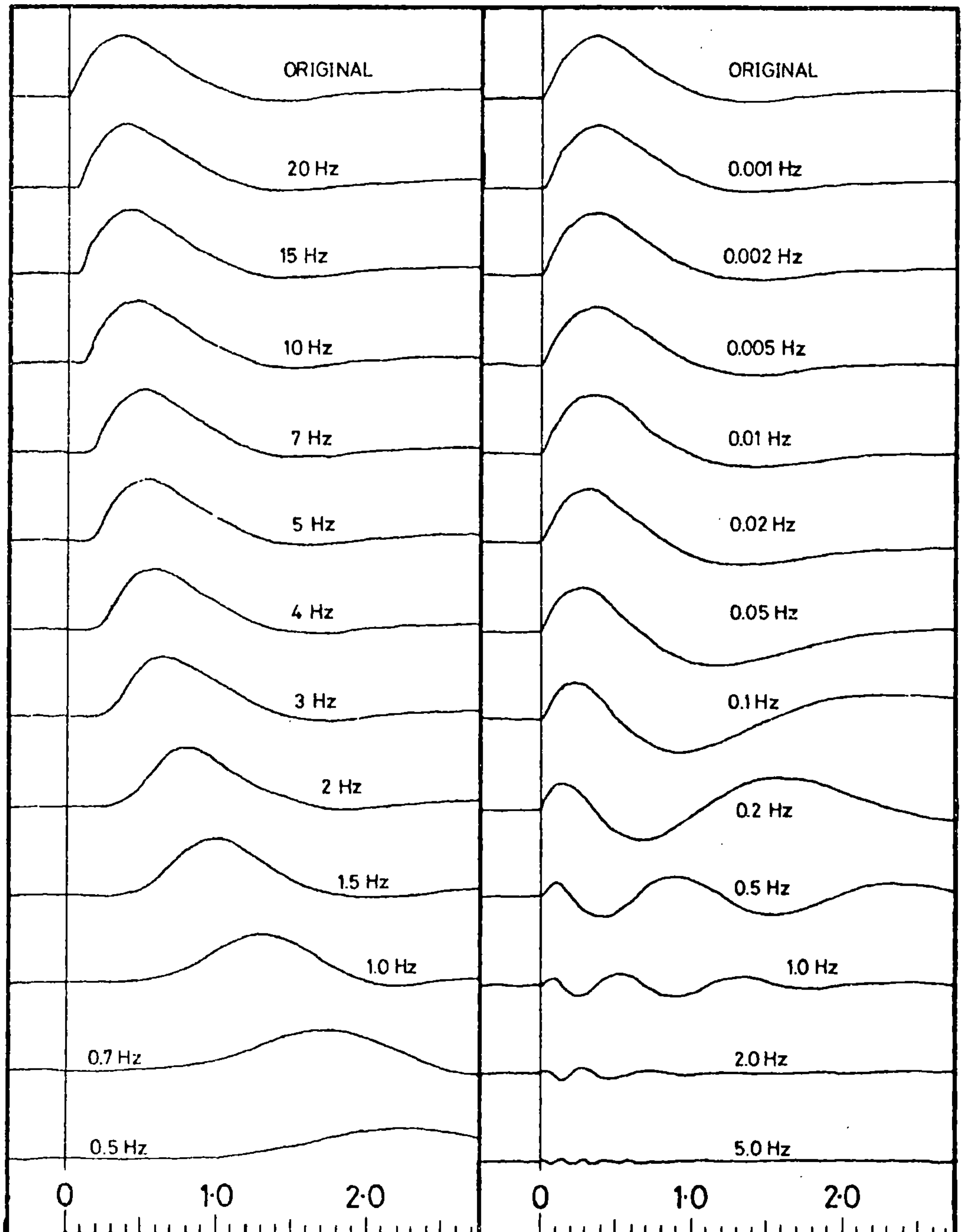

The Effect of Low-Pass (48 dB/Oct.) Filtering, at Various Frequencies, on a Calibration Pulse.

The Effect of High-Pass (48 dB/Oct.) Filtering, at Various Frequencies, on a Calibration Pulse.

The traced waveform is then placed over the filtered waveform and moved about until the optimum match is obtained. The selected point is then transferred to the filtered trace by pricking it through the original hole. The corresponding marks on the two paper waveforms are then measured relative to the time code using the same method, described in Section 3.9, as for GMT pips. The difference between the two times is taken as the filter delay. A set of four calibration pulses is used for each filter setting, giving four measurements of each delay. The mean and standard deviations for a series of such determinations, for low-pass and high-pass 48 dB/Octave filtering at various cut-off frequencies, are given in Table 3.1. The low standard deviations indicate the repeatability and precision of these measurements. The variation of delays with cut-off frequency is shown graphically in Figure 3.4.

Alternative techniques for determining relative onset times of similar waveforms are described in Chapter 4 where the use of waveform matching is justified for the similar timing of onsets of teleseismic arrivals. The same method was used for filter delays because of its repeatability, and to be consistent with the teleseismic delay measurements.

Waveform matching cannot be used with arrivals from local events since the signals vary enormously in character from station to station. In this case it is necessary to measure the onset, or first departure of the arrival from the zero line. Measurements on the calibration pulses

TABLE 3.1

MEASURED FILTER DELAYS

Delays due to LOW-PASS filtering using KEMO filters at 48 dB/Octave

CORNER FREQUENCY (Hz)	FILTER DELAY (Seconds)	STANDARD DEVIATION (Seconds)
20.0	0.055	0.014
15.0	0.071	0.008
10.0	0.089	0.018
7.0	0.143	0.006
5.0	0.186	0.006
4.0	0.230	0.019
3.0	0.293	0.020
2.0	0.425	0.009
1.5	0.531	0.009
1.0	0.834	0.020
0.7	1.203	0.034

Delays due to HIGH-PASS filtering using KEMO filters at 48 dB/Octave

CORNER FREQUENCY (Hz)	FILTER DELAY (Seconds)	STANDARD DEVIATION (Seconds)
0.001	-0.002	0.005
0.002	-0.012	0.016
0.005	-0.001	0.019
0.01	-0.005	0.018
0.02	-0.034	0.007
0.05	-0.097	0.025
0.1	-0.146	0.031
0.2	-0.245	0.015

FIGURE 3.4

VARIATION IN FILTER DELAY WITH CORNER FREQUENCY

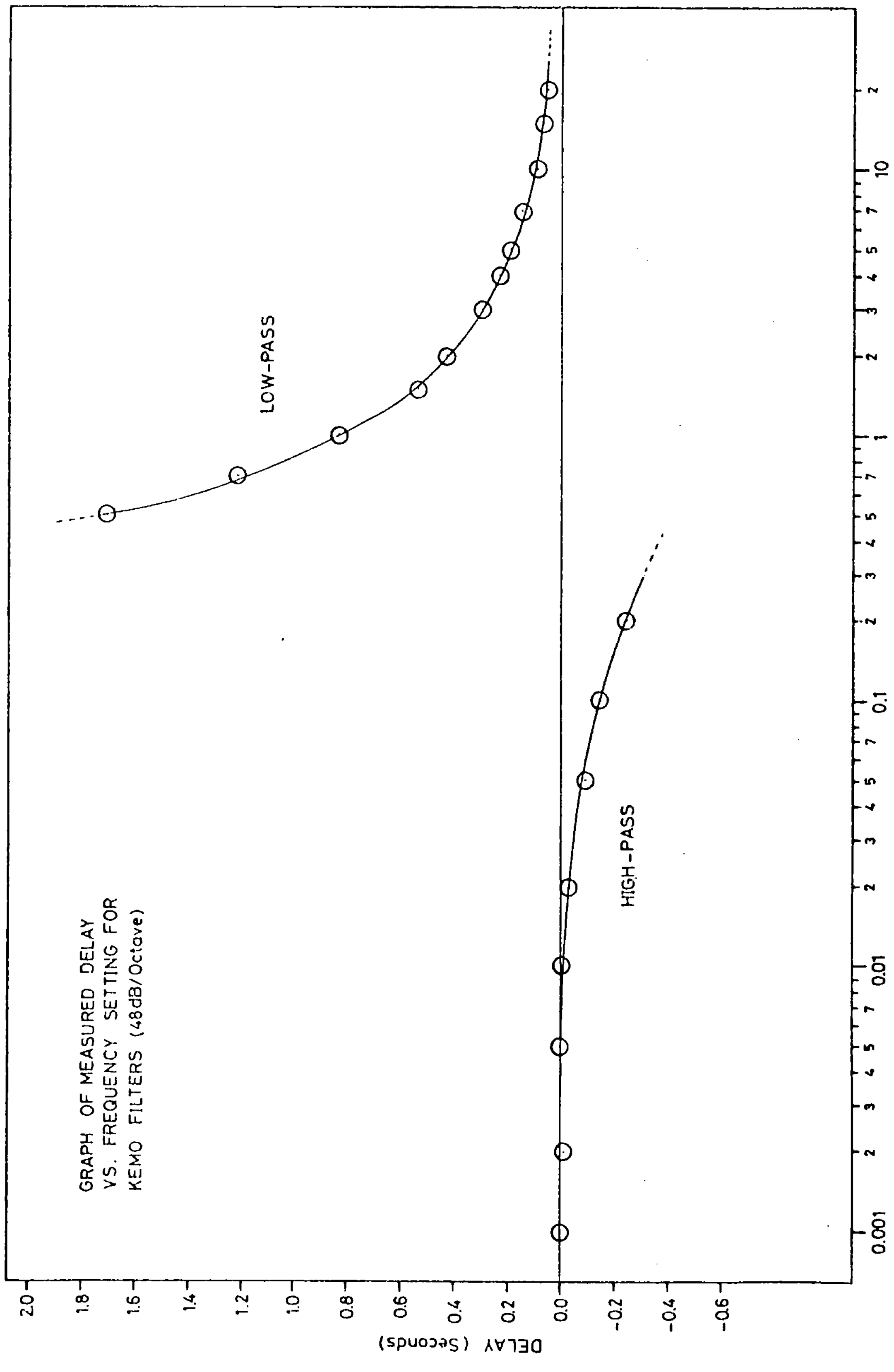

indicate that for low-pass filtering down to 4 Hz (below this the onset is not well defined) the delay suffered by the onset point is precisely the same as for the waveform as a whole. For high-pass filtering however, the onset time is unaffected. Thus, when correcting the measured onset of local arrivals for filter delay, only that due to low-pass filtering should be taken into account.

As previously stated, the figures given in Table 3.1 are for 48 dB/Octave, roll-off characteristics. Measurements using single section KEMO filters and KROHN-HITE filters, where the roll-off rate is 24 dB/Octave, showed that the corresponding delays are half those for 48 dB/Octave. Moreover it was found that the delay due to band-pass filtering is equal to the sum of the delays due to the high-pass and low-pass sections. Using these empirical relationships the effect of any type of filtering may be calculated.

Measurements on filtered and unfiltered seismograms of selected local and teleseismic events showed that the delay measurements obtained from the calibration pulses were entirely adequate for correcting onset times.

3.11 Errors in Seismogram Timing

3.11.1 Timing Method

Accurate timing of seismograms is vital to this study. Timing of a particular event divides naturally into two parts: firstly, the required point on the displayed waveform must be properly identified, and secondly, the instant of time corresponding to the selected point must be determined. This section only deals with the latter part, and discusses errors which may be introduced.

Timecode is invariably displayed either side of the other waveforms, and timing of the selected point is made by measuring the point's position in relation to lines ruled between corresponding leading edges on the two timecode traces. The time of the preceding second is determined by inspection of the pulses forming the timecode. The fractional part of the second is obtained from measurements of the point's distance from one of the ruled lines either side and the distance between the ruled lines, as for GMT pips.

The time measured in this way is then corrected for clock error and filter delay giving an absolute time measurement. Errors in this measurement may arise from a number of sources which will be considered one by one.

3.11.2 Instrumental Timing Errors

The timecode is calibrated relative to GMT pips recorded alongside on tape, as described in Section 3.9. Delay due to the propagation of the radio signals from

London to Kenya, a great circle distance of about 7,000 km, is approximately 0.025 seconds. The distance across the network, from Station 50 to 30, is approximately 700 km, which would introduce relative errors between stations of not more than 0.0025 seconds. Electronic delays within the radio recievers and recorders are negligible.

Delays of the radio signals relative to timecode within the playback system, which may exist, for example, due to the frequency detection circuit, and head misalignment, introduce no error, as the calibration process automatically takes them into account. The same is not true however, of the signals recorded on the seismic channels, which undergo somewhat different processing to the timecode and radio signals. Significant delays in the seismic channels can be detected however, since the calibration pulses are synchronised to the ten second pulses of the timecode. The sharp onsets of the unfiltered calibration pulses are not measurably displaced from the leading edges of their corresponding timecode pulses, so this source of error, if it exists, is negligible.

Another potential source of instrumental timing errors is due to flutter. Tape speed variations cause the recorded information to be written on to paper at a non-uniform rate which gives rise to random errors in timing. The magnitude of this effect can easily be determined. Suppose the tape runs with an average speed, V_a, and that the instantaneous speed differs from this amount by $V(t)$. After a time t, the tape will have moved a distance d, whereas in the absence of speed variations the distance would have been d_a, these distances being given by the equations:

$$d = \int_{\emptyset}^{t} (Va+V(\tau))\,d\tau \qquad (3.2)$$

$$d_a = \int_{\emptyset}^{t} Va\ d\tau = V_a t \qquad (3.3)$$

The difference in these two distances corresponds to the time error, t_e, which is given by

$$t_e = (d-d_a)/V_a \quad = \int_{\emptyset}^{t} f(\tau)\,d\tau \qquad (3.4)$$

where f(t) is the instantaneous fractional change in speed.

Assuming for the moment that f(t) is sinusoidal, with amplitude f_o, and angular frequency w, we have

$$f(t) = f_o \mathrm{Sin}(wt) \qquad (3.5)$$

whence

$$t_e = f_o \int_{\emptyset}^{t} \mathrm{Sin}(w\tau)\,d\tau \quad = -(f_o/w)\mathrm{Cos}(wt) \qquad (3.6)$$

Thus lower frequency components introduce relatively larger timing errors.

Short sections of flutter are approximtely sinusoidal with a frequency of about 1.5 Hz. The higher frequency components are of smaller amplitude and may be ignored. Total tape speed variations are 15%, so that f_o in our case is Ø.Ø75. $w = 1.5x2\pi = 9.5$ radians per second, giving a maximum time error of about Ø.ØØ8 seconds.

The frequency modulation-demodulation process limits time resolution, since frequency can only be determined over one or more cycles of the waveform. In practice about 2 cycles are required, and since the lowest carrier frequency is about 50 Hz, time resolution better than about 0.040 seconds cannot be expected. Since arrivals are equally likely to be measured late as early, this gives an effective time error of 1/50 = 0.02 seconds.

3.11.3 Measurement Errors

Skew between traces on the jet pen oscillograph is reduced to less than 0.2 mm as described in Section 3.4. Measurements made by ruler are also accurate to about 0.2 mm, so assuming that these errors add randomly, a total measurement accuracy of about 0.3 mm may be assumed.

For most measurements, waveforms are displayed at a speed of 25 mm/sec or greater, giving an accuracy of about 0.010 seconds. Sometimes however, signals are too weak and deeply immersed in noise to be easily recognised in the expanded playouts at 25 mm/sec. Measurements are then made on records played out at 10 mm/sec; in the latter case time errors are expected to be about 0.025 seconds.

3.11.4 Errors in Clock Calibration

At least ten measurements of clock error are usually used to derive each segment of a drift curve. The R.M.S. residuals after polynomial fitting are around 0.02 sec., which implies a standard error in the calculated drift curve of about $0.02/\sqrt{10} = 0.006$ seconds.

3.11.5 Errors in Determination of Filter Delays

The standard deviations given in Table 3.1 represent the errors in the determination of filter delays. The mean of these standard deviations is 0.015 sec.

Since the majority of seismograms are played out with standard filter settings, the same figures are used time and time again. Thus the error introduced is systematic, although those seismograms played out with alternative settings are effectively subject to an additional random error of about 0.020 seconds.

3.11.6 Combination of Errors and Conclusion

Systematic errors arise from error in the determination of the standard filter delay and the delay due to propagation of radio waves from London to Kenya. Combining these two sources of error, we conclude that events are timed later than they should be by about 0.025 +/- 0.015 seconds. Such systematic errors are only important when comparisions are made with recordings at other stations. Tacit comparison is made with the WWSSN stations in using published earthquake onset times determined using these stations. Since clock errors at these stations are also determined relative to GMT pulses, and since propagation corrections are not applied to these measurements (Kimano, NAI WWSSN, Pers. Comms.) an equivalent delay is therefore introduced which will tend to cancel. At any rate published onset times are only quoted to 0.1 seconds, so the systematic delay can safely be ignored.

Random errors arising from various sources as described above are listed in Table 3.2.

Combining these errors in the usual way, assuming no correlation, we obtain typical total errors of 0.025 seconds. The worst case error, when measurement is made on a 10 mm/sec playout, and non-standard filter settings are used, is 0.040 seconds.

TABLE 3.2

MAGNITUDE OF RANDOM TIMING ERRORS

SOURCE	MAGNITUDE
Transit time of radio sigs. across network	0.002 sec
Flutter	0.008 sec
Modulation	0.020 sec
Measurement	0.010-0.025 sec
Clock Calibration	0.006 sec
Non-standard Filter Settings	0.0-0.020 sec

CHAPTER 4

TELESEISMIC DELAY MEASUREMENTS

4.1 Introduction

This chapter describes the measurements of delay times made from recordings of teleseismic arrivals at the 24 DKSP stations. The method of relative delays, a modified form of which is used in this study, is discussed, and the magnitude of errors calculated. The raw delay time measurements are separated into source and station components, preserving the relative station delays as accurately as possible. The station delay baseline is corrected for the travel time tables used, and the accuracy of the baseline determination discussed.

4.2 Selection of Events and Playout Procedure

Possible teleseismic arrivals recorded on tape were detected by careful examination of continuous paper playouts made on the drum oscillograph. The onsets were timed to the nearest minute, so that they could be compared directly with predicted onset times of listed events. The listings of predicted onset times, for the duration of DKSP, at a hypothetical station within the Gregory rift, were made available by the Atomic Weapons Research Establishment (AWRE) Seismology Unit. The listings are in the form of printout produced by the Unit's computer program, GEDESS

(Young and Gibbs, 1968), which utilizes the Preliminary Determination of Epicentre (PDE) listings of the United States Coast and Geodetic Survey (USCGS) to predict onset times at selected stations. These listings are sent routinely to Durham University, to aid preliminary analysis of seismograms recorded at the University's own permanent seismic station (DUR), and include predicted onset times for this station, amongst others.

Many of the suspected teleseisms detected on the helicorder playouts could not be correlated with the GEDESS listings. Some of these were played out in greater detail using the jet pen oscillograph. The more detailed playouts revealed all these "teleseisms" to be noise, or low frequency phases from local events. The GEDESS listings were therefore quite complete as regards the listing of events with sufficient magnitude to be detectable. All events which were recorded with amplitudes high enough to be useful had listed magnitudes of 5.0 or greater.

The onset recorded at each functional station for each detected event was played out in expanded form, using the jet pen oscillograph. Playouts were usually made at the following speeds: 5 mm/sec, 10 mm/sec and 25 mm/sec, relative to recorder time. The standard format given in Table 4.1 was used whenever possible. This format was modified when jet pen channels broke down, but certain features of the standard format were always retained. For example, timecode was always displayed on the two outer

TABLE 4.1

STANDARD PLAYOUT FORMAT FOR JET PEN OSCILLOGRAPH

JET-PEN CHANNEL NUMBER	SIGNAL DISPLAYED	TAPE TRACK	RELATIVE JET PEN GAIN	PROCESSING
1	Timecode	8	1	
2	Radio	7	1	
3	Reference	6	4	
4	Horizontal Seismic (1)	5	4	
5	Vertical Seismic	3	4	Unfiltered
6	Horizontal Seismic (2)	1	4	
7	Timecode	8	1	
8	Horizontal Seismic (2)	5	4	
9	Vertical Seismic	3	4	Filtered
10	Horizontal Seismic (2)	1	4	
11	Horizontal Seismic (1)	5	10	
12	Vertical Seismic	3	10	Filtered
13	Horizontal Seismic (2)	1	10	
14	Timecode	8	1	
15	Vertical Seismic	3	40	Filtered
16	Timecode	8	1	

Playouts are usually made at the three following speeds: 5, 10, and 25 mm/sec (relative to recorder time).

tracks so that timing lines perpendicular to the direction of motion could be drawn, and all the seismic signals were displayed, both filtered and unfiltered. The waveform from the vertical seismometer is especially important as all onset timing is made from this signal. Consequently, the filtered vertical seismometer waveform was always displayed at a variety of gains.

As explained in Chapter 2, standard filter settings of 2 Hz low-pass, 48 dB/Octave roll-off were used whenever possible when playing out teleseisms. Occasionally however, non-standard filter settings had to be used, and a careful account of these was kept.

4.3 Measurement of Onset Times: Waveform Matching

As is explained in the section following, it is vital to this study that measurement of onset times should preserve their relative timing as accurately as possible. To this end, a waveform matching technique was used to identify the relative onset points on each waveform. The method proceeds as follows:-

The vertical seismometer waveforms recorded at each station are compared. A representative "average" waveform is selected, against which the others are matched.

The waveform of the selected seismogram is then traced (vertical seismic channel only), and the estimated position of the first break marked. The tracing is then laid over the vertical channel of each of the other seismograms in turn, and moved about until a good fit is obtained. The first break marked on the tracing paper can then be compared with that which would have been picked from the underlying seismogram. Sometimes what is at first taken as noise preceeding the first arrival, turns out to have a coherent component at other stations and therefore is part of the arrival. Alternatively what seems to be the first cycle of the P-wave arrival cannot be correlated at the other stations, implying that it is merely noise. By making these comparisons, a consensus as to the true position of the first break is obtained, and is marked using a fine point, making a hole in the tracing.

The corresponding point is transferred to each of the other seismograms by carefully overlaying the tracing, sliding it about until the best match is obtained between the two waveforms, and then pricking the paper through the hole in the tracing. The points thus marked on each paper record are then timed, using the method described in Section 3.11, and corrected for filter delay and clock error.

In making the above comparisons between paper records, a careful account of the relative vertical seismometer polarities must be maintained. Some of the waveforms are inverted due to the use of seismometers with coils wound in the opposite direction to normal, or with reversed magnets. The relative seismometer polarities are known from tilting experiments performed at the time of seismometer installation, and noted on field log sheets. Such inversion of the waveform is easily taken care of by inverting the tracing paper before laying it on the paper record.

Mistakes were sometimes made in keeping track of the seismometer polarities. Often the asymmetry of the waveform rendered such mistakes obvious, but in other cases they went unnoticed until later analysis. Such mistakes give errors of half a period of the dominant frequency, usually about 1 sec, in the resulting delay time and are detected as correspondingly large residuals in the later process of separation into source and station components (see Section 4.6). Similar errors arise from misidentification of the corresponding cycles of the traced and paper seismograms, but the errors are correspondingly larger, typically 2 sec.

The author is confident that all such mistakes were detected and corrected, as the residuals formed when the delays were separated into source and station components were small.

Naturally, the above method relies heavily on similar waveforms being received at each station for each event. The waveforms recorded at different stations were, on the whole, surprisingly close, especially for the larger magnitude events. Figures 4.1, 4.2 and 4.3 illustrate the vertical seismometer waveforms for typical large, moderate and small amplitude arrivals as recorded at several stations. To aid comparison, the waveforms have been

FIGURE 4.1

VERTICAL SEISMOMETER SIGNALS FOR A TYPICAL WELL RECORDED EVENT

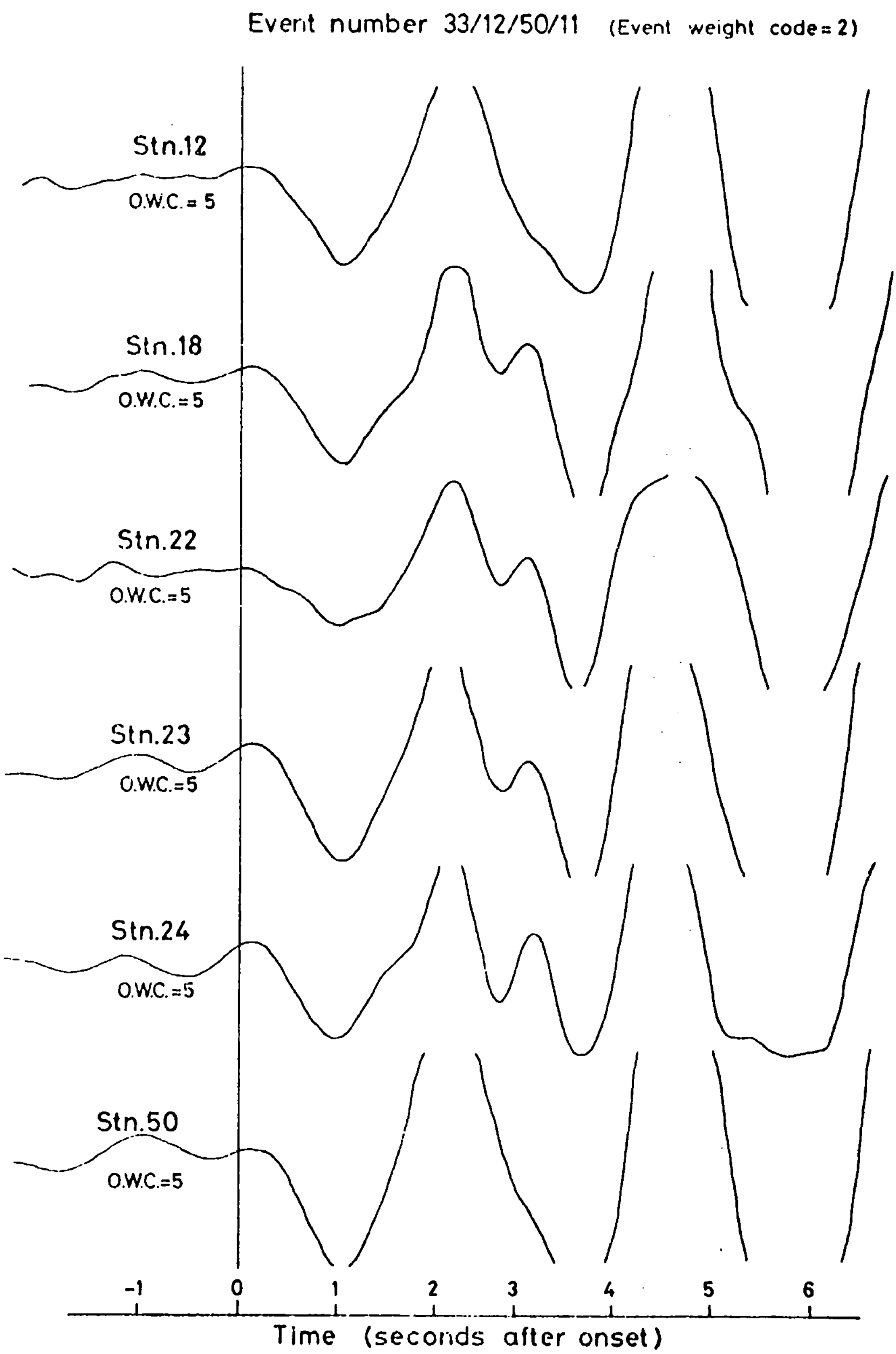

FIGURE 4.2

VERTICAL SEISMOMETER SIGNALS FOR A TYPICAL MODERATELY WELL RECORDED EVENT

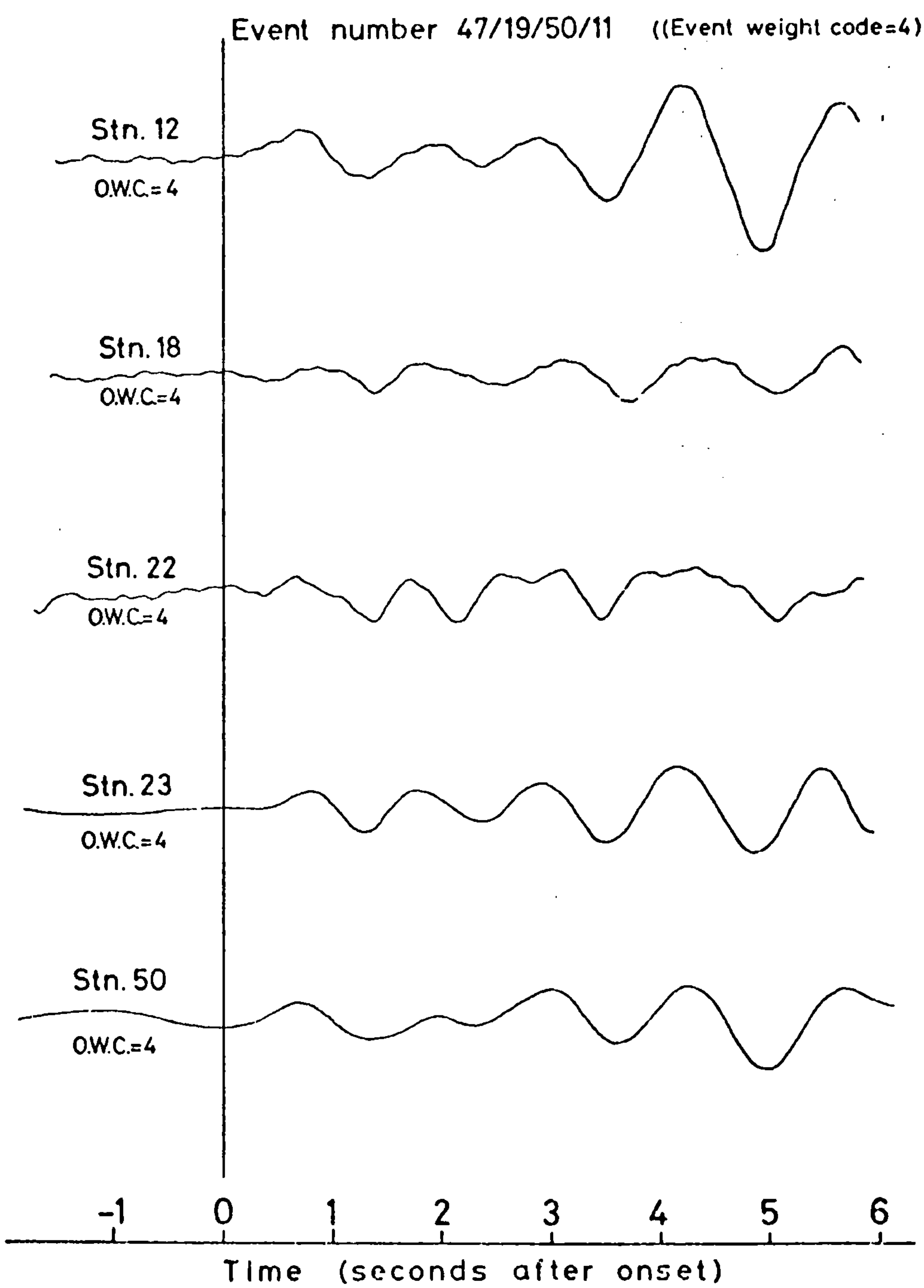

FIGURE 4.3

VERTICAL SEISMOMETER SIGNALS FOR A TYPICAL POORLY RECORDED EVENT

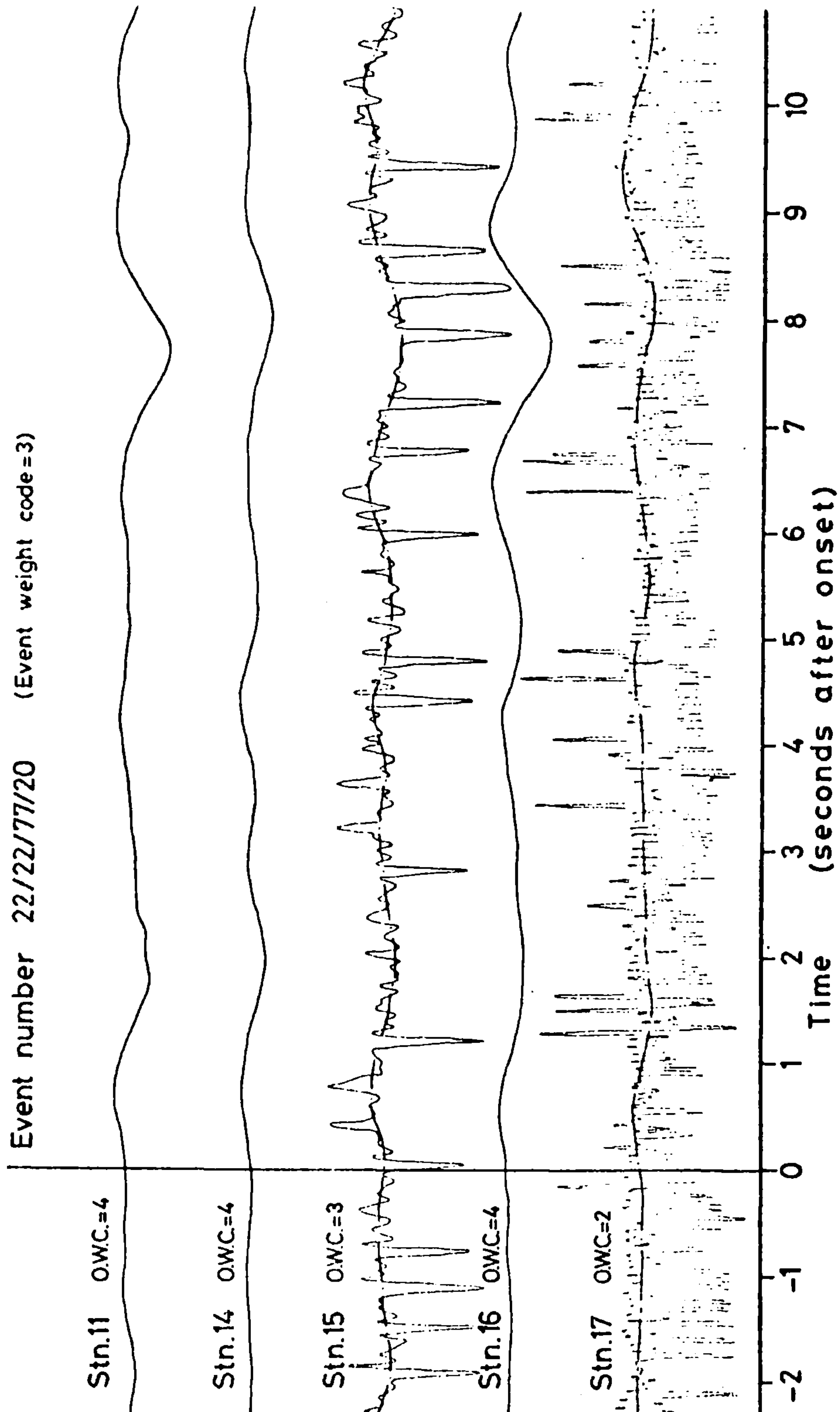

aligned and, where necessary, inverted. The strong overall similarity of the waveforms can be seen. It is, perhaps, surprising that waveform uniformity extended as far as Station 50, which forms the northwest limit of the network and is about 300 km from the farthest simultaneously recording station. The overall waveform coherence and the occasional poor matches that were observed, even for high amplitude arrivals, are discussed further in Chapter 7.

The quality of the recordings, and hence the waveform match, varies considerably due to the wide range of signal amplitudes and the variable levels of superimposed noise. Ambient seismic noise has a similar frequency content to P-arrivals, and is particularly troublesome when attempting to match small signals. Noise due to poor recording usually occurs as sharp, high amplitude spikes. Despite the high amplitude of this kind of interference, the frequency content and shape are such that the the underlying seismic signal can often be recognised, and its waveform matched. To demonstrate this, the noisy waveforms obtained at two stations have been hand-smoothed in Figure 4.3.

Two weighting codes were introduced, each consisting of a single digit number.

The first, called the event weight code or EWC, corresponds to the estimated accuracy with which the first break is identified, one being assigned to each event. Large amplitude impulsive onsets which are easily and unambiguously picked are assigned high EWC's, say 5 or 6, while low amplitude emergent onsets are assigned EWC's of 2 or 3.

The second type of weighting is characterised by the onset weight code or OWC. The OWC's correpond to the estimated accuracy with which the relative onset times are determined. While matching the tracing to the relevant paper record, an estimate of the closeness of fit can be obtained by sliding the tracing back and forth. The distance that the tracing can be moved from the judged optimum position in either direction, while still retaining a plausible fit, is taken as the estimated accuracy. Weight codes are then assigned on the following basis:-

Estimated Accuracy (secs)	0.05	0.1	0.2	0.3	0.4
Onset weight code	6	5	4	3	2

This proceedure is obviously inconsistent for the seismogram traced, since the "match" in this case is perfect. To retain a degree of consistency, the onset time for the traced record is assigned an OWC equal to the highest OWC assigned to any other onset corresponding to the same event. This is logical, since the closest matching waveforms are assigned the same highest weight, preserving the symmetry.

The waveform matching technique is greatly superior to the individual picking of onset times. Even with large amplitude impulsive arrivals the first break is often hidden in noise which can easily introduce considerable errors. Using the waveform matching technique, the accuracy of the relative onset timing is maintained at the highest level, whilst the consensus approach to identifying the first break increases the reliability of the absolute timing, in a similar manner to velocity filtering using array station data (Corbishley, 1969).

Other waveform comparison techniques might have been used, identifying specific common points on the waveform, and measuring the relative times of these. Steeples and Iyer (1976) have used first peaks or troughs in the waveform, and also first or second zero crossings. They found that using zero crossings gave more consistent results, as noise tended to alter the positions of the zero gradient points.

In this study, measurements on peaks and troughs would have been impractical, as they are often clipped due to saturation in the amplifiers of the recorders. Measurements of zero crossing times would have provided reasonable values of relative onset times for large amplitude arrivals, but such a procedure for smaller amplitude arrivals would have resulted in large errors due to superimposed noise. Only techniques involving comparisons over a cycle or more of the waveform can satisfactorily reduce the effect of noise, which inevitably leads to the misidentification of specific points. Corbishley (1969) has shown that waveform matching gives better results for array data than either of the methods used by Steeples and Iyer.

Techniques equivalent to waveform matching, but using computer-derived correlation functions of waveforms, might have been used in this study. These would be less subjective but not necessarily more accurate, since comparisons by eye can ignore noise, especially instrumental noise, which would degrade any computer aided technique. It would also be difficult and time-consuming to reliably digitise large numbers of arrivals. In view of all of these considerations, this approach was not pursued.

4.4 Calculation of Predicted Arrival and Raw Delay Times

A raw delay time measurement is merely the difference between the measured onset time of an arrival at a station, and that predicted from predetermined hypocentral coordinates and recognised travel times tables. If the actual onset is later than predicted, the delay is positive, and if earlier, negative. This section describes the calculation of the predicted arrival times and presents the raw delay times derived from them and from the onset time measurements.

The predicted arrival times are calculated from the station and hypocentral coordinates using travel time tables. Corrections are applied for the earth's ellipticity, and for the station's height above datum (mean sea level). All calculations are performed using the author's program MANETA, written in FORTRAN for the NUMAC system. The program is listed in Appendix 2, along with a brief description of its use. The principal calculations used in the program are described in the following four sub-sections.

4.4.1 Calculation of Epicentral Distances

The calculation of epicentral distance from the station and epicentral coordinates is a simple matter of spherical trigonometry. A complete set of formulae is given by Bullen (1963) for calculating epicentral distances and the relative azimuths of the station and epicentre. The numerical accuracy of each of the formulae depends on epicentral distance and, if using four figure tables, one should be careful to select the optimum for each case (Bullen, 1963). MANETA uses double precision variables throughout so that (on NUMAC at least) calculations are accurate to about 1 part in 10^{15}. Rounding errors can reasonably be ignored therefore, independent of which formula is used. Following Bullen we define the following quantities:-

$$A = \sin\theta \cos\phi \qquad B = \sin\theta \sin\phi \qquad C = \cos\theta$$
$$D = \sin\phi \qquad E = -\cos\phi \tag{4.1}$$
$$G = \cos\theta \cos\phi \qquad H = \cos\theta \sin\phi \qquad K = \sin\theta$$

where θ and ϕ are the colatitude and longitude respectively of the epicentre. Using primes to indicate equivalent quantities for the station we use

$$\Delta = \cos^{-1}(A'A + B'B + C'C) \tag{4.2}$$

to calculate the epicentral distance, Δ, in angular units.

Other useful quantities which are calculated by MANETA are the relative directions of the event and station. The term "azimuth" is used in this study to denote the eastward angle, from the meridian through the epicentre, to the shorter segment of the great circle through both the epicentre and the station. The corresponding direction at the station is termed the back-bearing. Representing these two angles by α and β respectively we have, from Bullen:

$$\begin{aligned}
\sin\alpha &= [(A'-D)^2 + (B'-E)^2 + C'^2 - 2]/2\sin\Delta \\
\cos\alpha &= [(A'-G)^2 + (B'-H)^2 + (C'-K)^2 - 2]/2\sin\Delta \qquad (4.3) \\
\sin\beta &= [(A-D')^2 + (B-E')^2 + C^2 - 2]/2\sin\Delta \\
\cos\beta &= [(A-G')^2 + (B-H')^2 + (C-K')^2 - 2]/2\sin\Delta
\end{aligned}$$

Having evaluated these expressions for $\sin\alpha$, $\cos\alpha$, $\sin\beta$ and $\cos\beta$, α and β may be obtained unambiguously throughout the full angular range from -180 to +180 degrees.

These formulae require the use of geocentric coordinates. The epicentral and station coordinates are given in geographical coordinates, which must first be converted. The geocentric and geographic longitudes are equal, but the latitudes differ slightly. Denoting the geocentric and geographic latitudes by ψ_c and ψ_g respectively we have

$$\tan\psi_c = (1-\epsilon)^2 \tan\psi_g \qquad (4.4)$$

(Young & Gibbs, 1968) , where ϵ is the earth's ellipticity factor.

4.4.2 Use of Travel Time Tables

The travel time tables used in this study are those due to Herrin et al (1968). The travel times for P are given in the form of a two-dimensional table at discrete values of epicentral distance and focal depth. The travel times for PKIKP are given in the form of a one-dimensional table against epicentral distance, with depth corrections given in a separate two-dimensional table. These are converted into a single two-dimensional table similar to that for P. The corresponding travel time for the given focal depth and calculated epicentral distance is interpolated from these tables.

To perform the interpolation, a small section of the complete table surrounding the required point is taken. This sub-table consists of the sixteen travel times corresponding to the four nearest focal depth values and four nearest epicentral distances values. The interpolation is carried out using the NAG subroutine E01ACF which is written to perform two-dimensional interpolation using cubic splines.

The apparent surface velocity, V_S, is of interest and is needed to calculate the station height correction. To find this velocity, MANETA also computes the travel time for epicentral distances of $\Delta+k$ and $\Delta-k$, where k is a small angle. The velocity, in degrees per second, is then given by the approximate finite difference formula

$$\frac{d\Delta}{dt} \simeq \frac{2k}{t(\Delta+k)-t(\Delta-k)} \qquad (4.5)$$

which may then be converted to kilometers per second:-

$$V_S = (\pi r_0/180)(d\Delta/dt) \qquad (4.6)$$

where r_0 is the earth's mean radius.

The value used for k in this study is 0.5^o. This is quite large enough to avoid significant rounding errors. Indeed, it may at first sight seem rather too large a value to use considering that the formula is an approximation, but the curvature of the travel time tables is quite small, and the values calculated agree with those given by Herrin et al (1968).

4.4.3 Corrections for the Earth's Ellipticity

The travel times calculated thus far refer to a spherical earth with a radius equal to the earth's mean radius. A correction must be applied for the earth's aspherical shape.

The chosen method is that due to Dziewonski and Gilbert (1976). They use Fermat's principle of stationary time to calculate the correction, t_e, assuming that the earth's figure is ellipsoidal, as predicted from the hydrostatic principle, and give the following formula:-

$$t_e = (1/4)(1+3\mathrm{Cos}2\theta)\,\tau_0 + (\sqrt{3}/2)\mathrm{Sin}2\theta\mathrm{Cos}\alpha\,\tau_1 + (\sqrt{3}/2)\,\mathrm{Sin}^2\theta\,\mathrm{Cos}^2\alpha\,\tau_2 \qquad (4.7)$$

where τ_0, τ_1 and τ_2 are functions of Δ and the focal depth, h, and are calculated from real earth models. Dziewonski and Gilbert found that the choice of model is unimportant, providing it is an acceptable fit to gross earth data. They tabulate values of τ_0, τ_1 and τ_2 for eight phases, including P and PKIKP. They also found that the effect of focal depth is significant and that errors of up to 0.27 sec can occur for a focal depth of 650 km if the effect is neglected.

The values of τ_0, τ_1 and τ_2 are tabulated at epicentral distance intervals of 5° and at focal depths of 0, 300 and 650 km. Two-dimensional linear interpolation is used to determine intermediate values, as the curvatures are very small.

Other methods of calculating the ellipticity correction are available. The formula

$$t_e = (H+H')f(\Delta) \qquad (4.8)$$

where H and H' are the vertical deviations of the earth's figure from the mean sphere at the epicentre and station, and $f(\Delta)$ is a function of the epicentral distance alone, is given by Bullen (1963). Tables of $f(\Delta)$ are available (e.g. Jeffreys and Bullen, 1967), and this formula has often been used in other studies. However this formula is approximate and gives significantly different values to that of Dziewonski and Gilbert.

Accurate tables of ellipticity correction against θ, Δ and α are available (e.g. Bullen 1937), but only for a limited range of latitudes, and only for surface foci. These tabulated values agree with those calculated from Equation 4.7 to within 0.1 sec. Thus Dziewonski and Gilbert's formula provides a simple and accurate method of determining the correction due to the earth's ellipticity, entirely suitable for a study such as this.

4.4.4 Corrections for the Station's Height above Datum

A correction must also be applied for the station's height above the earth's ellipsoidal datum surface, which may be taken as mean sea level. In making this correction, account must be taken of the slant of the ray which arrives at the station.

Referring to Figure 4.4, we see that the calculations so far have given the travel time to S', the final section of the ray path being along O'S'. The ray which actually arrives at the station, S, passes the datum level at point A, nearer the epicentre, and therefore earlier. The distance S'B is small, so the two ray segments O'S' and OA are effectively parallel. Drawing S'B perpendicular to AS, we therefore reconstruct a wavefront in the medium above datum, which we will assume has a uniform velocity V_0.

The arrival times at B and S' are therefore the same, and the height correction, t_z, to be applied to the travel time, corresponds to the travel time over BS. Thus

$$t_z = z \operatorname{Cos}(i)/V_0 \qquad (4.9)$$

The angle of incidence, i, can be determined from a consideration of the apparent surface velocity, V_S. The difference in arrival time at A and S' (or B), u, is given by

$$u = AS'/V_S = AB/V_0 \qquad (4.10)$$

whence

FIGURE 4.4

DIAGRAM ILLUSTRATING THE CALCULATION OF THE STATION HEIGHT CORRECTION

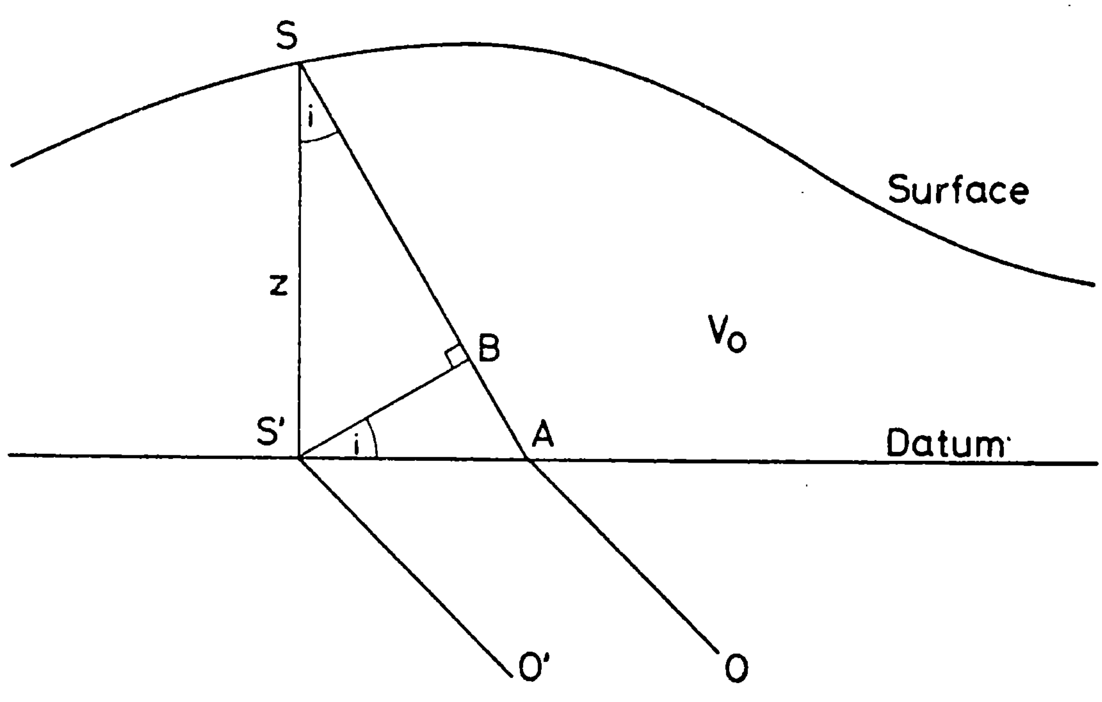

$$\mathrm{Sin}(i) = AB/AS' = V_o/V_s \tag{4.11}$$

Using the trigonometrical identity

$$\mathrm{Cos}(i) = (1-\mathrm{Sin}^2(i))^{1/2} \tag{4.12}$$

we obtain from Equations 4.9 and 4.11

$$t_z = z((1/V_o)^2 - (1/V_s)^2)^{1/2} \tag{4.13}$$

Using the upper crustal velocity of 5.8 km/sec derived by Maguire and Long (1976) at Kaptagat, and the apparent surface velocity V_s, the height correction is calculated for each arrival using Equation 4.13.

4.4.5 The Formation of Raw Delay Times

The program MANETA calculates the travel times, ellipticity corrections and station height corrections as described above, and adds these to the given origin times to give the predicted arrival times, which are output. To form the raw delay times used in subsequent calculations, these predicted arrival times are subtracted from the corresponding measured onset times. The hypocentral coordinates of the events used, and the raw (measured) delay times are given in the form of output from the program SEPD (see Section 4.6) in Appendix 4. Figure 4.5 shows a map of the world using an azimuthal equidistant projection centred on Nairobi, with the epicentres of the events used indicated.

(The event numbers referred to in the list, and elsewhere in this work, each consist of four 2-digit numbers, representing the nearest clock minute, hour, day

FIGURE 4.5

DISTRIBUTION OF EVENTS USED IN THIS STUDY

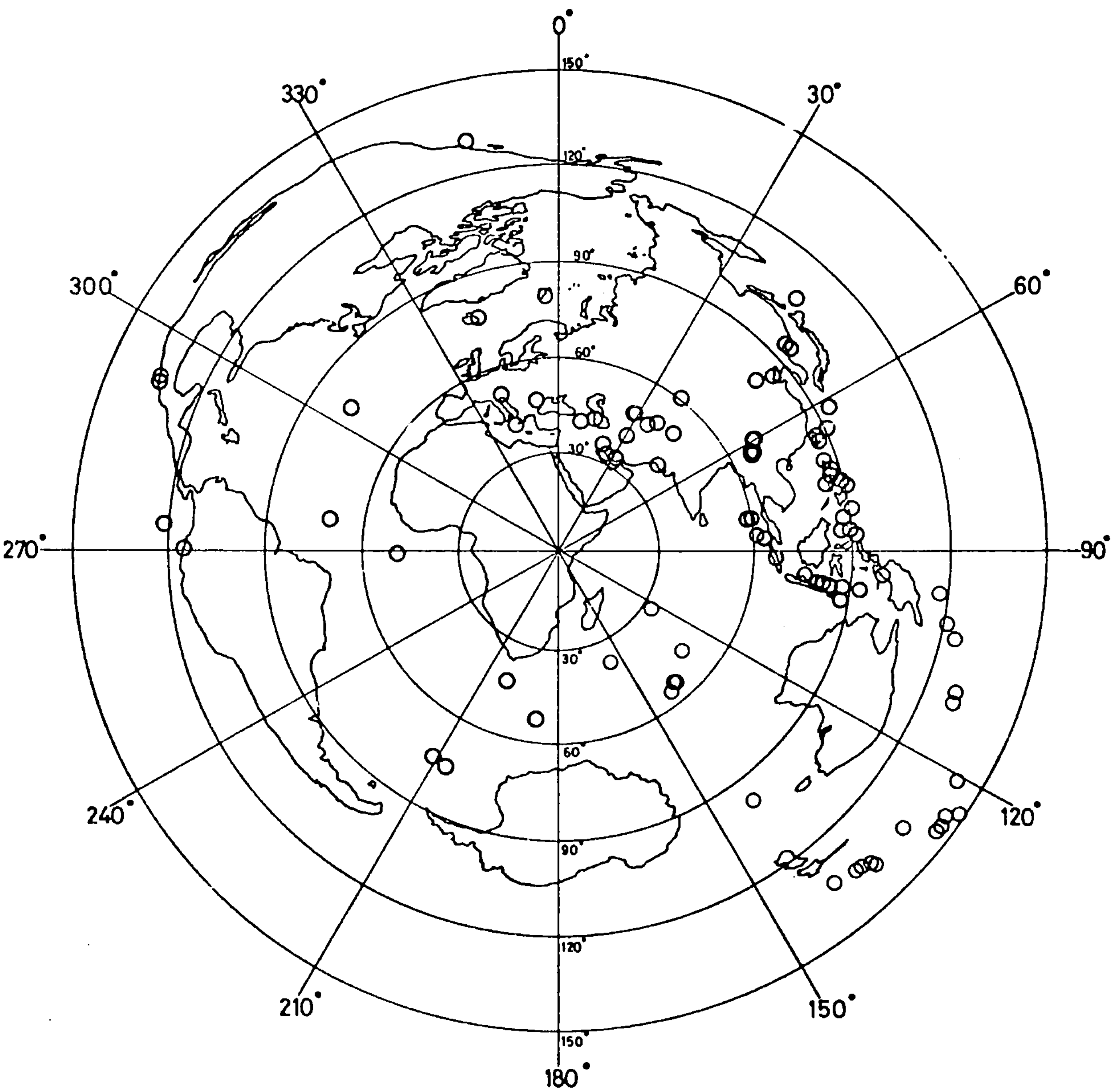

and "year" of the first onset. Since earthquake arrivals rarely occur in the same minute, this system of numbering is largely unambiguous. When two events do arrive in the same minute, the earlier is assigned a number corresponding to the previous minute, thus resolving the ambiguity.)

4.5 The Method of Relative Delays

A single raw delay time measurement is almost worthless since the value obtained, which should only reflect anomalies in the velocity structure immediately beneath the station, will be contaminated by other effects. Velocity anomalies anywhere along the ray path will have an effect, as will errors in the hypocentral location, origin time, travel time tables and onset time measurements.

The effect of random errors and of velocity inhomogeneities far from the station may be reduced by taking the mean of many single measurements. The errors arising from these sources will tend to fluctuate around zero, and cancel. However, this mean will still be contaminated by systematic errors, which may occur, for example, because of non-random timing errors or errors in the travel time tables. These systematic errors are difficult to eliminate.

A more satisfactory method of reducing errors is to measure relative delays between stations. Long and Mitchell (1970) discuss the method of relative delays in some detail, expressing each raw delay time as a sum of six terms:-

$$T = S + T_o + T_e + T_t + T_i + E \quad (4.14)$$

where

- S is the required delay time arising from the effect of material with anomalous velocity beneath the station,
- T_o arises from errors in the assumed earthquake focal data,
- T_e arises from material with anomalous velocities beneath the source,
- T_t is the error due to inaccuracies in the travel time tables and calculations,
- T_i is the instrumental delay for which correction may be made, and
- E is the error due to misreading and poor timing of the seismogram.

A relative delay measurement between two stations consists of the difference, $T-T'$, between two such individual measurements using the same source event.

Under these circumstances the error terms T_o-T_o', T_t-T_t', T_i-T_i' and $E-E'$, will tend to cancel. Thus the remaining difference term, $S-S'$, is better determined than by using independent sets of delay time measurements at the two stations.

The efficacy of this method depends on the station distribution and the travel time tables used. In particular, it is important that the distance between stations be small in comparison with the epicentral distance, so that the rays follow substantially the same path, except near the stations.

Errors arise from non-zero values of the difference terms $T_o - T_o'$, $T_e - T_e'$, $T_t - T_t'$, $T_i - T_i'$ and $E - E'$. Following Long and Mitchell, we consider each difference term separately.

(1) Errors in hypocentral location lead to non-zero values of the term $T_o - T_o'$. An error in the origin time will have no effect, since it will exactly cancel. However errors in the epicentral location do not exactly cancel, because of the curvature of the travel time curve. We may calculate the approximate magnitude of the error arising from this cause.

Suppose that the true epicentral distances to the two stations are Δ and Δ', and that the travel time as a function of epicentral distance and focal depth, h, is $t(\Delta,h)$. Suppose also that the epicentral distances are subject to an error in mislocation which increases each by an amount $\delta\Delta$. Then

$$T_o = t(\Delta+\delta\Delta)-t(\Delta) \simeq (\partial t/\partial\Delta)_{\Delta}\delta\Delta \qquad (4.15)$$

$$T'_o = t(\Delta'+\delta\Delta)-t(\Delta') \quad (\partial t/\partial\Delta)_{\Delta'}\delta\Delta \qquad (4.16)$$

The resultant error will be

$$\delta T_o = ((\partial t/\partial\Delta)_{\Delta} - (\partial t/\partial\Delta)_{\Delta'})\delta\Delta$$

$$= (\Delta-\Delta').\delta\Delta.(\partial^2 t/\partial\Delta^2) \qquad (4.17)$$

The effect of errors in the focal depth is also to introduce errors into relative delay measurements. The derivation of the corresponding formula

$$\delta T_o = (\Delta-\Delta').\delta h.(\partial^2 t/\partial\Delta\partial h) \qquad (4.18)$$

where h is the error in focal depth, is entirely analogous to that for Equation 4.17.

These formulae are derived assuming that the station pairs and mislocation errors align with the great circle path between the event and the stations. In practice, these directions are random, or nearly so, and the average errors will be less than those given by Equations 4.17 and 4.18. Each misorientation will introduce a separate cosine term into the equation, which when averaged in an R.M.S. sense will give a factor of $1/\sqrt{2}$. For Equation 4.17, there are two such terms which combine to give a total correction factor of 0.5, while for Equation 4.18 there is only one, corresponding to a factor of approximately 0.7.

Values of $\partial^2 t/\partial\Delta^2$ for P were obtained from the values of apparent velocity given in Herrin's tables, using a simple finite difference formula. The maximum value over the epicentral distance range 30° - 100° is 0.085 sec $\deg^{-2}$, occurring at about 85°. Beyond 105°, where PKIKP is used, values of $\partial^2 t/\partial\Delta^2$ obtained from travel times were considerably smaller. The epicentral locations used in this study are those given in the USCGS PDE listings, which are normally taken to have errors of about 0.25° (P.Marshall, AWRE Seismology Unit, pers.comms.). All but one of the DKSP stations are within 3° of each other, although the leap-frogging of equipment from site to site decreases the maximum distance between simultaneously recording stations to 2°. The one exception is station 50 which is 5° from the farthest simultaneously recording station. Thus we may use the following values, $\Delta-\Delta' = 2^{\circ}$, $\delta\Delta = 0.25^{\circ}$ and $\partial^2 t/\partial\Delta^2 = 0.085$ sec deg^{-2}, in Equation 4.17 and divide by 2 (for random orientations) to obtain an estimate of the errors due to mislocation. The error thus calculated is 0.020 sec.

Values of $\partial^2 t/\partial\Delta\partial h$ were obtained in the same way. The largest value obtained was -0.0006 sec deg^{-1} km^{-1}, in the epicentral distance range 30°-100°, with an average value about one half of this. At epicentral distances above 105°, the $\partial^2 t/\partial\Delta\partial h$ values obtained (for PKIKP) were zero.

Focal depths are notoriously difficult to estimate from onset times alone, and the listed values of 33 km indicate that the iterative location technique used by the USCGS, cannot improve upon this initial guess. pP-P measurements however often give reliable measurements for the deeper events, for which $\partial^2 t/\partial\Delta\partial h$ is larger. Nevertheless we may assume that the depths are accurate to about 40 km (P.Marshall, AWRE Seismology Unit, pers.comms.). Using $\Delta-\Delta' = 2^{\circ}$, $\partial^2 t/\partial\Delta\partial h = 0.0004$ sec deg^{-1} km^{-1} and $\delta h = 40$ km in Equation 4.18, and multiplying by the random orientation factor 0.7, we obtain the value 0.022 sec for the error in relative delay due to inaccuracy in focal depth estimates.

The above values, which ignore the larger distance of Station 50, are too large due to the use of maximum values in Equations 4.17 and 4.18, and an average value should therefore be smaller. Inclusion of the relatively few arrivals from Station 50, which will have errors approximately 5/2 times as large as estimated above, will tend to increase the average error. Assuming that the two effects cancel, we may reasonably settle on the above values as representing the average error. Combining two of these in the usual way for random errors, the total error in relative delay due to inaccuracies in hypocentral data, is estimated as 0.030 sec.

(2) Delays due to material with anomalous velocities near the source and along the paths in the mantle and core will to a great extent cancel, especially if lateral variations are not rapid. Rapid lateral changes in velocity are known to occur around subduction zones, which are major sources of events for this study. However, even in these cases the first phase to arrive at each station will take almost the same path near the source, even if it is one refracted through a highly anomalous region such as a down-going lithospheric slab. Davies and MacKenzie (1969) quote examples where this effect gives rise to relative station residuals of as much as 5 sec. However, these anomalous travel times are confined to a small range of epicentral distance ($\sim 10^{\circ}$), and confined to the range 0°–40° (for slabs dipping at 45°). Since only 5 of the 112 events used are in this range, and in all probability will not lie in the critical ranges of azimuths and distance, this source of error may safely be ignored.

(3) Errors in the travel time tables and calculations

made from them may give rise to non-zero values of $T_t - T_t'$, and thus introduce errors. Long and Mitchell (1970) used Jeffreys-Bullen (1940) tables, and those due to Herrin et al (1968), to measure relative delays between stations in Iceland and others in Greenland, Sweden and Scotland. They observed a scatter in the relative delays against distance when Jeffreys-Bullen tables were used, which "vanished" when Herrin's tables were used. Consequently Herrin's tables are used throughout this study.

Long and Mitchell (1970) noted that other travel time tables compiled in the previous few years, for example those due to Cleary and Hales (1966), had very similar shapes to Herrin's, differing only in a base line shift, which cancels when relative delays are used. They considered that for the Iceland experiment, where inter-station distances were up to 15°, errors due to inaccuracies in the gradients of Herrin's tables were negligible. For DKSP where inter-station distances are less than one sixth of this, it is reasonable to conclude that these errors are negligible.

Interpolation will give rise to maximum errors which are of the order of twice the accuracy with which the travel times are quoted, or about 0.020 sec.

The calculations of ellipticity and height corrections, which are slowly varying functions of epicentral distance and position, introduce insignificant errors into the relative delay measurements.

(4) Any instrumental delays which exist are very small,

probably less than 0.020 sec (see Section 3.11) and are approximately equal at each station. As such they will cancel to give a zero value for $T_i - T_i'$.

(5) The term (E-E') represents the error due to misidentification and mistiming of the relative onsets. The error due to misidentification corresponds to the estimated error in aligning the traced waveform with the paper seismograms and hence to the assigned onset weight codes as described in Section 4.3. The error in timing results from all the random errors inherent in playback, filtering and measurement as described in Chapter 3.

The misidentification error varies widely from one station pair to another and is the largest single factor in the corresponding relative delay measurement. For example, combining the errors for two onsets, with onset weight codes of 2 and 3, gives a corresponding error in relative delay of $(0.4^2 + 0.3^2)^{1/2} = 0.5$ sec. If the two codes are 6, the corresponding error will be only $(0.05^2 + 0.05^2)^{1/2} = 0.07$ sec.

Typical timing errors as calculated in Chapter 3 amount to about 0.025 sec, with a "worst case" error of 0.040 sec. We may adopt an "average" value of about 0.030 sec, which must be included twice, one for each onset, to give a total error of 0.040 sec.

Having discussed the various sources of error in relative delay measurements, it is now desirable to combine these to give an average figure which may be compared with residuals formed in subsequent quantitative interpretations. Since simple relative delays of the sort T-T' are not explicitly formed in this study, corresponding errors for pairs of measurements are not particularly useful.

For reasons discussed in the section following, individual delay measurements retain their identity until quite late in interpretation. Hence it is advantageous to assign a corresponding probable error to each raw delay time. These errors must be assigned in such a way that if two are combined, the total error equals the error in the corresponding relative delay. An estimate of the error in relative delay would be calculated using the formula

$$\epsilon_r^2 = \delta T_o^2 + \delta T_e^2 + \delta T_t^2 + \delta T_i^2 + \epsilon_o^2 + \epsilon_o'^2 + 2T_m^2 \qquad (4.19)$$

where δT_o, δT_e, δT_t and δT_i are the errors corresponding to the difference terms, as discussed previously, and ϵ_o and ϵ_o' represent the expected errors in identification, corresponding to the two onset weight codes, and T_m is a single timing error.

If we estimate individual errors using the formula

$$\epsilon^2 = 0.5(\delta T_o^2 + \delta T_e^2 + \delta T_t^2 + \delta T_i^2) + \epsilon_o^2 + T_m^2 \qquad (4.20)$$

the combinational requirement is fulfilled, and Equation 4.19 is properly divided up.

The magnitude of each term has been estimated, and a corresponding total error estimate may be assigned to each onset weight code. A corresponding weighting factor, w, may be calculated using the relation

$$w = a/\epsilon^2 \tag{4.21}$$

where a is an arbitrary constant of proportionality, here chosen to be 0.01.

Estimated total errors, and corresponding assigned weights, are given for each OWC in Table 4.2 Also given in the table is the number of occurrences of each onset weight code.

Using these figures we may calculate an unweighted R.M.S. error using the formula

$$\epsilon_u = (\sum_i r_i{}^2/m)^{1/2} \tag{4.22}$$

and a corresponding weighted value

$$\epsilon_w = (\sum_i w_i r_i{}^2/\sum_i w_i)^{1/2} \tag{4.23}$$

The values obtained for E_u and E_w are 0.196 and 0.114 sec respectively. The figure for E_w will be examined later, when the efficacy of interpretation techniques is discussed.

4.6 The Calculation of Station Delays

Having obtained individual delay measurements, and discussed the method of relative delays, there only remains the problem of the best method of reducing these to give station delays.

Usually in a study of this sort, one station is chosen as standard, and delays are calculated in relation to it. Generally, several measurements of each station delay relative to the standard station are available, one for each

TABLE 4.2

TOTAL ERROR AND NUMBER OF OCCURRENCES

FOR EACH ONSET WEIGHT CODE

ONSET WEIGHT CODE	ESTIMATED ONSET ERROR (sec)	ESTIMATED TOTAL ERROR (sec)	ASSIGNED WEIGHT	NUMBER OF PICKS
6	0.05	0.064	2.47	74
5	0.1	0.107	0.86	135
4	0.2	0.204	0.24	146
3	0.3	0.303	0.11	77
2	0.4	0.402	0.06	12

Total number of measurements, $k = 44$

Unweighted R.M.S. error, $E_u = 0.195$ sec.

Weighted R.M.S. error, $E_w = 0.113$ sec.

event simultaneously recorded at both sites. The mean of these several measurements is taken as the best estimate of the relative delay, while an estimate of the error can be deduced from the scatter. This is essentially the method used by Long and Mitchell (1970) and by Steeples and Iyer (1976).

Steeples and Iyer comment that the standard station should, preferably, be removed from the influences of the structure under investigation (but, of course, sufficiently close for the method of relative delays to be effective). If the velocity structure under the standard station is known from other investigations, this procedure simplifies interpretation of the relative delays. The use of a standard station is particularly advantageous when it can be assumed that the layering under it is laterally homogeneous. Under these circumstances the rays received at the standard station are not subject to perturbations dependent on the back-bearing of the event, and any such dependence at the other stations may be recognised more easily.

The use of a standard station for this study is impractical because no single DKSP station recorded simultaneously with all the others. The permanent WWSSN station at NAI satisfies this requirement, but the seismograms from NAI are in such a compressed format that waveform matching with the DKSP playouts would have been impractical. Thus the advantage of accurate relative onset timing would have been lost. Moreover, the large delay time at Nairobi, both absolute, and relative to BUL, and which seems to have a considerable back-bearing dependence (e.g. Lilwall and Douglas, 1970), indicates that it lies on anomalous material and that horizontal stratification is unlikely to exist beneath it. In fact there is no a priori reason to believe that horizontal layering exists beneath any of the DKSP stations.

We may however use an alternative technique, which does not consider any one station to be standard, but which preserves the relative delays. This technique relies on two assumptions, implicit in the method of relative delays.

The first assumption is that individual delay measurements consist of the sum of two terms thus:

$$T_{ij} = S_j + E_i \qquad (4.24)$$

where T_{ij} is the delay measured at the j^{th} station using the i^{th} event, S_j is the station delay, and E_i is the event residual. The second is that the terms S_j are independent of event position. Comparison with Equation 4.15 shows that the event residual is in fact the sum of the terms T_o, T_e, T_t, T_i and E.

Letting k be the number of raw delay measurements, n be the number of stations, and m be the number of events, it may be seen that k, the number of equations, considerably exceeds n+m, the number of unknowns. Hence we may attempt to solve for each of the unknowns, and in particular for the S_j.

However it is easy to see that no matter how large k is relative to n+m, the set of Equations 4.24 cannot be solved unambiguously, for they are not affected if we add an arbitrary constant to each of the E_i providing we subtract the same constant from each of the S_j. In other words we need to fix a baseline for the station delays in precisely the same way as we would by using a standard station. This base line may be fixed by adding one further equation to the set.

There is a wide range of equations which will perform the required function. We could follow the standard station method and fix one of the station delays to some arbitrary value. However, it is more logical to attempt to fix the baseline in an absolute sense, by making use of the fact that the onsets are measured absolutely. This may be done by formulating the additional equation as

$$\emptyset = \sum_{i=1}^{m} E_i \tag{4.25}$$

We now have to solve k+1 equations in n+m unknowns. We may rewrite them in matrix notation

$$\underline{T} = C\underline{U} \tag{4.26}$$

where

$\underline{T}$ is a k+1 element vector, the first element of which is zero, corresponding to the left hand side of Equation 4.25, and the remaining k elements are the left hand sides of the Equations 4.24,

$\underline{U}$ is the n+m element vector of the unknown E_i and S_j corresponding to the right hand sides of Equations 4.24 and 4.25, and

C is a (k+1) by (n+m) matrix of zeros and ones linking the knowns to the unknowns according to the Equations 4.24 and 4.25.

Since the matrix C is not in general square, Equation 4.26 cannot be exactly solved. We must solve it in a "least squares" sense by introducing a k+1 element vector of residuals, $\underline{r}$, and rewriting the equation

$$\underline{\Upsilon} + \underline{r} = C\underline{U} \qquad (4.27)$$

The least squares solution is the one which minimizes the "objective function", F, given by

$$F = 1/k \sum_{i}^{k+1} r_i^2 \qquad (4.28)$$

Standard techniques are available for finding $\underline{U}$ such that this criterion is fulfilled. Using matrix algebra it is easy to show that $\underline{U}$ is then given by

$$U = (C^T C)^{-1} C^T \qquad (4.29)$$

No account has yet been taken of the variable quality of the measurements. Each of the Equations 4.24 has been given equal weight, which is not justified in view of the wide range in expected error between the individual Υ_i. Since the residuals, r_i, are in effect the differences between the measured values, Υ_i, and the theoretical values formed by $C\underline{U}$, they are equivalent to the errors in the T_{ij}. Thus the ideal weighting method would, on average, give residuals proportional to the expected errors. This is achieved by minimizing the objective function

$$F_W = (\sum_{i=1}^{k+1} w_i r_i{}^2)/(\sum_{i=1}^{k+1} w_i) \qquad (4.30)$$

It can easily be seen that this function is minimised if each Equation 4.24 is multiplied by the square root of its corresponding weight.

We may also take account of the variable quality of the absolute onset determinations represented by the event weight codes, V_j. We assign a corresponding event weight v_j using the formula

$$v_j = 2^{(V-5)}, \qquad V_j \neq 0$$

$$v_j = 0, \qquad V_j = 0 \qquad (4.31)$$

and replace Equation 4.25 by

$$0 = \sum_{j=1}^{m} v_j E_j \qquad (4.32)$$

Since picking errors in the absolute onset times cannot easily be estimated, and other errors are impossible to quantify, no statistically rigorous scheme of weighting can be introduced for event weights. Nevertheless, the above scheme is intuitively reasonable.

Introducing weights according to the above scheme alters the elements of $\underline{\Upsilon}$ and C, but not the form or essential character of Equation 4.26.

Calculations for forming the vector and the matrix C and solving for $\underline{U}$ are all performed using the computer program SEPD written in FORTRAN for the NUMAC system. The program is listed in Appendix 4, where a brief description of input formats is given. The solution of the matrix equation is performed by the NAG subroutine F04AMF, designed for accurate least squares inversion.

Having calculated $\underline{U}$, the program calculates theoretical values of the individual delay times by evaluating $C\underline{U}$, and dividing each term by the corresponding weight. The residuals are also calculated and the value of the objective function, F_W, determined using Equation 4.30. This quantity is, in fact, the weighted R.M.S. of residuals.

The approximate error in each unknown may also be calculated. The formula

$$e_i^2 = \frac{\sum_{j=1}^{N+1} \delta_{ij} w_i r_i^2}{\left(\sum_{j=1}^{N+1} \delta_{ij} w_i\right)\left(\sum_{j=1}^{N+1} \delta_{ij} - 1\right)} \qquad (4.33)$$

is used, where $_{ij}$ is the Kroneker delta function defined by

$$\delta_{ij} = 1, \quad j=i \qquad (4.34)$$

$$\delta_{ij} = 0, \quad j \neq i$$

and merely selects the weights and residuals applicable to the unknown. This formula is based on one given by Berry and West (1966) for estimating errors in time term analysis, which uses very similar mathematical techniques to those described here. Their formula does not involve weights, and the modification is merely to include these.

The output produced by SEPD is given in Appendix 4, and includes all the theoretical and measured delays together with the residuals. The event delays are also given with corresponding error estimates, and relevant hypocentral data. The station delays are also listed, with their corresponding error estimates.

The station delays are given in Table 4.3. The weighted RMS residual, F_W, is 0.127 sec, in good agreement with the estimate for the weighted RMS error, E_W, of 0.114 sec calculated in Section 4.5. This close agreement between

TABLE 4.3

STATION DELAYS

STN. NO.	STATION NAME	DELAY TIME (sec)	NO. OF EVENTS	ERROR (sec)
08	MOLO	3.604	15	0.054
09	LONDIANI	3.586	15	0.057
10	EGERTON	3.866	19	0.019
11	NAKURU	3.404	37	0.023
12	GREENSTEDS	3.417	29	0.021
13	OL KALOU	3.687	21	0.032
14	NJORO	3.917	8	0.032
15	ELMENTEITA	3.484	4	0.024
16	ILKEK	3.649	8	0.034
17	NAIVASHA	3.313	3	0.033
18	LONGONOT	3.209	30	0.025
19	KIJABE	2.906	9	0.039
21	UPLANDS	3.291	9	0.058
22	NAIROBI	3.016	9	0.038
23	ISINYA	2.770	25	0.026
24	ULU	2.524	8	0.049
25	KESIKAU	2.599	31	0.015
26	SULTAN HAMUD	2.648	13	0.045
27	MAKINDU	2.631	48	0.013
28	KIBWEZI	2.542	27	0.021
29	MTITO ANDEI	2.269	26	0.020
30	TSAVO	2.260	26	0.021
31	OLOITOKITOK	2.969	2	0.121
50	LODWAR	3.168	22	0.057

the two figures indicates that the basic assumption behind the method of relative delays, that the relative delay between two stations is independent of the event used, seems to hold for this experiment. The station delays have average relative errors of about 0.03 sec.

4.7 Accuracy of the Baseline Determination

Absolute timing of the onsets has enabled the station delays to be fixed as a group in an absolute sense, as well as with great relative accuracy. We may estimate the random error in the baseline fix by considering the spread of the event residuals. The standard error in the mean of these, χ, is estimated using the formula

$$\chi = [(\sum_{i=1}^{m} v_i E_i)/((m-1)\sum_{i=1}^{m} v_i)]^{1/2} \tag{4.35}$$

Using this equation a value of 0.089 sec is obtained.

All the delays presented here are larger than the largest station residual (for AAE) obtained by Lilwall and Douglas (1970). Thus it seems that there must be a large systematic error in the raw delay time measurements which gives rise to an overall baseline shift in the station delays. Such a systematic error can arise for two reasons. Firstly it may arise as a result of systematic late picking of onset times and secondly it may arise as a result of a baseline error in the travel time tables used.

Systematic late picking of onset times might be expected for smaller amplitude events, where the first arrival could be hidden in noise. This would not however be the case with the larger amplitude events. Any such tendency would be revealed as a correlation between event residual and event weight code, since late picking of the onset is taken up as a larger event residual and the event weight code is a subjective estimate of the quality of the arrival. Fitting a straight line between these quantities using linear regression gives a gradient of 0.076 ± 0.096 and a correlation coefficient of between -0.039 and 0.152 (both at 65% confidence limits). These estimates are entirely consistent with there being no such correlation. Thus we can be confident that there is no tendency to pick poor onsets later than the better ones and, assuming that the better ones are reliably picked, that there is no systematic tendency to pick late.

This analysis does not rule out the possibility of some instrumental delay introducing a systematic error. It has already been shown, in Chapter 3, that the method of timing employed in this study introduces a negligible systematic delay in measuring impulsive onsets. However, teleseismic arrivals are never truly impulsive, and some ambiguity must occur in identifying onsets, which is a somewhat subjective exercise. Since origin times are determined from observations made by others from substantially different instruments employing a vastly reduced display scale, it is more likely than not that some sort of systematic error, resulting in an overall baseline shift, is present. There is no easy method of detemining the magnitude of this error, but it is unlikely to amount to more than one second.

That a significant baseline shift would arise through the use of alternative travel time tables can easily be deduced by looking at Figure 4.6. Here the differences between the travel time tables used in this study (Herrin et al, 1968) and four others (Jeffreys-Bullen, 1967; Lilwall and Douglas, 1970; Cleary and Hales 1966; Carder, Gordon and Jordan, 1966) are indicated for P, over the epicentral distance range 30°-100°. Figure 4.7 indicates the corresponding differences for PKIKP (for Jeffreys-Bullen only, as the others do not give travel times other than for P). Since these differences are all positive over the entire epicentral distance range, the use of any other tables would have resulted in systematically later predicted arrival times and hence smaller delays. The relative delays would not be substantially affected, since the difference curves are only slowly varying functions of distance. Thus the major effect of using alternative tables would be to shift the baseline.

The baseline shift, Q, resulting from the use of alternative tables may be calculated using the formula

$$Q = \sum_{i=1}^{m} v_i R_i \qquad (4.36)$$

Where R_i is the difference between the two given travel times corresponding to the epicentral distance of the i^{th} event. This formula corresponds exactly with Equation 4.32, which fixes the baseline in the first instance. Q is to be subtracted from each of the station delays to give the

FIGURE 4.6

DIFFERENCES BETWEEN TRAVEL TIME TABLES FOR P

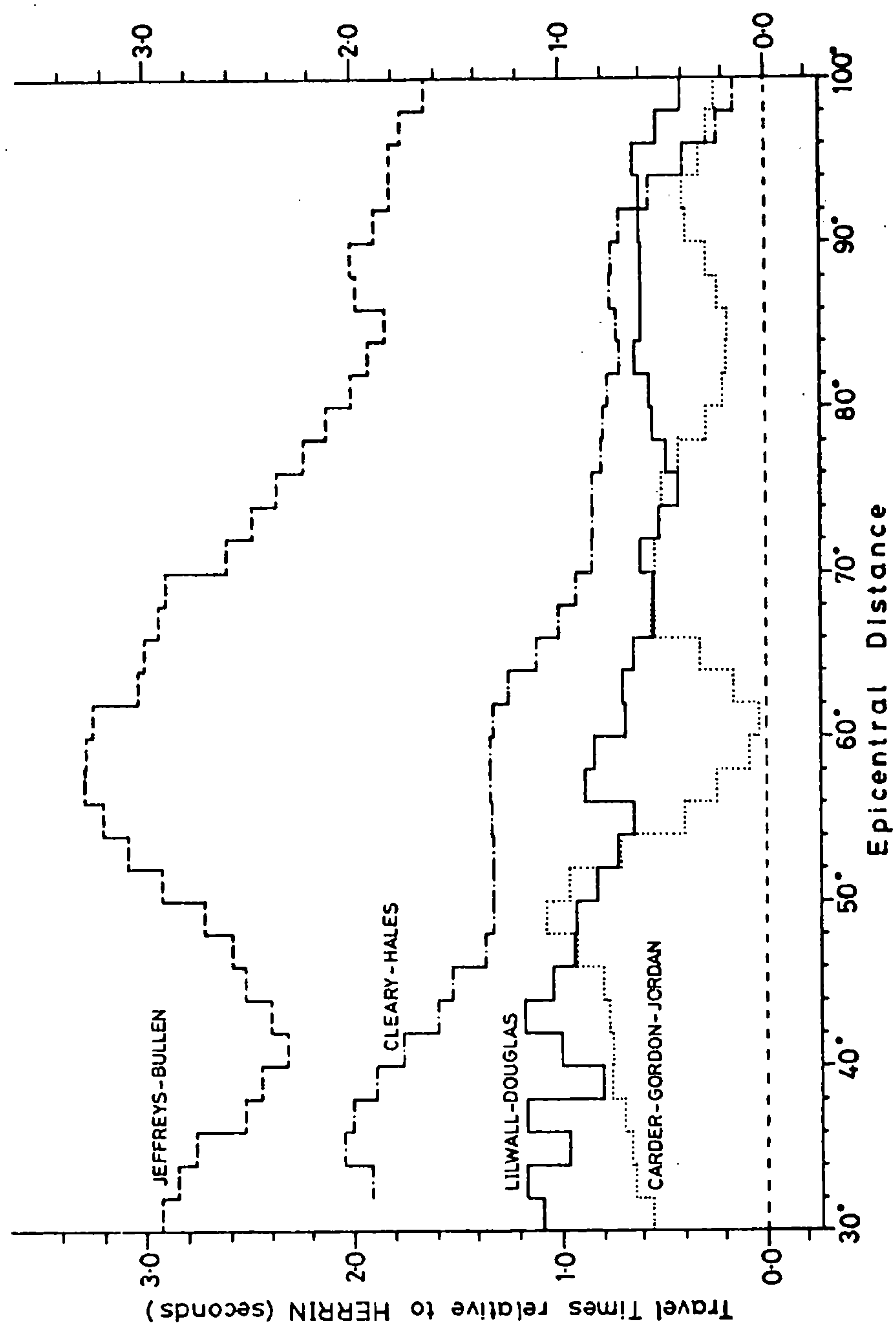

FIGURE 4.7

DIFFERENCES BETWEEN TRAVEL TIME TABLES FOR PKIKP

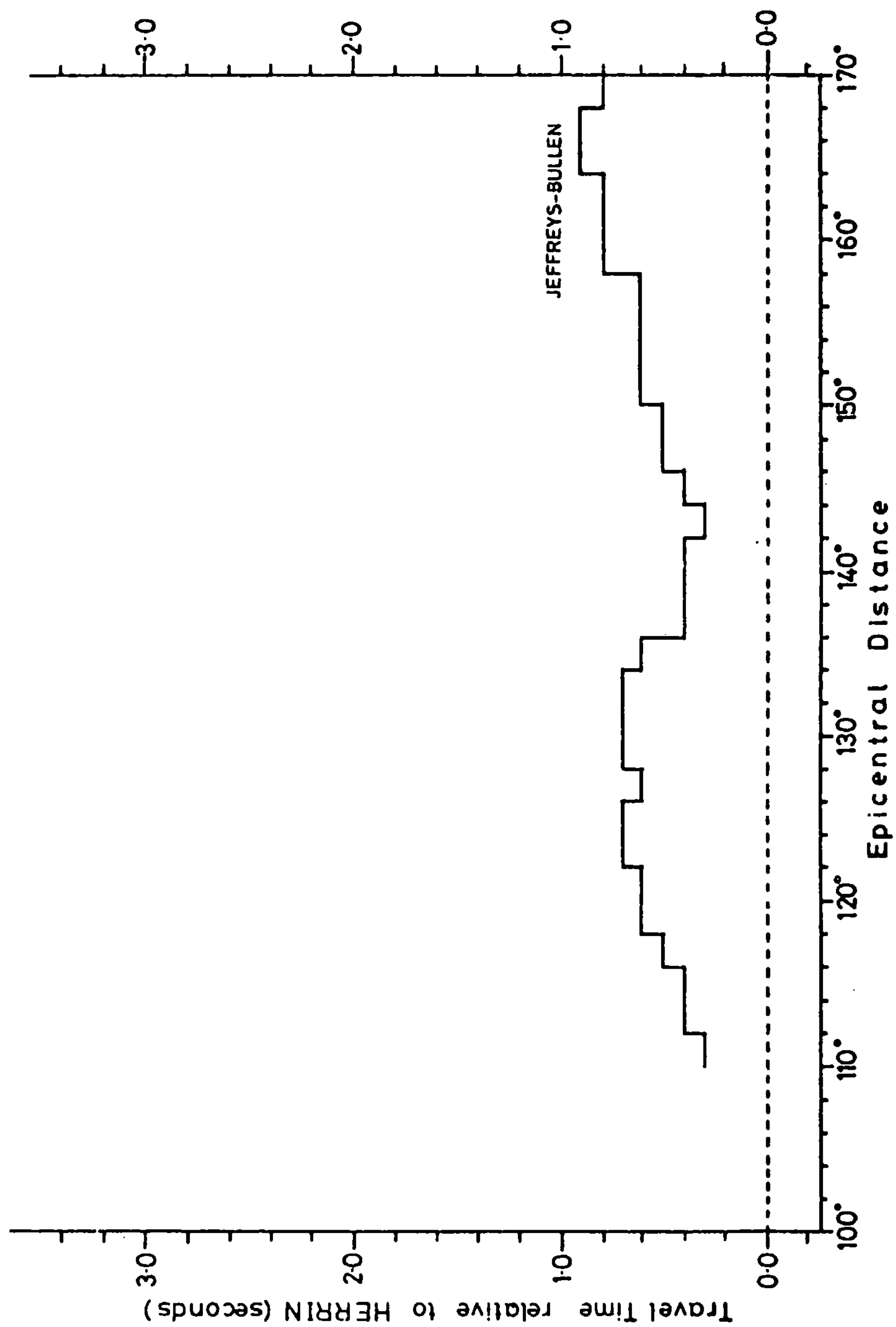

alternative values.

Values of Q have been calculated, using P only, for each of the travel time tables represented in Figure 4.6. A fifth value has also been calculated corresponding to Jeffreys-Bullen P and PKIKP travel times combined. The corresponding station delays for each value of Q are listed in Table 4.4, along with the values of Q themselves.

The baseline shifts calculated in this way vary from 0.405 to 2.336 sec. We must consider which value, if any, best fixes the baseline.

Differences in baselines for the different travel time tables illustrate the main problem inherent in the classical approach to determining travel times, which uses earthquakes only as sources. The problem is simply that the hypocentral coordinates of the events used must all be determined precisely during the process. This is relatively easy for the epicentral coordinates, where even approximate tables will give quite good estimates, providing that the stations are reasonably well distributed (Bullen, 1963). Even focal depths can be estimated accurately for some events if, for example, phases such as pP are pickable. However, origin times are difficult to estimate, and these are obviously crucial to the baseline determination.

Nuclear explosions, for which accurate origin times are known, can be used to fix the baseline, but the number of such events is small and restricted to a very few geographical areas which may not have crustal and upper

TABLE 4.7

STATION DELAYS CORRECTED FOR BASELINE SHIFTS BETWEEN HERRIN S AND OTHER TRAVEL TIME TABLES

STN. NO.	UNCORR. DELAY	J-B P ONLY	J-B WITH PKIKP	LILWALL AND DOUGLAS	CLEARY AND HALES	CARDER GORDON JORDON
08	3.604	1.268	1.514	2.923	2.619	3.199
09	3.586	1.250	1.496	2.905	2.601	3.181
10	3.866	1.530	1.776	3.185	2.881	3.461
11	3.404	1.068	1.314	2.723	2.419	2.999
12	3.417	1.081	1.327	2.736	2.432	3.012
13	3.687	1.351	1.597	3.006	2.702	3.282
14	3.917	1.581	1.827	3.236	2.932	3.512
15	3.484	1.148	1.394	2.803	2.499	3.079
16	3.649	1.313	1.559	2.968	2.664	3.244
17	3.313	0.977	1.223	2.632	2.328	2.908
18	3.209	0.873	1.119	2.528	2.224	2.804
19	2.906	0.570	0.816	2.225	1.921	2.501
21	3.291	0.955	1.201	2.610	2.306	2.886
22	3.016	0.680	0.926	2.335	2.031	2.611
23	2.770	0.434	0.680	2.089	1.785	2.365
24	2.524	0.188	0.434	1.843	1.539	2.119
25	2.599	0.263	0.509	1.918	1.614	2.194
26	2.648	0.312	0.558	1.967	1.663	2.243
27	2.631	0.295	0.541	1.950	1.646	2.226
28	2.542	0.206	0.452	1.861	1.557	2.137
29	2.269	-0.067	0.179	1.588	1.284	1.864
30	2.260	-0.076	0.170	1.579	1.275	1.855
31	2.969	-0.067	0.879	2.288	1.984	2.564
50	3.168	0.832	1.078	2.487	2.183	2.763
CORRECTION Q=		2.336	2.090	0.680	0.985	0.405

mantle structures representative of the global average. Although the use of man made sources can help to reduce the errors in the baseline fix, an accurate global average cannot be obtained.

The main effect of errors in the baseline of the travel time tables, when they are used to locate events, is to introduce errors into the estimates of focal depth and/or origin time. If other tables are then used to measure delay times using these hypocentral coordinates, these errors will show up as a systematic delay. Only if the same tables are used to measure the delays as are used to locate the events will the systematic error be eliminated.

Since Jeffreys-Bullen tables were used, by the USCGS, to locate the events in space and time (Engdahl and Gunst, 1966) these tables should be used to fix the baseline. Consequently, the Jeffreys-Bullen correction (including the PKIKP measurement, since these are used in fixing the baseline initially) is used. The station delays thus corrected are used in all subsequent interpretation.

It might be argued that Jeffreys-Bullen tables should have been used throughout this study. However, Herrin's tables were preferred as the gradients, critical to accurate relative delay measurements, are better determined than in Jeffreys-Bullen tables (Long and Mitchell, 1970).

The corrected delays, which range from 0.170 to 1.827 sec, compare well with the range of values obtained in other studies of the rift zones of Africa. However, the systematic error in the baseline of the station delays has probably not been entirely eliminated, for the reasons discussed above. Thus interpretative techniques should concentrate on the relative station delays which are determined with an accuracy of about 0.03 sec.

CHAPTER 5

INTERPRETATION OF STATION DELAYS

5.1 Introduction

The station delays derived in the previous chapter are discussed, and simplified interpretations based on assumed horizontal layering beneath each station presented. A small correction is made for the effects of epicentral distance. The strong correlations of station delay with height and Bouguer anomaly are demonstrated and reasons for these discussed. Finally, the assumption of horizontal layering is considered.

5.2 Delays due to Horizontally Layered Structures

Throughout this chapter it is assumed that the velocity structure beneath each station is horizontally stratified. This simplifying assumption is made in order that we may derive an expression for the delay time in terms of the velocity profile, and which will not depend on epicentral back-bearing.

To derive such an expression we divide the Earth's outer regions into n concentric layers such that within the i^{th} layer the velocities V_i and V_i', corresponding to normal and anomalous material respectively, are uniform, as shown in Figure 5.1. We then trace rays from the base of the n^{th} layer (below which the structure is normal), through both

FIGURE 5.1

DIAGRAM ILLUSTRATING THE DERIVATION OF THE DELAY TIME EQUATION FOR HORIZONTAL LAYERING

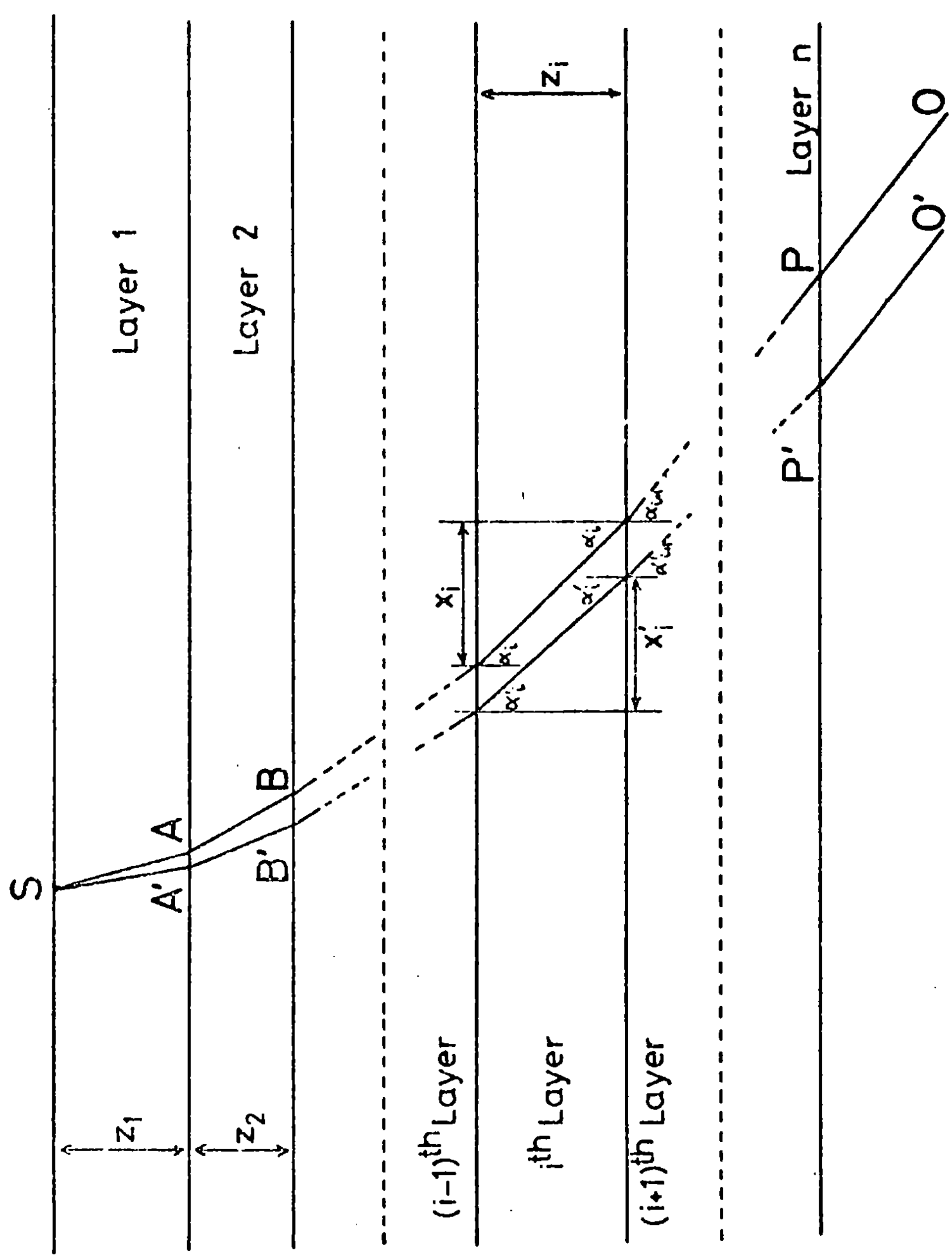

the normal and anomalous velocity structures.

The normal ray follows the path OP...BAS, and the ray through the anomalous material O'P'...B'A'S. Assuming now that the depth to the base of the n^{th} layer is small compared with the Earth's radius, and therefore that the layers are parallel sided, it is apparent that the distance PP' is small compared with the epicentral distance, and that the rays OP and O'P' are effectively parallel.

Let the layer thicknesses be $z_1, z_2 \ldots z_n$. Let also the angle of incidence for the normal ray in the i^{th} layer be α_i, and the horizontal distance which it travels in layer i be x_i. Let primes indicate the equivalent quantities for the ray through the anomalous material.

The travel times, t_i and t_i', for the two rays in the i^{th} layer are then

$$t_i = \frac{z_i}{V_i \operatorname{Cos}\alpha_i}$$

$$t_i' = \frac{z_i}{V_i' \operatorname{Cos}\alpha_i'} \tag{5.1}$$

The horizontal distances covered in the i^{th} layer are

$$x_i = z_i \operatorname{Tan}\alpha_i$$

$$x_i' = z_i' \operatorname{Tan}\alpha_i' \tag{5.2}$$

Snell's law of refraction then gives us

$$\frac{\operatorname{Sin}\alpha_i}{V_i} = \frac{\operatorname{Sin}\alpha_j'}{V_j} = \frac{1}{V_s} \qquad \text{(all i,j)} \tag{5.3}$$

where V_s is the apparent horizontal velocity within the each layer. The value of V_s depends on on epicentral distance, and focal depth.

The total travel times, T and T', are then given by the equations

$$T = \sum_{i=1}^{n} t_i = \sum_{i=1}^{n} z_i/(V_i \cos\alpha_i)$$
$$T' = \sum_{i=1}^{n} t_i' = \sum_{i=1}^{n} z_i/(V_i' \cos\alpha_i') \qquad (5.4)$$

and the total horizontal distances, X and X', by

$$X = \sum_{i=1}^{n} x_i = \sum_{i=1}^{n} z_i \tan\alpha_i$$
$$X' = \sum_{i=1}^{n} x_i' = \sum_{i=1}^{n} z_i \tan\alpha_i' \qquad (5.5)$$

The delay time, d, however is not just the difference between T and T', since P and P' are at different distances from the epicentre and the rays arrive at the base of the n^{th} layer at different times. The ray arrives at P later than at P' by an amount τ, where

$$\tau = (X'-X)/V_s \qquad (5.6)$$

Therefore d is given by

$$d = T' - T - \tau \qquad (5.7)$$

Using Equation 5.3, this can be written

$$d = \sum_{i=1}^{n} z_i\{(1/V_i'^2 - 1/V_s^2)^{1/2} - (1/V_i^2 - 1/V_s^2)^{1/2}\} \qquad (5.8)$$

For rays arriving vertically, for which the angles of incidence are zero, the vertical delay time, d_v, is given by

$$d_v = \sum_{i=1}^{n} z_i(1/V_i' - 1/V_i) \qquad (5.9)$$

From the form of Equations 5.8 it can be seen that each layer contributes its own term to the total delay time, independently of the others. It is also apparent that delay time is a function of V_s and hence of epicentral distance and focal depth.

Since the measured station delays represent averages over the epicentral distances covered by the events used, it is worthwhile investigating the effect of, and compensating for, variations in apparent surface velocity.

From Equations 5.8 and 5.9 the ratio, g, between a true delay time, d, and the vertical delay time, d_V, is given by

$$g = \frac{d}{d_V} = \frac{(1/V'^2 - 1/V_S^2)^{1/2} - (1/V^2 - 1/V_S^2)^{1/2}}{1/V' - 1/V} \qquad (5.10)$$

for a one layer case.

Values of V_S are easily obtained from Herrin's tables and these are used to calculate values of g for a range of epicentral distances and anomalous velocities. Table 5.1 gives values of g for V = 8.1 km/sec, which is typical of normal upper mantle beneath Africa (Gumper and Pomeroy, 1970). Although the individual values vary quite widely, especially with epicentral distance, from 1.0 to 1.3, the averages over epicentral distances (which are also tabulated) are all around 1.090 and vary by less than 1.5% from this value. Dividing the station delays by this figure gives a good estimate of the vertical delay times, and it is these which will be used in interpretations presented in this chapter.

The vertical delay times are given in Table 5.2, along with other station information.

5.3 Magnitude of the Vertical Delay Times

The vertical delay times vary from 0.164 sec (Station 30) to 1.674 sec (Station 14), a substantial variation of more than 1.5 sec in less than 400 kilometres horizontal distance. The larger values are associated with the

TABLE 5.1

RATIO BETWEEN SLANT AND VERTICAL DELAY TIMES

EPICENTRAL DISTANCE (degrees)	APPARENT SURFACE VELOCITY (km/sec)	NO. OF EVENTS	RATIO, g, FOR SEVERAL VALUES OF ANOMALOUS P-WAVE VELOCITY				
			7.8	7.5	7.0	6.5	6.0
30	12.5	4	1.296	1.279	1.254	1.230	1.202
40	13.4	7	1.242	1.230	1,210	1.191	1.178
50	14.7	14	1.189	1.180	1.165	1.151	1.137
60	16.2	13	1.148	1.141	1.130	1.119	1.108
70	18.0	9	1.115	1.109	1.101	1.093	1.085
80	20.6	11	1.084	1.080	1.074	1.069	1.063
90	23.7	28	1.061	1.059	1.055	1.051	1.046
100	24.4	4	1.058	1.055	1.051	1.047	1.044
110-160	60	22	1.009	1.009	1.008	1.007	1.007
MEANS			1.103	1.098	1.090	1.086	1.075

TABLE 5.2

TELESEISMIC DELAY AGAINST GRAVITY, HEIGHT AND PROFILE DISTANCES

STA. NO.	HEIGHT (m)	CORRECTED DELAY TIME (sec)	BOUGUER ANOMALY (mgal)	DISTANCE ALONG FLANK PROFILE (km)	DISTANCE FROM FLANK PROFILE (km)	DISTANCE FROM RIFT AXIS (km)
08	2745	1.389	-224	-164.5	-17.0	-44
09	1919	1.372	-215	-164.5	5.6	-22
10	2255	1.629	-232	-141.7	-0.5	-23
11	1888	1.206	-198	-135.4	19.3	-2
12	1922	1.217	-200	-123.3	21.2	2
13	2360	1.465	-228	-110.0	37.3	21
14	2168	1.676	-228	-142.4	2.9	-20
15	1834	1.279	-216	-114.9	4.0	-13
16	1940	1.430	-199	-88.4	16.8	6
17	1900	1.122	-194	-79.0	-5.5	-5
18	1695	1.027	-184	-44.3	-5.0	20
19	2188	0.749	-192	-45.7	7.5	28
21	2306	1.102	-202	-25.9	6.5	42
22	1691	0.850	-188	0.0	0.0	
23	1640	0.624	-148	36.0	-27.1	
24	1660	0.398	-112	72.8	-12.0	NOT
25	1321	0.467	-100	94.1	-4.5	USED
26	1178	0.512	-92	121.3	-18.1	IN
27	978	0.496	-86	156.9	3.9	RIFT
28	867	0.415	-83	178.8	14.3	PROFILE
29	797	0.164	-81	212.1	1.9	
30	618	0.156	-62	254.4	0.0	
31	399	0.806	-104	179.7	-60.1	
50	564	0.989	-70	-445.2	243.0	

culmination of the Kenya dome and the Gregory rift. Thus the delays measured in this study seem to be intimately linked with the subsurface processes responsible for these structures. We now consider possible reasons for these large delay times.

5.3.1 Crustal Variations and Delay Times

Figure 5.2 illustrates a conjectural model where uniform crustal thickening, by a factor k, gives rise to the higher delay times observed over the rift zone. We may readily use Equation 5.9 to derive the following expression for the relative vertical delay time, d_v, between thickened and normal crust

$$d_v = (k-1)(Z_1/V_1 + Z_2/V_2 - Z_1/V_m - Z_2/V_m) \qquad (5.11)$$

where Z_1 and Z_2 are the thicknesses of the upper and lower normal crustal layers respectively, V_1 and V_2 are the corresponding velocities, and V_m is the upper mantle velocity.

Using Herrin's (1968) model to represent typical continental crust and assuming a typical upper mantle velocity we have

$Z_1 = 15$ km $\qquad Z_2 = 25$ km

$V_1 = 6.0$ km/sec $\qquad V_2 = 6.75$ km/sec $\qquad V_m = 8.1$ km/sec

whence

$$d_v = 1.265(k-1) \text{ sec} \qquad (5.12)$$

Using the maximum relative vertical delay time (Stn 14 - Stn 30) of 1.520 sec, gives a corresponding value

FIGURE 5.2

CONJECTURAL MODEL TO EXPLAIN DELAY TIME VARIATIONS IN TERMS OF CRUSTAL THICKENING

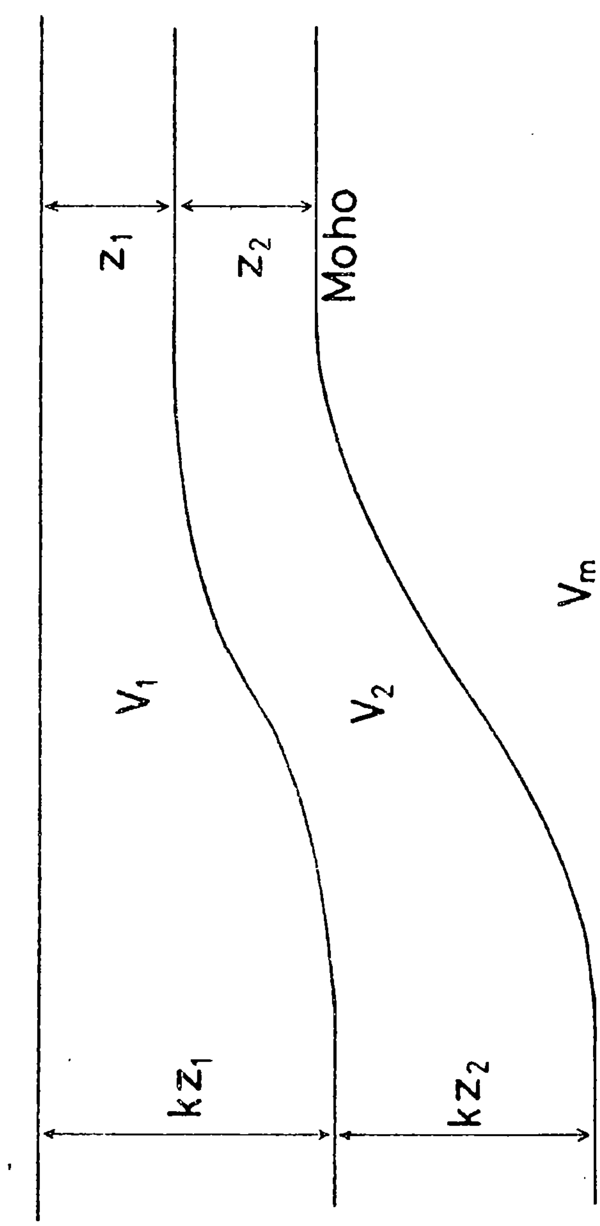

of 2.2 for k. If normal, 35 km thick crust exists away from the rift, this would suggest a thickness of nearly 70 km under it. The existence of such a pronounced crustal thickening, by a factor of about 2, under the rift zone is implausible for a number of reasons.

Firstly, crustal thickness determinations at Kaptagat (Maguire and Long, 1976) and Nairobi (Bonjer, Fuchs and Wohlenberg, 1970), where station delays are substantial, indicate a normal thickness of about 40-44 km.

Secondly, a doubling of crustal thickness, presumably contemporaneous with surface uplift, could only take place by compression, resulting in crustal shortening and folding (Bott, 1969). There is no evidence for folding having occurred since the early Palaeozoic (Baker et al, 1971), and fault plane solutions of strong earthquakes in the region imply a tensional stress pattern (Fairhead and Girdler, 1972).

Thirdly, the expected Bouguer anomaly due to crustal thickening may be calculated, and the resultant figures are higher than observed. Using the slab formula, the Bouguer anomaly, g, would be

$$g = -2\pi\rho G(k-1)(Z_1+Z_2) \qquad (5.13)$$

where ρ is the density contrast between crust and upper mantle, and G is the universal constant of gravitation. Woodard (1966) has studied regional isostatic relations, and deduced a value of 0.39 g/cm3 for ρ. Using a value of 40 km for Z_1+Z_2 we obtain

$$g = -654(k-1) \text{ mgals} \quad (5.14)$$

Bouguer anomaly differences of about 790 mgals would therefore be expected for crust thickened by a factor of 2.2.

Anomaly values have been obtained from the Bouguer Anomaly Map of Kenya, compiled at Leicester University (Swain and Khan, 1978), and values are listed in Table 5.2. The largest difference obtained, between Stations 10 (sited only 3.5 km from Station 14) and 30, is 170 mgals. The factor of 4.6 difference between observed and theoretical gravity values cannot be explained by reduction of the 2π geometric factor in Equation 5.13, so that gravity observations indicate that crustal thickening, if it occurs, is insufficient to account for the measured delays.

Thus we must reject crustal thickening as a hypothesis to explain the measured delays.

Suppose now that we have lateral velocity variations within the crust, reducing these by a factor k under the rift zone. Then, from Equation 5.9,

$$d_v = (k-1)(Z_1/V_1 + Z_2/V_2) \quad (5.15)$$

Using the same values for Z_1, Z_2, V_1 and V_2 as previously,

$$dv = 4.10(k-1) \text{ sec} \quad (5.16)$$

giving a maximum value of 1.41 for k. The crustal velocities for the upper and lower layers would then be 4.3 and 4.9 km/sec in the immediate vicinity of the Gregory rift, gradually increasing away from the centre of uplift.

This contradicts the results of seismic experiments which have been carried out within and near the rift. To the north of the DKSP rift valley stations, Griffiths et al (1971) showed that crustal seismic velocities along the axis were considerably higher than normal. The preferred interpretation of the results of this refraction experiment is that 6.4 km/sec material overlies 7.5 km/sec material, the interface being at about 20 km depth. Great confidence cannot be placed on this interpretation since each velocity was observed only in one direction. Nevertheless, the travel time graphs indicate unambiguously that velocities higher, rather than lower, than normal are present.

Studies of local earthquake recordings made at the Kaptagat array station, just to the west of the Gregory rift (Maguire and Long, 1976), and in the Southern Gregory rift at networks of independent stations (Rykounov et al, 1972), indicate normal upper and lower crustal velocities, that is 5.8 km/ sec material overlying 6.4 km/sec material.

Velocities as low as 5.0 km/sec throughout the thickness of the crust are very unlikely. There is no evidence from geological and petrochemical studies that the crustal rocks are abnormal either in composition or in their physical state, except along a narrow region confined to the rift axis.

If lateral variations were restricted to a particular fraction of the crust's thickness, the velocity decrease would have to be even larger. Very low seismic velocities could occur within the volcanic pile which covers the crystalline basement, and these could contribute significantly to the delay times of some stations. However, Stations 24, 25, 26, 27, 28, 29 and 30 are all either situated on basement outcrops, or on the red-brown soil which forms a thin veneer overlying the basement (Parkinson, 1945; Baker, 1954; Searle, 1954; Walsh, 1963), and so the significant delays (up to 0.512 sec), for these stations at least, cannot be due to low velocity superficial deposits. Even within the trough of the rift valley, average velocities for the volcanic pile are unlikely to be lower than 3 km/sec, and the total thickness is probably only 2 km (Baker et al, 1971), which would give a maximum vertical delay time of 0.42 sec, only one third of that typical of the area.

Thus lateral variations of velocity within the crust cannot account for the whole of the vertical delay times observed, although the effect of low velocity material within the volcanic overburden may not be insignificant.

5.3.2 Velocity Anomalies within the Upper Mantle

In the preceding subsection it has been shown that the measured station delays are too large to be accounted for by crustal variations alone, and that other evidence makes these hypotheses untenable. The major portion of these delays must therefore be due to the existence of material within the upper mantle with anomalously low compressional wave velocity The velocity anomalies may occur anywhere within the upper mantle, that is above about 400 km depth. Allowing 350 km thickness for the assumed anomalous material, the velocity need only be lowered to 7.8 km/sec in order to account for a 1.68 sec delay.

Beneath shield regions, studies have generally indicated constant or slowly increasing velocities with depth from the Mohorivicic discontinuity down to about 400 km depth (Gumper and Pomeroy, 1970; Brune and Dorman, 1963). Studies in other areas have demonstrated beyond reasonable doubt that low velocity zones exist in the upper mantle (Gutenberg, 1959; Toksoz, Chinnery and Anderson,1967), and that such low velocity layers can vary laterally in intensity quite rapidly (Lehmann,1964). Unfortunately, velocity profiles within low velocity channels cannot be constructed unambiguously from travel time data alone. However, Brooks (1962) has used a method due to Gutenberg to estimate seismic velocities at the foci of intermediate and deep earthquakes in the New Guinea-Solomon Islands region and thus obtain direct measurements of upper mantle P-wave velocities for that area. These indicate a sub-Moho velocity of 7.9 km/sec decreasing to a minimum of 7.5 km/sec at 115 km depth. The large delay times observed in Iceland have been linked unambiguously with anomalously low velocities within the upper mantle beneath the region. (Tryggvasen, 1964; Long and Mitchell, 1970). Velocities as low as 7.4 km/sec throughout a depth range between 160 km and 240 km have been suggested. These interpretations assume that velocities do not decrease beneath the 7.4 km/sec sub-Moho velocity detected by Bath (1960) but, as Long and Mitchell (1970) suggest, this may represent the seismic velocity within a relatively cool top of a rather thinner layer with substantially lower velocities in the centre.

Considerable lateral variations in upper mantle seismic velocities occur, and may readily be invoked to explain the delay times derived in this study.

5.4 Interpretation of the Flank Profile

Figure 5.3 shows the DKSP stations located on a Bouguer Anomaly map (Swain and Khan, 1978) of the area. Most of the stations lie close to the straight line AB, drawn on this map, which passes through Stations 22 and 30. Between Stations 21 and 30, this line intersects the Bouguer anomaly contours at right angles. It also cuts the topographic contours at right angles and is therefore presumably perpendicular to the strike of the underlying anomalous structures. We therefore take this line as representing a suitable profile for interpreting the delays at Stations 21, 22, 23, 24, 25, 26, 27, 28, 29 and 30. These form the flank group. The other stations are too close to or within the Gregory rift, where strikes of the main topographic features and Bouguer anomaly contours cross at acute angles, or (Stations 31 and 50) are situated too far from the profile to be representative.

FIGURE 5.3

BOUGUER ANOMALY MAP OF THE GREGORY RIFT

AND SOUTH-EAST FLANK OF THE KENYA DOME

(Swain and Khan, 1978)

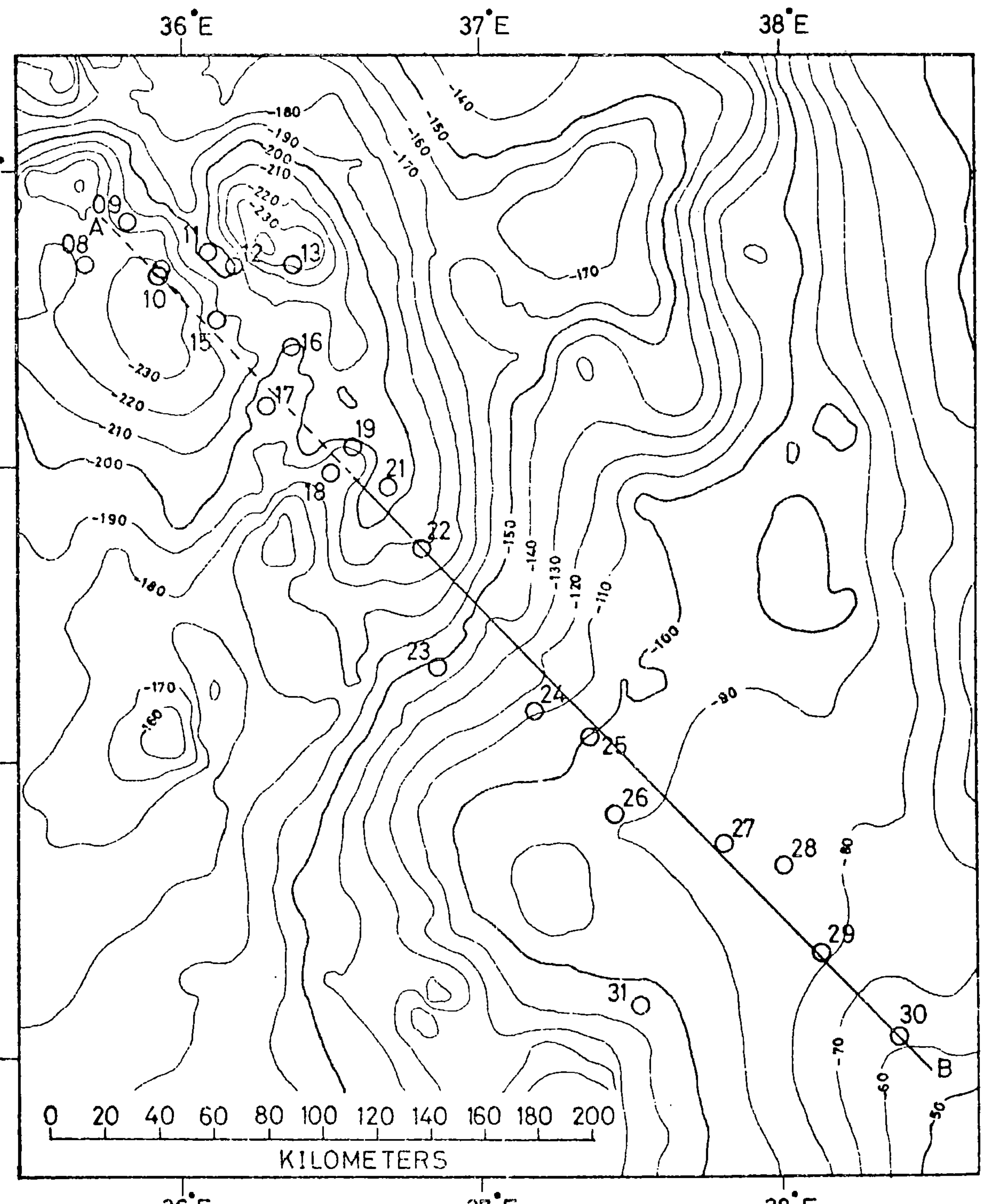

FIGURE 5.4

DELAY TIME VARIATION ALONG FLANK PROFILE

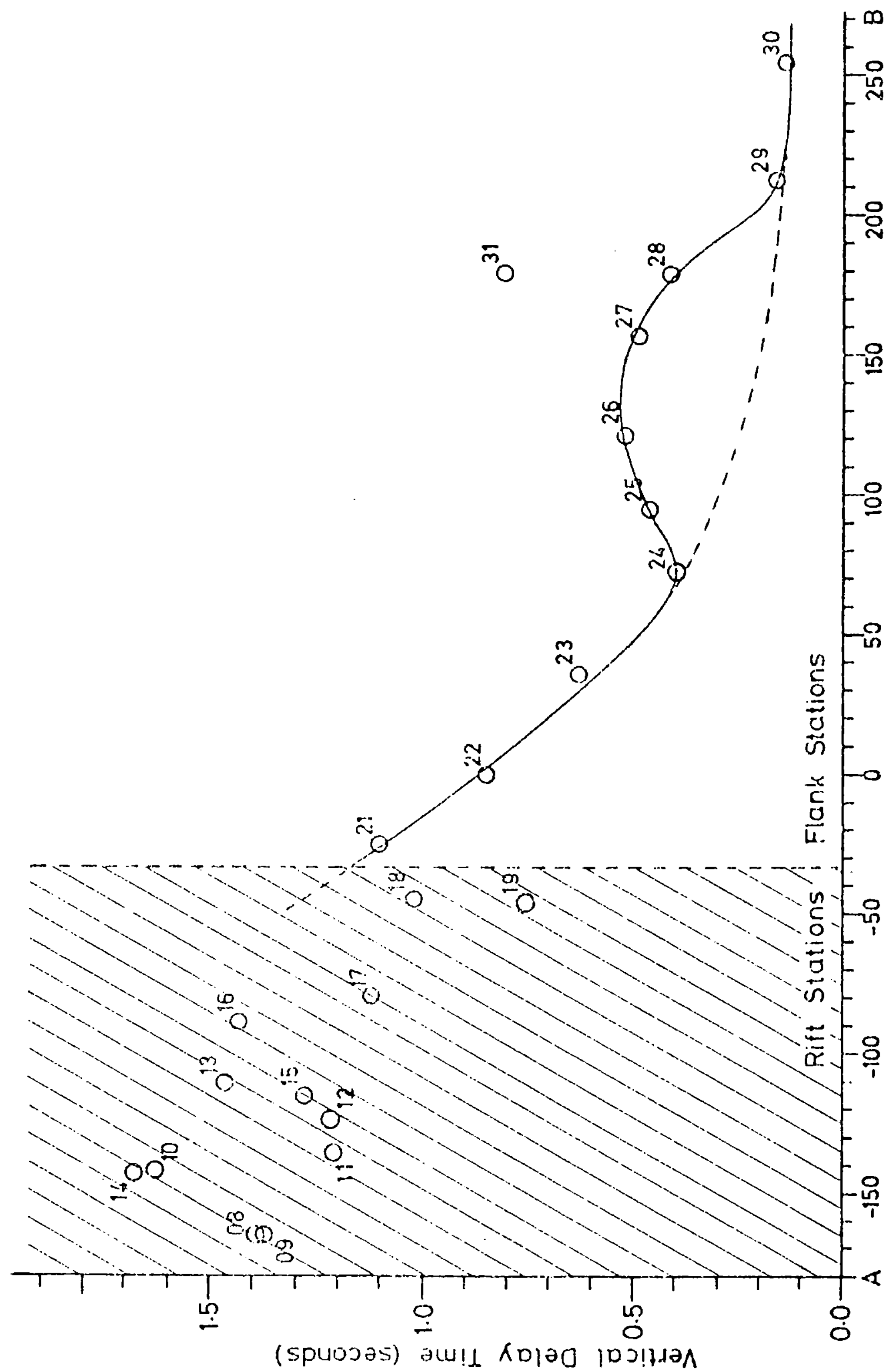

Distances along the profile are measured from Station 22, and given in Table 5.2. The positive values indicate the south-east direction. The vertical station delays are plotted as a function of profile distance in Figure 5.4.

The vertical delays plotted in Figure 5.4 have been joined with a smooth solid curve, which is composed of two parts. The major trend is for a smoothly increasing vertical delay time from a value of 0.156 sec, at Station 30, to 1.102 sec at Station 21, the increase becoming distinctly more rapid nearer the rift. Superimposed on this is a "hump" between Stations 24 and 29, which has a maximum amplitude of about 0.32 sec. This hump seems to be associated with Mt. Kilimanjaro, as it peaks at the point on the profile nearest to the volcano. This supposition is supported by the observed higher delay time at Station 31, which is still closer to the volcano.

We must now consider the possible velocity structures which could account for the observed delays along this profile. It is obvious from the nature of the vertical delay time, that there is an infinity of possible structures, ranging from those which explain the delays entirely as a variable thickness of anomalous material with a uniform velocity to those with lateral velocity variations within a uniformly thick layer. Moreover, within the limits stated above, the depth of the anomalous material is also infinitely variable. Other considerations must be used to choose between possible models.

Let us first consider models with anomalous regions of uniform velocity, V'. The anomalous zone consists of a layer of variable thickness, Z, determined by the equation

$$Z = d_V(1/V' - 1/V_m)^{-1} \qquad (5.17)$$

where d_V is the measured vertical delay time and V_m the normal upper mantle velocity. Figure 5.5 illustrates graphically the variation in layer thickness with distance for several values of V'. Assuming a value of 7.5 km/sec for V', four possible models have been drawn in Figure 5.6.

These models differ in the relative flatness of the top and bottom surfaces. Model A can be rejected immediately for several reasons. Firstly, if the top surface were flat, uniform volcanic activity would be expected over the region. Secondly, as will be argued in the next section, there is good reason to believe that the region of anomalous upper mantle material connects with a crustal intrusion along the axis of the rift, while away from the Kenya dome it must merge with the asthenosphere at a depth of 90 km or more. Thirdly, if, as seems likely, the anomalous material is formed by a thermal perturbation of the unstable asthenosphere-lithosphere boundary, the disturbance would tend to develop upwards rather than downwards, since this is the direction in which hotter, lighter and less viscous, fused material would migrate (Gass,1972).

The third consideration favours model C over B, although an absolutely flat horizontal bottom interface is also improbable. Of these four models, D probably

FIGURE 5.5

GRAPH OF ANOMALOUS MANTLE MATERIAL THICKNESS AGAINST DISTANCE ALONG FLANK PROFILE

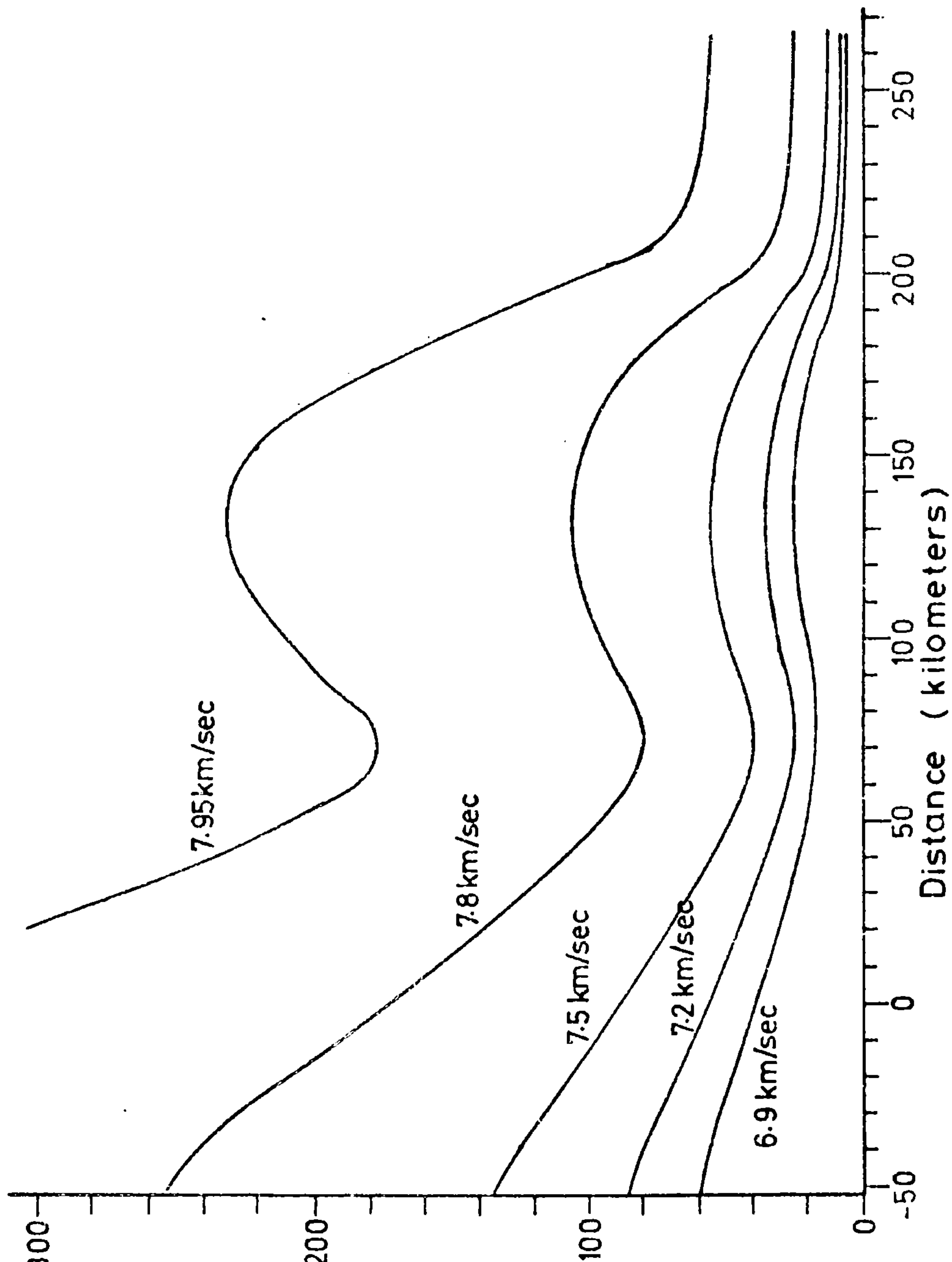

FIGURE 5.6

UPPER MANTLE MODELS FOR THE FLANK PROFILE

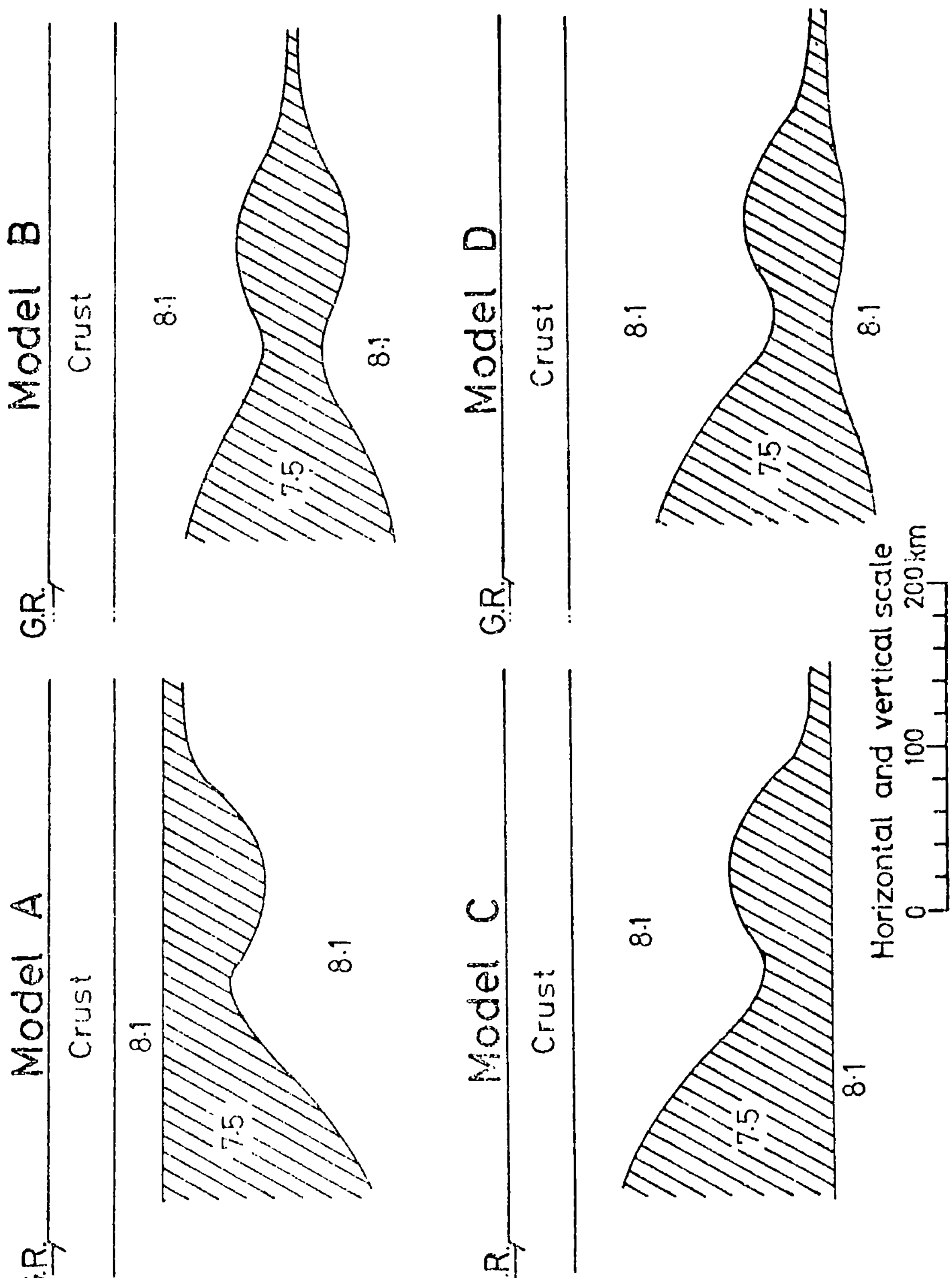

represents the closest approach to the real velocity structure along the flank profile.

However, none of these uniform velocity models accurately represents the real velocity structure. Sharp boundaries between regions of differing temperature would soon be smoothed out by thermal conduction and migration of hot fluids. Such sharply bounded regions could never arise in the first place, and we should therefore seek models with smoothly varying upper mantle velocities.

Model E, illustrated in Figure 5.7, is a variation on model, D employing smoothly varying velocities. This model has been calculated assuming that the upper mantle velocity profile is defined by the analytical function

$$V'(z) = V_m\left(1 - \frac{C}{1+(z-z_o)^2/b_1^2}\right) \quad (z \leqslant z_o)$$
$$V'(z) = V_m\left(1 - \frac{C}{1+(z-z_o)^2/b_2^2}\right) \quad (z \geqslant z_o) \qquad (5.18)$$

This function gives a minimum velocity at a depth z_o which increases smoothly, to reach the normal upper mantle velocity, V_m, asymptotically. The velocity profile has characteristic half widths, b_1 and b_2, above and below z_o respectively.

The delay time, d_v, due to such a velocity profile can be calculated by modifying Equation 5.9 to incorporate smoothly varying velocities. The modified equation is

$$d_v = \int_{\infty}^{\emptyset} (1/V'(z) - 1/V(z))\,dz \qquad (5.19)$$

whence it can be shown by substitution and integration that for the profile defined by Equation 5.18

FIGURE 5.7

FLANK MODEL EMPLOYING SMOOTH VARIATIONS IN VELOCITY

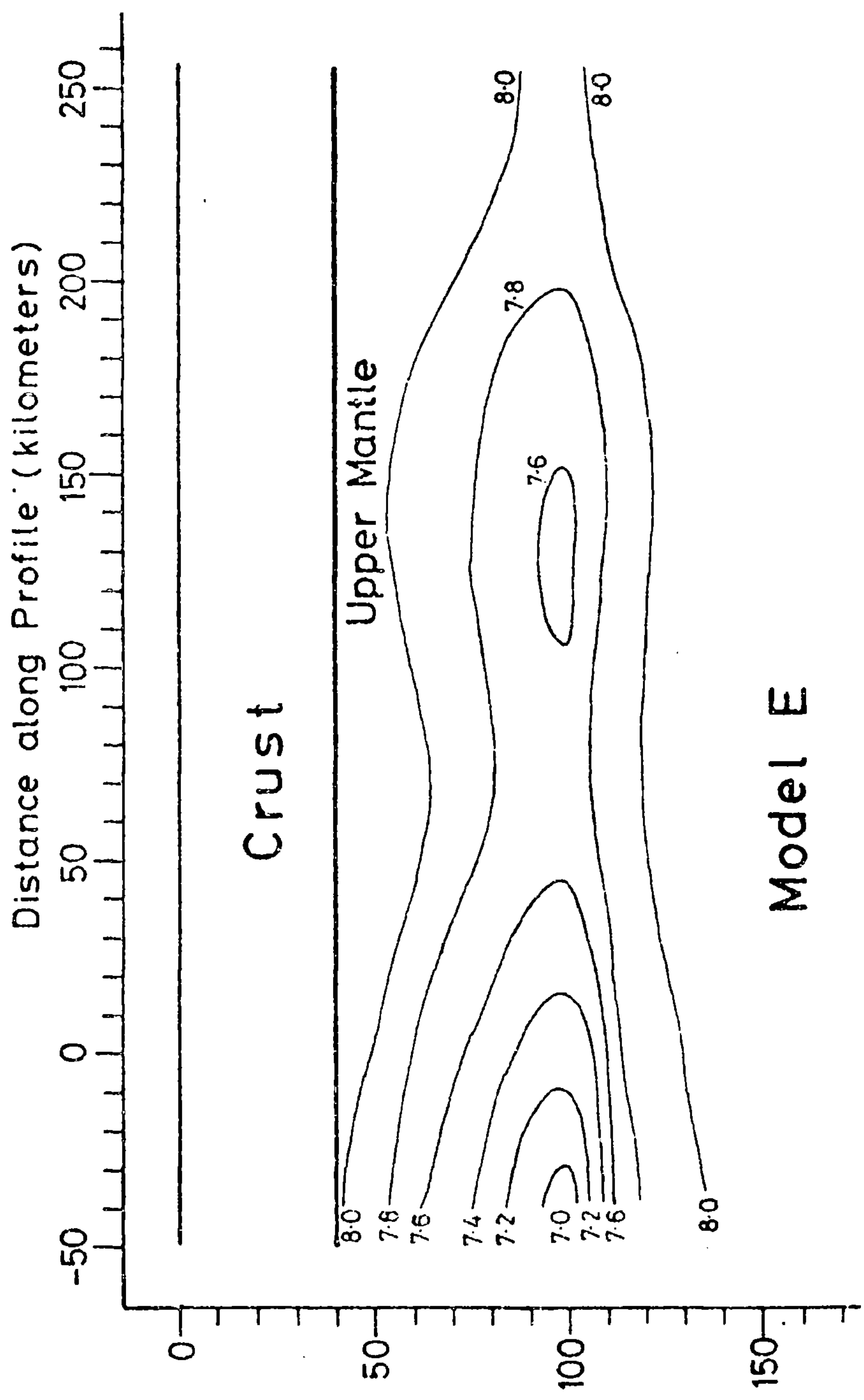

$$d_v = C(b_1 + b_2)/V_m \tag{5.20}$$

The small correction which should be made, because of finite integration limits in reality, is ignored.

We may choose to vary any or all of b_1, b_2, and C with distance to fit the measured values of d_v. In addition, z_o may be varied arbitrarily, providing it is not too small. For model E, however, z_o, b_1, and b_2 are fixed at 100 km, 30 km and 10 km respectively, and only C varies with distance. Equation 5.20 is then used to find C as a function of distance, and Equation 5.18 used to reconstruct the velocity structure along the profile.

Model E does not suffer from the unrealistic assumption that sharp boundaries exist. However, it has been constructed in a very arbitrary manner, with ease of analytical integration as the dominant factor in choosing the form of the function. There is no reason to suppose that this model is a closer approximation to reality than, say, models C or D. Since the ambiguities inherent in delay time interpretation cannot be resolved, there is little point in pursuing over-elaborate models. Providing we bear in mind the limitations of simplifying assumptions, simple models such as C suffice to illustrate the main features of the subsurface velocity structure.

Henceforth, modelling will therefore make the following simplifying assumptions. Firstly, regions of anomalous material will have a uniform velocity, and secondly the bottom surface of such regions will be planar and horizontal.

5.5 Interpretation of the Rift Station Delays

The rift valley stations, numbered 08-19, do not fall on a useful profiling line in the same way that the stations of the flank group do. Nevertheless we can observe the general behaviour of delay time across the rift by constructing a pseudo-profile.

Figure 5.8 shows the locations of the rift valley stations on a Bouguer anomaly map (Swain and Khan, 1978). In the northern half, the major axis of symmetry is the line CD, which follows the ridge of the positive axial anomaly and bisects the rift. The Bouguer anomaly is fairly symmetrical about this line, and the overall trend of prominent surface features is parallel to it. Thus, distances from this line provide a convenient measure of distance along the pseudo-profile.

A similar line, EF, has been tentatively drawn along the approximate axis of the rift in the southern section. This line has been drawn along a local Bouguer anomaly ridge, but may not represent the true rift centre as it is somewhat closer to the western escarpment than the eastern.

Using the nearer of the two lines, the distance of each rift station from the assumed axis has been measured, negative distances implying locations to the west. These distances are given in Table 5.2, and the derived vertical delay time pseudo-profile plotted in Figure 5.9.

FIGURE 5.8

BOUGUER ANOMALY MAP OF THE CENTRAL PORTION

OF THE GREGORY RIFT

(Swain and Khan, 1978)

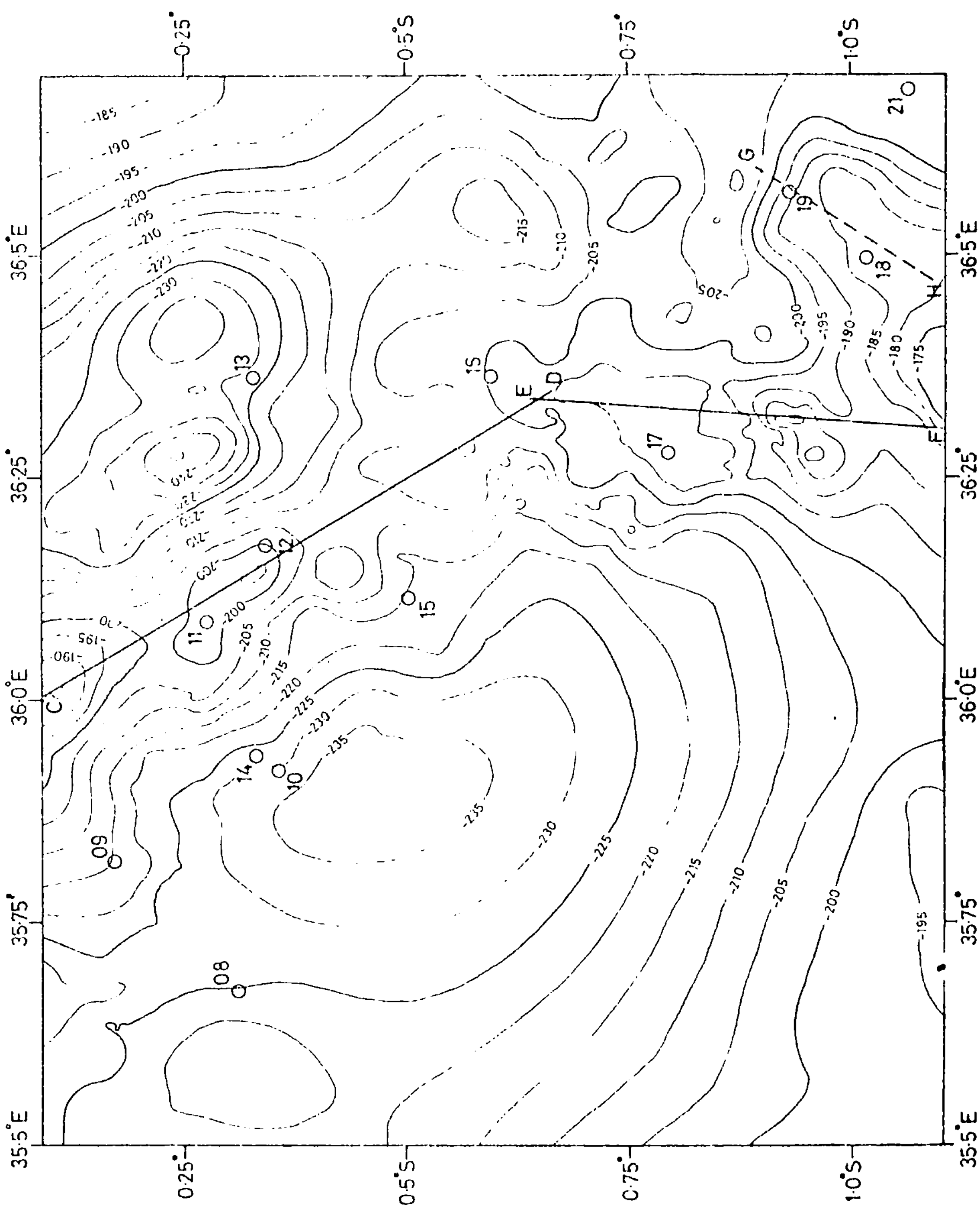

FIGURE 5.9

DELAY TIME VARIATIONS ACROSS THE GREGORY RIFT

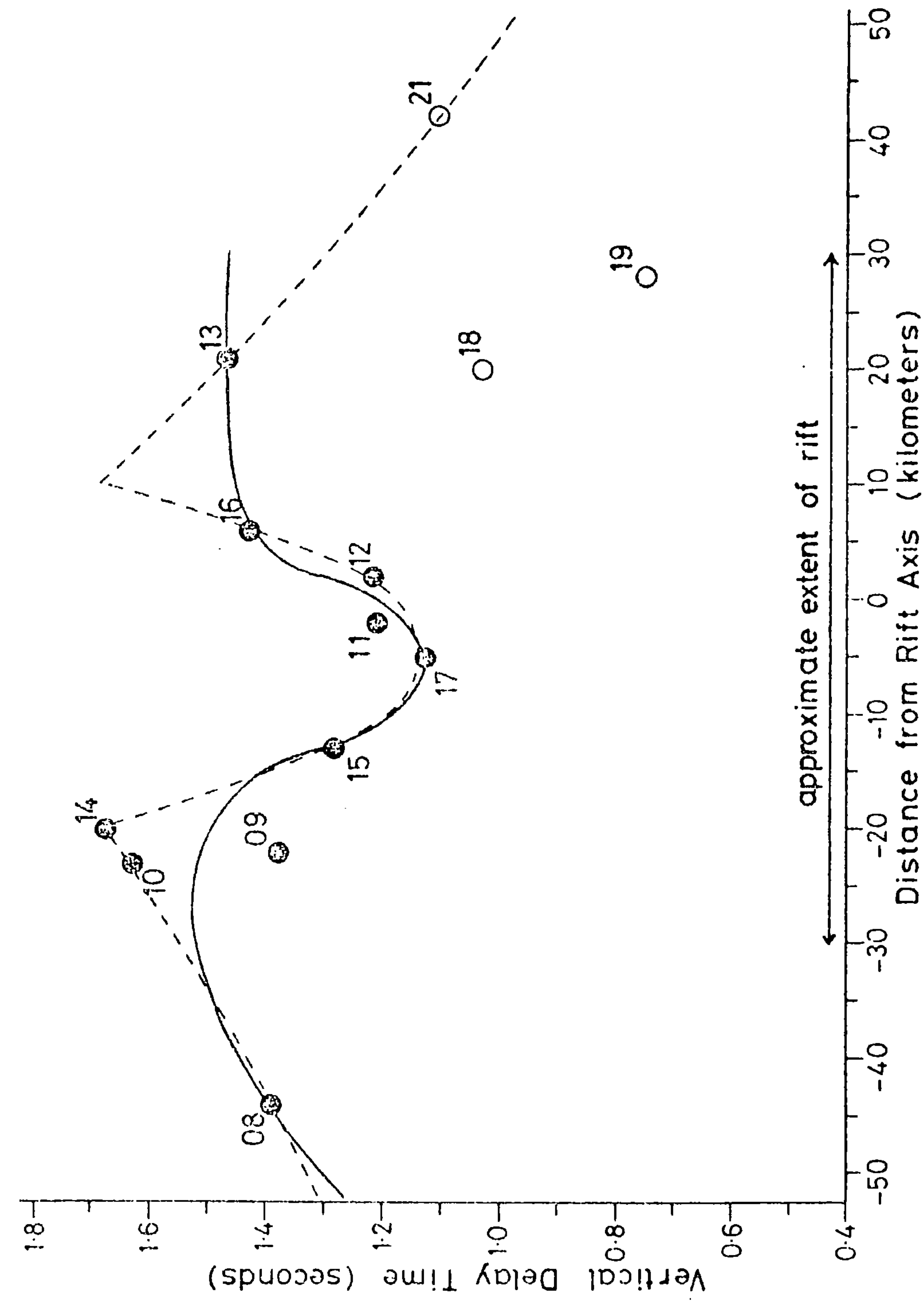

The mean value of the delay times for the northern rift stations (filled circles) is 1.38 sec, but with a range of about 0.6 sec. This average value is higher than for any of the flank stations and indicates that the major trend apparent on the flank profile continues to reach a maximum in the vicinity of the rift.

Superimposed on this overall peak is a distinct trough, coincident with the positive axial Bouguer anomaly. This is illustrated by the solid curve drawn through the points on Figure 5.9.

The scatter of the points about the smooth curve is almost certainly a reflection of delay time variations which probably occur along the strike of the rift as well as across it. Because of these variations and the limited coverage, a truly representative profile cannot be drawn. Nevertheless, the minimum in delay time which occurs along the axis is a real feature, and can be seen clearly in the pattern of delays formed by the six Stations 08, 10, 14, 11, 12 and 13 which lie close to an east-west line traversing the rift.

As will be demonstrated in Section 5.7, there is a strong negative correlation between Bouguer anomaly values and vertical delay times for the rift stations. Since the axial positive anomaly can easily be traced along this section of the rift, it follows that the axial minimum in delay times probably also follows the same line.

Supposing for the moment, that material with anomalous velocities is confined to the upper mantle, we may use a flat bottomed uniform density model such as that depicted in Figure 5.10 to investigate the shape of the upper surface. This model incorporates a trough in the upper surface corresponding to the axial minimum in delay time.

The difference in delay time between Stations 11 and 14 is 0.47 sec, and the horizontal distance between them 17.8 km, giving an average delay time gradient of 26.4 msec/km. This is considerably larger than the maximum gradient of 9.9 msec/km for the flank group, averaged between Stations 22 and 21, and implies correspondingly steeper dips.

Using these values, the "valley" depth and mean dip in the upper anomalous zone interface between Stations 11 and 14 have been calculated for several values of anomalous velocity. These are given in Table 5.3.

The dips and depth differences are large, implying steep sides for the postulated axial valley, even for large velocity contrasts. It is difficult to envisage a mechanism which would give rise to such a complicated structure, and there are two other reasons for rejecting it as a model. Firstly, the steep gradients in the Bouguer anomaly imply crustal depths for the density contrasts causing the axial anomaly (Searle, 1970). Since the Bouguer anomaly and the vertical delays are highly correlated (see Section 5.7), a common cause within the crust must be assumed. Secondly, the bulk of volcanic activity would be expected to occur

FIGURE 5.10

HYPOTHETICAL SEISMIC MODEL FOR THE GREGORY RIFT ASSUMING NORMAL CRUST

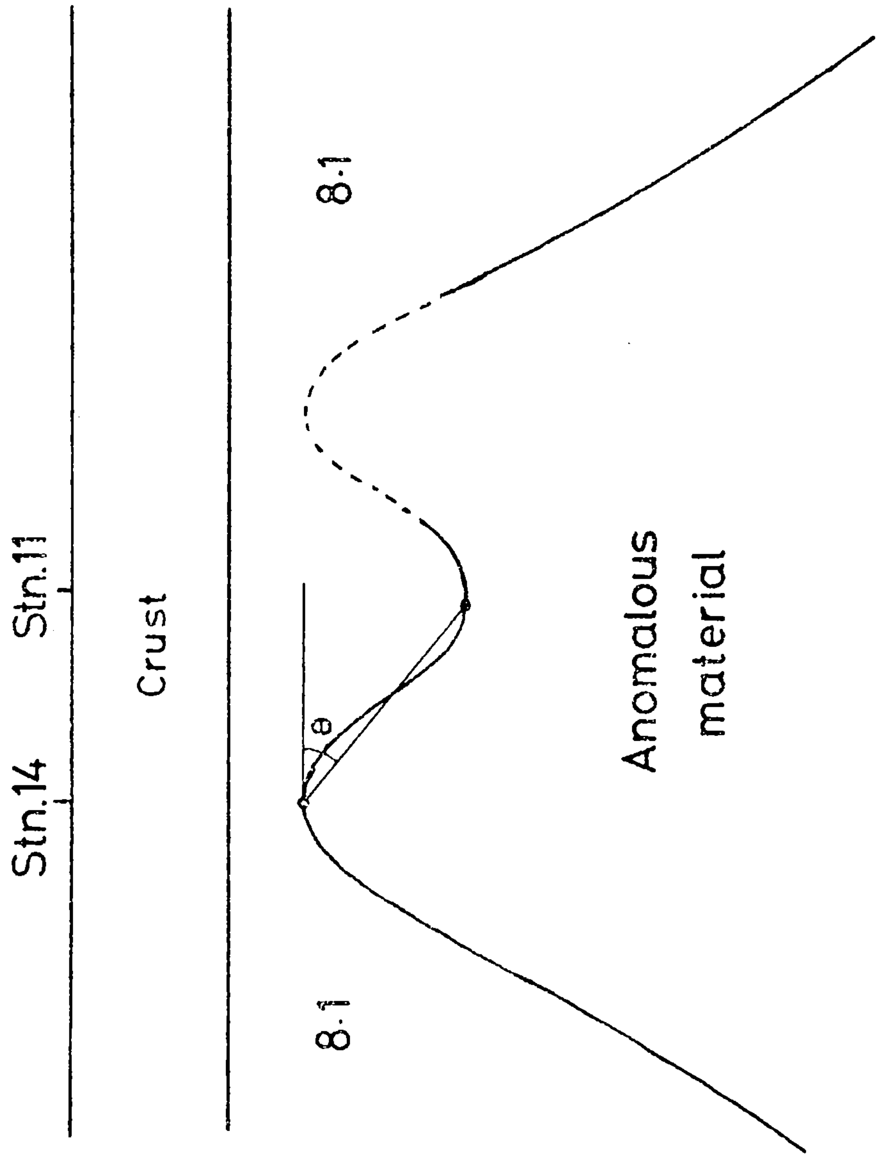

TABLE 5.3

DEPTH DIFFERENCES AND MEAN DIPS ON CONJECTURED UPPER INTERFACE OF THE ANOMALOUS MANTLE ZONE BETWEEN STATIONS 11 AND 14

ANOMALOUS ZONE VELOCITY	DEPTH DIFFERENCE (km)	MEAN DIP (degrees)
7.8	99	80
7.5	48	69
7.0	24	54
6.5	15	41
6.0	11	31

over the two ridge crests, and not in between. Searle and others point out that central volcanoes tend to occur along the axis.

Thus the axial vertical delay time dip is almost certainly due to lateral variations at depths shallower than the base of the normal crust. Such variations might exist either in the form of variable thicknesses of superficial volcanic deposits or in the form of an intrusion of high velocity material within the crust. Let us first examine the former possibility.

Suppose that the volcanic overburden has a uniform velocity, V', and overlies normal upper crustal material with a P-wave velocity of 5.8 km/sec. We may easily calculate the difference in thickness beneath any two stations. Taking the case of Stations 11 and 14, and assuming that V' is 3.0 km/sec, this difference is 2.9 km. Since this is greater than the estimated total thickness, of the volcanic pile within the rift (2.0 km, Baker et al, 1971), variations in the thickness cannot account for the whole of the observed axial delay time dip although, as noted before, they may not be insignificant.

Thus the delay time measurements derived and presented in this study confirm the existance of a high velocity intrusion along the axis of the rift, as detected by Griffiths et al (1971) further north. The existence of a high density intrusion along the axis has been inferred from gravity data (Searle, 1970; Khan and Mansfield, 1971; Baker and Wohlenberg, 1971). That the high densities and high velocities are due to the existence of a single region of anomalous material is clear from the superposition of the delay time dip and the axial Bouguer anomaly.

The crustal intrusion is, presumably, connected with the anomalous zone within the upper mantle from which it would have been derived. Thus if the whole anomalous zone, both within the crust and upper mantle, has a uniform P-wave velocity V', this velocity will have to lie between those which are normal for the crust and upper mantle. Figure 5.11 shows model F, based on V'= 7.5 km/sec , the velocity obtained by Griffiths et al for the top of the crustal intrusion.

For a uniform velocity model such as this, the largest delay time occurs where the upper surface of the anomalous zone intersects the normal Moho, probably near or under Station 14 on the western side. The intrusion probably comes closest to the surface under Stations 11 and 12, and assuming a vertical lower crustal velocity of 6.4 km/sec would penetrate the crust by 24 km. Assuming a normal crustal thickness of 44 km (Maguire and Long, 1976), the intrusion would then reach to 20 km depth. This gives good general agreement with the seismic model of Griffiths et al (1971), except that the Griffiths model includes higher than normal velocities within the upper crust also. Other velocities for the crustal intrusion would give different values for the minimum depth to which it rises.

FIGURE 5.11

SEISMIC MODEL OF THE AXIAL INTRUSION

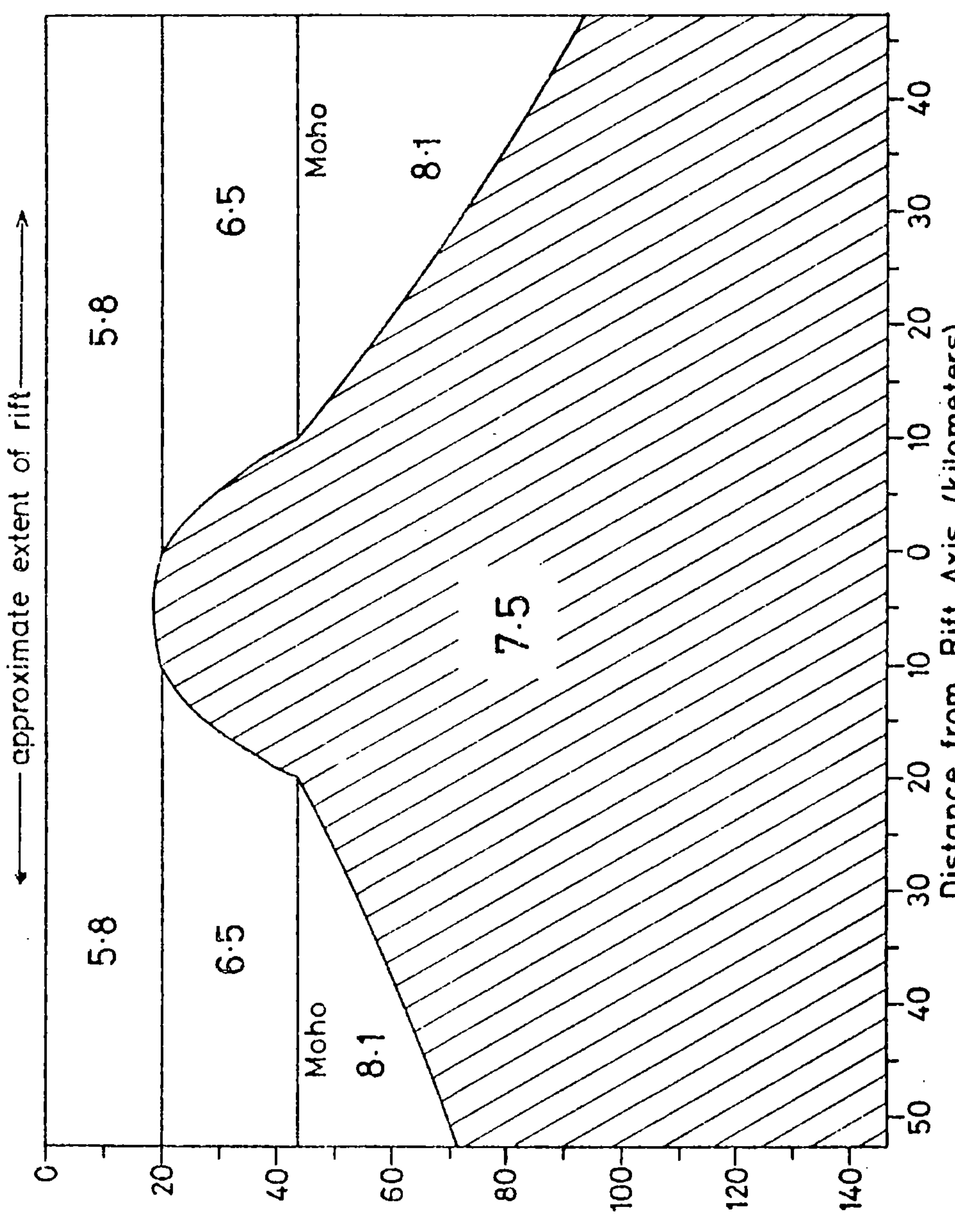

It is very difficult to give a reliable estimate of the width of the intrusion from the sparse data available. The western interface at the base of the crust is defined by the delay time peak at Station 14, but the corresponding peak to the east is not represented by a measurement. The dotted curve drawn on the pseudo-profile (Figure 5.9) assumes symmetry about the position of Station 17, and includes the sharp peaks which would be observed for model F. On the basis of this assumed symmetry, the intrusion is some 30 km wide at the base of the normal crust.

So far, the measurements of vertical delay time for Stations 18 and 19 have been ignored. These stations lie to the southeast of the main rift group, where the line of the axial Bouguer positive is ill-defined. As plotted in Figure 5.9, both stations have lower delays than their positions would suggest.

This might be due to the existence of an offshoot of the main axial intrusion, as possibly indicated by the Bouguer high along the line marked GH on the gravity map (Figure 5.8).

Williams (1978) has speculated that the semi-circular embayment in the Kikuyu escarpment at Kijabe represents the remains of a huge caldera, some 35 km in diameter. The postulated caldera is considerably larger than the Ngorongoro crater, and would have an area of about 3,800 km^2. This is about twelve times the area of other calderas in the rift, which are associated with the main trend of the axial intrusion, and suggests the existence of a correspondingly larger magma chamber beneath. If this is the case, then this offshoot may represent the nearest approach of the intrusion to the surface. Station 19 is situated on the edge of the embayment, and has a lower delay time than those situated on the main axis of the intrusion, possibly due to its proximity to this part of the intrusion. This is only suggested tentatively, but additional support for the existence of this nearby offshoot is given by the existence of the central volcanoes Longonot and Kijabe.

An alternative hypothesis for the low delay time at Station 19 is that its situation, on a step of the Kikuyu escarpment, brings it much nearer the basement than it would otherwise be, due to the arrangement of faulting. Figure 5.12 illustrates the geometry, and shows how the thickness of the volcanic pile may be effectively lessened. This would reduce the delay time relative to stations both above (Station 21) and below (Station 18) the escarpment, as observed.

The reduction in the thickness of the volcanic overburden cannot be greater than the height difference between Station 19 and the top of the escarpment, which is 565 m. Therefore, the maximum decrease in delay time from this cause, assuming a 3.0 km/sec velocity for the volcanics, is only 0.091 sec. This is insufficient to account for the observed delay time difference of 0.353 sec between Stations 19 and 21 , or the 0.278 sec difference

FIGURE 5.12

THE ARRANGEMENT OF FAULTING UNDER STATION 19

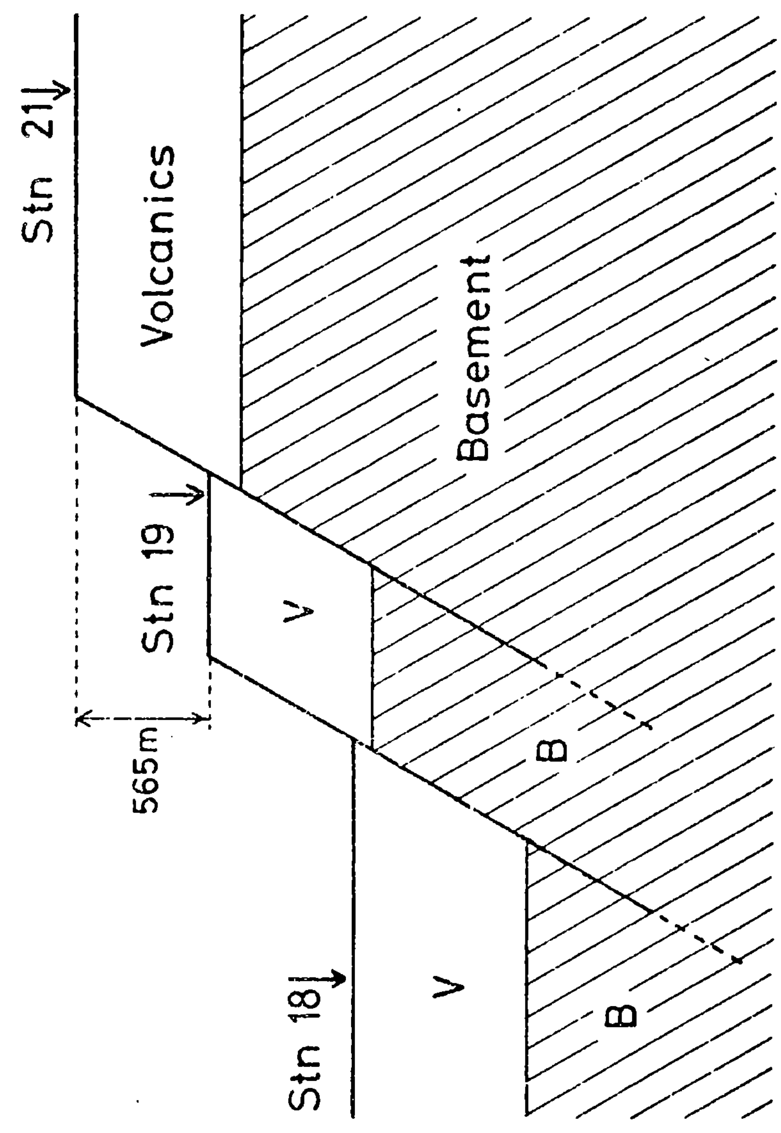

FIGURE 5.13

A COMBINED INTERPRETATION

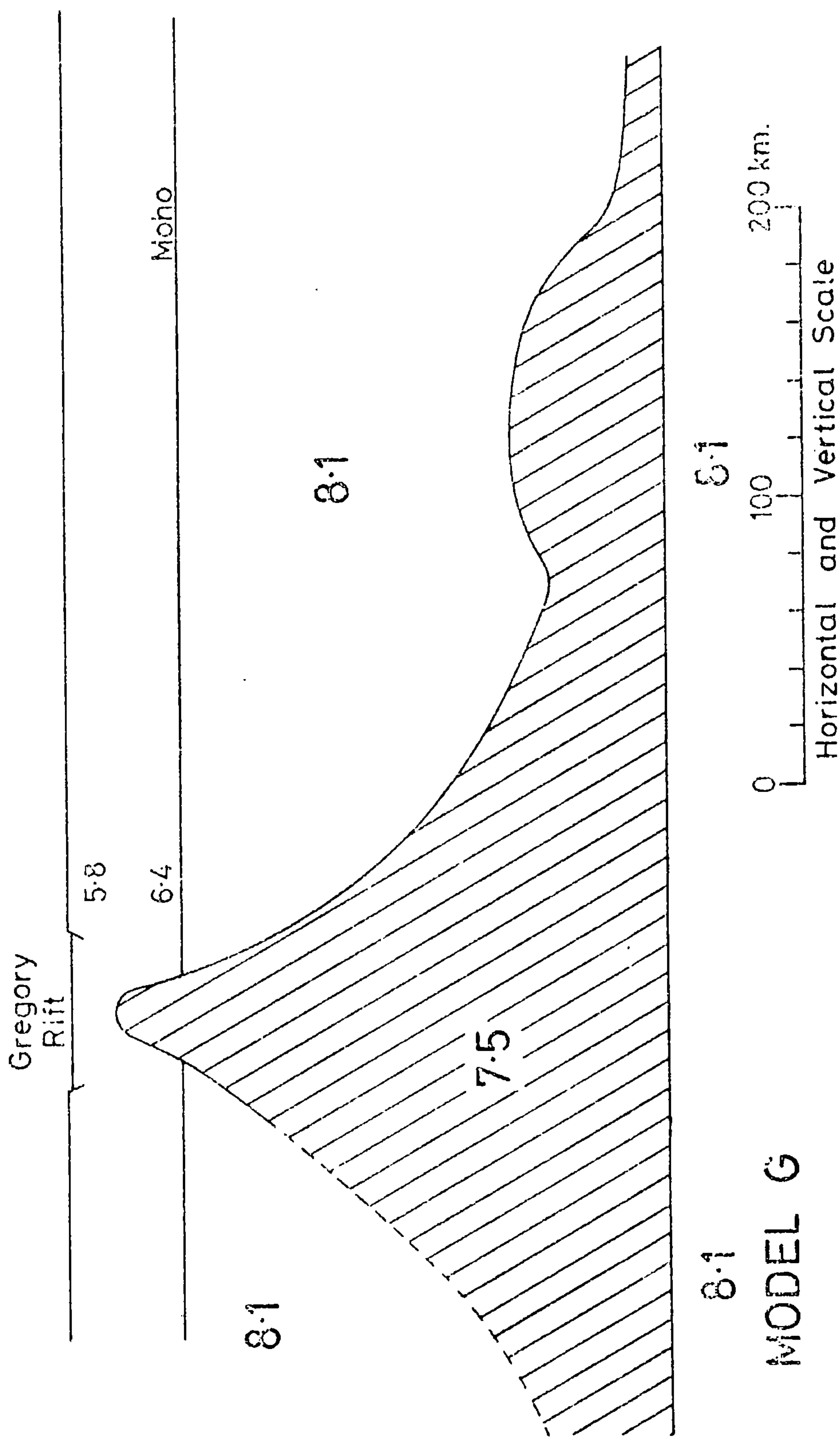

between Stations 19 and 18.

5.6 A Combined Interpretation

Having investigated the possible causes of the measured station delays, and derived models for the two main areas covered by the DKSP network, an attempt must now be made to combine these to give a complete picture of the likely velocity structure.

To this end, model G, depicted in Figure 5.13 has been devised. The model assumes a uniform velocity of 7.5 km/sec for the anomalous zone, and a 44 km thick normal crust with a seismic velocity of 6.4 km/sec in the lower half. The intrusion is assumed not to penetrate the upper half of the crust. The bottom surface of the anomalous zone is assumed to be flat.

Model G represents the probable velocity structure along a profile running west-east, crossing the rift at about latitude 0.25°S. The upper surface in the region of the rift is taken from model F and extrapolated eastward using the flank model C.

The depth to the base of the anomalous region is estimated from the measured delay at Station 14, assuming a uniform velocity of 8.1 km/sec for the normal upper mantle. This gives a depth of 170 km.

In model G, the hump apparent on model C has been retained. The association of Mt. Kenya with such a hump, as for Mt. Kilimanjaro, might be expected as there is a distinct Bouguer anomaly low associated with this volcano. Banks and Ottey (1974) have inferred the existence of anomalously high conductivity material, at a depth of approximately 100 km, extending from the rift to the position of this postulated hump. Possibly there exists a ridge of anomalously hot upper mantle material along a line connecting Mt. Kilimanjaro and Mt. Kenya, and lying about 100 km to the east of the Gregory rift. This would account for the existence of these volcanoes.

The profile has been extrapolated for a short distance to the southwest (dotted curve), assuming symmetry about the rift axis. The form of the upper surface is very similar to that inferred to the northeast of the dome from studies of teleseismic slowness anomalies at the Kaptagat station (Forth,1975; Long and Backhouse, 1976)

This combined interpretation agrees remarkably well with the main features of the numerous gravity interpretations for the region.

5.7 Correlation of Station Delay with Height and Gravity

Attention has already been drawn to the observation that as station height increases, station delays tend to increase and Bouguer anomaly values tend to decrease. This is to be expected over an area of laterally varying upper mantle temperature. The hotter the upper mantle material, the lower will be the seismic velocity and density, decreasing density giving rise to higher elevations in order to maintain isostatic equilibrium.

The correlation between vertical delay and height is clearly indicated in the form of the scatter-graph illustrated in Figure 5.14. The correlation coefficient is 0.72 and the gradient of the linear regression line, delay time on height, is 0.52 sec/km.

Of greater interest is the correlation between vertical delay time and Bouguer anomaly. Figure 5.15 shows the scatter-graph drawn between these two variables. The sample correlation coefficient including all stations, is -0.876, with a single linear regression line gradient, delay on gravity, of -6.6 sec/gal.

A closer inspection of the scatter-graph shows that the rift and flank stations seem to lie on straight lines with different gradients, or possibly on a curve. This is borne out when the two groups are treated separately. For the rift group, the correlation coefficient is -0.88, and the regression line gradient -10.6 sec/gal. For the flank group, the correlation coefficient is reduced somewhat to -0.62, because of the scatter on Stations 50 and 31. The regression line gradient is -3.7 sec/gal. (If Stations 50 and 31 are removed, the correlation coefficient is -0.91, and the gradient -5.0 sec/gal). The gradients for the two straight lines in Figure 5.15 are statistically separate at the 95% confidence limit.

These gradients may be compared with a theoretically derived value. Suppose that velocity and density variations

FIGURE 5.14

VARIATION IN DELAY TIME WITH TOPOGRAPHY

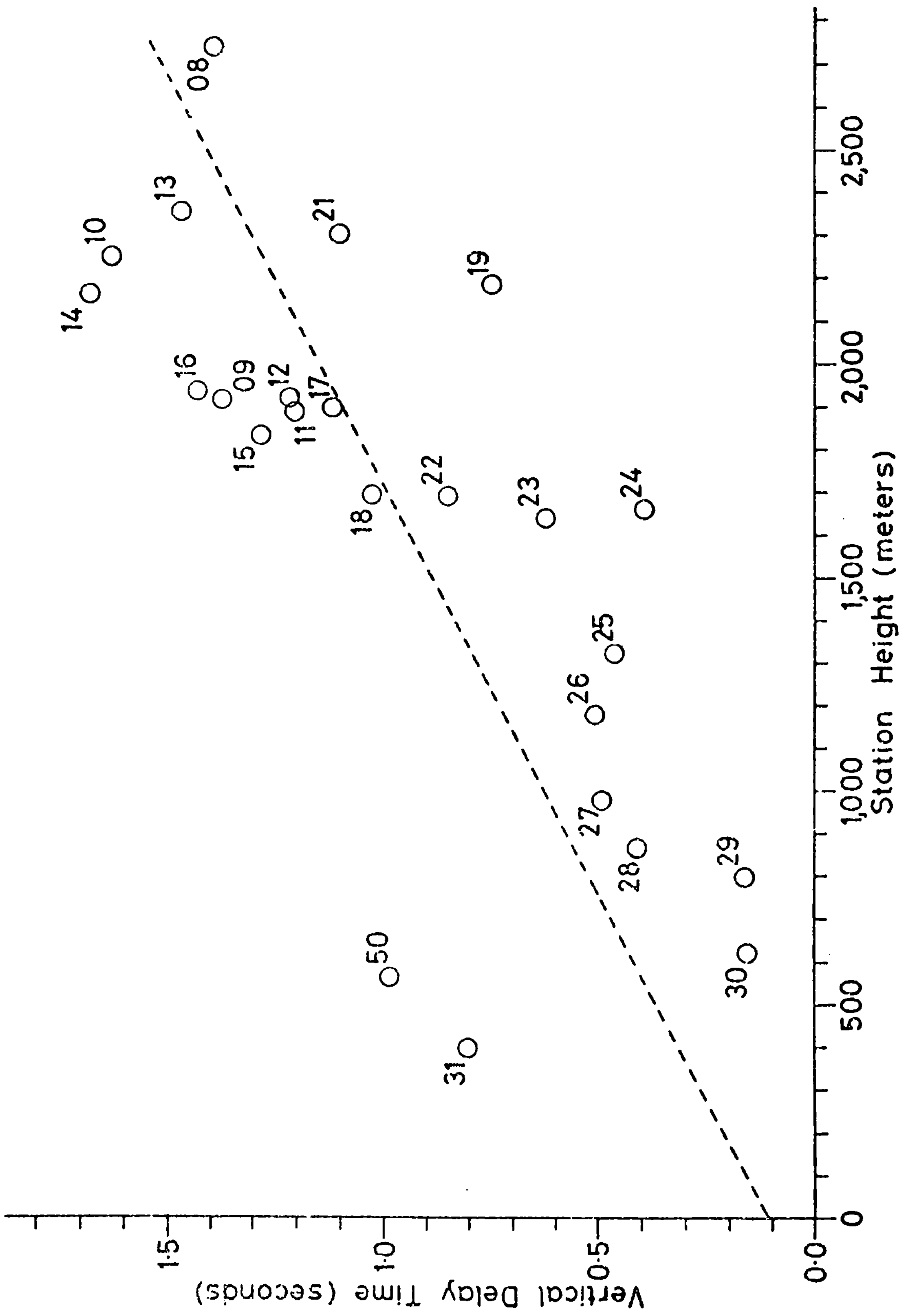

FIGURE 5.15

VARIATION IN DELAY TIME WITH BOUGUER ANOMALY

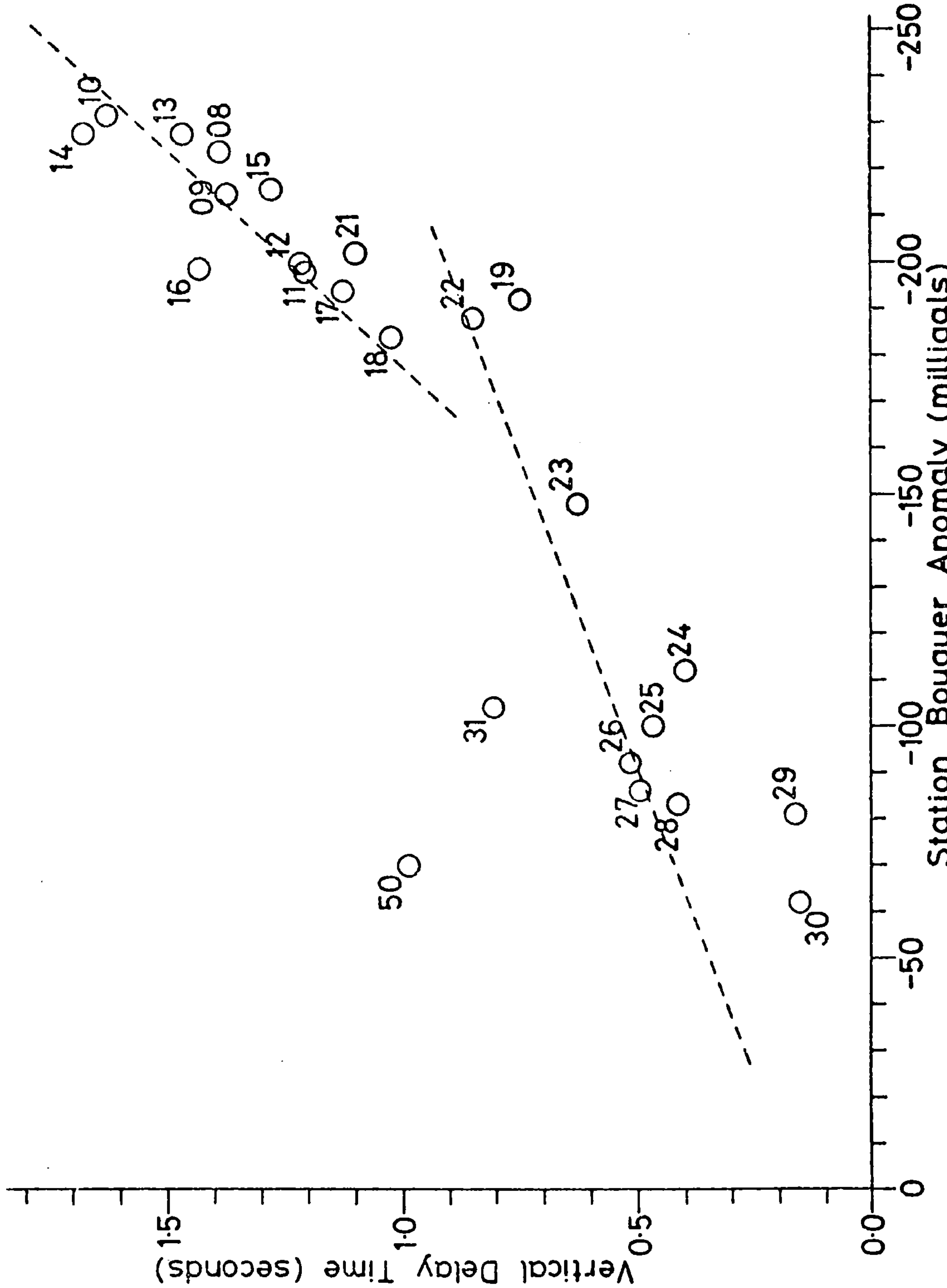

are confined to and are uniform within a certain depth range, of thickness Z. Suppose now that we move from a region where the velocity and density are V and ρ to one where they are $V+\delta V$ and $\rho+\delta\rho$. The delay time difference, δt, will then be given by the equation

$$\delta t \;=\; Z(1/(V+\delta V)-1/V) \;\simeq\; -Z\,\delta V/V^2 \qquad (5.21)$$

and the Bouguer anomaly difference, δg, based on the slab formula, is given by

$$\delta g \;=\; 2\pi k G Z\,\delta\rho \qquad (5.22)$$

where G is the universal constant of gravitation and k is a geometric factor, approximately equal to one if lateral variations are not rapid compared to the range of depths over which the variations occur.

Combining Equations 5.21 and 5.22 we have, in the limit,

$$\frac{dt}{dg} \;=\; -\frac{1}{2\pi k G V^2}\,\frac{dV}{d\rho} \qquad (5.23)$$

Laboratory experiments at pressures below 10 kbar have shown that for crustal rocks, and probably subcrustal rocks as well, that typical values of $dV/d\rho$ are about $2.9\ m^4sec^{-1}kg^{-1}$ (Birch, 1961). Taking the value of k as being unity for the moment, and taking a mean upper mantle velocity of 7.8 km/sec, gives a corresponding theoretical value for dt/dg of -1.1 sec/gal.

This theoretical value is lower than the measured values by a factor of 3.4 for the flank stations, and a factor of 9.7 for the rift stations. It is quite probable that higher values of $dV/d\rho$ pertain to the anomalous upper mantle, where the effects of partial melting are likely to be significant (Bott, 1965). Nevertheless Birch's figure will be adopted for the time being, and an explanation sought in terms of low geometric factors, k. For the rift and flank we shall require k values of 0.10 and 0.29 respectively.

Simple calculations show that low geometric factors are to be expected. Let us approximate the shape of the anomalous region by a right cone with a flat base, having its apex at the surface. For a delay measurement taken at the apex, the full depth of the cone is taken into the calculations. For a gravity measurement at the same point, however, the value will be considerably less than that given by the unmodified slab formula. We may easily calculate the factor by which it is less, since each horizontal section within the body subtends the same solid angle, ω, at the measurement point, which is less than 2π steradians. The geometric factor in this case is clearly given by the equation

$$k = \omega/2\pi \qquad (5.24)$$

The solid angle, ω, is easily calculated from the half angle, θ, at the cone's apex by the equation

$$\omega = 2\ (1-\text{Cos}\theta) \qquad (5.25)$$

whence

$$k = 1-\text{Cos}\theta \qquad (5.26)$$

A reasonable value for θ, taken from model G, is 30°, which gives a value of 0.13 for k. This is in good agreement with the value of 0.10 needed to resolve the discrepancy between theory and measurement for the rift stations.

Over the flank, the estimation of the value of k is slightly more cumbersome, although relying on the same principles. Dividing model G into a number of horizontal layers of equal thickness, and assuming each of these is circular in plan and centred under the apex, we can approximate the shape of the anomalous zone by a series of stacked cylinders. Each cylinder approximates to a thin sheet. The solid angle subtended by each of these sheets at the point of measurement can be obtained by referring to a chart given by Dobrin (1974, page 378). The mean is taken of the solid angles for all the sheets which extend laterally as far as the point of measurement. Dividing this mean by 2π steradians then gives the geometric factor.

Geometric factors calculated in this way for various distances from 75 km to 250 km from the apex, range from 0.40 to 0.53.

It might be argued that, in the calculations of the geometric factor for a particular surface point over the flank, that the effect of those sheets which do not extend laterally as far as this point should also be taken into account. Since these sheets contribute to the Bouguer anomaly at the point, but not the delay time, the correct method of taking these into account is to subtract the total of the solid angles for these sheets from the total for the sheets which do extend laterally as far as the surface point, before dividing by the number of the latter in forming the mean.

It is found that the contribution of those sheets which do not extend beneath the station is rather small, and the effect on the calculated geometric factor is to reduce it by about 10%.

Using these geometric factors of 0.13 for the rift group and of 0.45 for the flank group gives theoretical delay on gravity gradients of -8.5 sec/gal and -2.4 sec/gal respectively. Considering the approximate manner in which the geometric factors were obtained, and that k was assumed to be constant in deriving Equation 5.23, these figures agree remarkably well with the measured values of -10.6 sec/gal and -3.7 sec/gal respectively, being only about 20% low.

In practice, these calculations will tend to underestimate values of k, as the anomalous zone is elongated, as indicated by the gravity and the Kaptagat results. A more accurate determination of k values, based on a sounder knowledge of the three-dimensional structure would probably indicate higher values of $dV/d\rho$ than Birch's figure. Bott's (1965) interpretation of the upper mantle structure beneath Iceland suggests a $dV/d\rho$ value of 26 $m^4 sec^{-1} kg^{-1}$, an order of magnitude geater than Birch's figure. A significant degree of partial melting is inferred to explain the high $dV/d\rho$ values. Bott's figure is large enough (rather too large for the flank stations) to account for the high values of dt/dg obtained here.

Whether the high dt/dg values are explained by low geometric factors, or by high $dV/d\rho$ values due to partial melting, a source within the upper mantle is necessary.

5.8 Discussion of the Assumption of Horizontal Layering

The simplifying assumption used throughout this chapter, that a horizontally stratified velocity structure exists beneath each satation, is now examined in the light of the models which have been proposed. It is obvious from these models that the assumption is invalid, especially near the rift.

Dips have two effects on delay time calculations, both depending on the direction of the impinging rays. Firstly, rays will tend to pass through a greater or lesser thickness of anomalous material than is present immediately beneath the station, depending on whether the event back-bearing points up- or down-dip. The consequence of this on delay time is obvious. Secondly, refraction at sloping interfaces will ensure that Equation 5.3, vital to the calculations used in this chapter, no longer holds. The effect of this is to alter the position at which the ray which arrives at the station enters the anomalous zone, thus affecting the magnitude of Υ in Equations 5.6 and 5.7.

The treatment of situations other than plane horizontal layering generally requires the use of more complicated techniques, such as the iterative ray tracing described in the next chapter. In general it is impossible to formulate an expression for delay time as a single equation. It is for this reason, primarily, that the horizontal layering assumption was made at the beginning or this chapter.

There is one other situation wnich is amenable to reasonably simple analytical techniques. It is the case of a wedge-shaped anomalous zone, of uniform velocity V', within a region of uniform velocity V. Even in this case we can only treat analytically the case where rays impinge on the zone from directions perpendicular to the strike of the wedge. Figure 5.16 illustrates the simplest case of this type, where the bottom surface is horizontal and the upper interface comes to the surface.

This model very crudely represents the velocity structure beneath the eastern flank stations. A method of calculating delays through such a wedge is described here and the technique used to obtain an estimate of the likely errors introduced. Figure 5.16 illustrates a crustless model, but this is of little consequence as the ray deviations produced by refraction at the upper dipping interface are not large, and the effect on relative crustal delay times will be insignificant in these approximate calculations.

Referring to Figure 5.16 for the geometry, we note that the ray which reaches the station travels in the plane of the paper along the path ABS. In the absence of

FIGURE 5.16

DIAGRAM ILLUSTRATING THE CALCULATION OF DELAY TIMES THROUGH A WEDGE SHAPED ANOMALOUS ZONE

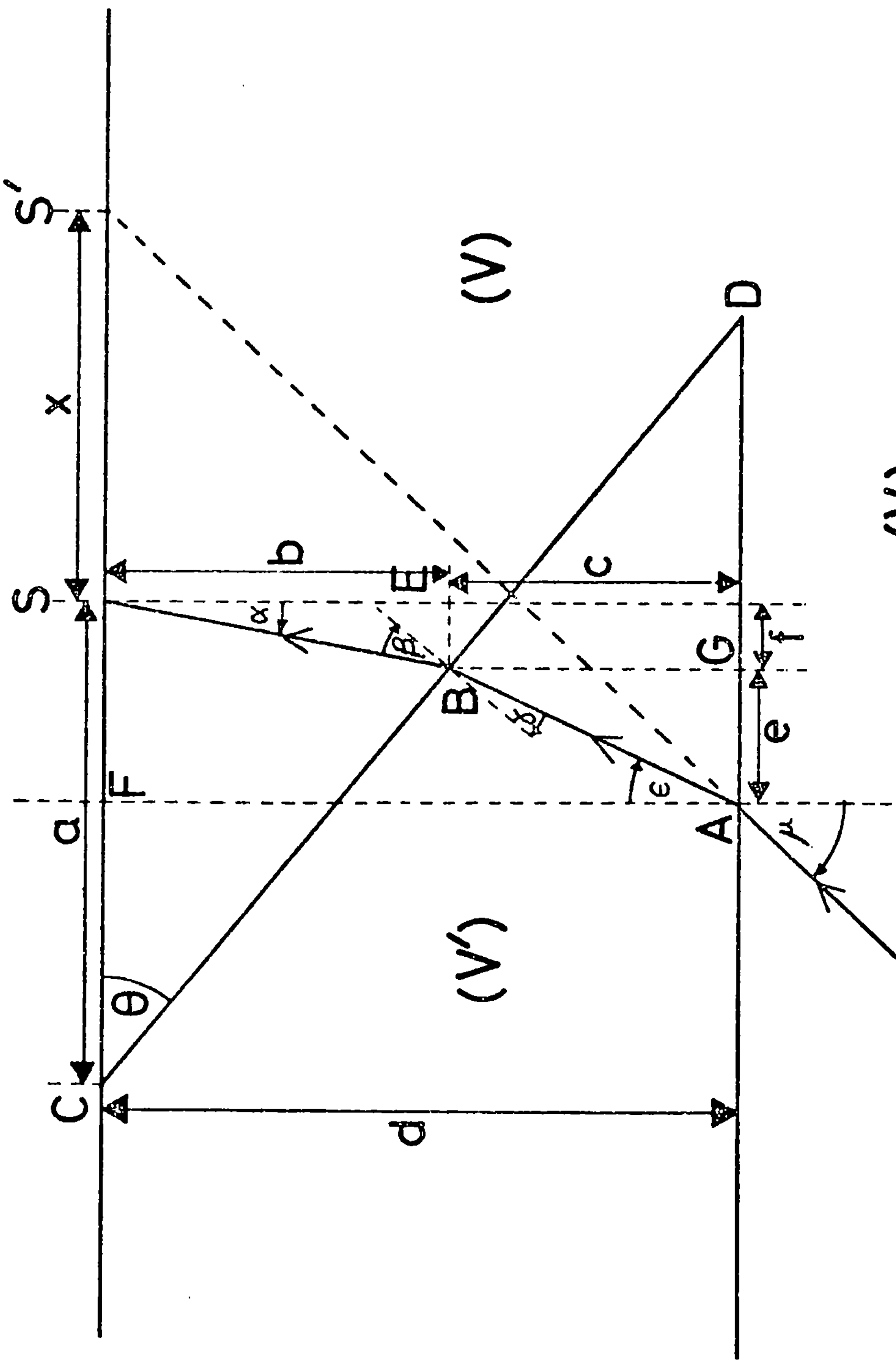

anomalous material, this ray would take the path AS', emerging a horizontal distance x farther from the epicentre. Thus the delay time, d, is given by the equation

$$d = t_{AB} + t_{BS} - t_{AS'} + \Upsilon \quad (5.27)$$

Where t_{AB}, t_{BS} and $t_{AS'}$ are the travel times along the paths AB, BS and AS' respectively, and is the difference in arrival times at S and S' for the unperturbed rays. We have

$$\left.\begin{aligned} t_{AB} &= AB/V' \\ t_{BS} &= BS/V' \\ t_{AS'} &= AS'/V \\ \Upsilon &= x/V_s \end{aligned}\right\} \quad (5.28)$$

Thus the problem reduces to one of calculating these various distances. This is accomplished by first calculating the angles μ, ϵ, δ, β and α. By Snell's law of refraction and the geometry of the figure we have

$$\text{Sin}\epsilon = V'\text{Sin} /V = V'/V_S \quad (5.29)$$

$$\delta = \theta - \epsilon \quad (5.30)$$

$$\text{Sin} = V\ \text{Sin} /V' \quad (5.31)$$

$$\alpha = \theta - \beta \quad (5.32)$$

The various distances are then calculated from simple trigonometrical reliationships

$$BS = a\ \text{Sin}\theta/\text{Sin}(\theta+\alpha) \quad (5.33)$$

$$b = BS\ \text{Sec}\alpha \quad (5.34)$$

$$f = BS\ \text{Cosec}\alpha \quad (5.35)$$

$$c = z - b \quad (5.36)$$

$$e = c\ \text{Tan}\epsilon \quad (5.37)$$

$$BA = c\ \text{Sec}\epsilon \quad (5.38)$$

$$x = d \, \mathrm{Tan}\mu - e - f \qquad (5.39)$$

$$AS' = d \, \mathrm{Sec}\mu \qquad (5.40)$$

Thus, for a given structure, all the distances in Equations 5.28 may be calculated, obtaining V_S from travel time tables.

These calculations fail under three distinct circumstances. Firstly, if the station rests on anomalous material, that is A is to the left of C in Figure 5.16, the ray which arrives at the station no longer undergoes refraction at the upper interface. The formulae derived in Section 5.2 are then relevant.

Secondly, the angle μ may be negative, and of sufficient magnitude that the ray misses the anomalous zone entirely. Under this circumstance the delay is obviously zero. The range of μ for which this happens is easily calculated by considering the angle S'SD. It is easy to show that this is given by the Equation

$$\angle S'SD = \mathrm{Cot}^{-1}(\mathrm{Cot}\theta - a/d) \qquad (5.41)$$

Thus the delay time will be zero if

$$\mu \leqslant -\mathrm{Cot}^{-1}(\mathrm{Cot}\theta - a/d) \qquad (5.42)$$

Thirdly, the ray may impinge on one or other of the interfaces at an angle greater than the critical angle. In the case where V' is less than V, relevant to this study, this can only happen at the upper interface, and is apparent when one evaluates $V \, \mathrm{Sin}\gamma / V'$ in Equation 5.31. If this quantity has a magnitude greater than one, total internal reflection takes place, and rays cannot penetrate through the wedge.

One further point is worth noting. If V' is less than V, rays passing through the wedge are deflected up-dip, that is to the left in Figure 5.16. Since the rays passing to the down dip side of the edge of the wedge, that is to the right of D in Figure 5.16, are unaffected, it is immediately apparent that there will be a region at the surface where no rays are received. Thus the edge represented by point D casts a shadow. By the same reasoning, for a point on the surface, there will be a certain range of for which a specified phase will not be seen.

In any realistic situation such sharp edges could not exist, and sharply defined shadow zones would not be detected. Even if sharp edges did exist, diffraction would tend to "fill in" the shadow zones. Nevertheless it is likely that amplitudes will vary strongly from one point to another due to the focussing effect of differential refraction within a laterally varying anomalous zone such as is proposed.

The procedure described above has been used to calculate delay times for two such wedge shaped models, intended to represent the inferred structure at two points on the flank of model G. A third set of delay times has also been calculated, representing the structure at the maximum of the eastern bulge. Here the top surface is horizontal and planar, and Equation 5.8 was used.

The parameters for these models are as follows:-

Model	A	B	C
Dip of Top Interface (Degrees)	63	45	0
Depth beneath Station (km)	20	58	115
Anomalous Velocity, V' (km/sec)	7.5	7.5	7.5
Normal Velocity V (km/sec)	8.1	8.1	8.1
Depth to bottom interface (km)	170	170	170

Models A, B, and C correspond approximately to the structures under Stations 21, 23 and 26 respectively (see Figure 5.4). Graphs of delay time against angle of incidence are illustrated in Figure 5.17.

Although in each case the curved upper interface has been replaced by a planar dipping interface, and consequently these graphs do not accurately represent the actual variation in delay that is to be expected, the general features of the behaviour are apparent.

Firstly, the effect of dip is to alter dramatically the way in which delay time varies with angle of incidence. Down dip, the delay decreases with increasing angle of incidence, until the shadow zone is reached. For the corresponding horizontally layered model the delay time would increase. Secondly, the range of variations is much increased. Over the expected range of angles of incidence, from about -30° to $+30^{\circ}$ for the epicentral distances used in this study, the total variation in relative delay times can be as large as 1.8 sec. Although more realistic models would probably give smaller variations, the effect is certain to be considerably in excess of the expected experimental errors in measurement, as estimated in Chapter 4.

FIGURE 5.17

DELAY TIME AGAINST ANGLE OF INCIDENT RAY

FOR THREE WEDGE SHAPED MODELS

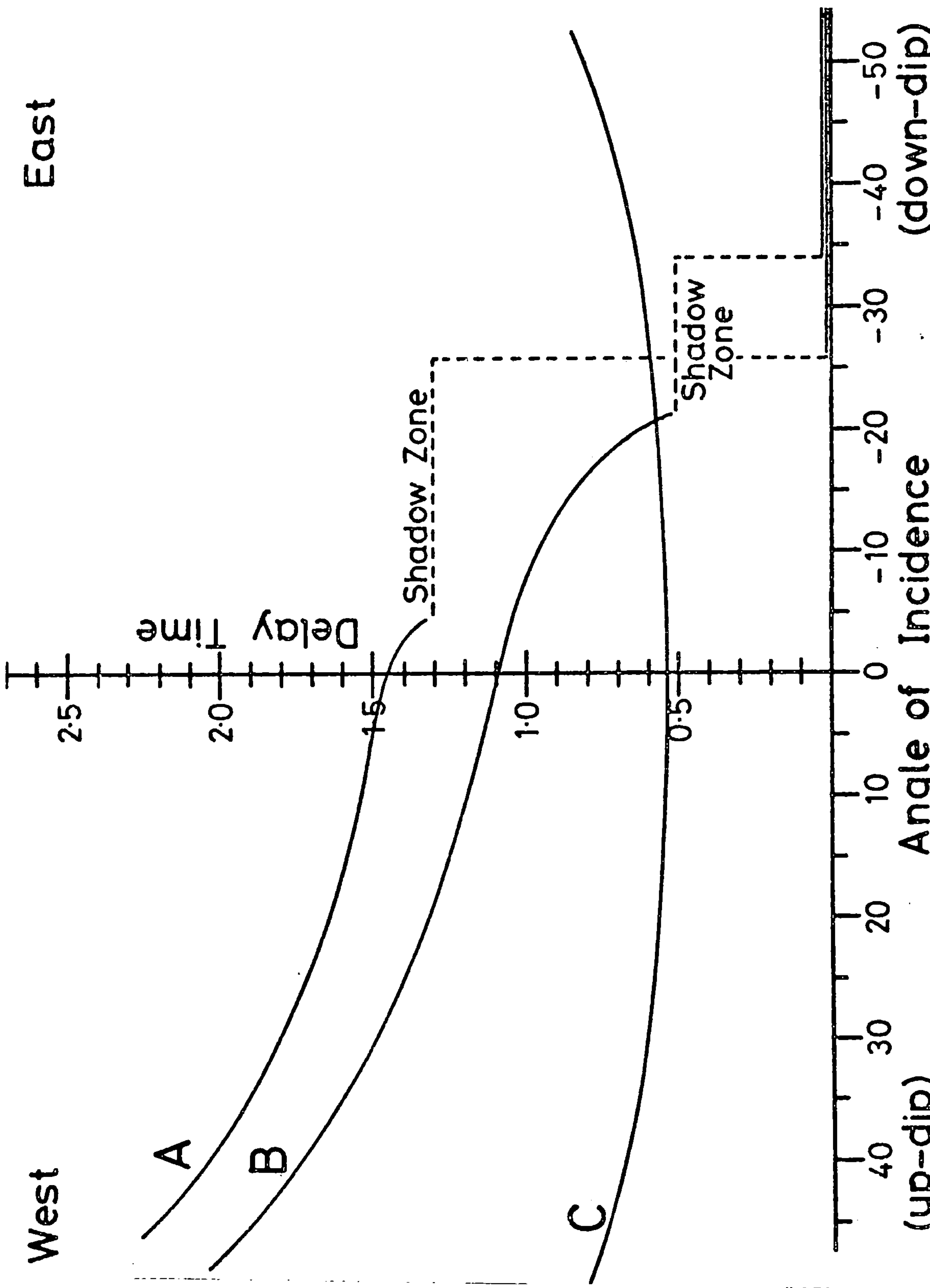

Thus the concepts that each point has a unique teleseismic delay associated with it, and that relative delays are independent of the events used to measure them are not strictly applicable to this study.

Nevertheless, the methods used in chapter 4 and in this chapter have provided a simple and useful means of analysing and interpreting the delay time measurements, and the models derived are almost certainly correct in their main features.

In the next chapter a method of interpretation is described which avoids the main assumption made in this chapter.

CHAPTER 6

THREE-DIMENSIONAL RAY TRACING MODELLING

6.1 Introduction

In this chapter the concept that each station has a unique delay time associated with it is discarded, along with the assumption that horizontal stratification exists beneath each station. Relaxing these simplifying assumptions, made in the previous chapter, allows potentially important directional information, which is lost when raw delay times are combined to form station delays, to be included.

A new interpretation method is formulated, which is designed to make full use of the fact that rays which arrive at a single station from different hypocenters emerge from the lower mantle with a wide range of back-bearings and angles of incidence, and thus sample different parts of the anomalous zone with differing dips and thicknesses. The models used, and the techniques for testing them, will be fully three-dimensional.

The advantages to be expected from the use of three-dimensional models are several. Firstly, as is clear from the limited north-south extent of the Kenya dome, Gregory rift, and their associated gravity anomalies, and from the discussions of the previous chapter, the underlying structure is not easily represented by two-dimensional models. The three dimensional approach is more realistic. Secondly, full use can be made of all the data, including measurements of Stations 18, 19, 31, and 50 which were not easily incorporated into the profiles discussed in Chapter 5. Thirdly, since the technique will fully take into account the directions of the impinging rays, bias due to the preponderance of events from certain regions of the earth will be reduced to a minimum. Fourthly, by taking into account the directional information, some control on depth and seismic velocities may be acheived.

Certain disadvantages are also to be expected. Three-dimensional structures are more difficult to visualise and represent, both as diagrams on paper and numerically for computations. The forward problem of calculating theoretical delay times through a three-dimensional velocity structure is not generally amenable to analytical techniques, and some form of ray tracing must be used. If the dips on interfaces vary laterally, the ray which arrives at a specified point must be found by iteration. Since the forward problem is no longer amenable to analytical methods, the inverse problem of finding suitable models is essentially one of trial and error. Theoretical delays for very many models will have to be calculated, and compared with their corresponding measured values, before a reliable optimum choice can be made. The use of a high speed digital computer is therefore essential, and large demands for central processing unit (CPU) time are to be expected. In view of the potentially large number of computations involved, models must be relatively simple, and characterised by as few parameters as possible. Simple models run the risk of not being able to conform sufficiently accurately to the real structure. On the other hand, the use of too many parameters can lead to instability. However, careful choice of the form of the models should reduce these risks.

6.2 Choice of Model Types

In choosing between model types, care must be taken in deciding how the three-dimensional velocity structure should be represented for computational purposes. There are several criteria to be considered.

Firstly, the models should embody the main features of structure revealed by the simple interpretations of Chapter 5. Secondly, the models should be sufficiently flexible to conform accurately to realistic structures. Thirdly, computer storage requirements for the velocity structure must not be excessive. Fourthly, the models should be amenable to rapid ray-tracing procedures through them. Fifthly, the number of parameters characterising the models should be small, so that the behaviour of the models may be explored rapidly. Finally, rounding and other errors in the ray-tracing calculations should not become excessive.

In consideration of the above criteria it was decided to employ models which divide the three-dimensional space into a small number of regions, each with a uniform velocity. Within each region of such a model, rays follow straight paths, and calculations of angles of dip and refraction at interfaces are easily accomplished and performed a relatively few times for each ray.

Alternatively, variations in velocity from point to point might have been allowed. Such structures might be represented either by values defined at points on a three-dimensional grid, with interpolation to obtain intermediate values, or by some form of analytical function. However, excepting certain special cases for example linearly increasing velocity in a constant direction, ray tracing would be from point to nearby point along the ray path. The stepping interval would have to be small to represent accurately the curved ray path, enormously increasing the number of calculations and hence the demandfor CPU time.

Far from the rift zone, normal horizontal layering may be expected, and this forms the basis of the assumed "unperturbed" structure. A two layered crust is assumed, with P-wave velocities of 5.8 and 6.5 km/sec in the upper and lower layers respectively. The intermediate and Mohorovičic discontinuities are assumed to be at 20 km and 44 km depth respectively. This crustal structure is based on those derived from studies carried out away from the immediate vicinity of the Gregory rift (Maguire and Long, 1976; Rykounov et al, 1972; Bonjer Fuchs, 1970). At depths below 44 km the model is based on the AFRIC P-wave model of Gumper and Pomeroy (1970), slightly modified so that only one interface is present, placed at 120 km depth. Above and below this depth, P-wave velocities of 8.1 and 8.2 km/sec respectively are assumed.

The unperturbed model is illustrated graphically in Figure 6.1. The P-wave velocity model of Herrin et al (1968) and the AFRIC model of Gumper and Pomeroy (1970) are also shown for comparison. To represent the anomalous material, a region of uniform velocity, V, is embedded within the unperturbed structure. It is the shape and depth of this region, and the magnitude of V, that are to be determined.

In order to simplify of the calculations, and in accordance with the discussion of Section 5.4, a horizontal lower interface, at depth z_o, is assumed. Thus, the only dipping interface is the upper boundary of the anomalous zone which is descibed by an analytical function of the form

$$z = f(x,y) \tag{6.1}$$

where x and y are coordinates of horizontal position on a Cartesian system, chosen so that the positive y-axis points northwards on a local meridian, and z is the depth, positive downwards, to the interface. In choosing a suitable form for f(x,y) the following criteria must be fulfilled:

a) f(x,y) must have at least one minimum to represent the thickening of the anomalous zone under the rift, and preferably more to allow for subsidiary thickenings,

FIGURE 6.1

ASSUMED UNPERTURBED LITHOSPHERIC STRUCTURE

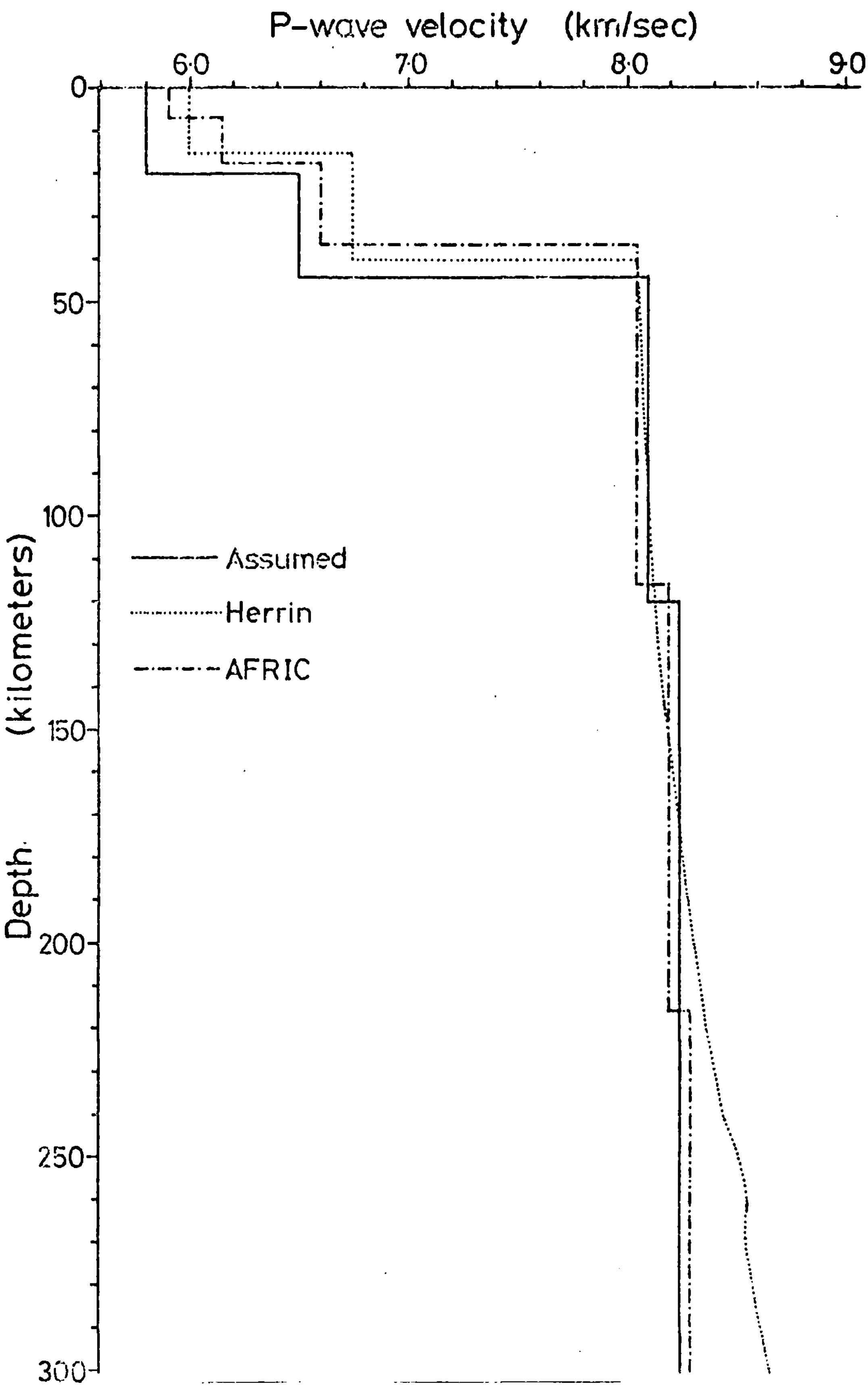

for example that present to the southeast of the main culmination (see Figure 5.6). Henceforth, each such thickening will be referred to as a 'hump'.

b) $f(x,y)$ must be a continuous function, so that delay times vary as smoothly as possible with position.

c) $f(x,y)$ must be analytically differentiable, so that expressions for calculating the dip and strike (or equivalently, the direction of the normal to the surface) may be formed easily.

d) $f(x,y)$ must approach z_o asymptotically far from the centres of the humps so that sharp corners of the kind present at the edge of the wedge shaped models of Section 5.8 are not present to cast shadows.

A function which fulfils all of these requirements is given by the equation

$$z = z_o - \sum_{i=1}^{n} \frac{C_i}{1+A_i(x-X_i)^2+B_i(y-Y_i)^2+D_i(x-X_i)(y-Y_i)} \qquad (6.2)$$

Using this function the upper surface is, in effect, the superposition of n humps. The i^{th} hump is centered on (X_i,Y_i) and has a height C_i, while A_i, B_i and D_i control its lateral extent. Contours of equal height for the i^{th} hump are given by equations of the form

$$k_i = A_i(x-X_i)^2+B_i(y-Y_i)^2+D_i(x-X_i)(y-Y_i) \qquad (6.3)$$

where k_i is a positive constant representing the contour height. Equation 6.3 is the general equation of an ellipse, and we may speak of the individual humps as being elliptical in plan. When $k_i = 1$, the contour representing half the peak height of the hump is represented, and this will have semi-major and semi-minor axes of lengths L_i and M_i respectively, with the major axis being rotated clockwise through an angle θ_i from the y-axis. We may refer to L_i and M_i as being the Y- and X-dimensions of the i^{th} hump respectively, and to θ_i, as its orientation (eastward from north). L_i, M_i and θ_i characterise the hump fully. It is easy to show that A_i, B_i and D_i are related to L_i, M_i and θ_i by the following equations:

$$\begin{aligned} A_i &= (\mathrm{Cos}\theta_i/L_i)^2 + (\mathrm{Sin}\theta_i/M_i)^2 \\ B_i &= (\mathrm{Sin}\theta_i/M_i)^2 + (\mathrm{Cos}\theta_i/L_i)^2 \\ D_i &= 2\ \mathrm{Cos}\theta_i\ \mathrm{Sin}\theta_i\ (1/L_i^2 - 1/M_i^2) \end{aligned} \tag{6.4}$$

In the following models humps will be described by the corresponding values of L_i, M_i and θ_i, as these are more easily appreciated in physical terms. Calculations, however, are performed in terms of A_i, B_i and D_i, using Equation 6.2.

Equation 6.2 gives a surface with a great deal of flexibility. The major restriction is in the degree of kurtosis, or peakedness of each hump, which is fixed. Even this can be altered to an extent by the superposition of two or more humps with a common centre and orientation, but with different dimensions.

The greater the number of humps the greater is the flexibility. However, for reasons stated at the beginning of this section, it is desirable to keep the number of parameters and hence the number of humps to a minimum, four being considered enough to adequately represent the likely structure. The humps are described in the following paragraphs.

Hump No. 1. This hump, the Ethiopian hump, is initially placed at approximately 8°N, 38°E, and is intended to represent a major anomalous zone beneath the Ethiopian uplift and rift. Clear evidence of the existence of such a zone is provided by the large positive travel time residuals, determined at Addis Ababa, both absolute (Lilwall and Douglas, 1970; Herrin and Taggart, 1968; Cleary and Hales, 1966) and relative to other African stations (Sundaralingam, 1971). Although the influence of this hump on delay times at the DKSP stations is likely to be small, in view of its considerable distance from them, first motion studies of teleseismic P-wave arrivals at Station 50 have indicated azimuth and slowness anomalies which have been interpreted in terms of a connection at depth between the anomalous zones under the Kenya and Ethiopia domes (Micenko, 1977). The postulated connection may be reflected in the pattern of delay times for Station 50. It is on this tentative basis that the Ethiopian hump is included.

The present data could not be expected to define the dimensions and orientation of the Ethiopian hump with any degree of certainty. Consequently it was decided to make this hump circular in plan, fixing $D_1=0$ and $B_1=A_1$. Its lateral extentcan therefore be characterised by only one quantity, its radius.

Hump No. 2. This hump, the Main hump, is intended to represent the major part of the anomalous zone underlying the Kenya dome. The position of the peak of this hump is expected at the culmination of the dome (~0.5°S, ~36°E). From the models of Chapter 5, and the Kaptagat models (Long and Backhouse, 1976) we would expect X- and Y-dimensions of the order of 200 km and 300 km respectively. The major axis is likely to be aligned with the peak of the Ethiopian hump, giving an orientation of about 12°.

Hump No. 3. This hump, the Crustal hump, will represent the much narrower, elongated part of the anomalous zone which penetrates the crust along the axis of the rift. This hump is superimposed on the main hump and its peak may be expected somewhere along the line CD of Figure 5.8, probably at about 0.3°S, 36.2°E. The orientation of this hump would align its major dimension along this line, giving an orientation of about -20°. The X-dimension is likely to be a very few tens of kilometres and the Y-dimension about 100 km.

Hump No. 4. This, the Kilimanjaro hump, is initially centered on Mt. Kilimanjaro (~3.1°S, ~37.1°E) and is expected to have an orientation of about 30°, crossing the line of Stations 21-30 and accounting for the increased delay times at Stations 25, 26, and 27.

The four-humped model described above, forming the basis of the ray tracing modelling to be described, has 24 variable parameters. There are six for the position, height, orientation, and dimensions of each of humps 2, 3, and 4, and four for hump No. 1. The other two parameters are z_o, the depth of the lower interface and V, the P-wave velocity within the anomalous zone. Perhaps it is rather ambitious to attempt to use models with so many parameters, but simpler models are unlikely to give the degree of flexibility required by the models of Chapter 5.

6.3 Delay Times for Three-Dimensional Models

Much the same approach is adopted here for calculating delay times through the three-dimensional structure as was used for deriving the expressions for delay time through horizontally stratified structures (Section 5.2). We calculate travel times for both the ray which actually arrives at the designated surface point and the one which travels through the unperturbed structure. We subtract the latter travel time from the former, and make a correction, Υ, for different points at which the two rays enter the base of the anomalous zone.

Figure 6.2 illustrates a model with the number of unperturbed layers reduced to two for clarity. The unperturbed ray OPAS is refracted only once, at A. The real ray follows the path O'P'U'A'S, undergoing two further refractions, at P' on the lower and U' on the upper interface of the anomalous zone.

The travel time, T, and the horizontal distance, X, for the unperturbed ray are obtained from Equations 5.4 and 5.5. When α_i is substituted using Equation 5.3, we have

FIGURE 6.2

DIAGRAM ILLUSTRATING THE CALCULATION OF DELAY TIMES

FOR THREE-DIMENSIONAL MODELS

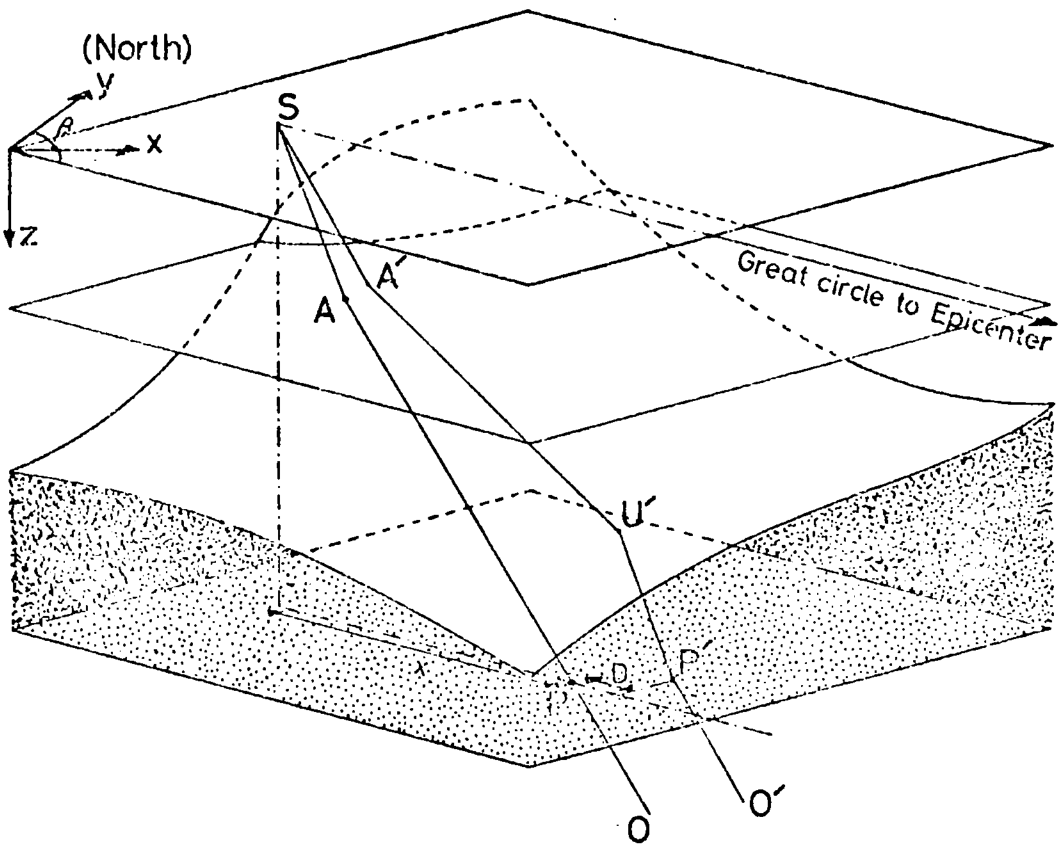

$$X = \sum_{i=1}^{n} z_i/((V_s/V_i)^2-1)^{1/2} \tag{6.5}$$

$$T = \sum_{i=1}^{n} Z_i/(V_i(1-(V_i/V_s)^2)^{1/2}) \tag{6.6}$$

where V_s is the apparent surface velocity obtained from travel time tables, given the epicentral distance and focal depth.

It is convenient to represent the positions of points such as those in Figure 6.2 by vectors referred to the Cartesian coordinate system described in the previous section. Ray and other directions may then be represented by other vectors of unit length, the components of which will be the direction cosines. Vectors representing the positions of points will be symbolised by the corresponding lower-case characters, underlined, while direction vectors will be symbolised by upper case characters, also underlined and with a circumflex.

Thus, the position of P will be given by the vector $\underline{p}$ where

$$\underline{p} = \underline{s} + (X\sin\beta, X\cos\beta, z_o) \tag{6.7}$$

and β is the back-bearing of the event.

The calculation of the travel time for the real ray is made more complicated than for the horizontally stratified case by the refraction at U' on the upper, dipping interface. Here the ray is not only bent vertically, but, in general, twisted out of the plane containing its previous motion. Thus P' and U' will generally lie outside the plane which contains the unperturbed ray. Because of the awkward refraction at U' the positions of P' and U', cannot be determined by analytical techniques and an iterative procedure must be used. An initial estimate of $\underline{p}'$, $\underline{p}_o' = \underline{p}$, is used as a starting point, and a ray traced through the anomalous zone to a corresponding surface point $\underline{s}_o'$, using the techniques described in the section following. The initial direction is known since the ray entering the anomalous zone at P_o' may be assumed to be parallel to OP (see Section 6.5). At the same time, the travel time for this ray, T_o', may be calculated.

In general, $\underline{s}_o'$ will not coincide with $\underline{s}$, and the ray traced will not be the required one. A better estimate of $\underline{p}'$, $\underline{p}_1'$, may be obtained from the position error vector, $\underline{s}'-\underline{s}_o'$, thus

$$\underline{p}_1 = \underline{p}_o' + q(\underline{s} - \underline{s}_o') \tag{6.8}$$

where q is a factor close to one. A new ray is traced from $\underline{p}_1'$ to the corresponding surface point $\underline{s}_1'$, the new travel time calculated and a new error vector $\underline{s}-\underline{s}_1$, formed. This iterative procedure is repeated until

$$|\underline{s} - \underline{s}_n| \leqslant \epsilon \tag{6.9}$$

where ϵ is a prescribed error limit, equal to 225 m in this study. The error in delay time due to this tolerance is discussed in Section 6.5.

During initial experiments with this technique, a constant value of one was used for q. (For horizontal stratification, the second iteration closes exactly with this value.) However it was immediately apparent that with this value, and for likely forms of anomalous zone, the procedure tends to over-correct. It was found that the average number of iterations needed to calculate a set of theoretical delay times could be reduced substantially by lowering the value of q. A value of 0.75 was found to give good results. Even with the lowered value of q, a few arrivals took as many as 50 iterations to converge due to unstable oscillations of $\underline{s}'$ about $\underline{s}$, and some would not converge at all. To increase the stability of the procedure it was decided to use a smaller value of q for each iteration. After a little experimentation, an initial value of 1 for q, decreasing with each iteration by a factor of 0.9, was found to give slightly better results. The average number of iterations required was very similar to that obtained with q = 0.75, and some of the previously unstable iterations converged. Not all the rays could be made to converge, however. This problem is discussed in Section 6.5.

Assuming that the real ray has been traced satisfactorily, and T and T' calculated, there only remains the calculation of τ, the time correction for the differing positions of $\underline{p}$ and $\underline{p}'$. It is clear from Figure 6.2 that $\underline{p}'$ is closer to the epicentre than $\underline{p}$ by an amount D, where

$$D = (\underline{p}' - \underline{p}).(\mathrm{Sin}\beta, \mathrm{Cos}\beta, 0) \tag{6.10}$$

whence

$$\tau = D/V_s \tag{6.11}$$

The theoretical delay time, d, is then given by

$$d = T' - T - \tau \tag{6.12}$$

6.4 Outline of the Ray Tracing Method

Ray tracing techniques have been developed by a number of workers, usually with rather specific structures in mind (for example, Sattlegger, 1965; Otsuka, 1966; Sorrels et al, 1971). Shah (1973) describes a general method for calculating the paths, and travel times, of rays through a series of regions each with a uniform seismic velocity. This method is essentially the one adopted here. Shah goes on to discuss ray tracing through regions where seismic velocity changes continuously.

In the present case we are given the initial point, $\underline{p}_i'$, where the ray enters the base of the anomalous zone. We assume that below this boundary the rays entering are all parallel with an angle to the vertical of α_i. This allows us to calculate the initial direction of the ray within the anomalous zone. The problem then is to find, firstly where this ray encounters the next interface, and secondly how it is then refracted. This, in effect, gives us a new initial point, and we can repeat the procedure for each new region in turn until the ray meets the surface.

The vector equation representing the straight ray path, from an initial point described by the position vector $\underline{a}$, in a direction specified by the vector $\underline{U}$ is

$$\underline{\chi} = \underline{a} - r\underline{U} \tag{6.13}$$

where r is the distance from the initial point. The next interface may be expressed by the general form

$$\phi(\underline{\chi}) = 0 \tag{6.14}$$

Substituting for $\underline{\chi}$ gives the equation

$$\phi(\underline{a}-r\underline{U}) = 0 \qquad (6.15)$$

which can be solved analytically for r, if $\phi(\underline{\chi})$ is not too complicated.

For example, if the next interface is horizontal at a depth d, we have

$$\phi(\underline{\chi}) = z-d = 0 \qquad (6.16)$$

whence

$$r = d/U_z \qquad (6.17)$$

where U_z is the z-component of U.

Substituting for r in Equation 6.13 then gives us the point at which the ray meets the interface.

This is the procedure adopted for calculating the path through the horizontal layers above the upper interface of the anomalous zone.

Calculating the point at which the ray meets the upper interface of the anomalous zone is far less straightforward. Equation 6.15 becomes

$$f(r) = a_z + rU_z - z_o + \sum_{i=1}^{n} C_i/\{1+A_i(a_x-X_i+rU_x)^2+B_i(a_y-Y_i+rU_y)^2 + D_i(a_x-X_i+rU_x)(a_y-Y_i+rU_y)\} = 0 \qquad (6.18)$$

A satisfactory method of solving to find the minimum positive root of this equation was devised, but since its decription is somewhat lengthy it is deferred until Appendix 5.

Having obtained the value of r, Equation 6.13 is used to derive the coordinates of the intersection point. We now calculate the unit vector, $\hat{\underline{N}}$, representing the direction of the normal to the surface at this point. Using the general form of Equation 6.14 to describe the surface, the direction of $\underline{N}$ may be obtained by forming the vector gradient

$$N = \nabla\phi(\underline{X}) = \begin{Bmatrix} \sum_{i=1}^{n} C_i(2A_i(x-X_i)+D_i(y-Y_i))/u_i^2 \\ \sum_{i=1}^{n} C_i(2A_i(y-Y_i)+D_i(x-X_i))/u_i^2 \\ -1 \end{Bmatrix} \qquad (6.19)$$

where

$$u_i = 1+A_i(x-X_i)^2+B_i(y-Y_i)^2+D_i(x-X_i)(y-Y_i) \qquad (6.20)$$

This vector must be normalised to unit length

$$\underline{N} = \underline{N}/|\underline{N}| \qquad (6.21)$$

The behaviour of the ray at interfaces is governed by laws of refraction. The directions of the incident ray, the refracted ray and the normal to the surface at the point of incidence are given by the unit vectors $\hat{\underline{I}}$, $\hat{\underline{R}}$, and $\hat{\underline{N}}$ respectively, as illustrated in Figure 6.3. The velocities of the incident refracted rays are V_I and V_R respectively.

The angles of incidence, i, refraction, r, and deviation, d, are given by

$$\text{Cos } i = \alpha = \hat{\underline{I}}.\hat{\underline{N}} \qquad (6.22)$$

$$\text{Cos } r = \beta = \hat{\underline{R}}.\hat{\underline{N}} \qquad (6.23)$$

$$\text{Cos } d = \gamma = \hat{\underline{I}}.\hat{\underline{R}} \qquad (6.24)$$

Snell's first law states that $\hat{\underline{I}}$, $\hat{\underline{N}}$ and $\hat{\underline{R}}$ all lie in the same plane and are therefore linearly dependent. Thus we may write

$$\underline{R} = \mu\underline{I} + \nu\underline{N} \qquad (6.25)$$

FIGURE 6.3

DIAGRAM ILLUSTRATING THE CALCULATIONS OF REFRACTION AT AN INTERFACE

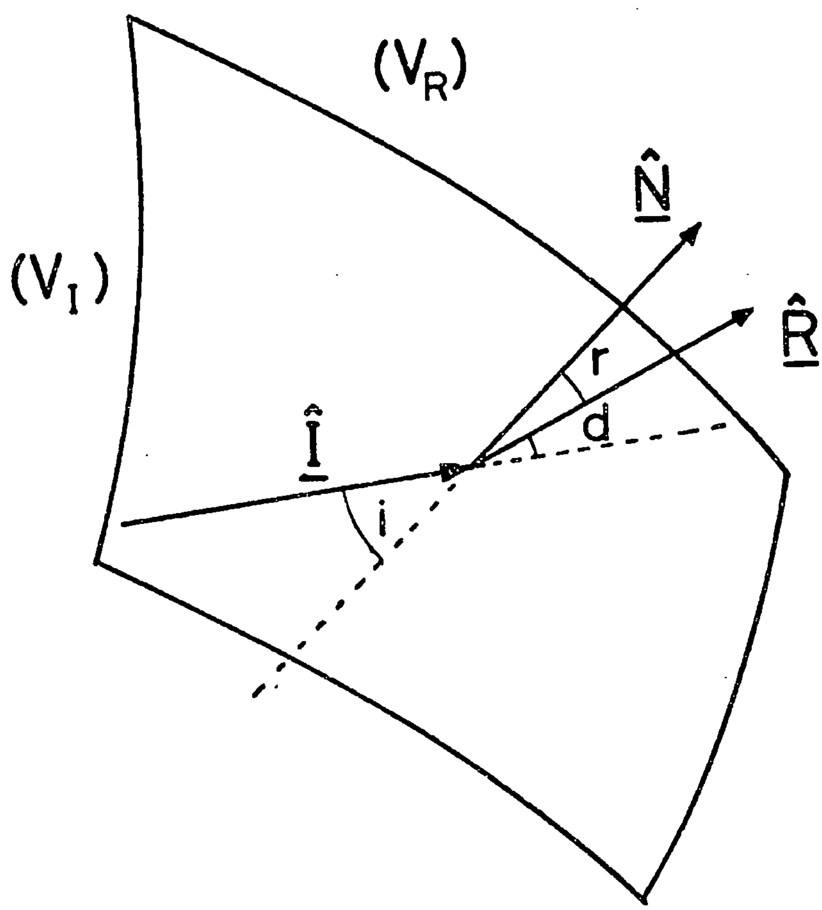

and

$$d = i - r \tag{6.26}$$

Using the trigonometrical identities

$$\begin{aligned} \operatorname{Cos}(\theta-\emptyset) &= \operatorname{Cos}\theta \operatorname{Cos}\emptyset + \operatorname{Sin}\theta \operatorname{Sin}\emptyset \\ \operatorname{Cos}^2\theta + \operatorname{Sin}^2\theta &= 1 \end{aligned} \tag{6.27}$$

we have

$$\gamma = \operatorname{Cos}(d) = \operatorname{Cos}(i-r) = \alpha\beta + \sqrt{(1-\alpha^2)(1-\beta^2)} \tag{6.28}$$

Forming the dot product of Equation 6.25 with $\underline{I}$ and $\underline{N}$ respectively, from Equations 6.22, 6.23, and 6.24, we have

$$\begin{aligned} \gamma &= \mu + \nu\alpha \\ \beta &= \nu + \mu\alpha \end{aligned} \tag{6.29}$$

whence

$$\begin{aligned} \mu &= (\gamma - \beta\alpha)/(1 - \alpha^2) \\ \nu &= (\beta - \gamma\alpha)/(1 - \alpha^2) \end{aligned} \tag{6.30}$$

Snell's second law allows us to calculate β. We have

$$\frac{V_I}{V_R} = \left(\frac{1 - \operatorname{Cos}^2 i}{1 - \operatorname{Cos}^2 r}\right)^{1/2} = \left(\frac{1 - \alpha^2}{1 - \beta^2}\right)^{1/2} \tag{6.31}$$

whence

$$\beta^2 = 1 - V_R^{\ 2}(1 - \alpha^2)/V_I^{\ 2} \tag{6.32}$$

The calculation of $\underline{R}$ proceeds thus:-

1) Calculate α from Equation 6.22

2) Calculate β^2 from Equation 6.32.

   If $\beta^2 \leq 0$ total internal reflection takes place at the interface, and no refracted ray is produced. If $\beta^2 > 0$, calculate β.

3) Calculate γ from Equation 6.28.

4) Calculate μ and ν from Equation 6.30.

5) Use Equation 6.25 to calculate $\underline{R}$.

This approach avoids the explicit use of trigonometrical functions in calculations, and is rapid.

The calculation of $\underline{N}$ for the upper interface of the anomalous zone has already been described. For the other interfaces, which are horizontal, $\underline{N}$ is simply given by

$$\underline{N} = (0 , 0 , -1) \quad (6.33)$$

6.5 Errors and Limitations of the Ray Tracing Method

Although rounding errors in the calculations inevitably give rise to errors, these are of the order of 1 part in 10^7 and may be neglected in comparison with the allowed tolerances in the iterative calculations.

The allowed tolerance on r, for example, is one part in 10^4, giving a maximum absolute error of about 30 m. In the case of a vertical ray, this error will be directly translated to an error in the height of the interface. For a velocity contrast of 6.4 km/sec to 8.1 km/sec the corresponding travel time error, and thus delay time error, is only 0.6 msec and can safely be ignored.

The tolerance on the location of the surface point of the ray is 225 m and the magnitude of the corresponding error in delay time is dependent, firstly on the error in Υ, and secondly on the error in T' in Equation 6.12. The error in Υ is entirely due to the error in D, in Equation 6.11, which is no more than 225 m. The corresponding error, taking the worst case value of V_s (13 km/sec), is 17 msec. T' is affected by errors in the surface point location, because the point where the ray intersects the upper surface is also mislocated. Errors arise in this case when the ray strikes the interface at an acute angle, as illustrated in Figure 6.4, where two adjacent rays are shown. They are separated by a distance, e, of the order of the mislocation error, and intersect the interface at points a distance g apart. Neglecting the deviation of the rays, and the curvature of the interface, both of which give rise to second order terms in the error, and hence putting r=i we have

$$\delta T' = 2e/(\text{Cos } r\ (1/V'-1/V)) \qquad (6.34)$$

For angles up to 80°, and with a worst case velocity contrast, the error is still less than 10 msec. Although certain rays may arrive at angles of incidence greater than 80°, the chances are that these will be stopped by total internal reflection, unless $V' \approx V$, in which case $\delta T'$ will be small anyway. The curvature on the surface will in any case prevent g, and hence the errors, from becoming excessive.

To simplify calculations, a constant value of V_s is assumed for all stations for each event. The assumed value is that calculated for a central station, usually 22. For other stations there will be an error in the calculated delay time due to the error in V_s. Station 50 is the most distant being about 4.5° from Station 22. Taking a maximum value of 0.085 km/sec^{-2} for the curvature in the travel time

FIGURE 6.4

DIAGRAM ILLUSTRATING ERROR DUE TO TOLERANCE ON r

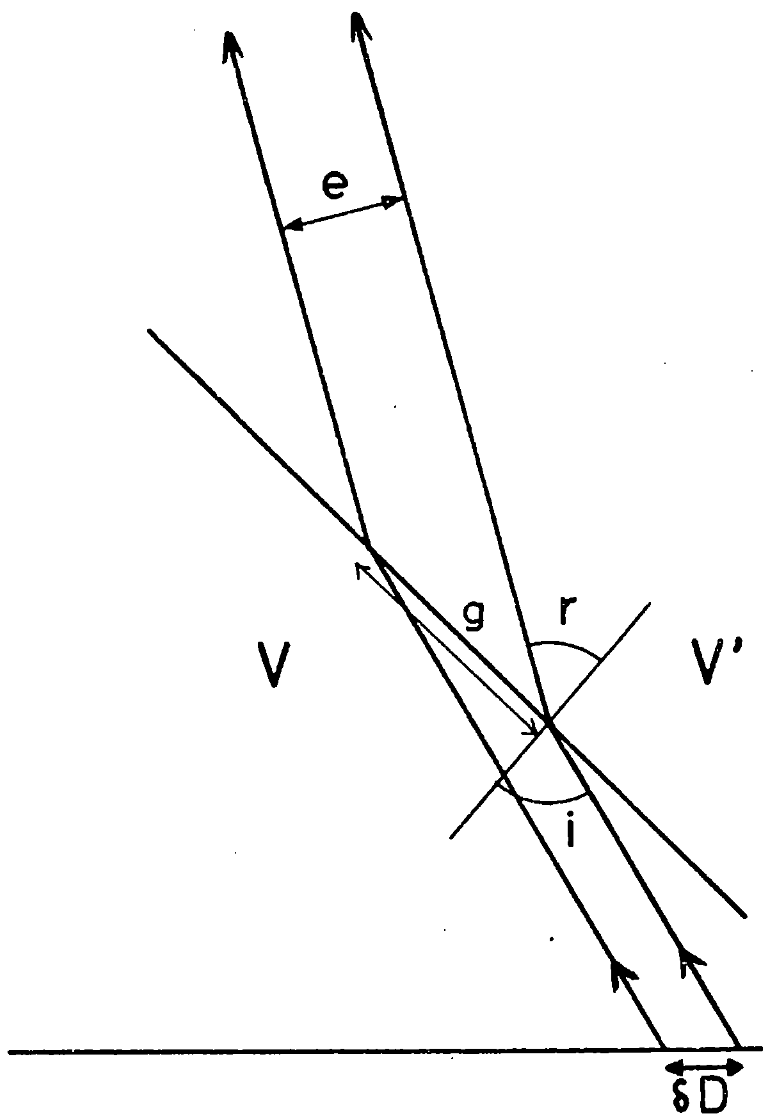

tables (Section 4.5), it can be shown that the maximum error in the angle of incidence is about 2.3°. From Figure 5.17, which illustrates the delay time variation with angle of incidence for wedge shaped models, typical errors of less than 0.02 sec are inferred. These are small enough to be ignored.

Thus with the prescribed tolerances as given, delay times would appear to be sufficiently accurately calculated. The total error is well below the estimated onset picking errors.

However, close examination of the ray tracing procedure, and experimentation with the technique as outlined above, reveals some defects. To illustrate these, and to determine the general behaviour of delay time variations over a single-humped body, a simple two-dimensional ray tracing program was written.

Rays are traced, using the techniques described in the previous section, from points equally spaced along the base of the anomalous zone, with initial directions dependent on the input (unperturbed) apparent surface velocity. Each ray is traced to the upper interface of the anomalous zone and, if it is not totally internally reflected, on to the surface. The true delay time for the ray and the corresponding vertical delay time (neglecting refractions) are calculated and plotted. A typical plot is illustrated in Figure 6.5.

Because of the change of sign for the velocity contrast

FIGURE 6.5

RAYS TRACED AND DELAY TIMES OBTAINED

FOR A SINGLE-HUMPED TWO-DIMENSIONAL MODEL

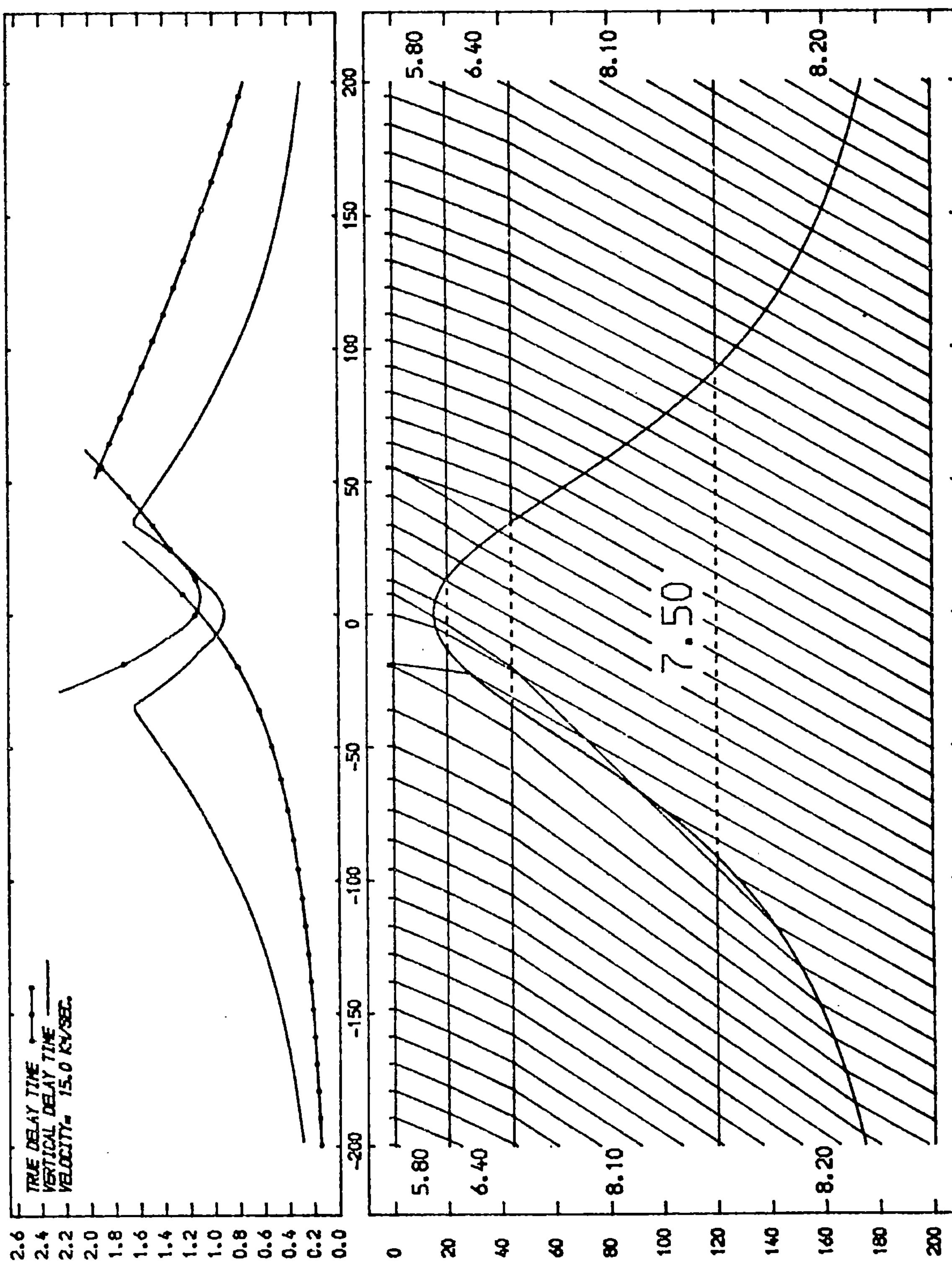

at the Moho, some surface points receive two rays, and thus the delay time curve is duplicated. The iterative technique, as described, is unable to cope with the sudden transition from one branch of the curve to another, and it is for this reason that the method sometimes does not converge.

Even when convergence does take place, it may not be for the ray which gives rise to the least delay time, and which corresponds to the first arrival. Errors, all in the same direction, of up to 1.5 sec are suggested by the delay times presented in Figure 6.5.

A quick and easily implemented method of ensuring that the iterative technique converges to give the correct delay time has not been found, and these large non-random errors must be accepted as a major inadequacy of the technique.

A further defect of the method is that the possibility of rays reimpinging on the anomalous zone is ignored. Examples of this can be seen in Figure 6.5. The number of cases where this happens, and where the ray is then used to calculate a delay time, is thought to be small.

6.6 Calculation of the Objective Function

To facilitate the automatic search for optimum models, it is essential to be able to represent, by some single value, the closeness of fit between the measured values of delay time and the corresponding theoretical values. Such a yardstick then provides a convenient method for differentiating the better models from the worse. Numbers designed to reflect the closeness of fit between theoretical values and measurements, which will vary with changes in the parameters characterising the theoretical model, are called objective functions. Usually these functions are calculated in such a way that smaller values correspond to better fitting models.

Objective functions based on the sum of residuals squared, thus,

$$f = \sum r_i^2 \tag{6.35}$$

where r_i is the i^{th} residual, are the most frequently encountered. Such expressions are very often entirely justifiable, when measured values have errors which are normally distributed and with zero mean, or nearly so. Instances where this is not the case are also common, for example when data are subject to occasional mistakes in calculation or transcription which give the corresponding measurements highly improbable values.

Claerbout and Muir (1973) have examined the problem of finding robust models for "erratic" data. They argue for the use of absolute error estimates as the basis of objective function expressions in a wide range of geophysical modelling tasks, when non-normally distributed errors are present. They suggest the use of objective functions given by

$$f = \sum |r_i| \tag{6.36}$$

this being the sum of the absolute errors, and show that this can give better results.

In the present study we may expect the measured delays to be subject to errors which are normally distributed, or at least approximately so. Mistakes, such as those due to picking one or more half cycles from the correct position, have been eliminated, as explained in Section 4.3. However, some of the theoretical delay time values are subject to errors which are all in the same direction, and far from normally distributed, as explained in the previous section. The magnitude of these errors may be considerable, and therefore, it might be argued thatan absolute error estimate should be used as an objective function here. However, the proportion of theoretical delays which are subject to gross errors is likely to be small, and in view of the difficulty that would arise in removing the effect of delays at source, if absolute error estimates were used, it was decided to use the more traditional least squares approach.

For each earthquake we must compare the relative magnitudes of the measured delay times with the relative magnitudes of the calculated delay times. A direct comparison cannot be made because the measured delays are subject to a source bias, equivalent to the E_j of Equation 4.24.

The first task, in forming the objective function value, must therefore be to remove the "d.c. bias" from both the measured and the calculated delays. This is done by subtracting the weighted means. Thus if the d_{ij} and d_{ij}'

are the measured (raw) and calculated delay times respectively and w_{ij} is the corresponding onset weight as described in Chapter 4 at the i^{th} station for the j^{th} event we form

$$E_j = \sum_i w_{ij} d_{ij} \Big/ \sum_i w_{ij}$$
$$E_j' = \sum_i w_{ij} d_{ij}' \Big/ \sum_i w_{ij} \qquad (6.37)$$

The relative delays are then represented by the differences, thus

$$r_{ij} = d_{ij} - E_j$$
$$r_{ij}' = d_{ij}' - E_j' \qquad (6.38)$$

The weighted r.m.s. residuals, F, can be formed thus

$$F = \sum_{i,j} w_{ij}(r_{ij} - r_{ij}')^2 \Big/ \sum_{ij} w_{ij} \qquad (6.39)$$

This is the objective function which is to be minimised by the procedures described in Section 6.8. Where the theoretical delay cannot be calculated, for one or other of the reasons outlined in Section 6.5, the corresponding terms are left out of the summations in Equation 6.39. This is equivalent to setting the corresponding value of w_{ij} to zero.

The objective function has no dependence on the source components of the raw delays. It would be possible to introduce a term dependent on the values of the $E_j - E_j'$ into the expression for F, and thus attempt to relate the measured and calculated delays in an absolute sense. However, the possibility of systematic errors and/or bias existing within the measured delays makes the inclusion of such a term undesirable.

This expression for F is entirely analogous to the calculation of F_W in Equation 4.30, which is the objective function minimised in forming the station delays. Thus the minimum value of F, obtained by the present method, should be compared with the value of 0.127 sec obtained for F_W in Chapter 4. A lower value would indicate a superiority of the ray tracing models over the models derived from the simple station delays calculated in Chapter 4.

6.7 The MHUMP Subprogram

To perform all the ray tracing, theoretical delay time and objective function calculations, a subroutine, called as "FCN" but here referred to as MHUMP, was written in FORTRAN for use on NUMAC. The subroutine is designed to be called from the non-linear optimisation package, MINUIT, which is described in the section following. The subroutine is listed, and the inputs to it described, in Appendix 6.

Among the arguments of the subroutine is an array, U, which supplies it with values of the model parameters, and IND, the value of which indicates the action required.

The first call to MHUMP (IND=1) directs it to read all input data from disk file, or equivalent device. The data read consist of the velocity structure, the station names and coordinates, the weight values for each onset weight code (these are as estimated in Chapter 4) and the measured delay times. During optimisation (IND=4), the subroutine calculates a value of F each time it is called, based on the values of the model parameters presented to it.

In the output mode (IND=3), the calulations are performed as for optimisation, but the subroutine goes on to list, event by event, measured delays, the calculated delay, the values of the r_{ij}, E_j, r_{ij}' and E_j'. Other output information includes the coordinates of the points where the rays start at the base of the anomalous zone, and where they intersect the upper interface. Information calculated and listed for each station includes the weighted mean of the residuals, R_i, and the mean calculated delay times, D_i. These are calculated using

$$R_i = \frac{\sum_j w_{ij}(r_{ij} - r_{ij}')}{\sum_j w_{ij}} \tag{6.40}$$

and

$$D_i = \frac{\sum_j w_{ij} r_{ij}}{\sum_j w_{ij}} \tag{6.41}$$

Clearly, the R_i should be small for closely fitting models, large values for particular stations indicating a misfit in the corresponding regions. The D_i should match the station delays as calculated in Chapter 4, except possibly for a d.c. shift.

In the plotting mode (IND=7), the calculations for F are performed as for optimisation, after which the subroutine comes under the control of additional commands inserted into the MINUIT command sequence. MHUMP can draw vertical profiles between selected points to show the shape of the anomalous zone, and how it is embedded within the horizontal layers of the unperturbed structure. Each region is annotated with its assigned seismic velocity. Maps can also be drawn of selected areas, with the depth to the upper interface optionally contoured. Alternatively, or additionally, the positions where the real rays enter and/or leave the anomalous zone can be plotted. A facility is also provided whereby only the exit points are plotted, but with symbols whose sizes are proportional to the magnitudes of the delay time residuals, and whose shape and colour represent the polarity. This latter option is intended to illustrate if and where the model is seriously inconsistent with the data.

6.8 The MINUIT Non-Linear Optimisation Package

The optimum value of F cannot be found by analytical techniques, so an alternative procedure must be used. The most straightforward approach is to evaluate F at points on a rectangular grid in hyperspace. Since at least three points on each of the 24 axes would have to be tested before a minimum could be reliably identified, F would have to be evaluated at least 2.8×10^{11} times. MHUMP, even when compiled to produce optimum run-time code, requires about two seconds of CPU time to calculate each value of F with the DKSP data, and would require some 18,000 years to search through even this simple grid.

Fortunately, the general problem of finding minimum values of difficult n-dimensional functions, has been tackled by a number of workers. Various "non-linear optimization" techniques have been found which are considerably more efficient than searches over rectangular grids (e.g. Rosenbrock, 1960; Nelder and Mead, 1964; Davidon, 1967; James, 1967).

James (1967) describes the Monte Carlo method, which is essentially a trial and error method. For each trial the values of the n variable parameters are chosen randomly with uniform distributions centred on the previous best value, and with widths equal to the estimated errors. This method allows a rapid search of the hyperspace around the initial point, and will usually find the approximate location of a minimum, providing sufficient calls are made.

Other methods attempt to define the behaviour of the objective function more precisely, and may be called derivative methods. The Davidon variable matrix algorithm (Davidon, 1967) estimates the quadratic part of the function, by use of a covariance matrix. An approximate covariance matrix is from values of F at points around the initial point. During each iteration, F is calculated, and the estimated position of the function minimum calculated from it and the covariance matrix. During each iteration the covariance matrix is also refined. This method converges exactly in n iterations if the function is quadratic, and is very fast near minima. However, the function must be reasonably well behaved, or the method becomes unstable.

The method devised by Nelder and Mead (1964) is also a derivative type, although derivatives are not explicitly formed. It relies on the creation of better and better simplexes (n+1 sided polygons) which move along the line of steepest gradient to engulf and contract in upon the minimum. The initial simplex is formed by coordinate variation. During each iteration, either the worst point of the existing simplex is replaced by the estimated minimum along a line joining it and the centre of gravity or the simplex is contracted linearly or a new simplex formed, based on the best existing point. This method is very stable, and converges rapidly in regions far from the minimum. Nearer the minimum, it is not as rapid as the Davidon algorithm.

These three methods have been built into a single non-linear optimisation package, MINUIT (James and Roos, 1971), which is available on NUMAC. This program calls the user written subroutine FCN (in this case MHUMP), providing it with parameter values. FCN then returns an objective function value. When running MINUIT, starting values and step sizes (estimated errors) for each of the parameters must be input. If the assigned step size is zero, the corresponding parameter is fixed at its initial value. Additionally, lower and upper bounds for any of the parameters may be specified. A command sequence then directs MINUIT as to which optimisation procedure to use, and the number of trials (calls to FCN) to be made. The Monte Carlo method was used to obtain a rough position of the minimum, and the simplex method used to locate it more precisely. The Davidon algorithm could not be used, as the objective function is too poorly behaved to allow the calculation of an initial covariance matrix.

Some 600 values of F may be calculated in a single run (the maximum CPU time limit on NUMAC is 1200 secs). This is sufficient to allow about eight parameters to be optimised in a single run. In practice, therefore, a succession of runs was made, varying a few of the parameters at a time.

6.9 Optimised Models

Initial models were set up, based on the hump parameter values given in Section 6.2.

Optimised models were obtained for only two values of V, 7.5 and 7.0 km/sec, lack of time precluding further investigations. The parameter and objective function values for these models are given in Table 6.1, and the depth to the upper interface contoured in Figures 6.6 and 6.7. Solid contours are drawn over regions which are properly controlled by the data. The dotted contours represent the extrapolation based on the assumed form of the upper interface. Sections along the flank profile of Chapter 5 are illustrated in Figure 6.8.

The sections, especially that for the 7.5 km/sec model, indicate the same features as are present on the combined

TABLE 6.1

PARAMETER VALUES FOR OPTIMIZED MODELS

	PARAMETER		VALUE	
	ANOMALOUS ZONE SEISMIC VELOCITY	(km/sec)	7.5	7.0
1	Latitude of Ethiopian hump	(deg N)	8.0	8.0
2	Longitude of Ethiopian hump	(deg E)	38.0	37.9
3	Height of Ethiopian hump	(km)	170.0	123.6
4	Radius of Ethiopian hump	(km)	300.0	239.9
6	Depth to base of anomalous zone	(km)	221.8	141.7
7	Latitude of Main hump	(deg N)	-0.30	1.24
8	Longitude of Main hump	(deg E)	35.59	35.98
9	Height of Main hump	(km)	107.4	61.1
10	X-Dimension of Main hump	(km)	129.1	115.8
11	Y-Dimension of Main hump	(km)	600.0	788.4
12	Orientation of Main hump	(deg)	12.7	12.7
13	Latitude of Crustal hump	(deg N)	-0.61	-0.64
14	Longitude of Crustal hump	(deg E)	36.24	36.27
15	Height of Crustal hump	(km)	114.6	96.6
16	X-Dimension of Crustal hump	(km)	27.2	20.5
17	Y-Dimension of Crustal hump	(km)	61.8	73.1
18	Orientation of Crustal hump	(deg)	-20.0	-22.3
19	Latitude of Kilimanjaro hump	(deg N)	-3.10	-3.10
20	Longitude of Kilimanjaro hump	(deg E)	37.10	37.10
21	Height of Kilimanjaro hump	(km)	97.5	46.2
22	X-Dimension of Kilimanjaro hump	(km)	86.2	35.6
23	Y-Dimension of Kilimanjaro hump	(km)	146.3	142.7
24	Orientation of Kilimanjaro hump	(deg)	37.6	44.9
	OBJECTIVE FUNCTION VALUE	(sec)	0.155	0.165

FIGURE 6.6

CONTOURED UPPER SURFACE FOR 7.5 KM/SEC

OPTIMIZED MODEL

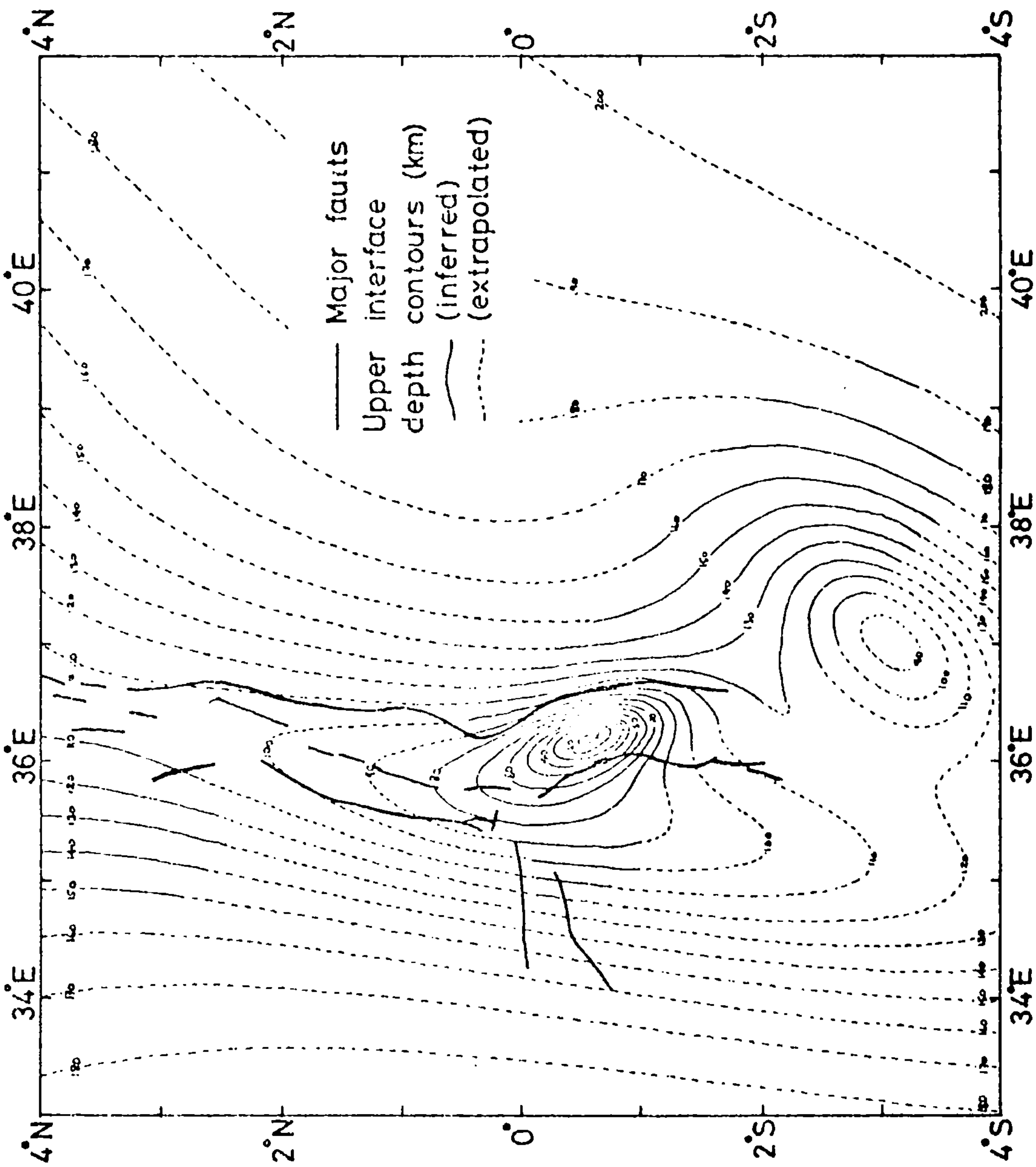

FIGURE 6.7

CONTOURED UPPER SURFACE FOR 7.0 KM/SEC

OPTIMIZED MODEL

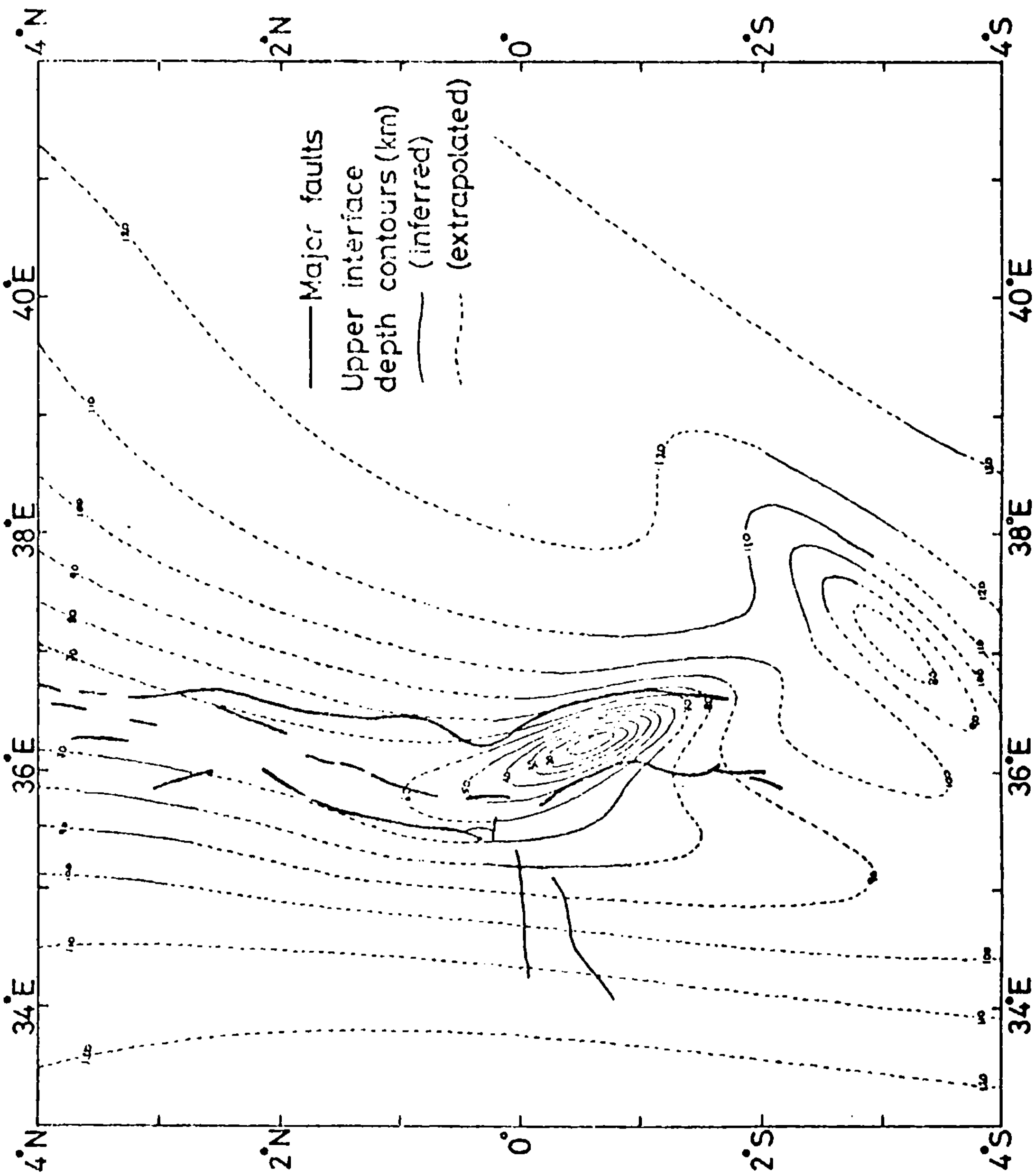

FIGURE 6.8

SECTIONS THROUGH OPTIMIZED MODELS

ALONG FLANK PROFILE

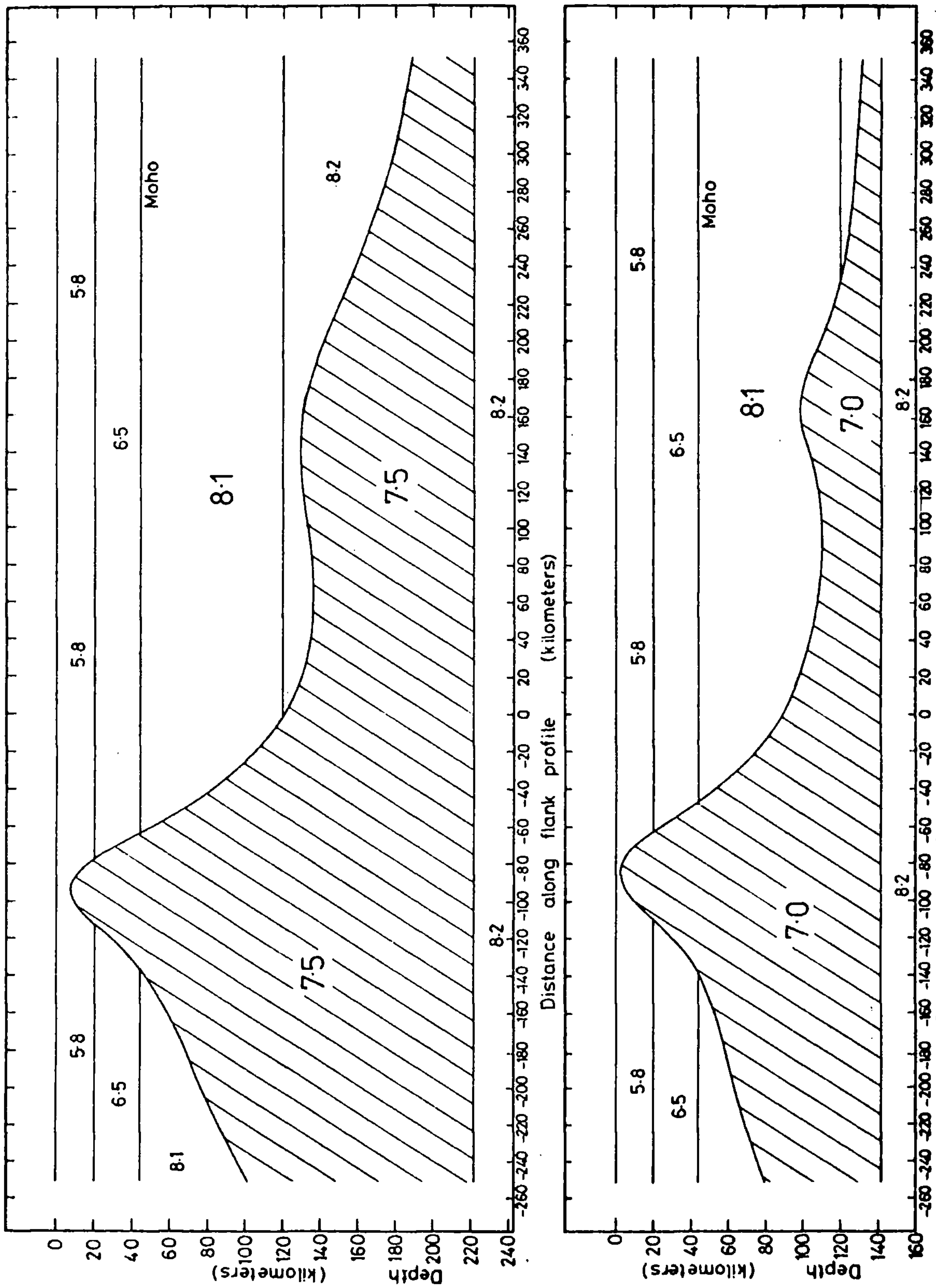

two-dimensional interpretation, model G, proposed in Chapter 5. The depth of the base of the zone is almost the same, about 220 km, and the eastern (Kilimanjaro) hump is clear on both, although rather thicker (95 km) on the three-dimensional model than for model G (55 km). The crustal part of the anomalous zone has approximately the same width (30-50 km), at the base of the normal crust, in the three-dimensional models as in model G, and is elongated in the direction of the local Bouguer anomaly ridge. Thus the three-dimensional models tend to confirm the two-dimensional profiles obtained in Chapter 5.

6.10 Accuracy of the Optimised Models

The two three-dimensional structures proposed are the best that have been obtained in a series of many computer runs, involving the testing of about 18,000 models and consuming some 5 hours total of CPU time. The objective function values obtained, are 0.155 sec for the 7.5 km/sec model and 0.165 sec for the 7.0 km/sec model. These optimum values are still above the 0.127 sec value obtained for the simpler calculation of station delays. Continued optimisation may reduce the minimum values slightly, but is unlikely to reduce them below 0.150 sec. Despite the rather high values obtained, we may examine the reliability of the the solutions by examining the behaviour of F around the minimum. Al-Chalabai (1971) used computer drawn sections of objective function hyperspace to illustrate the non-uniqueness of gravity models. We follow the same course here by contouring F against pairs of parameters. For each of these plots the other parameters are held at their optimum values. Several of these plots are presented in Appendix 7.

These plots, being restrained to two dimensions, can only give a glimpse of the real complexity of the hyperspace. However, certain features are revealed, and we may use a method given by Shuey (1974) to delineate regions of confidence on the plots. The contour corresponding to a particular confidence level is given by the equation

$$F = F_o\{1 + n(N-n)^{-1}f_{n,N-n}(1 - a)\}^{1/2} \qquad (6.42)$$

where n is the number of parameters, N is the number of observations and $f_{n,N-n}(1-a)$ is a fractile of the variance-ratio or F-distribution. (Equation 6.42 appears different to that given by Shuey, by the inclusion of the square-root. In fact the equations are identical. Shuey's F is proportional to the variance or sum of the residuals squared, whereas F is here proportional to the square-root of that quantity.) Since the 111 event residuals are also effectively adjustable parameters, the total number of parameters, n, is 135. The number of observations, N, is the number of raw delay times, 444. Using a 70% confidence limit, corresponding roughly to the usual standard error, and the statistical tables due to Abramowitz and Stegun (1964), a contour level at

$$F_{70\%} = 1.21\ F_o = 0.190 \text{ sec} \qquad (6.43)$$

is obtained.

Regions within the 0.190 sec contour level are statistically indistinguishable from the optimum model at the 70% confidence limit. This contour level is hatched on the plots which are all for the 7.5 km/sec model. The poor accuracy revealed by this analysis, and the trade-off which exist between some parameters, is clear from an examination of these plots and will be described breifly here.

The Ethiopian hump is largely uncontrolled by the data, as expected. Its centre may be placed anywhere on Plot 1, and Plot 2 demonstrates the complete trade between its radius and height. Probably, this hump only contributes a small, nearly d.c. component, to the anomalous zone thickness which, if it were removed, could be entirely compensated for by slight increases in the heights of the other humps.

The Main hump parameters are not well controlled either. Plot 3 shows that the humps centre may lie anywhere within a 1.5° wide band with a SSW-NNE trend. The X-dimension may take any value between 55 km and 180 km, and the only restriction on the Y-dimension is that it shall not be less than 200 km (Plots 4 and 5). Plots 6, 7 and 8 show that the orientation of the main hump may lie between -5° and 50°, and that a rather complicated trade off relationship exists between it and other parameters.

The crustal hump is, unfortunately, not well controlled either. Its centre could lie anywhere to the north, or more than 150 km to the west of the optimum position (Plot 8). Plots 9 and 10 indicate that the X-dimension is less than 35 km, and that some trade off exists with the Y-dimension which is poorly controlled (Plots 9 and 11). Plots 12 and 13 show that the crustal hump must have an approximately NW-SE orientation, but a range of at least 45° is allowed.

An alternative to the optimum position of the Kilimanjaro hump is indicated by the two confidence regions of Plot 14. The two positions are mirror images of each other in the line of the flank profile. This seems to indicate that the directional information in the arrivals at the flank stations and the limited data from Station 31 are unable to resolve the NE-SW components of dips beneath them. Both confidence regions are quite well defined, having an error radius of about 40 km. Compared with the other humps, the size of the Kilimanjaro hump is also fairly well controlled, errors in the X- and Y-dimensions being about 50% (Plot 15). The orientation of this hump is not particularly well defined, but a direction in the northeast quadrant is certain (Plots 16, 17 and 18).

Plots 19 and 20 indicate that the depth to the base of the anomalous lies between 160 km and 260 km (for V=7.5 km/sec). A degree of trade-off between the depth of the base and the heights of the crustal and main humps is indicated in these plots. Some trade-off between the heights of the crustal and main humps is also indicated in Plot 21.

It is unfortunate that the model parameters are so poorly defined. The poor resolution results mainly from the deficiencies in the theoretical delay time calculations, as already discussed (Section 6.5). Errors in some of the theoretical delays, amounting to about 1.5 sec are likely to exist, and it is obvious that that just a few of these will increase the objective function values significantly.

Inflexibility of the model may also contribute to the poor resolution. However, since the models derived here show all the main features of those derived in Chapter 5, it is unlikely that this is a major problem. The region where such inflexibility is most likely to be a problem is in forming the "valley" between the Main and Kilimanjaro humps.

The value obtained for F_O, 0.155 sec, is significantly larger than the value of 0.127 sec obtained for the equivalent F_W when calculating station delays in Chapter 4. By this criterion alone, the three-dimensional models must be considered inferior to those derived from the station delays, and assuming horizontal layering. Jackson (1976) has pointed out that if r.m.s. residuals (objective function values) are in excess of those expected, undermodelling is indicated. This is the case here, where the expected value, ϵ_W, calculated in Section 4.5, is only 0.114 sec. In such cases, better models should be sought, either by increasing the number of parameters, or by adopting an inherently more realistic approach.

6.11 Suggestions for Improvements

Clearly, the ray tracing method described here must be improved before it can yield the lower objective function values which are the criterion of merit. Lack of time prevents the author from making improvements himself, but some suggestions are made here for the benefit of anyone wishing to continue this work.

1) An improved iterative technique should be sought, so that theoretical delays are calculated correctly, taking account of multi-path arrivals. Failing this, some method of detecting the wrongly calculated delay times should be devised. If a better method cannot be found, those delays for which residuals are larger than (say) two standard deviations might be removed. The last suggestion is, in the author's opinion, a somewhat underhand trick, but may be the only way of improving the method. Alternatively, an absolute error estimator for the objective function might be devised.

2) The form of the upper surface may be insufficiently flexible. The author is aware that the $1/(1+x^2)$ function, which forms the basis of the humps, is rather broad at its base, making difficult the construction of valleys, such as exists between the main and Kilimanjaro humps. The narrower Guassian function, based on $Exp(-x^2)$, might prove better.

3) Perhaps the ray tracing procedure, relying heavily as it does on an optical type approach, is fundamentally

inappropriate. Smooth variations in velocity would be more realistic, and it has yet to be shown that the type of model proposed here can reproduce the behaviour of such a structure. Even models with smooth variations in velocity may be unrealistic. If the Gass theory of rift evolution involving penetrative convection pertains to the upper mantle beneath the Gregory rift (see Chapter 7), randomly distributed pockets of more highly fused material might exist. Treating the anomalous zone as a random medium might then yield better results, as has an investigation of the slowness anomalies obtained at LASA (Capon, 1974).

6.12 Conclusions

A three-dimensional modelling technique has been developed and described. The two optimised models obtained, assuming uniform anomalous zone velocities of 7.5 km/sec and 7.0 km/sec, embody all the main features of the two-dimensional models proposed in Chapter 5. The thickness varies inversely with anomalous zone velocity, as expected.

However, the minimum objective function values obtained are larger than expected. Moreover, the very wide volume of objective function hyperspace enclosed by the 70% confidence level illustrates the poor precision with which the model parameters are determined.

The technique is capable of refinement to overcome the difficulties described above, and suggestions have been made for improvements.

CHAPTER 7

DISCUSSION AND CONCLUSIONS

7.1 The Present Work in relation to Previous Studies.

Several models have been proposed to explain the observed delay time variations over the southeast flank of the Kenya dome and the central portion of the Gregory rift. These models vary slightly in shape but show the same broad features. A substantial low velocity zone exists within the upper mantle beneath the Gregory rift, and this penetrates the base of the crust along a narrow zone confined to the rift axis. The intruded part of the crust has a higher average seismic velocity than normal.

Moving southeastwards away from the culmination of the Kenya dome, the low velocity zone is attenuated; that is, either the thickness decreases, or the velocity contrast with normal mantle decreases, or both. A subsidiary intensification exists about 200 km to the southeast of the culmination of the dome, probably linked with Mt. Kilimanjaro.

A uniform velocity, V, has generally been assumed for the anomalous zone, primarily to facilitate interpretation. A flat base for the anomalous zone has also generally been assumed, and this is justified in Section 5.4. The same assumptions were made by Forth (1975) and Long and Backhouse (1976) when deriving models from slowness anomaly measurements at Kaptagat, for the anomalous zone under the northwest flank of the Kenya dome. Figure 7.1. shows the combined model G derived in Chapter 5 (V= 7.5 km/sec) alongside a NW-SE section of the Kaptagat model (V= 7.3) given by Long and Maguire (1976). The two models have been combined where they overlap under the western escarpment. (The overall section is for a profile running NW-SE across the dome, but in the central portion the profile runs E-W across the rift.)

The Kaptagat model differs from the DKSP models in that its upper interface has a steeper average dip and extends deeper into the upper mantle. The base of its anomalous zone is placed deeper, and would have to be deeper still if the same anomalous zone velocity were used as for the DKSP models. Moreover, the base of the anomalous zone is placed deeper on the Kaptagat model than on the DKSP model. These discrepancies would be greater if the same anomalous zone velocity had been assumed for the two studies. These differences are significant and should be explained, as an approximately symmetrical shape might be expected for the anomalous zone.

The teleseismic slowness measurements at Kaptagat are related to dips, not to depths or thicknesses. There is considerable scatter on measurements from groups of closely spaced events, which would imply corresponding errors in the assigned dips. The upper surface is formed by continued northwestward extrapolation from an assumed intersection

FIGURE 7.1

KAPTAGAT (NORTHEAST FLANK) AND DKSP (RIFT AND SOUTHEAST FLANK) MODELS OF THE KENYA DOME.

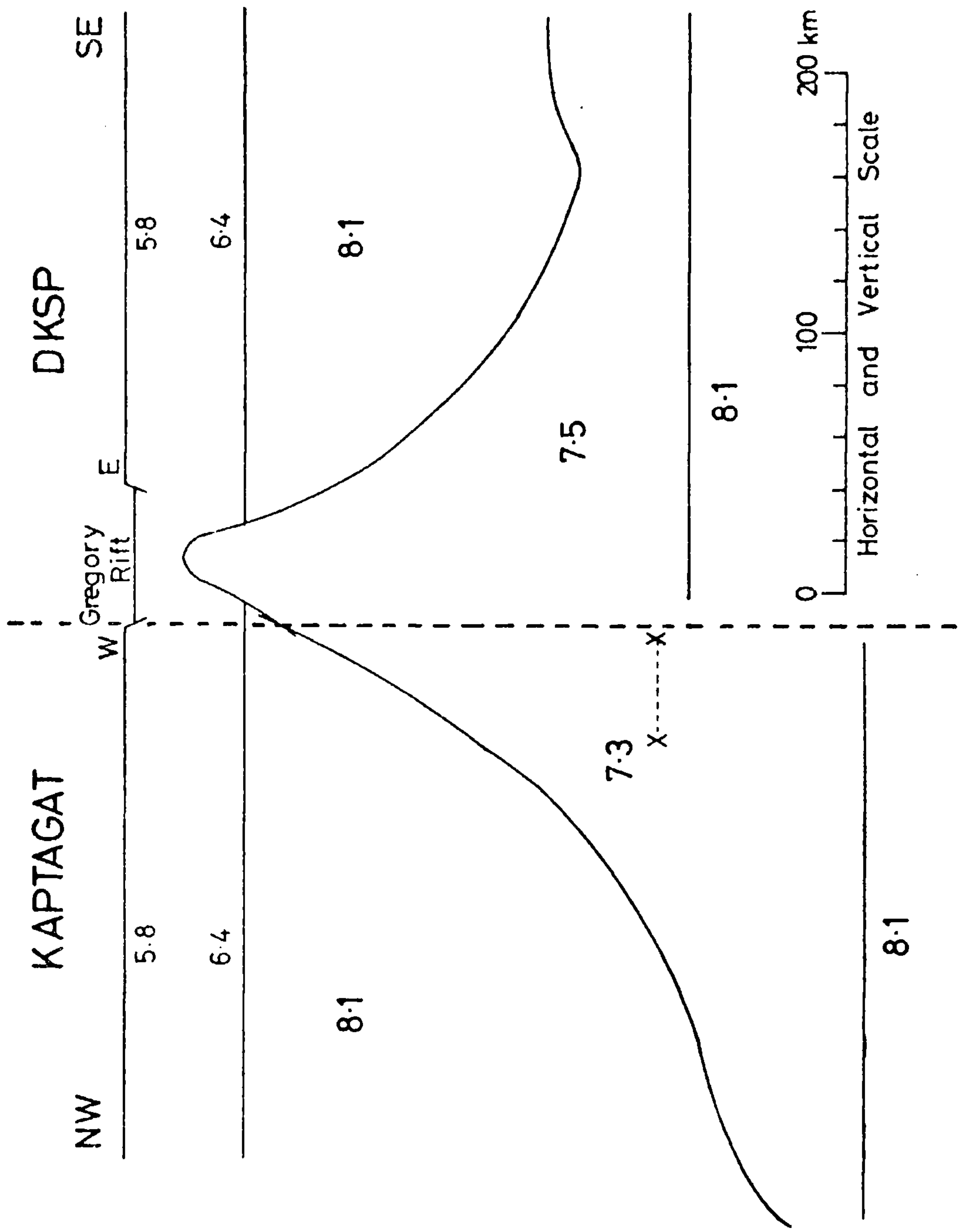

with the normal Moho 30 km west of the rift axis (Long and Backhouse, 1976). Errors in this process will tend to increase northwestwards, and may give considerable errors in the inferred depths.

The lower boundary of the zone is drawn on the diagram given the anomalous zone thickness of 200 km inferred under KAP by Long and Backhouse (1976). This value is derived from relative delay time measurements between KAP and BUL (2.4 0.7 sec), assuming normal upper mantle velocities beneath BUL and assuming that crustal differences beneath the two stations can be ignored. However, if we accept that the crust beneath KAP has a thickness of 44 km (Maguire and Long, 1976), and assume that the crust under BUL has a structure typical, especially in thickness, of southern Africa (e.g. Hales and Sacks, 1959), a crustal contribution of 1.1 sec may be present in the delay time difference. A reduction of the measured relative delay time by this amount would result in a reduction by 80 km in the thickness of the anomalous zone under KAP, bringing its lower boundary up to the depth marked X---X on Figure 7.1. This gives a much better correlation for the two depth estimates of the lower boundary. The correlation would be improved still further if the same velocities were used for the Kaptagat and DKSP interpretations.

Similar anomalous zone thicknesses for the northwest and southeast flanks are indicated by the very similar delay time measurements given by Long and Backhouse (1976) for NAI and KAP relative to BUL. Thus differences between the Kaptagat and DKSP models out to about 150 km from the culmination of the dome are probably due to inaccuracies in extrapolation of slowness data than real structural differences. We may conclude that the seismic structure is symmetrical within this region. Beyond about 150 km, there is the Kilimanjaro thickening to the southeast which seems to have no counterpart in the northwest.

In Chapter 5 it was inferred that the crust along the rift axis was intruded to within 20 km of the surface (assuming V=7.5 km/sec). This is in good agreement with the results of the refraction experiment performed in the northern sector of the Gregory rift (Griffiths et al, 1971) and indicates continuity and uniformity of the intrusion along the rift axis.

In view of the high correlation observed in this study between delay time variations and Bouguer anomaly variations (Section 5.7) it is not surprising that gravity models (Figure 1.8) and seismic models derived in this and the Kaptagat study show broadly similar shapes for the anomalous upper mantle zone and crustal intrusion.

The low seismic velocities and densities and the high conductivity observed for the upper mantle beneath the dome all indicate elevated temperatures or an increased degree of partial fusion (Bott, 1965; Anderson, 1967; Walsh, 1969; Duba et al, 1974). The increased degree of partial melting has given rise to the vast amount of magmatic activity and hence to the rift volcanics, and accounts for the existence of the zone of intrusion along the rift axis.

7.2 Further Observations and Discussion

This section is devoted to a few additional remarks which were omitted from previous chapters as not being directly relevant to their main lines of argument.

7.2.1 Correlation of Waveforms

Signals recorded at DKSP stations for individual events were in general very well correlated, at least over the first 2-6 cycles. This enabled the waveform matching technique to be used with confidence. However, close matches were not always obtained, even for large amplitude arrivals. Fairly often there was a hint of a superimposed second arrival, which sometimes had a different apparent velocity. Such an arrival is visible in Figure 4.1 as a difference in waveform shape about 3 sec after onset. Occasionally, more frequently at Stations 18 and 19 than at the others, the waveform at one or two stations would be sufficiently different that a match could not easily be obtained.

Similar behaviour seems to be observed at the large aperture seismic array (LASA) in Montana, USA. The waveforms illustrated in a paper by Iyer and Healy (1972) are easily matched over a distance of 200 km, comparable to the largest inter-station distances for DKSP. Mack (1969), on the other hand, shows that signals can vary significantly for seismometers located less than 20 km apart, and interprets the differences in terms of crustal variations over the array

The generally uniform appearance of DKSP waveforms, especially between rift and flank stations, would tend to indicate a degree of uniformity of crustal structure across the region. Perhaps closer examination of the waveforms, using spectral response ratios or similar techniques, might reveal significant differences, especially near the rift axis where this and other geophysical studies indicate large scale variations.

Waveform differences might be linked to multipath effects and the superposition of two or more arrivals, as suggested by the ray tracing illustrated in Figure 6.5. These effects might explain the poorly matched waveforms observed at Stations 18 and 19, which are located just where duplicated arrivals would be expected.

7.2.2 The Non-Random Distribution of Source Events

Figure 4.5 illustrates the distribution of events used in this study, and it can be seen that there is a considerable preponderance of events from back-bearings between 40° and 140°. Because the average ray direction for all events will slant towards the east, the pattern of station delays obtained in Chapter 4, where effectively vertical paths were assumed, will be offset slightly to the west of the corresponding subsurface structures. This may account for the 5 km westward shift in the delay time minimum relative to the Bouguer anomaly peak, as seen in Figure 5.9. Assuming an average eastward slant of 15° for the rays, this would imply an approximate minimum depth of 20 km for the anomalous zone, if refractions are ignored. This is in good agreement with the interpretations presented here, and the depth obtained for the 7.5 km/sec layer detected by Griffiths et al (1971). This westerly shift, increasing in magnitude for deeper regions of the anomalous zone, would tend to steepen the dips of eastward dipping interfaces and lessen those of westward dipping interfaces for the interpretations of Chapter 5.

Ignoring the effects of refraction is, of course, a gross over-simplification. The ray tracing diagram (Figure 6.5) shows that the pattern of delay time variations can be significantly distorted from the corresponding pattern assuming vertical rays and no refraction. Applying this diagram to the models derived, and noting the preponderance of easterly back-bearings, we would expect the eastern peak on the delay time curve of Figure 5.9 to be reduced in amplitude. This peak is poorly defined, as noted previously. The reason given in Chapter 5 was lack of stations in the area, but a contributary factor might be the effect just noted. This effect could also contribute to the low delay times observed at Stations 18 and 19, but is insufficient to account for them entirely.

7.2.3 The Effect of the Volcanic Overburden

Throughout this study, the effect of the volcanics overlying the basement in the region of the rift has been ignored. Low velocities are expected and these could, in part, explain the generally higher delay times in the rift region reltaive to the flanks, as already noted. The vertical delay time for a 2 km layer of 3 km/sec material is 0.42 seconds. King (1978) suggests a total thickness for the rift trough of 5.5 km, giving a delay time (assuming the same velocity) of 0.89 seconds. Thus if the volcanics really attain such thicknesses and have such low average velocities, they are bound to contribute significantly to the delay time variations. The largely unknown thicknesses of the volcanics, which have considerably lower densities than normal crustal rocks, also hamper reliable gravity interpretations.

To elucidate the upper crustal structure of the rift floor in the region of Lake Baringo, two small scale refraction lines were shot by Leicester University in 1975. The results are as yet unpublished, but a preliminary report has been received (Swain et al, 1978). The interpretation of the east-west line, between Lake Baringo and Chebloch Gorge, indicates a 2-3.5 km thickness of 3.7 km/sec material overlying 5.7-5.8 km/sec material. (There was no indication of the 6.4 km/sec refractor detected by Griffiths et al (1971), as had been expected, but the existence of this layer was not ruled out.) The 5.7-5.8 km/sec material is thought to be crystalline basement, and the 3.7 km/sec velocity is linked to the volcanics. These results suggest a deep basement, depressed to as much as 2.5 km below sea level, but this is hard to reconcile with basement outcrops seen only 10 km north of the central part of the line.

Clearly, more detailed work to determine the thicknesses of the volcanics would be highly desirable.

7.3 The Present Study and Theories of Rift Formation

The theory of thermal perturbation of and the upward migration of the lithosphere - asthenosphere boundary, as described by Gass in a number of papers (for example, 1972) has already been outlined in Chapter 1. Diagrams illustrating four main stages in the process, together with Gass' captions, are shown in Figure 7.2. There is a clear similarity between the anomalous zone inferred in this and other studies, and the zone of magma generation (high degree of partial melting) represented by stage b. This lends considerable weight to the Gass explanation.

Gass' theory also explains domal uplift and the observed evolution of volcanism from srongly alkaline basalts to transitional basalts and tholeiites. The domal uplift is entirely adequate to explain graben formation as the clay models of Cloos (1939) and finite element analysis of Neubauer (1978) demonstrate. Indeed these studies show well how a trough, limited in overall extent, with a splayed pattern of faulting at each end and the existence of

LEGEND OF FIGURE 7.2

SCHEMATIC REPRESENTATION OF MAGMA GENETIC AND TECTONIC STAGES IN TRANSCONTINENTAL RUPTURE

(a) Perturbation in asthenosphere; development of tabular magmatic body; doming of the surface and eruption of alkalic undersaturated basalts.

(b) Concentration of magmatic activity along major rift zone, attenuation of th lithosphere beneath the rift and eruption of transitional basalts within the rift.

(c) Continuing magmatic activity along the major rift zone elevates the mantle isotherms so that magma can equilibriate at very shallow deopths. With continued intrusion of basltic dykes along the fracture, the once contiguous lithosphere plates are separated.

(d) Idealized three-dimensional diagram to show how the magma genetic zone in (c) is elongate, and exists all along the rift zones.

(Gass, 1972)

FIGURE 7.2

(Gass, 1972)

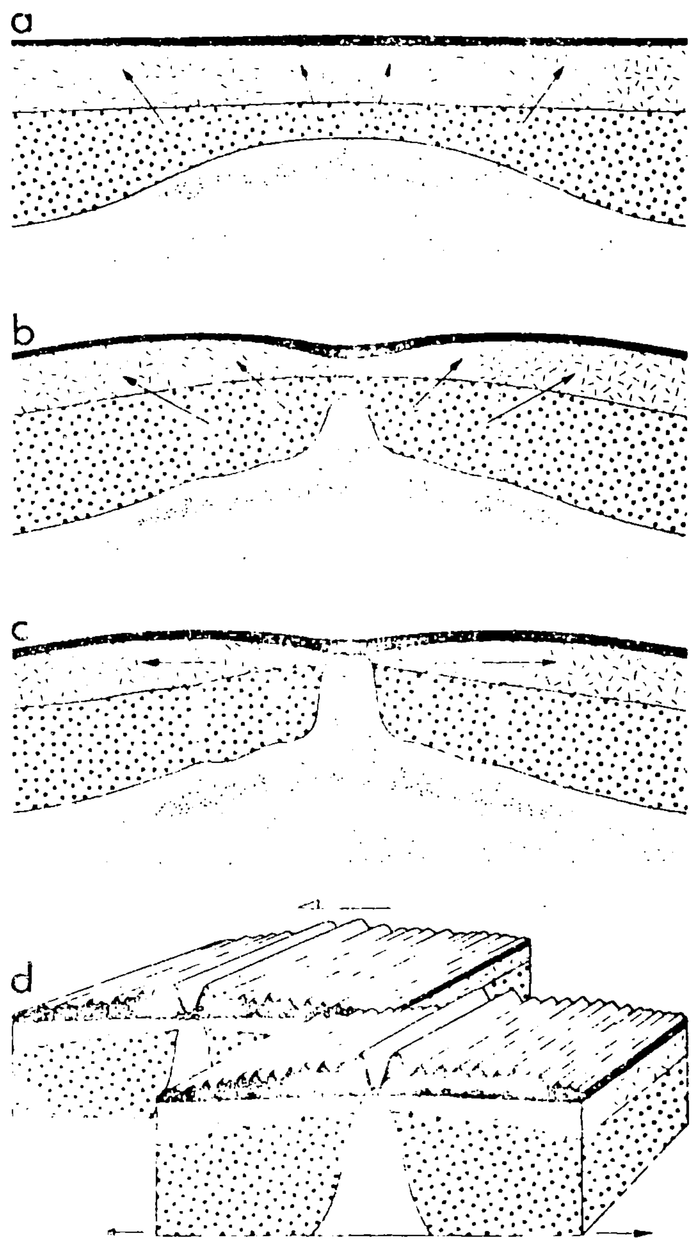

three-armed structures, as seen in the Gregory rift (Figure 1.2), may arise.

Gass does not specify the nature of the initial disturbances which might trigger magma genesis, but one could easily envisage some sort of mantle plume activity to initiate the disturbance.

Oxburgh (1978) argues that mantle plumes are insufficient of themselves to produce continental rifting. Divergent flow at the top of the plume can induce shear stresses of no more than 10 kbar at the base of the lithosphere, and this is insufficient to cause fracture. The heating effect, if conduction is the only form of heat transfer, of a mantle plume on the base of a plate is also of limited extent. A plate moving at a typical speed of 4 cm/yr over a 400 km wide plume would only be significantly heated in the lower 20 km.

Nevertheless, such heating would be sufficient to induce litospheric thinning if Gass type instability exists in the upper mantle. This would be especially true if the plume were to inject volatiles into the lithosphere. The effect of these would be to depress the melting point, and possibly to increase the temperatures within the lithosphere. If this were the case, then a significant increase in the degree of partial melt could take place without a significant temperature rise (Oxburgh, 1978).

Thermal perturbation seems to be such a significant factor in rift formation that serious doubt must be cast on any theory in which lithospheric stresses are the primary cause. The membrane tectonic theory of Oxburgh and Turcotte (1974) shows that lithospheric stresses sufficient to cause fracture can be induced by plate motions. However, the mechanisms proposed for the generation of magma are implausible. Oxburgh (1978) suggests that either volatiles rise to the surface from the asthenosphere through cracks in the lithosphere, or that melting is induced in localized zones of strain in the lithosphere. Griggs et al (1960) have shown that above 500°C and 5 kbar pressure (15-20 km depth) almost all rocks are ductile, and on this basis it is hard to imagine cracks and large strains developing.

The main evidence in favour of membrane tectonics as an explanation for rift formation in East Africa is the southward migration of the onset of volcanic activity, due to the northward motion of the African plate. However, this is not an obstacle to the Gass theory, since the northward migration of the African plate over some stationary, possibly variable, heat source would have initiated a series of localized disturbances corresponding to the Afro-Arabian triple junction, the East African Plateau, and a newer disturbance in central-southern Africa. The existance of the last is indicated by by well defined zones of considerable seismicity (Fairhead and Girdler, 1972; Fairhead and Henderson, 1977) and anomalously high heat flow (Chapman and Pollack, 1975, 1977)

The Gass model is eminently applicable to the

Arabian-African rift systems. In the case of the Red Sea and the Gulf of Aden, the process has gone to completion with the formation of active spreading axes. In Southern Ethiopia, Kenya and Tanzania we see an earlier stage, preceeding continental rupture. In central-southern Africa the process is at an even earlier stage. It is hard to resist the idea that a new ocean is being initiated along these rift and incipient rift zones.

However, before active spreading can take place, isolated magmatic regions must be linked. The degree to which the Ethiopian and Kenyan magmatic centres are linked is not at all certain. The Kaptagat models (Forth, 1975; Long and Backhouse, 1976) suggest that the Kenya zone is limited in its northward extent, but the interpretations do not extend to the northeast quadrant. Micenko (1977), on the basis of slowness anomaly measurements of uncertain accuracy made from recordings at Station 50, suggests a tenuous connection at depth between the two zones. The three-dimensional models proposed in Chapter 6 tend to support this conclusion, but this is as likely to be a spurious consequence of the inclusion of the Ethiopian hump as a reflecton of the data.

7.4 Suggestions for Further Research

7.4.1 The Upper Mantle Structure between Domes

Possibly the most vital question outstanding is whether or not the African continent is about to split. This question is most likely to be resolved by geophysical studies to elucidate the upper mantle stucture between the Kenya and Ethiopia domes and to the southwest of the east African Plateau, where incipient rifting is thought to be taking place (Fairhead and Henderson, 1977; Chapman and Pollack, 1977). A two-pronged attack, using gravity and seismic observations, would yield useful, complementary information. The delay time method has proved effective for the Kenya dome and there is every reason to believe that a network of independent seismic stations would yield equivalent useful information in these areas. The waveform matching technique works so well that reliable determinations of relative delays can probably be obtained with as few as two or three well recorded events at each station, requiring just a week or or two's occupation of each site instead of the 20 weeks averaged for DKSP. With reliable recorders, and access by air to remoter areas, a greater number of sites could be occupied, giving closer coverage than obtained for DKSP. Local monitoring of earthquake activity and recording quality would be essential to an efficient operation. Further information on slowness anomalies could be obtained by having small arrays included within the network. Arrays of 5-10 km diameter, using telemetered links to a central recorder, would be ideal.

7.4.2 Upper Crustal Structure of the Gregory Rift

Domal uplift is an important part of the Gass theory of rift formation, and doubt has been cast on the extent to which the level of the basement has been raised (King, 1978). To aid gravity and delay time interpretations and resolve the conflict about the extent of doming, further information is required on the upper crustal structure near and within the rift.

Seismic reflection work could easily penetrate the volcanic pile and provide detailed mapping of the thickness of the volcanics. Unfortunately, the cost of acquiring and processing relection data is probably well beyond the means of most British academic institutions. Refraction work is the only alternative, but refraction studies for the Gregory rift have so far yielded rather unsatisfactory results, mainly due to the local noise and to logistical difficulties. Nevertheless further refraction work along the lines of the KRISP experiment should be undertaken.

7.4.3 Crustal Structure to the East of the Gregory Rift

The Kaptagat experiment has yielded a model for the crustal structure to the west of the Gregory rift (Maguire and Long, 1976). Swain (1979) has noted that the gravity field across the margin of the East African plateau and

Gregory rift has a component which is inexplicable from the seismic structure deduced from Kaptagat. This "regional" gives lower Bouguer values to the west than the east, and might be due either to a layer of anomalous upper mantle material under the plateau (see the gravity models of Sowerbutts (1969), Darracott et al (1972), Khan and Mansfield (1971), Figure 1.8), or to an eastward thinning crust. Analysis of events originating locally (especially in the Oloitokitok area on the northeast flank of Mount Kilimanjaro (Johns, 1977)) and recorded at the DKSP stations might yield a model for the crustal structure to the east and enable this question to be resolved.

7.5 Conclusions

Chapters 2, 3 and 4 described the acquisition of recordings of teleseismic P-wave arrivals and their reduction to give station delays for the DKSP network.

In Chapter 5 the variation in delay time was discussed, and it was shown that the major part of the variations could only be explained by the presence of anomalously low velocity material within the upper mantle.

The delay time variations along the profile running southeastwards from the culmination of the Kenya dome show that the anomalous zone extends 270 km laterally in this direction. If the anomalous zone is modelled as a region of uniform velocity, it is clear from the delay time profile that it thins very rapidly away from the rift zone, but that the rate of thinning decreases farther away. A subsidiary thickening, thought to be linked with the magmatic activity responsible for Mt. Kilimanjaro, is clearly indicated by a local increase in delay time.

A dip in the generally high delay times for the rift valley stations, largely coincident with the rift axis, is shown to be due to a high velocity intrusion within the crust. Assuming that the velocity of the anomalous material is 7.5 km/sec, corresponding to the lower refractor detected by Griffiths et al (1971), and a depth of 44 km for the normal Moho, this intruson rises to about 20 km depth. The high velocity body is linked unambiguously with the anomalously dense body inferred from the axial Bouguer high. A possible offshoot of the main intrusion was detected, near the Kijabe section of the Kikuyu escarpment, and may approach the surface more closely than the main branch.

Assuming the same uniform velocity for both the crustal and upper mantle components of the anomalous zone, the combined flat bottomed model G was proposed. The depth of the base is tentatively placed at 220 km, but this may be in error due to a systematic error in the base line of the station delays.

Three-dimensional models were derived using the technique described in Chapter 6. Although the models gave similar sections to those inferred in Chapter 5, they were shown to be poorly controlled and therefore unreliable. Suggestions were made for improving the technique.

The models derived are consistent with upward perturbation of the lithosphere-asthenosphere boundary, and with subsequent injection of magma along the axis of the graben, which is formed by tension induced by crustal arching.

APPENDICES

APPENDIX 1

A NOTE ON THE DURHAM UNIVERSITY SEISMIC RECORDING AND PLAYBACK EQUIPMENT

This note describes the results of standard tests to determine the frequency response and dynamic range of the Durham three channel portable seismic recording equipment and associated playback electronics. The set tested has been used in the field in Iceland, Ethiopia and elsewhere, and is still in use.

A theoretical explanation is given for the observed poor flutter compensation of large amplitude signals played back at Durham.

Recording

Tests were carried out on a seismic recording set chosen at random after reconditioning by Departmental technical staff. The tape recorder was operated at 0.1 in/sec, the faster of its two design speeds. Correct operation of the set was verified, using its own comprehensive built-in monitoring facilities.

A sinusoidal voltage from an ADVANCE VLF function generator, type SG88, was input via an attenuator to the central seismic channel of the recorder. The amplified and frequency modulated signal was recorded on to the same 1/4 inch Agfa triple-play tape as is used in the field. Also recorded was encoded time from the internal clock and a standard, 100 Hz, clock-derived reference frequency. The latter is used to control tape speed on playback, and for flutter compensation. To test the frequency response an input voltage was selected to give approximately 75% at 1 Hz of the maximum signal obtainable without saturation. A one minute length of tape was recorded at each of a range of input frequencies varied between 0.01 Hz and 40 Hz. The dynamic range of the equipment was measured by recording a 1 Hz input over a range of voltage amplitudes. Both procedures were carried out at five different gain settings of the recorder's amplifier. Additionally, an input voltage was recorded to test the dynamic range at 8 Hz and a gain of 12800 (gain setting, n,=8). This was the gain used in Ethiopia, and the frequency was selected to represent the P phases of recorded Ethiopian local earthquakes.

Playback

The test tape was played back in the Durham seismic processing laboratory. Here the tape transport unit is the shell of a commercial NAGRA IV deck, modified to run at ten times the recording speed (i.e. 1 in/sec in this case). This speed is obtained directly from the standard reference frequency recorded on the tape, the deck motor being incorporated in a feedback loop to allow automatic compensation on playback for fluctuations of recording speed in the field. Demodulation is carried out by electronics designed and built within the Department.

The playback system was set up for optimum flutter compensation by adjusting the tape head of the NAGRA deck and the gain of the seismic signal demodulator. These adjustments must be made whenever a tape is to be processed. In this case they were facilitated by using a section of the test tape specifically recorded with no input to the seismic channel under test. The demodulated output was displayed on paper by means of a jet pen recorder. Paper records were made of the output signal both unfiltered and after various degrees of band-pass filtering accomplished by KEMO dual variable filters type VBF/8K.

Performance

To determine the frequency response the jet pen trace amplitude, A_f, was measured at each recorded frequency. The response in decibels, D_f, relative to the response at 1 Hz (trace amplitude A_1), was then calculated from the relation

$$D_f = 20 \log_{10}(A_f/A_1)$$

The resultant curves are shown in Figures A1.1 and A1.2, and the bandwidths are given in Table A1.1.

Attenuation rates at low and high frequencies are approximately 13 dB/Oct and 27 dB/Oct respectively. In the field the recording equipment is normally operated at a gain of 12800 or 25600 (n=7 or 8). At quiet sites gain 51200 (n=9) has been used. At high gains in particular the results shown here fall short of the published amplifier

FIGURE A1.1

LOW FREQUENCY RESPONSE OF THE SEISMIC PROCESSING EQUIPMENT

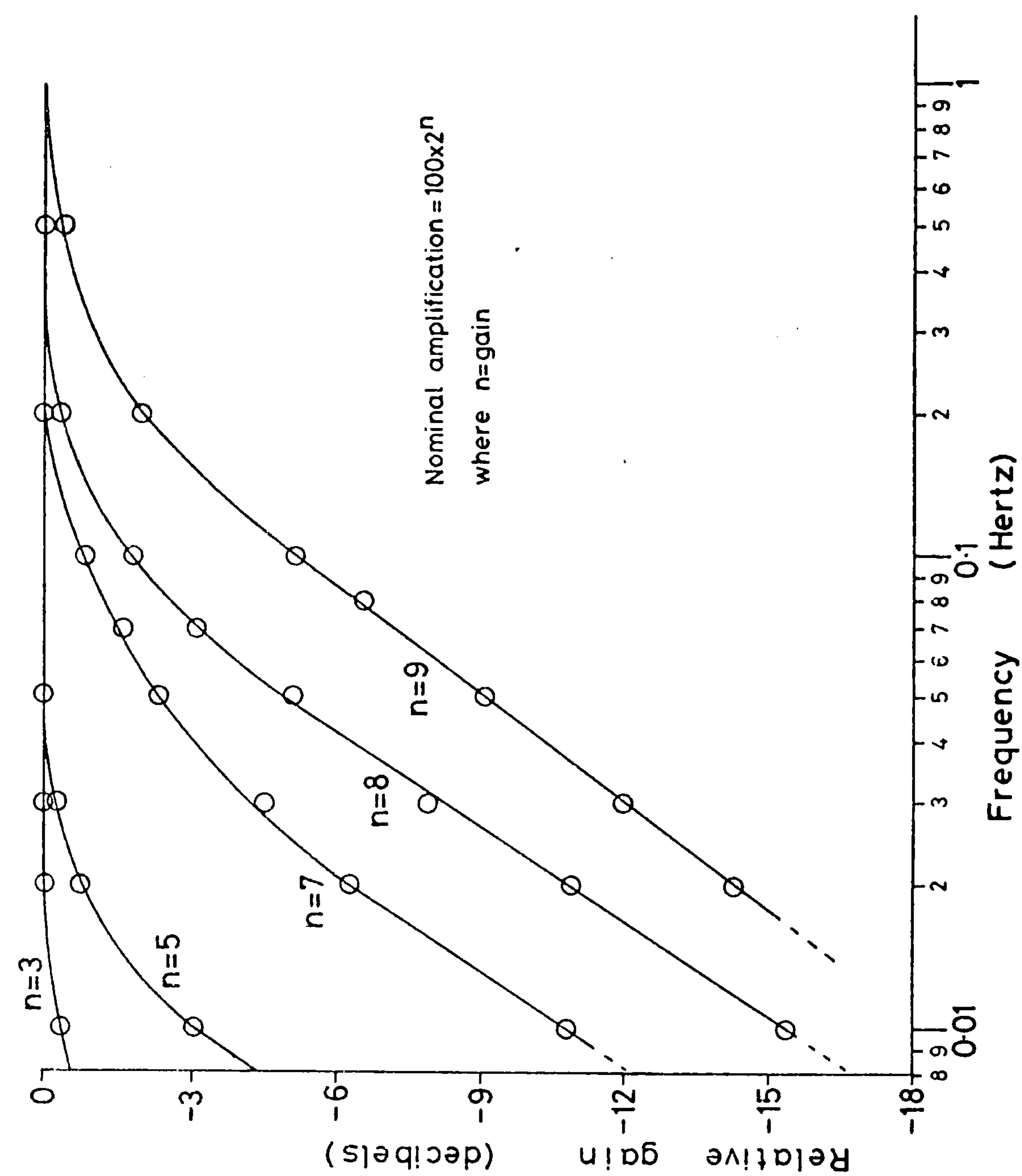

FIGURE A1.2

HIGH FREQUENCY RESPONSE OF THE SEISMIC PROCESSING EQUIPMENT

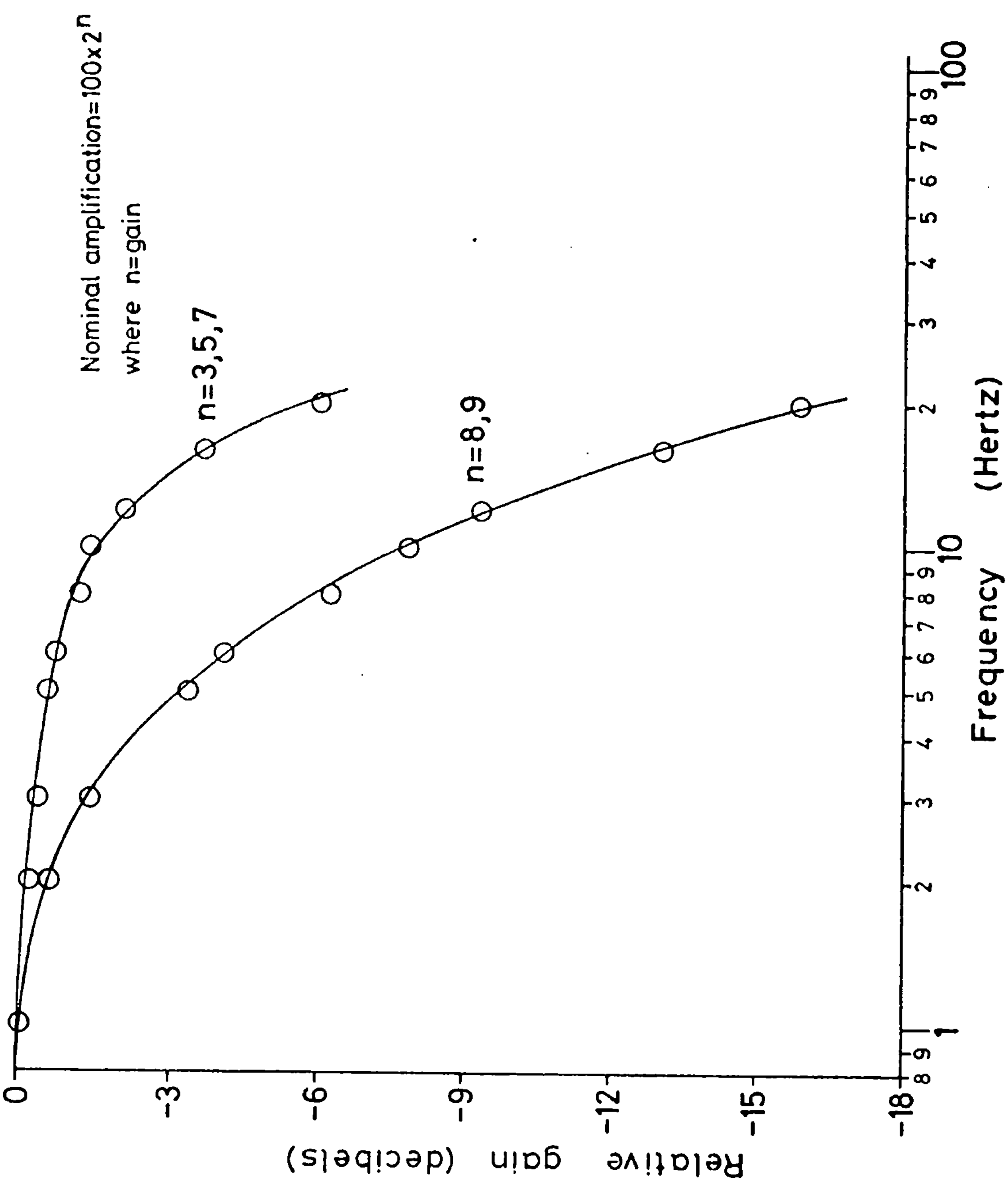

TABLE A1.1

BANDWIDTH

This table gives half power (-3dB) frequency points

at various gains

GAIN SETTING (n)	NOMINAL GAIN	LOW FREQUENCY (Hz)	HIGH FREQUENCY (Hz)
9	51200	0.15	5
8	25600	0.07	5
7	12800	0.04	15
5	3200	0.01	15
3	800	0.01	15

TABLE A1.2

DYNAMIC RANGE AT 1 HZ

(Accuracy ±3dB)

GAIN SETTING	9	8	7	5	3
NOMINAL GAIN	51200	25600	12800	3200	800
DYNAMIC RANGE (dB)	32	36	36	37	37

frequency response for the portable seismic recorder (LONG, 1974, p.94 and fig. 2A).

The dynamic range was found by measuring the lowest voltage 1 Hz input (V_L) for which the output signal was still visible above system noise on playback, and the voltage input (V_U) at which the output waveform began to saturate. The dynamic range is then expressed in decibels as 20 $\log_{10}$ (V_U/V_L). The results are given in Table A1.2. They were not significantly improved by narrow-band (0.5-2Hz) filtering. At 8 Hz and a gain of 12800 the dynamic range did not exceed 30 dB.

It should be noted that the dynamic range figures "in excess of 50 dB" reported by Long were achieved using a standard set of E.M.I. frequency demodulation electronics that has now been superceded by the equipment described above. Accepting Long's specification for the portable seismic recorder, it must be concluded that this demodulation equipment is much inferior to commercially available systems.

Flutter Compensation

During play-out of low frequency sinusoids to assess the frequency response, incomplete flutter compensation of large amplitude signals was unusually evident (Figure A1.3).

For simplicity, the following explanation of this observation omits consideration of other types of noise generated during the modulation/demodulation process.

FIGURE A1.3

INCOMPLETE FLUTTER COMPENSATION OBSERVED ON DISPLAYED SIGNALS

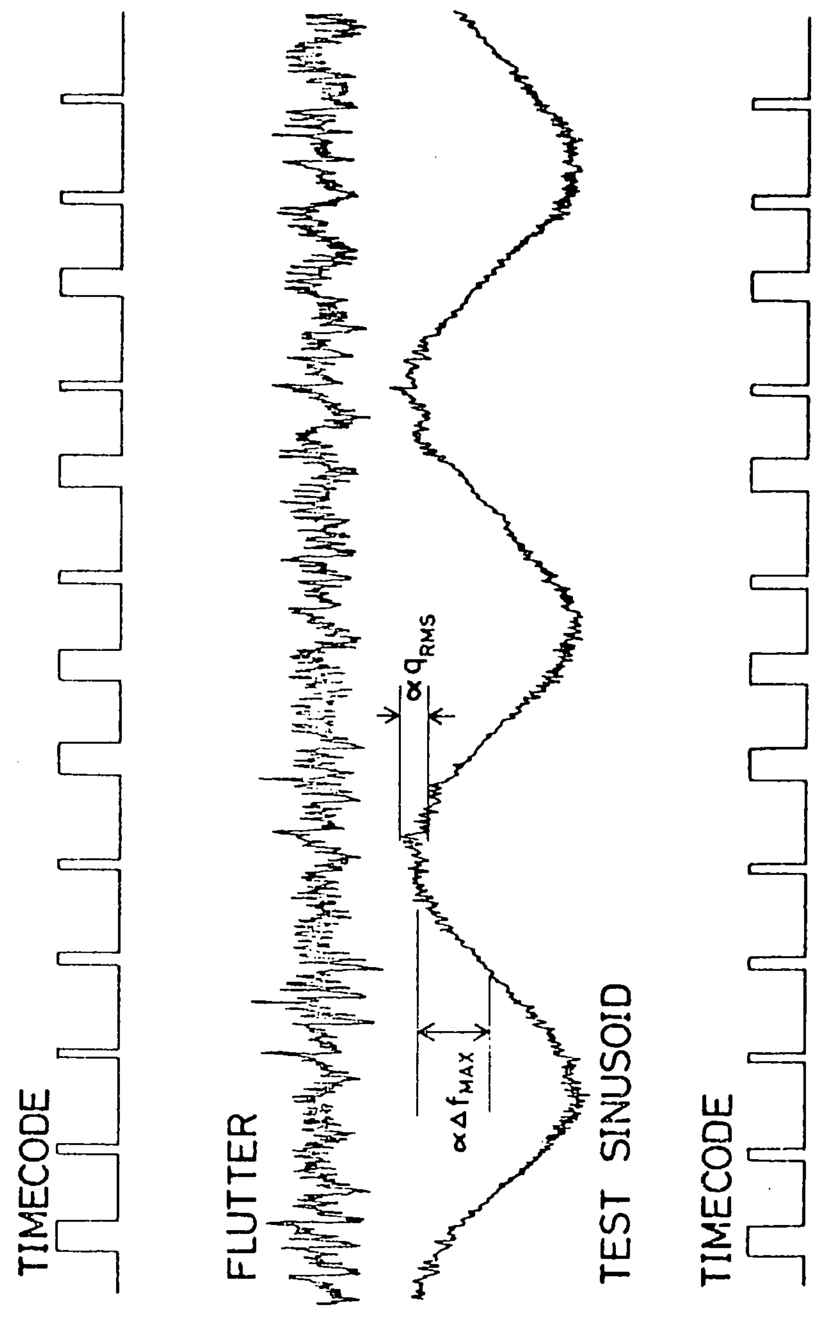

Consider the effect on a seismic signal, S, of the successive operations of frequency modulation, speed compensation by the tape transport unit, frequency demodulation and flutter compensation (Figure A1.4A).

After modulation, the seismic signal is represented by the frequency $(f_S + kS)$, where f_S is the carrier centre frequency and k is a constant.

At any instant, let r be the ratio of the tape playback speed to the expected value of ten times the recording speed. r will vary from unity because of the effect of flutter on the speed of the deck. The effect of the tape transport unit is to impose a multiplication by r on both the modulated seismic signal and the frequency, f_R, recorded on the reference channel. These become, respectively, $r(f_S + kS)$ and rf_R.

After demodulation, the carrier frequency has been subtracted and the voltage, V_S, on the seismic channel is given by

$$V_S \propto r(f_S + kS) - f_S$$

$$\therefore V_S = C_S((r - 1)f_S + rkS)$$

Similarly, the voltage, V_R, on the reference channel is

$$V_R \propto rf_R - r$$

$$\therefore V_R = C_R(r - 1)f_R$$

where C_S and C_R are demodulator gain constants.

The seismic channel output voltage is then flutter compensated by subtracting from it the reference channel output voltage. The resultant seismic voltage is

FIGURE A1.4

BLOCK DIAGRAMS OF THE PROCESSING EQUIPMENT

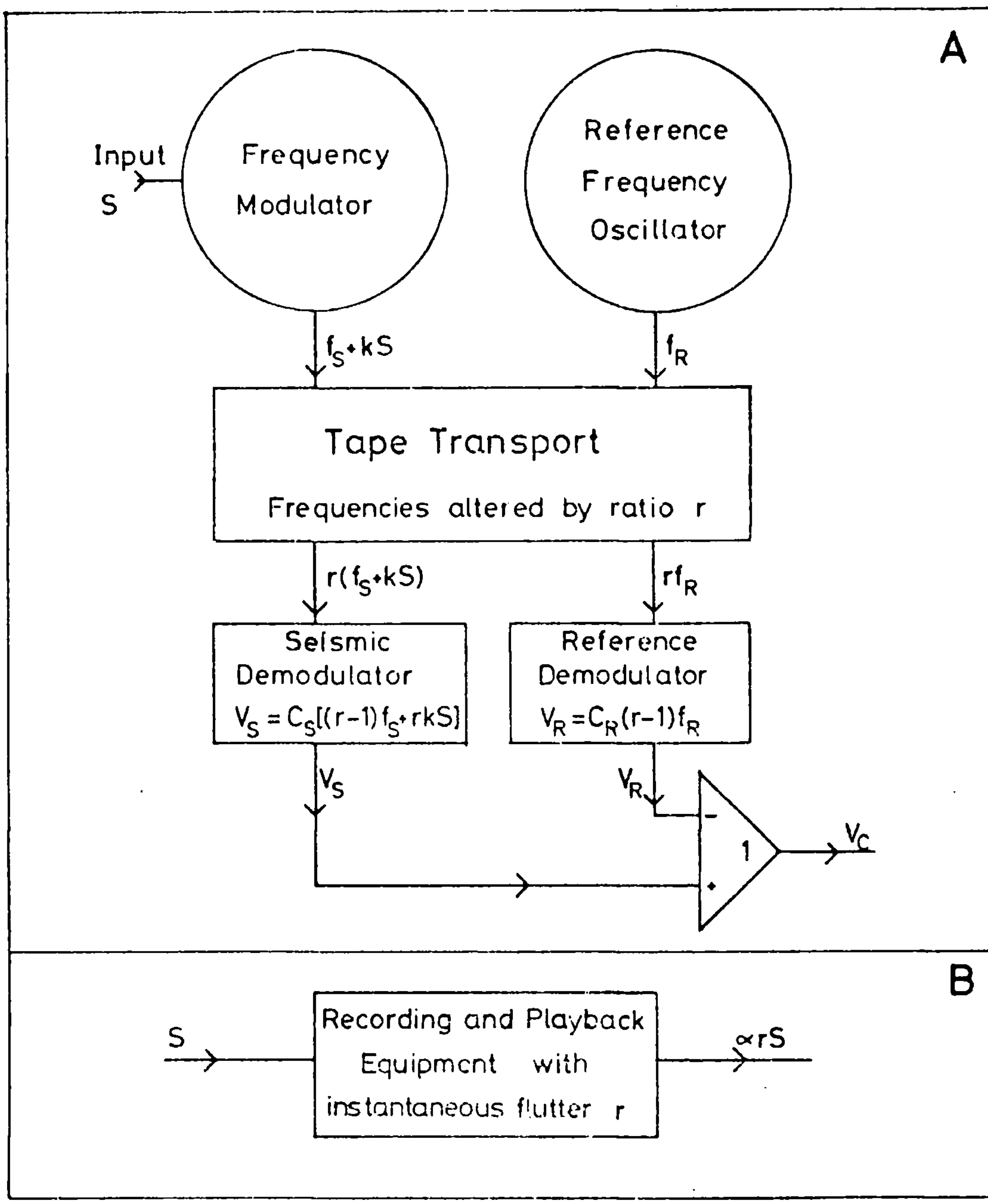

$$V_C = V_S - V_R$$
$$= C_S((r-1)f_S + rkS) - C_R(r-1)f_R \qquad (1)$$

To achieve full flutter compensation the constants C_S and/or C_R are so adjusted as to give zero output voltage on the seismic channel in the absence of a seismic signal, whatever the value of r. Writing $V_C = 0$ when $S = 0$ in Equation 1 yields the condition $C_S f_S = C_R f_R$, whence Equation 1 may be rewritten

$$V_C = C_S rkS$$

Thus the modulation/demodulation process has the effect of multiplying the original seismic signal by the ratio r. This is represented schematically in Figure A1.4B. The result is a noise voltage, V_N, due to uncompensated flutter,

$$V_N = C_S rkS - C_S kS$$

Writing kS = f, where f is the change in the carrier frequency, f_S, due to the seismic signal, S, and setting q = r - 1, the r.m.s. noise due to flutter is

$$V_N = C_S q_{RMS} \Delta f$$

This reaches a maximum value of $C_S q_{RMS} \Delta f_{MAX}$, where Δf_{MAX} represents the frequency deviation caused by a seismic signal on the point of saturation. The dynamic range is consequently reduced to

$$-20 \log_{10} \left(\frac{q_{RMS} f_{RMS}}{2 f_{RMS}}\right) = -20 \log_{10} \left(\frac{q_{RMS}}{2}\right)$$

Measurements on the low frequency sinusoidal output indicate not less than 15% flutter at maximum signal amplitude. The dynamic range at maximum amplitude is therefore only $-20 \log_{10} (0.15/2) = 22.5$ dB.

This compensation problem has become apparent only because of the very high level of flutter generated by the current electronics. The wow and flutter characteristic of the commercial NAGRA IV deck, running at its lowest design speed of 3.75 in/sec, is about 0.11%. The recommended solution is to modify the electronics that allow the NAGRA deck to run so slowly, in such a way as to reduce the flutter level dramatically. Should this not prove feasible a different deck must be used.

W.G. Rigden &
J.E.G. Savage
25/4/77

APPENDIX 2

PROGRAM MANETA

INTRODUCTION

This program, written in FORTRAN, calculates arrival times for the first P-phase at a number of stations, for a number of events, given their locations. Corrections are made for station height above sea level, and the Earth's ellipticity. The latter correction uses the method of Dzeiwonski and Gilbert (1976). The main calculations are described in Chapter 4, and a compiled version of this program is available in the file GPT9:MANETA.

INPUT

UNIT 2 Travel time tables for first P-phase, and table of corresponding ellipticity correction factors:

TABL,EQR,ECC,PLR,CVEL (A8,2X,5F10.3)

TABL	:Name of travel-time tables.
EQR	:The Earth's equatoral radius.
ECC	:The Earth's eccentriciy factor.
PLR	:The Earth's polar radius.
CVEL	:Upper crustal velocity (km/sec).

The travel time tables are split up into several blocks, (maximum of 5) each of which has the following input and represents a single phase:

PHS,PLMN,PLMX,NN,N (A8,2X,2F10.3,2I10)

PHS	:Phase name.
PLMN	:Least epicentral distance covered by block in degrees.
PLMX	:Greatest epicentral distance covered by block

in degrees.

NN :Number of epicentral distances covered in block (maximum total for all blocks=400).

N :Number of focal depths covered in block (maximum 25).

```
(DP(J),J=1,N)    (5(8F10.3/))
```

DP :Focal depths (in kilometers) at which travel times are tabulated.

NN card groups, one for each epicentral distance, as follows:

```
PL,(M(J),P(J),J=1,N)

(F10.3,7(I4,F6.3)/(10X,7(I4,F6.3)))
```

PL :Epicentral distance in degrees.

M(J) :Minutes part of travel time for J^{th} depth.

P(J) :Seconds part of travel time for J^{th} depth.

Flag card with zero or blank in columns 31-40, then ellipticity correction tables.

```
(TL(J),((TOR(I,J,K),I=1,3),K=1,3),J=1,37)

(37(F4.1,3(3F6.2,1X)))
```

TL(J) :J^{th} Epicentral distance.

TOR(I,J,K) :I^{th} Ellipticity correction factor for J^{th} epicentral distance and K^{th} depth. Depths are as follows;

K	1	2	3
Depth (km)	0	300	650

The travel time tables for P and PKP given by Herrin et al (1968), with corresponding ellipticity correction factors given by Dziewonski and Gilbert (1976), are available in the file GPT9:HERRIN

<u>UNIT 3</u> Lists of geographical areas and regions used for annotating the output. The use of this facility is optional, and *DUMMY* may be attached.

Up to 80 cards giving regions names:

I,CHR (I5,A40)

I	:Region number.
CHR	:Region name.

The end of this list is flagged with I=0.

Then up to 800 cards with area names:

I,II,CHA (I3,I5,2X,A40)

I	:Region number for area.
II	:Area number.
CHA	:Area name.

The end of this list is flagged by "$ENDFILE"

Lists of geographical areas and regions, in the above format, are available in GPT9:GEOG.

<u>UNIT 5</u> List of stations, then the list of events.

Station cards, one per station:

SNAM,SLAT,SLON,SHT,SVEL,STAT (A16,4X,5F10.5)

SNAM	:Station name or number.
SLAT	:Station latitude (geographic) in degrees N. (S negative.)
SLON	:Station Longitude in degrees E. (W negative.)
SHT	:Station height above mean sea level in meters.
SVEL	:Average seismic velocity of material above datum and beneath station in km/sec.
STAT	:Station or other desired correction to be applied to E.T.A. in seconds. (Normally zero)

The end of this list is flagged by a card, blank except for "*" in column 1.

Event list. One event per card.

EDES,LOC,ELAT,ELON,EDEP,EMAG,IH,IM,ES,TLL

(A16,1X,I3,2F10.5,2F5.2,I2,1X,I2,F6.2,2 X,A2))

EDES	:Event name or number.
LOC	:Area number of epicentre.
ELAT	:Epicentral latitude (geographic) in degrees N. (S negative.)
ELON	:Epicentral longitude in degrees E.

	(W negative.)
EDEP	:Focal depth in kilometers.
IH	:Hours part of onset time.
IM	:Minutes part of onset time.
ES	:Seconds part of onset time.
TLL	:"GE" = Geographic latitudes to be used in calculations. "GC" = Geocentric latitudes to be used in calculations. "SM" = Seismic latitudes to be used in calculations. Default (blank) is "GC".

"$ENDFILE" flags end of list and stops program. A card, blank except for "*" in column 1 restarts execution, with a new station list.

OUTPUT

UNIT 6 All output appears in this unit.

EXTERNAL SUBROUTINES

The NAG MkIV library subroutine E01ACF is called by this program.

```
C********   PROGRAM MANETA   ***********
C
C**  THIS IS A COMPLETELY REWRITTEN, AND UPDATED VERSION OF
C   PROGRAM "ETA", WHICH WAS DEVISED BY HUGH EBBUTT.
C
C**  THE PROGRAM CALCULATES ARRIVAL TIMES OF P OR PKP AT
C   GIVEN STATIONS USING HERRIN'S TABLES. INTERPOLATION
C   BETWEEN GIVEN TIMES IS MADE USING ROUTINE E01ACF, IN THE
C   *NAG LIBRARY. FOR COMPATIBILITY WITH THIS ROUTINE, AND
C   PRECISION, REAL*8 IS USED THROUGHOUT.
C
C**  INPUTS ARE AS FOLLOWS:
C         UNIT 2:   TRAVEL-TIME TABLES+ELIPTICITY CORRECTIONS E.G. AS IN
C                   FILE GPT9:HERRIN
C         UNIT 3:   GEOGRAPHICAL REGIONS AS IN FILE GPT9:GEOG
C         UNIT 5:   STATION AND HYPOCENTRE DATA AS FOLLOWS
C   STATION DATA: (ONE STATION PER CARD), SNAME (STATION NAME);
C                 SLAT, SLON (GEOGRAPHIC LATITUDE AND LONGITUDE);
C                 SHT (HEIGHT IN METERS); SVEL (CRUSTAL VELOCITY
C                 IN KM/SEC.); STAT (DELAY IN SECONDS).
C
C          FORMAT(A16,4X,5F10.3)
C   FLAG CARD: BLANK EXCEPT FOR AN ASTERISK IN COLUMN 1.
C
C   HYPOCENTRAL DATA: (ONE EVENT PER CARD), EDES (EVENT NAME OR
C                  DATE); LOC (REGION NUMBER, 0 IF DON'T KNOW);
C                 ELAT, ELON (GEOGRAPHIC LATITUDE AND LONGITUDE);
C                 EDEP (DEPTH IN KM.); EMAG (MAGNITUDE); IH, IM,
C                 ES (TIME IN HOURS MINUTE AND SECONDS); TL (CODE
C                 FOR SELECTING LATITUDE TYPE IN CALCULATIONS:
C                 GG=GEOGRAPHIC, GC=GEOCENTRIC, SM=SEISMIC,
C                 DEFAULT IS GEOCENTRIC, WHICH IS RECOMMENDED
C                 FOR THE TYPE OF ELIPTICITY CORRECTIONS USED.)
C          FORMAT(A16,1X,I3,2F10.5,2F5.2,I2,1X,I2,F6.2,2X,A2)
C
      IMPLICIT REAL*8(A-H,O-Z)
      REAL*8 K(3)
      DIMENSION SNAM(2,51),SLAT(51),SLON(51),SHT(51),SVEL(51),STAT(51),
     % TOR(3,37,3),P(400,25),PHS(5),PLMN(5),PLMX(5),
     % NLAT(5),NDP(5),NS(5),M(25),EDES(2),A(3),B(3),C(3),G(3),H(3),
     % REG(5,800),AR(5,80),NAR(800),CLT(3),CHR(5),DP(5,25),PL(400),
     % SA(3,50),SB(3,50),SC(3,50),SD(50),SE(50),SG(3,50),SH(3,50),
     % SK(3,50),X(4),Y(4),Z(4),ELAT(3),
     % W1(4),W2(4),W3(4),TD(3),TL(50),ZP(4,4),ZV(4,4),TAU(3),CLTT(3)
      COMMON/A/ RTOD,DTOR,FAC2
      DATA AST,BLNK,CLT/'*       ','        ','GG','GC','SM'/,
     % CLTT/'GEOGRAPH','GEOCENTR','   SEISM'/
C
C**  READ IN TRAVEL TIME TABLES
C
   30 NL=1
      NPH=0
      READ(2,31)TABL,EQR,ECC,PLR,CVEL
   31 FORMAT(A8,2X,5F10.3)
   32 NPH=NPH+1
      READ(2,33)PHS(NPH),PLMN(NPH),PLMX(NPH),NN,N
   33 FORMAT(A8,2X,2F10.3,2I10)
      IF(NN.LE.0)GO TO 43
      NLAT(NPH)=NN
      NDP(NPH)=N
```

```
      NS(NPH)=NL
      READ(2,35)(DP(NPH,J),J=1,N)
   35 FORMAT(5(8F10.3/))
      NN=NN+NL-1
      DO 42 I=NL,NN
      READ(2,39)PL(I),(M(J),P(I,J),J=1,N)
   39 FORMAT(F10.3,7(I4,F6.3)/(10X,7(I4,F6.3)))
      DO 42 J=1,N
   42 P(I,J)=P(I,J)+60.DO*DFLOAT(M(J))
      NL=NL+NLAT(NPH)
      GO TO 32
C
C**  READ IN ELIPTICITY CORRECTIONS.
C
   43 TD(1)=0.DO
      TD(2)=300.DO
      TD(3)=650.DO
      READ(2,45,END=50)(TL(J),((TOR(I,J,KK),I=1,3),KK=1,3),J=1,37)
   45 FORMAT(37(F4.1,3(3F6.2,1X)/))
C
C**  READ IN LIST OF GEOGRAPHICAL AREAS AND REGIONS.
C
   50 NPH=NPH-1
      DO 53 I=1,80
      DO 53 J=1,4
   53 AR(J,I)=BLNK
      DO 55 I=1,800
      NAR(I)=80
      DO 55 J=1,4
   55 REG(J,I)=BLNK
   56 READ(3,57,END=70)I,CHR
   57 FORMAT(I5,5X,5A8)
      IF(I)60,60,58
   58 DO 59 J=1,5
   59 AR(J,I)=CHR(J)
      GO TO 56
   60 READ(3,61,END=70)I,J,CHR
   61 FORMAT(I3,I5,2X,5A8)
      NAR(J)=I
      DO 63 KK=1,5
   63 REG(KK,J)=CHR(KK)
      GO TO 60
C
C**  SET VARIOUS CONSTANTS
   70 DTOR=DATAN(1.DO)/45.DO
      RTOD=1/DTOR
      STOV=DTOR*(PLR+EQR)
      FAC1=DSQRT(3.DO)/2.DO
      FAC2=1.DO-2.DO/ECC
      DVEL=0.5DO
      VFAC=EQR*DTOR*DVEL
      PP1=0.DO
      PP2=0.DO
      PM1=0.DO
      PM2=0.DO
C
C**  READ IN STATION DATA.
C
   71 NST=1
   72 READ(5,73)(SNAM(I,NST),I=1,2),SLAT(NST),SLON(NST),SHT(NST),
```

```
     % SVEL(NST),STAT(NST)
   73 FORMAT(2A8,4X,5F10.5)
      IF(SNAM(1,NST).EQ.AST) GO TO 80
      NST=NST+1
      GO TO 72
C
C**  CALCULATE GEOCENTRIC AND SEISMIC LATITUDES ETC FOR EACH
C   STATION, AND LIST STATION DATA.
C
   80 NST=NST-1
      WRITE(6,81) TABL
   81 FORMAT('1******    PROGRAM MANETA (22NOV78), JOHN E.G. SAVAGE.',
     % 10X,'TRAVEL TIME TABLES USED: ',A8/
     % '- STATION',12X,'LATITUDE   LONGITUDE    HEIGHT  VELOCITY  ',
     % '    DELAY    GC-LTTDE     SM-LTTDE')
      DO 85 I=1,NST
      CALL LATCON(SLAT(I),SLON(I),GCL,SML,A,B,C,D,E,G,H,K)
      SD(I)=D
      SE(I)=E
      DO 82 J=1,3
      SA(J,I)=A(J)
      SB(J,I)=B(J)
      SC(J,I)=C(J)
      SG(J,I)=G(J)
      SH(J,I)=H(J)
   82 SK(J,I)=K(J)
      WRITE(6,83)(SNAM(J,I),J=1,2),SLAT(I),SLON(I),SHT(I),SVEL(I),
     % STAT(I),GCL,SML
   83 FORMAT(1X,2A8,2X,2(F10.4,2X),F8.1,5X,F5.2,4X,F6.2,2(2X,F10.4))
   85 CONTINUE
      WRITE(6,87)CVEL,EQR,PLR,ECC
   87 FORMAT('- CONSTANTS USED IN CALCULATIONS:-'/
     % '0 CRUSTAL VELOCITY= ',F6.3,' KM/SEC.',5X,'EQUATORIAL RADIUS= ',
     % F7.2,' KM.',5X,' POLAR RADIUS= ',F7.2,' KM.'/
     % '0 ECCENTRICITY= ',F7.3)
C
C**  READ IN EVENT DATA, AND WRITE OUT HEADINGS ETC.
C
   90 READ(5,91,END=300)EDES,LOC,ELAT(1),ELON,EDEP,EMAG,IH,IM,ES,TLL
   91 FORMAT(2A8,1X,I3,2F10.5,2F5.2,I2,1X,I2,F6.2,2X,A2)
      IF(EDES(1).EQ.AST) GO TO 71
      CALL LATCON(ELAT(1),ELON,GCL,SML,A,B,C,D,E,G,H,K)
      ELAT(2)=GCL
      ELAT(3)=SML
      DO 95 I=1,3
      IF(TLL.NE.CLT(I))GO TO 95
      IL=I
      GO TO 96
   95 CONTINUE
      IL=2
   96 WRITE(6,97)EDES,LOC,(REG(I,LOC),I=1,4),(AR(J,NAR(LOC)),J=1,4),
     % ELAT(1),ELON,EDEP,EMAG,IH,IM,ES,CLTT(IL)
   97 FORMAT('0',126('*')/'0 EVENT ',2A8,4X,'REGION:',I4,2(2X,4A8)/
     %'0 HYPOCENTRAL DATA: LATITUDE= ',F10.4,' DEG , LONGITUDE= ',
     % F10.4,' DEG., DEPTH= ',F5.0,' KM., MAGNITUDE= ',F5.1/
     % '0 ORIGIN TIME: ',I2,' HRS. ',I2,' MNS. ',F7.3,' SEC.',4X,A8,
     % 'IC LATITUDES WILL BE USED IN CALCULATIONS.'/
     % '-  STATION',7X,'EPICENTRAL       BACK    AZIMUTH    TRAVEL',
     % '  VELOCITY',7X,'CORRECTIONS',7X,'ARRIVAL TIME  ',
     % '    SEISMIC'/
```

```
     % ' ',18X,'DISTANCE   BEARING',16X,'TIME',10X,
     % 5X,'ELIP' HEIGHT    HRS  MNS     SECS    PHASE')
C
C** CALCULATE DISTANCES, E.T.A. ETC., FOR EACH STATION IN TURN.
C
      DO 190 IS=1,NST
      DEL=RTOD*DARCOS(SA(IL,IS)*A(IL)+SB(IL,IS)*B(IL)+SC(IL,IS)*C(IL))
      AZ=RTOD*DATAN2((SA(IL,IS)-D)**2+(SB(IL,IS)-E)**2+
     % SC(IL,IS)**2-2.DO, (SA(IL,IS)-G(IL))**2+
     % (SB(IL,IS)-H(IL))**2+(SC(IL,IS)-K(IL))**2-2.DO)
      BB=RTOD*DATAN2((A(IL)-SD(IS))**2+(B(IL)-SE(IS))**2+
     % C(IL)**2-2.DO, (A(IL)-SG(IL,IS))**2+
     % (B(IL)-SH(IL,IS))**2+(C(IL)-SK(IL,IS))**2-2.DO)
      IF(AZ.LT.O.DO)AZ=AZ+360.DO
      IF(BB.LT.O.DO)BB=BB+360.DO
C
C**  FIND PHASE CORRESPONDING TO DEL.
C
      DO 105 J=1,NPH
      IF(DEL.LT.PLMN(J).OR.DEL.GT.PLMX(J))GO TO 105
      N=J
      GO TO 110
  105 CONTINUE
      WRITE(6,107)(SNAM(J,IS),J=1,2),DEL,BB,AZ
  107 FORMAT(' ',2A8,3F10.3,' TABLES DO NOT COVER THIS DISTANCE')
      GO TO 190
C
C** FIND LATITUDE POSITION IN TABLES
C
  110 IF=NS(N)+NLAT(N)-1
      IB=NS(N)
      DO 115 J=IB,IF
      IF(DEL.GT.PL(J)) GO TO 115
      ILAT=J-2
      GO TO 117
  115 CONTINUE
      STOP1
  117 IF(ILAT.LT.NS(N))ILAT=NS(N)
      IF(ILAT.GT.IF-3)ILAT=IF-3
C
C**  FIND DEPTH POSITION IN TABLES
C
      IF=NDP(N)
      DO 120 J=1,IF
      IF(EDEP.GT.DP(N,J)) GO TO 120
      IDEP=J-2
      GO TO 122
  120 CONTINUE
      WRITE(6,123)(SNAM(J,IS),J=1,2),DEL,BB,AZ
      GO TO 190
  123 FORMAT(' ',2A8,3F10.3,' TABLES DO NOT EXTEND TO THIS DEPTH')
  122 IF(IDEP.LT.1)IDEP=1
      IF(IDEP.GT.NDP(N)-3)IDEP=NDP(N)-3
C
C**  FILL WORKING ARRAYS WITH DISTANCES, DEPTHS, AND P AND
C   V VALUES AND INTERPOLATE.
C
      DO 125 J=1,4
      X(J)=PL(ILAT-1+J)
      Y(J)=DP(N,IDEP-1+J)
```

```
      DO 125 JJ=1,4
  125 ZP(J,JJ)=P(ILAT-1+J,IDEP-1+JJ)
      IFAIL1=1
      IFAIL2=1
      IFAIL3=1
      DLP=DEL+DVEL
      DLM=DEL-DVEL
      FM=0.5D0
      FP=0.5D0
      CALL E01ACF(DEL,EDEP,X,Y,ZP,PI1,PI2,IFAIL1,W1,W2,W3,W4,4,4,4)
      IF(DLP.LE.X(4))GO TO 502
      FP=0.D0
      FM=1.D0
      IFAIL2=0
      GO TO 510
  502 CALL E01ACF(DLP,EDEP,X,Y,ZP,PP1,PP2,IFAIL2,W1,W2,W3,W4,4,4,4)
      IF(DLM.GE.X(1))GO TO 510
      FP=1.D0
      FM=0.D0
      IFAIL3=0
      GO TO 520
  510 CALL E01ACF(DLM,EDEP,X,Y,ZP,PM1,PM2,IFAIL3,W1,W2,W3,W4,4,4,4)
  520 IF(IFAIL1.EQ.0.AND.IFAIL2.EQ.0.AND.IFAIL3.EQ.0)GO TO 130
      WRITE(6,127)(SNAM(J,IS),J=1,2),DEL,BB,AZ,IFAIL1,IFAIL2
  127 FORMAT(' ',2A8,3F10.3,' INTERPOLATION FAILURE:',2I3)
      GO TO 190
  130 PI=(PI1+PI2)/2.D0
      PP=(PP1+PP2)/2.D0
      PM=(PM1+PM2)/2.D0
      VI=VFAC/(FM*(PI-PM)+FP*(PP-PI))
      IF(VI.GT.999.D0)VI=999.D0
C
C** CALCULATE ELIPTICITY CORRECTIONS USING THE METHOD OF
C   DZIEWONSKI AND FREEMAN GILBERT (1976): SEE GEOPHYSICAL
C   JOURNAL OF THE ROYAL ASTRONOMICAL SOCIETY, VOL. 44,
C   PAGES 7-17.
C
  132 IF(DEL.GT.105.D0.AND.DEL.LT.120.D0)GOTO 134
      DO 133 J=1,37
      IF(DEL.GT.TL(J)) GO TO 133
      IT=J-1
      GO TO 135
  133 CONTINUE
  134 EL=1.D3
      GO TO 162
  135 IF(EDEP.GT.TD(3)) GO TO 145
      JT=2
      IF(EDEP.LT.300.D0)JT=1
      F1=(DEL-TL(IT))/(TL(IT+1)-TL(IT))
      F2=(TL(IT+1)-DEL)/(TL(IT+1)-TL(IT))
      F3=(EDEP-TD(JT))/(TD(JT+1)-TD(JT))
      F4=(TD(JT+1)-EDEP)/(TD(JT+1)-TD(JT))
      DO 140 I=1,3
  140 TAU(I)=TOR(I,IT,JT)*F2*F4+TOR(I,IT+1,JT)*F1*F4+
     % TOR(I,IT,JT+1)*F2*F3+TOR(I,IT+1,JT+1)*F1*F3
      GO TO 160
  145 DO 150 I=1,3
  150 TAU(I)=TOR(I,IT,3)*(TL(IT+1)-DEL)/(TL(IT+1)-TL(IT))
     % +TOR(I,IT+1,3)*(DEL-TL(IT))/(TL(IT+1)-TL(IT))
  160 CL=DTOR*(90.D0-ELAT(IL))
```

```
      CA=DTOR*AZ
      EL=TAU(1)*0.25D0*(1.D0+3.D0*DCOS(2.D0*CL))
     % +TAU(2)*FAC1*DSIN(2.D0*CL)*DCOS(CA)
     % +TAU(3)*FAC1*(DSIN(CL))**2*DCOS(2.D0*CA)
C
C**  CALULATE HEIGHT CORRECTION, USING CRUSTAL VELOCITY
C   GIVEN IN TRAVEL TIME TABLES, AND USING INTRPOLATED
C   APPARENT VELOCITY TO GIVE SLANT. (FORMULA IS EFFECTIVELY
C   THE SAME AS FOR HORIZONTAL REFRACTION DELAY TIME).
C
  162 IF(VI.EQ.0.D0)GO TO 168
      HT=1.D-3*SHT(IS)*DSQRT(VI**2-CVEL**2)/(VI*CVEL)
      GO TO 170
  168 HT=1.D-3*SHT(IS)/CVEL
C
C** TOT UP TIMES AND REWORK TO GIVE ARRIVAL TIMES IN HOURS,
C   MINUTES AND SECONDS.
C
  170 ART=ES+PI+HT
      MM=IM
      MH=IH
      IF(EL.LT.1.D2)ART=ART+EL
  171 IF(ART.LT.60.D0) GO TO 172
      ART=ART-60.D0
      MM=MM+1
      GO TO 171
  172 IF(MM.LT.60)GO TO 174
      MM=MM-60
      MH=MH+1
  174 IF(MH.GT.24)MH=MH-24
      IF(EL.GT.1.D2)GO TO 188
      WRITE(6,187)(SNAM(J,IS),J=1,2),DEL,BB,AZ,PI,VI,EL,HT,MH,MM,
     % ART,PHS(N)
  187 FORMAT(' ',2A8,7F10.3,2I5,F10.3,3X,A8)
      GO TO 190
  188 WRITE(6,189)(SNAM(J,IS),J=1,2),DEL,BB,AZ,PI,VI,HT,
     % MH,MM,ART,PHS(N)
  189 FORMAT(' ',2A8,5F10.3,'     *****',F10.3,2I5,F10.3,3X,A8)
  190 CONTINUE
      GO TO 90
  300 WRITE(6,301)
  301 FORMAT('-',120('*'))
      STOPO
      END
C
C*********************************************************************
C
      SUBROUTINE LATCON(GGL,LON,GCL,SML,A,B,C,D,E,G,H,K)
C
C**  TO CONVERT GEOGRAPHIC LATITUDE, GGL, TO GEOCENTRIC (GCL),
C   AND SEISMIC (SML) LATITUDES AND CALCULATE VARIOUS QUANTITIES
C   USED IN DISTANCE AND AZIMUTH CALCULATIONS. SEE BULLEN,
C   "AN INTRODUCTION TO SEISMOLOGY", THIRD EDITION PAGES 154,155,
C   AND 181 FOR DESCRIPTIONS OF THESE QUANTITIES.
C
      IMPLICIT REAL*8(A-H,O-Z)
      REAL*8 LON,K(3)
      DIMENSION A(3),B(3),C(3),G(3),H(3)
      COMMON/A/ RTOD,DTOR,FAC2
      GCL=RTOD*DATAN(FAC2*DTAN(GGL*DTOR))
```

```
      SML=1.1D0*GCL-0.1D0*GGL
      C(1)=DSIN(GGL*DTOR)
      C(2)=DSIN(GCL*DTOR)
      C(3)=DSIN(SML*DTOR)
      D=DSIN(LON*DTOR)
      E=-DCOS(LON*DTOR)
      K(1)=-DCOS(GGL*DTOR)
      K(2)=-DCOS(GCL*DTOR)
      K(3)=-DCOS(SML*DTOR)
      DO 10 I=1,3
      A(I)=K(I)*E
      G(I)=-C(I)*E
      H(I)=C(I)*D
   10 B(I)=-K(I)*D
      RETURN
      END
```

APPENDIX 3

PROGRAM SEPD

INTRODUCTION

This program separates raw delay times for a number of events, measured at stations within a network, into scource and station components. The main calculations are described in Chapter 4, and the compiled version of this program is available in the file GPT9:SEPD.

INPUT

UNIT 3 Lists of geographical areas and regions used for annotating the output. The use of this facility is optional, and *DUMMY* may be attached.

Up to 80 cards giving regions names:

I,CHR (I5,A40)

I	:Region number.
CHR	:Region name.

The end of this list is flagged with I=0.

Then up to 800 cards with area names:

I,II,CHA (I3,I5,2X,A40)

I	:Region number for area.
II	:Area number.
CHA	:Area name.

The end of this list is flagged by "$ENDFILE"

Lists of geographical areas and regions, in the above format, are available in GPT9:GEOG.

UNIT 5 Event selection data, event data and raw (measured) delay times:

ITMIN,ITMAX,DMIN,DMAX,BBMIN,BBMAX,AZMIN,AZMAX,NS,K

(2(I8,2X),6F5.0,3I5)

ITMIN, ITMAX	:If both of these are non-zero, only events occurring between the times represented by ITMIN and ITMAX are used. The eight digits of these numbers are paired, representing (from most significant to least significant) years, days, hours, and minutes, of the required times. (This is exactly analagous to event numbering).
DMIN, DMAX	:Minimum and maximum value of epicentral distance (in degrees) of events to be used in calculations.
BBMIN, BBMAX	:Minimum and maximum values of back-bearing (in degrees) of events selected for computations.
AZMIN, AZMAX	:Minimum and maximum values of azimuth (in degrees) of events selected for computations.
NS	:Number of stations used in network.
K	:Zero (blank) Full output Non-zero Restricted output.

II,(WLST(I),I=1,9)

(I5,9F5.2)

II	:Zero or less onset weights used as input. Greater than zero all weights set to unity.
WLST(I)	:Weight to be used for to onset weight code I.

(IST(J),J=1,NS) (16I5)

IST	:Station numbers.

List of Event data. One event per card.

IT,ELT,ELN,DPT,EMG,IR,IH,IM,SC,DL,BB,AZ,IWE

(I8,2F9.3,F4.0,F4.1,I4,2I3,F6.2,3F4.0,I2)

IT	:Event number (time) as for ITMAX and ITMIN (=0 flags end of list).
ELT	:Epicentral latitude in degrees N (S negative).
ELN	:Epicentral longitude in degrees E (W negative).
DPT	:Focal depths in kilometers.
EMG	:Magnitude.
IR	:Geographic area number.
IH	:Hour part of onset time.
IM	:Minute part of onset time.
SC	:Seconds part of onset time.
DL	:Approximate epicentral distance.
BB	:Approximate back-bearing of epicentre.
AZ	:Approximate azimuth of network for epicentre.

IWE :Event weight code.

List of raw delay times, using as many cards as it takes. Up to 7 delays for any one event may be entered on each card. A single event may use as many cards as required.

```
ITD,(IS(J),DR(J),IW(J),J=1,7)
(I8,2X,7(I3,F5.2,I2))
```

ITD :Event number as IT, ITMAX and ITMIN.
IST(J) :Station number for J^{th} delay time.
DR(J) :J^{th} raw delay time (seconds).
IW(J) :Onset weight code for J^{th} raw delay time. Note fields for which IS(J)=0 are ignored, and may be left blank.

$ENDFILE flags end of input.

OUTPUT

UNIT 6 All ouput appears on this unit, in a format suitable for the line printer.

EXTERNAL SUBROUTINES

The DURH:SUBLIB library routine DYNMIC is called to get the large quantity of core-space required for array storage. The NAG Mk V library functions and subroutines X02AAF and F04AMF are also required for least squares inversion.

Additional Notes

As written the program may accept up to 30 stations, 130 events and 500 raw delay times. These limits can easily be reset as described in comments (lines 20-28).

```
C        ********************************
C        *  PROGRAM SEPD  J.E.G.SAVAGE  *
C        ********************************
C
C     THIS PROGRAM SEPARATES DELAY TIMES OF UP TO 130 EVENTS,
C    RECORDED AT UP TO 30 SEISMIC STATIONS INTO SOURCE AND RECEIVER
C   COMPONENTS. EACH EVENT IS ASSUMED TO HAVE A DELAY E(I) ASSOCIATED
C    WITH IT, AND EACH RECEIVER A DELAY S(J). THUS THE DELAY OBSERVED
C    AT STATION J FROM EVENT I IS D(I,J)=E(I)+S(J).
C     PROVIDING THERE ARE MORE MEASUREMENTS OF D THAN UNKNOWNS (TOTAL
C    OF NUMBERS OF STATIONS AND EVENTS) THE PROGRAM SOLVES, IN A LEAST
C    SQUARES SENSE, THE SET OF OVER DETERMINED SIMULTANEOUS EQUATIONS.
C     HOWEVER, SINCE ANY CONSTANT MAY BE ADDED TO EACH OF THE E'S AND
C    SUBTRACTED FROM EACH OF THE S'S WITHOUT AFFECTING THE D'S, AN
C    ADDITIONAL EQUATION MUST BE ADDED. FOR THIS IT IS CHOSEN THAT A
C    WEIGHTED SUM OF THE E'S IS MADE ZERO. A WEIGHT FOR EACH OF THE
C    D.S MUST ALSO BE INPUTTED.
C
C
C***   30 MAX. STATIONS; 130 MAX EVENTS; 500 MAX. DELAYS.
C
C
C***   NOTE THAT WITH MAXIMUM LIMITS SET AS ABOVE,
C    THE PROGRAM USES ABOUT 1.4 MBYTES OF STORAGE,
C    WHICH IS REQUESTED USING SUBROUTINE DYNMIC.
C     TO REDUCE STORAGE REQUIREMENTS FOR SMALLER
C    QUANTITIES OF DATA MERELY CHANGE THE VALUES OF
C    ISMAX, IEMAX, AND IDMAX.
C
      COMMON ID1,ID2,ID3,ID4,IEMAX,ISMAX,IDMAX
      ISMAX=30
      IEMAX=130
      IDMAX=500
       ID1=IDMAX+1
      ID2=IEMAX+ISMAX
      ID3=IEMAX+1
      ID4=ISMAX
      JD1=ID1*2
      JD2=ID2*2
      JD3=ID3*2
      JD4=ID4*2
      JD5=JD1*ID2
      CALL DYNMIC(A,JD5,X,JD2,Y,JD1,IWD,ID1,IT,ID3,
    % ELT,JD3,ELN,JD3,DPT,JD3,EMG,JD3,IR,ID3,IH,ID3,IM,
    %  ID3,SC,JD3,DL,JD3,BB,JD3,AZ,JD3,IWE,ID3,IUS,ID2,
    % IUWS,ID4,IUWE,ID4,IST,ID4,QR,JD5,R1,JD2,R2,JD2,
    % R3,JD2,R4,JD2,R5,JD1,IPIV,ID2,E,JD2,R,JD1,NDU,ID2,
    % DUWD,JD4,IUWW,JD4)
      STOP
      END
C
C******************************************************************************
C
      SUBROUTINE MAINPR(A,I1,X,I2,Y,I3,IWD,I4,IT,I5,ELT,I6,ELN,I7,
    % DPT,I8,EMG,I9,IR,I10,IH,I11,IM,I12,SC,I13,DL,I14,BB,I15,
    % AZ,I16,IWE,I17,IUS,I18,IUWS,I19,IUWE,I20,IST,I21,QR,I22,
    % R1,I23,R2,I24,R3,I25,R4,I26,R5,I27,IPIV,I28,E,I29,R,I30,
    % NDU,I31,DUWD,I32,IUWW,I33)
      IMPLICIT REAL*8(A-H,O-Z)
      COMMON ID1,ID2,ID3,ID4,IEMAX,ISMAX,IDMAX
```

```
      DIMENSION A(ID1,ID2),X(ID2,1),Y(ID1,1),K1(4),K2(4),IWD(ID1),
     % IS(12),DR(12),IW(12),IT(ID3),ELT(ID3),ELN(ID3),DPT(ID3),EMG(ID3),
     % IR(ID3),IH(ID3),IM(ID3),SC(ID3),DL(ID3),BB(ID3),AZ(ID3),
     % IWE(ID3),IUS(ID2),IUWS(ID4),IUWE(ID4),IST(ID4),QR(ID1,ID2),
     % R1(ID2),R2(ID2),R3(ID2),R4(ID2),R5(ID1),IPIV(ID2),E(ID2),
     % R(ID1),DC(12),RR(12),NDU(ID2),DUWD(ID4),IUWW(ID4),REG(5,800),
     % AR(5,80),CHR(5),CHA(5),NAR(800),WLST(9)
      DATA BLNK/'        '/
      LOGICAL UWPR,ANG,EWS,PR1
      PR1=.TRUE.
      EWS=.FALSE.
      WF=2.D0
      WF2=DSQRT(WF)
      EPS=0.D0
      EPS=X02AAF(EPS)
C
C**  READ IN LIST OF GEOGRAPHICAL AREAS AND REGIONS.
C
      DO 53 I=1,80
      DO 53 J=1,5
   53 AR(J,I)=BLNK
      DO 55 I=1,800
      NAR(I)=80
      DO 55 J=1,5
   55 REG(J,I)=BLNK
   56 READ(3,57,END=70)I,CHR
   57 FORMAT(I5,5X,5A8)
      IF(I)60,60,58
   58 DO 59 J=1,4
   59 AR(J,I)=CHR(J)
      GO TO 56
   60 READ(3,61,END=70)I,J,CHR
   61 FORMAT(I3,I5,2X,5A8)
      NAR(J)=I
      DO 63 KK=1,5
   63 REG(KK,J)=CHR(KK)
      GO TO 60
   70 WRITE(6,89) IEMAX,ISMAX,IDMAX
   89 FORMAT('1',25X,26('*')/26X,'* PROGRAM SEPD (02APR79) *'/
     % 26X,26('*')/'0 MAXIMUM NUMBER OF EVENTS IS',I4,
     % ', MAXIMUM NUMBER OF STATIONS IS',I3,
     % ', MAXIMUM NUMBER OF DELAYS IS',I4,'.')
      READ(5,101)ITMIN,ITMAX,DMIN,DMAX,BBMIN,BBMAX,AZMIN,AZMAX,NS,K,L
  101 FORMAT(2(I8,2X),6F5.0,3I5)
      IF(NS.LE.ISMAX) GO TO 302
      WRITE(6,97) NS
   97 FORMAT('0 *** ERROR *** ATTEMPT TO USE',I4,' STATIONS.')
      STOP
  302 READ(5,303)II,(WLST(I),I=1,9)
  303 FORMAT(I5,9F5.2)
      IF(II)310,310,306
  306 WRITE(6,307)
  307 FORMAT('0 *** ALL WEIGHTS SET TO UNITY. ***')
      DO 309 I=1,9
  309 WLST(I)=1.D0
      GO TO 102
  310 WRITE(6,311)(I,I=1,9),(WLST(II),II=1,9)
  311 FORMAT(2X/'0 ONSET WEIGHT CODE:',9I5/
     % '     ASSIGNED WEIGHT:  ',9F5.2)
      DO 315 I=1,9
```

```
  315 WLST(I)=DSQRT(WLST(I))
  102 READ(5,103)(IST(J),J=1,NS)
  103 FORMAT(16I5)
      DO 104 J=1,NS
      IF(IST(J).NE.0)GO TO 104
      WRITE(6,99)
   99 FORMAT('0 ***ERROR***  ATTEMPT TO INPUT STATION NUMBERED ZERO')
      STOP5
  104 CONTINUE
      UWPR=.FALSE.
      IF(K.NE.0)UWPR=.TRUE.
      CALL DCNT(ITMAX,TMAX,K2(1),K2(2),K2(3),K2(4))
      CALL DCNT(ITMIN,TMIN,K1(1),K1(2),K1(3),K1(4))
      IF(TMAX.LE.0.D0) GO TO 107
      WRITE(6,105)K1,K2
  105 FORMAT('0 EVENTS USED ONLY FROM ',I2,3('/',I2),' TO ',I2,3('/',
     % I2),'.')
  107 TMAX=1.D10
      IF(DMAX.LE.0.D0) GO TO 111
      WRITE(6,109)DMIN,DMAX
  109 FORMAT('0 EVENTS USED ONLY IF IN DISTANCE RANGE',F7.1,' TO',F7.1,
     % ' DEGREES.')
      GO TO 112
  111 DMAX=400.0
  112 IF(BBMAX.LE.0.D0) GO TO 115
      WRITE(6,113)BBMIN,BBMAX
  113 FORMAT('0 EVENTS USED ONLY IF BACK-BEARING IN RANGE',F7.1,' TO',
     % F7.1,' DEGREES.')
      GO TO 116
  115 BBMAX=400.D0
  116 IF(AZMAX.LE.0.D0) GO TO 119
      WRITE(6,117)AZMIN,AZMAX
  117 FORMAT('0 EVENTS USED ONLY IF AZIMUTH IN RANGE',F7.1,' TO',F7.1,
     % 'DEGREES.')
      GO TO 120
  119 AZMAX=400.D0
  120 Y(1,1)=0.D0
      NW=0
      N=0
      NEQ=1
C
C***  READ IN EVENT CARD, CHECK IF TO BE USED, AND IF SO USE TO SET UP
C     FIRST EQUATION.
C
  200 N=N+1
      READ(5,201)IT(N),ELT(N),ELN(N),DPT(N),EMG(N),IR(N),IH(N),IM(N),
     % SC(N),DL(N),BB(N),AZ(N),IWE(N)
  201 FORMAT(I8,2F9.3,F4.0,F4.1,I4,2I3,F6.2,3F4.0,I2)
      IF(IT(N).EQ.0)GO TO 400
      IF(N.LE.IEMAX) GO TO 206
      WRITE(6,205) IEMAX
  205 FORMAT('0***ERROR*** ATTEMPT TO INPUT MORE THAN',I4,' EVENTS')
      STOP1
  206 CALL DCNT(IT(N),T,K1(1),K1(2),K1(3),K1(4))
      IF(.NOT.ANG(T,TMIN,TMAX)) GO TO 210
      IF(.NOT.ANG(DL(N),DMIN,DMAX)) GO TO 210
      IF(.NOT.ANG(BB(N),BBMIN,BBMAX)) GO TO 210
      IF(.NOT.ANG(AZ(N),AZMIN,AZMAX)) GO TO 210
      GO TO 220
  210 IUS(N)=0
```

```
      GO TO 200
  220 NW=NW+1
      IUS(N)=NW
      IF(IWE(N))800,222,224
  222 A(1,NW)=0.D0
      GO TO 200
  224 A(1,NW)=WF**(IWE(N)-5)
      EWS=.TRUE.
      GO TO 200
  400 N=N-1
      NUWS=0
      SW=0.D0
      DO 402 I=1,NW
  402 NDU(I)=0
      NU=NW+NS
      JS=NW+1
      DO 403 I=JS,NU
      A(1,I)=0.D0
  403 NDU(I)=0
C
C***  READ DELAY CARD AND MATCH WITH EVENT
C
  406 READ(5,407,END=500)ITD,(IS(J),DR(J),IW(J),J=1,7)
  407 FORMAT(I8,2X,7(I3,F5.2,I2))
      DO 409 I=1,N
      IF(ITD.NE.IT(I)) GO TO 409
      IE=I
      GO TO 420
  409 CONTINUE
C
C***  EVENT NOT FOUND, PRINT WARNING MESSAGE
C
      IF(PR1) WRITE(6,411)
  411 FORMAT('0 UNABLE TO MATCH FOLLOWING DELAY CARD(S) WITH EVENT(S):')
      WRITE(6,413)ITD,(IS(J),DR(J),IW(J),J=1,7)
  413 FORMAT(2X,I8,2X,7(I3,F5.2,I2))
      PR1=.FALSE.
      GO TO 406
C
C***  EVENT FOUND. CHECK IF DELAYS TO BE USED.
C
  420 IF(IUS(IE).EQ.0) GO TO 406
C
C***  FOR EACH STATION IN TURN FIND STATION INDEX, AND CONSTRUCT
C     EQUATION, AND STORE WEIGHTS.
C
      DO 490 J=1,7
      IF(IS(J).EQ.0) GO TO 490
      DO 440 I=1,NS
      IF(IS(J).NE.IST(I))GO TO 440
      II=I
      GO TO 460
  440 CONTINUE
      IF(NUWS.EQ.0)GO TO 450
      DO 448 I=1,NUWS
      IF(IS(J).EQ.IUWS(I)) GO TO 490
  448 CONTINUE
  450 NUWS=NUWS+1
      IUWS(NUWS)=IS(J)
      IUWE(NUWS)=ITD
```

```
      DUWD(NUWS)=DR(J)
      IUWW(NUWS)=IW(J)
      GO TO 490
  460 NEQ=NEQ+1
      IF(NEQ.LE.ID1) GO TO 465
      WRITE(6,463) IDMAX
  463 FORMAT('0 ***ERROR***  ATTEMPT TO USE MORE THAN',I4,' DELAYS')
      STOP3
  465 DO 466 I=1,NU
  466 A(NEQ,I)=0.DO
      IWD(NEQ)=IW(J)
      TD=WLST(IW(J))
      Y(NEQ,1)=DR(J)*TD
      A(NEQ,IUS(IE))=TD
      A(NEQ,NW+II)=TD
      SW=SW+TD**2
      NDU(IUS(IE))=NDU(IUS(IE))+1
      NDU(NW+II)=NDU(NW+II)+1
  490 CONTINUE
      GO TO 406
C
C***  CHECK FOR OMISSIONS IN DATA
C
  500 IF(NUWS.EQ.0) GO TO 512
      WRITE(6,501)
  501 FORMAT('0 *WARNING* THE FOLLOWING UNDECLARED STATIONS HAVE ',
     * 'AT LEAST ONE DELAY INPUTTED :/
     % '0 STATION EVENT NUMBER DELAY WEIGHT')
      DO 508 I=1,NUWS
       CALL DCNT(IUWE(I),TD,K1(1),K1(2),K1(3),K1(4))
      WRITE(6,505)IUWS(I),K1,DUWD(I),IUWW(I)
  505 FORMAT(1X,I9,I4,3('/',I2),F8.2,I8)
  508 CONTINUE
  512 DO 518 I=1,NU
      IF(NDU(I).GT.0) GO TO 518
      IF(I.GT.NW) GO TO 514
      DO 516 J=1,N
      IF(IUS(J).NE.I) GO TO 516
      CALL DCNT(IT(J),TD,K1(1),K1(2),K1(3),K1(4))
      WRITE(6,513)K1
  513 FORMAT('0 ***ERROR***  EVENT NUMBER',I3,3('/',I2),
     % ' HAS NO ASSOCIATED DELAYS INPUTTED')
      STOP4
  516 CONTINUE
      GO TO 800
  514 WRITE(6,519) IST(I-NW)
  519 FORMAT('0 ***ERROR***  STATION NUMBER',I3,
     % ' HAS NO ASSOCIATED DELAY INPUTTED')
      STOP6
  518 CONTINUE
      IF(EWS) GO TO 522
      WRITE(6,521)
  521 FORMAT('0 ***ERROR***  NO EVENT IS ASSIGNED A NON ZERO WEIGHT')
      STOP5
C
C*** CALCULATE UNKNOWNS
C
  522 IFAIL=0
      CALL F04AMF(A,ID1,X,ID2,Y,ID1,NEQ,NU,1,EPS,
     % QR,ID1,R1,R2,R3,R4,R5,IPIV,IFAIL)
```

```
C
C***  CALCULATE RESIDUALS, AND USE TO CALCULATE ERRORS IN UNKNOWNS.
C
      SR2=0.D0
      DO 530 I=1,NEQ
      R(I)=Y(I,1)
       DO 528 J=1,NU
  528 R(I)=R(I)-A(I,J)*X(J,1)
  530 SR2=SR2+R(I)**2
      SR2=DSQRT(SR2/SW)
      DO 540 I=1,NU
      E(I)=0.D0
      IE=0
      SW=0.D0
      DO 536 J=1,NEQ
      IF(A(J,I))536,536,533
  533 IE=IE+1
      E(I)=E(I)+R(J)**2
      SW=SW+A(J,I)**2
  536 CONTINUE
      IF(IE-1)800,537,538
  537 E(I)=-1.D0
      GO TO 540
  538 E(I)=DSQRT(E(I)/((IE-1)*SW))
  540 CONTINUE
C
C***  WRITE EVENT INFORMATION FOR EACH EVENT IN TURN
C
      WRITE(6,601)
  601 FORMAT('0',120('*'))
      DO 690 I=1,N
      DO 610 J=1,5
      IF(IR(I))800,602,606
  602 CHR(J)=BLNK
      CHA(J)=BLNK
      GO TO 610
  606 CHR(J)=REG(J,IR(I))
      CHA(J)=AR(J,NAR(IR(I)))
  610 CONTINUE
C
C***  TEST IF EVENT WAS USED
C
      IF (IUS(I).NE.0) GO TO 630
      CALL DCNT(IT(I),TD,K1(1),K1(2),K1(3),K1(4))
      IF(UWPR) WRITE(6,623)K1,IR(I),CHR,CHA,ELT(I),ELN(I),DPT(I),EMG(I),
     % IH(I),IM(I),SC(I),DL(I),BB(I),AZ(I),IWE(I)
  623 FORMAT('0 EVENT NUMBER',I3,3('/',I2),'  REGION',I4,2X,10A8/
     % '   LATITUDE',F10.4,' LONGITUDE',F10.4,' DEPTH',F5.0,
     % ' MAGNITUDE',F4.1,'  ORIGIN TIME',I3,'-',I2,
     % F7.2,' SEC.'/'  DISTANCE',F5.0,' B-BRNG.',F5.0,
     % ' AZMTH',F5.0,'  WT=',I1,' ***  EVENT NOT USED  ***'/
     % '0',120('*'))
      GO TO 690
C
C***  EVENT USED
C
  630 IC=IUS(I)
      CALL DCNT(IT(I),TD,K1(1),K1(2),K1(3),K1(4))
      WRITE(6,635)K1,IR(I),CHR,CHA,ELT(I),ELN(I),DPT(I),EMG(I),
     % IH(I),IM(I),SC(I),DL(I),BB(I),AZ(I),IWE(I),X(IUS(I),1),E(IUS(I))
```

```
  635 FORMAT('0 EVENT NUMBER',I3,3('/',I2),'  REGION',I4,2X,10A8/
     % '  LATITUDE',F10.4,' LONGITUDE',F10.4,' DEPTH',F5.0,
     % ' MAGNITUDE',F4.1,'  ORIGIN TIME',I3,'-',I2,
     % F7.2,' SEC.'/'  DISTANCE',F5.0,' B-BRNG',F5.0,
     % ' AZMTH',F5.0,'  WT=',I1,'  DELAY=',F7.3,' ERROR=',F6.3)
      IE=1
  640 II=0
  642 IE=IE+1
      IF(NEQ-IE)655,643,643
  643 IF(A(IE,IC))800,642,644
  644 DO 648 IJ=JS,NU
      IF(A(IE,IJ))800,648,646
  646 JJ=IJ
      GO TO 650
  648 CONTINUE
      GO TO 800
  650 II=II+1
      IS(II)=IST(JJ-NW)
      DR(II)=Y(IE,1)/A(IE,JJ)
      RR(II)=R(IE)/A(IE,JJ)
      DC(II)=DR(II)-RR(II)
      IW(II)=IWD(IE)
      IF(II-12)642,655,800
  655 IF(II)800,690,670
  670 WRITE(6,671)(IS(J),J=1,II)
  671 FORMAT('0 STATION   ',8X,12I8)
      WRITE(6,673)(DR(J),J=1,II)
  673 FORMAT('  MEASURED DELAY',4X,12F8.3)
      WRITE(6,675)(DC(J),J=1,II)
  675 FORMAT('  CALCULATED DELAY',2X,12F8.3)
       WRITE(6,677)(RR(J),J=1,II)
  677 FORMAT('  RESIDUAL',10X,12F8.3)
      WRITE(6,679)(IW(J),J=1,II)
  679 FORMAT('  WEIGHT',12X,12I8)
      WRITE(6,601)
      GO TO 640
  690 CONTINUE
      WRITE(6,701)
  701 FORMAT('1',26X,23('*')/27X,'* STATION INFORMATION *'/
     % 27X,23('*'))
      II=1
  704 IF=II+11
      IF(IF.GT.NS)IF=NS
      WRITE(6,711)(IST(J),J=II,IF)
  711 FORMAT('0 STATION NUMBER',6X,12I8)
      WRITE(6,713)(NDU(J+NW),J=II,IF)
  713 FORMAT('  NO. OF DELAYS USED',2X,12I8)
      WRITE(6,715)(X(J+NW,1),J=II,IF)
  715 FORMAT('  STATION DELAY',7X,12F8.3)
      WRITE(6,717)(E(J+NW),J=II,IF)
  717 FORMAT('  ERROR',15X,12F8.3)
      IF(IF.EQ.NS)GO TO 730
      II=II+12
      GO TO 704
  730 NEQ=NEQ-1
      TD=SR2/DSQRT(DFLOAT(NEQ-NU))
      WRITE(6,731)N,NW,NEQ,NS,SR2,TD
  731 FORMAT('0'//'  NUMBER OF EVENTS INPUT =',I4,
     % '  NUMBER USED =',I4,'  NUMBER OF DELAYS =',I5/
     % '  NUMBER OF STATIONS =',I3,'  R.M.S. OF RESIDUALS =',F8.4,
```

```
     % '  STANDARD ERROR OF SOLUTION =',F8.5)
      WRITE(6,601)
      STOP0
  800 WRITE(6,801)
  801 FORMAT('0***ERROR*** BUG IN PROGRAM TERMINATES EXECUTION')
      STOP2
      END
C
C***********************************************************************
C
      SUBROUTINE DCNT(I,T,MN,HR,DY,YR)
C
C***  TO CONVERT U.D.K.S.P. EVENT NUMBERS INTO MINUTES, HOURS, DAYS,
C    AND YEARS, AND ALSO INTO DAYS AND DECIMALS THEREOF AFTER 1ST
C    JANUARY 1976.
C
      REAL*8 T
      INTEGER MN,HR,DY,YR
      YR=I-100*(I/100)
      DY=I/100-100*(I/10000)
      HR=I/10000-100*(I/1000000)
      MN=I/1000000
      T=1.D2*DFLOAT(YR-10)+DFLOAT(DY)+(DFLOAT(HR)+DFLOAT(MN)/6.D1)/2.4D1
      IF(T.GT.1.D3)T=T-634.D0
      RETURN
      END
      LOGICAL FUNCTION ANG(X,XMIN,XMAX)
      REAL*8 X, XMIN,XMAX
      ANG=.TRUE.
      IF(XMAX.LT.XMIN) GO TO 5
      IF(X.GT.XMAX.OR.X.LT.XMIN) ANG=.FALSE.
      RETURN
    5 IF(X.LT.XMIN.AND.X.GT.XMAX) ANG=.FALSE.
      RETURN
      END
```

APPENDIX 4

EVENTS USED AND RAW (MEASURED) DELAY TIMES

As listed by program SEPD.

```
**************************
* PROGRAM SEPD (02APR79) *
**************************

MAXIMUM NUMBER OF EVENTS IS 130, MAXIMUM NUMBER OF STATIONS IS 30, MAXIMUM NUMBER OF DELAYS IS 500.

ONSET WEIGHT CODE:     1    2    3    4    5    6    7    8    9
  ASSIGNED WEIGHT:   0.0  0.06 0.11 0.24 0.86 2.47 0.0  0.0  0.0

*****************************************************************************************************

EVENT NUMBER 22/ 0/ 7/10  REGION 269  MOLUCCA SEA                                  BORNEO - CELEBES
LATITUDE    -0.1450 LONGITUDE  124.8320 DEPTH  79. MAGNITUDE 5.7  ORIGIN TIME  0- 9  52.50 SEC.
DISTANCE  88. B-BRNG  90. AZMTH 269.  WT=6  DELAY=  1.854 ERROR= 0.013

STATION                  30       27
MEASURED DELAY        4.090    4.510
CALCULATED DELAY      4.115    4.485
RESIDUAL             -0.025    0.025
WEIGHT                    6        6

*****************************************************************************************************

EVENT NUMBER 33/ 0/ 7/10  REGION 303  KASHMIR-INDIA BORDER REGION                  INDIA - TIBET - SZECHWAN
LATITUDE   32.8540 LONGITUDE   75.9640 DEPTH  50. MAGNITUDE 5.4  ORIGIN TIME  0-24  54.10 SEC.
DISTANCE  50. B-BRNG  44. AZMTH 235.  WT=4  DELAY=  2.689 ERROR= 0.051

STATION                  30       27
MEASURED DELAY        4.860    5.410
CALCULATED DELAY      4.950    5.320
RESIDUAL             -0.090    0.090
WEIGHT                    4        4

*****************************************************************************************************

EVENT NUMBER 43/21/ 9/10  REGION 277  JAVA                                         SUNDA ARC
LATITUDE    -7.8190 LONGITUDE  108.1970 DEPTH 101. MAGNITUDE 5.8  ORIGIN TIME 21-32  16.10 SEC.
DISTANCE  71. B-BRNG  98. AZMTH 271.  WT=5  DELAY=  0.043 ERROR= 0.014

STATION                  30       27       21
MEASURED DELAY        2.330    2.640    3.360
CALCULATED DELAY      2.303    2.674    3.334
RESIDUAL              0.027   -0.034    0.026
WEIGHT                    5        5        4

*****************************************************************************************************

EVENT NUMBER 13/ 0/10/10  REGION 186  NEW HEBRIDES ISLANDS                         NEW HEBRIDES ISLANDS
LATITUDE   -15.7590 LONGITUDE  167.8680 DEPTH 168. MAGNITUDE 6.1  ORIGIN TIME 23-54  35.60 SEC.
DISTANCE 129. B-BRNG 111. AZMTH 255.  WT=5  DELAY= -1.111 ERROR= 0.089

STATION                  30       27       21
MEASURED DELAY        1.220    1.390    2.480
CALCULATED DELAY      1.149    1.519    2.180
RESIDUAL              0.071   -0.129    0.300
WEIGHT                    5        6        5

*****************************************************************************************************

EVENT NUMBER 59/ 8/10/10  REGION 425  SOUTH INDIAN OCEAN                           INDIAN OCEAN
LATITUDE   -35.1010 LONGITUDE   54.3600 DEPTH  33. MAGNITUDE 5.7  ORIGIN TIME  8-52  51.80 SEC.
DISTANCE  37. B-BRNG 156. AZMTH 330.  WT=4  DELAY= -1.959 ERROR= 0.046

STATION                  30       27       21
MEASURED DELAY        0.370    0.470    1.320
CALCULATED DELAY      0.301    0.672    1.332
RESIDUAL              0.069   -0.202   -0.012
WEIGHT                    5        4        5

*****************************************************************************************************

EVENT NUMBER  1/13/10/10  REGION 332  NORTHERN SINKIANG PROV., CHINA               ALMA-ATA TO LAKE BAIKAL
LATITUDE    4[illegible].1360 LONGITUDE   83.3940 DEPTH  34. MAGNITUDE 5.4  ORIGIN TIME 12-51  25.00 SEC.
DISTANCE  60. B-BRNG  38. AZMTH 237.  WT=3  DELAY= -0.576 ERROR= 0.100

STATION                  27       21       30
MEASURED DELAY        2.220    2.440    1.600
CALCULATED DELAY      2.055    2.715    1.685
RESIDUAL              0.165   -0.275   -0.085
WEIGHT                    4        3        3

*****************************************************************************************************
```

EVENT NUMBER 41/13/13/10 REGION 637 ICELAND REGION ARCTIC ZONE
LATITUDE 66.1570 LONGITUDE -16.5820 DEPTH 33. MAGNITUDE 6.0 ORIGIN TIME 13-29 19.50 SEC.
DISTANCE 77. B-BRNG 340. AZMTH 125. WT=2 DELAY= 3.541 ERROR= 0.094

STATION	19	30	27	21
MEASURED DELAY	6.270	6.130	6.270	6.790
CALCULATED DELAY	6.446	5.801	6.172	6.832
RESIDUAL	-0.176	0.329	0.098	-0.042
WEIGHT	4	3	3	3

****

EVENT NUMBER 58/ 4/18/10 REGION 643 SVALBARD REGION ARCTIC ZONE
LATITUDE 77.8710 LONGITUDE 18.6360 DEPTH 33. MAGNITUDE 5.6 ORIGIN TIME 4-46 24.40 SEC.
DISTANCE 80. B-BRNG 356. AZMTH 162. WT=3 DELAY= 0.411 ERROR= 0.026

STATION	19	27	21
MEASURED DELAY	3.270	3.040	3.790
CALCULATED DELAY	3.316	3.042	3.702
RESIDUAL	-0.046	-0.002	0.088
WEIGHT	3	3	2

****

EVENT NUMBER 56/ 5/23/10 REGION 279 FLORES SEA SUNDA ARC
LATITUDE -7.4780 LONGITUDE 119.9050 DEPTH 614. MAGNITUDE 6.4 ORIGIN TIME 5-45 30.50 SEC.
DISTANCE 83. B-BRNG 97. AZMTH 270. WT=7 DELAY= -0.307 ERROR= 0.054

STATION	30	27	26	21	19
MEASURED DELAY	1.730	2.290	2.610	2.840	2.710
CALCULATED DELAY	1.954	2.324	2.342	2.984	2.599
RESIDUAL	-0.224	-0.034	0.268	-0.144	0.111
WEIGHT	6	5	6	6	6

****

EVENT NUMBER 7/22/24/10 REGION 177 KERMADEC ISLANDS REGION KERMADEC - TONGA - SAMOA
LATITUDE -28.6350 LONGITUDE -177.5930 DEPTH 78. MAGNITUDE 6.2 ORIGIN TIME 21-48 25.90 SEC.
DISTANCE 136. B-BRNG 135. AZMTH 238. WT=2 DELAY= -0.409 ERROR= 0.030

STATION	30	21	19
MEASURED DELAY	1.780	2.900	2.550
CALCULATED DELAY	1.851	2.882	2.497
RESIDUAL	-0.071	0.018	0.053
WEIGHT	4	4	4

****

EVENT NUMBER 36/ 7/29/10 REGION 278 BALI SEA SUNDA ARC
LATITUDE -6.8960 LONGITUDE 117.1740 DEPTH 458. MAGNITUDE 5.1 ORIGIN TIME 7-25 45.10 SEC.
DISTANCE 80. B-BRNG 97. AZMTH 270. WT=6 DELAY= -1.180 ERROR= 0.040

STATION	30	29	27	21	19
MEASURED DELAY	1.000	0.920	1.650	2.260	1.770
CALCULATED DELAY	1.080	1.089	1.451	2.111	1.726
RESIDUAL	-0.080	-0.169	0.199	0.149	0.044
WEIGHT	5	5	4	5	5

****

EVENT NUMBER 34/11/32/10 REGION 59 GUERRERO, MEXICO MEXICO - GUATEMALA AREA
LATITUDE 17.1720 LONGITUDE -100.1890 DEPTH 52. MAGNITUDE 5.7 ORIGIN TIME 11-14 57.30 SEC.
DISTANCE 135. B-BRNG 293. AZMTH 74. WT=3 DELAY= 0.269 ERROR= 0.112

STATION	30	29	19
MEASURED DELAY	2.270	2.370	3.370
CALCULATED DELAY	2.529	2.537	3.174
RESIDUAL	-0.259	-0.167	0.196
WEIGHT	3	3	4

****

EVENT NUMBER 38/10/32/10 REGION 289 TIMOR SUNDA ARC
LATITUDE -9.3170 LONGITUDE 123.7520 DEPTH 15. MAGNITUDE 5.7 ORIGIN TIME 14-25 54.40 SEC.
DISTANCE 87. B-BRNG 100. AZMTH 270. WT=3 DELAY= 1.663 ERROR= 0.114

STATION	30	29	19
MEASURED DELAY	3.760	3.740	4.820
CALCULATED DELAY	3.923	3.932	4.569
RESIDUAL	-0.163	-0.192	0.251
WEIGHT	4	3	4

****

EVENT NUMBER 35/ 5/34/10 REGION 262 CELEBES SEA BORNEO - CELEBES
LATITUDE 5.1030 LONGITUDE 122.0840 DEPTH 576. MAGNITUDE 5.1 ORIGIN TIME 5-23 37.40 SEC.
DISTANCE 86. B-BRNG 86. AZMTH 268. WT=5 DELAY= -0.700 ERROR= 0.069

STATION	30	29	27	19
MEASURED DELAY	1.650	1.300	2.070	2.070
CALCULATED DELAY	1.560	1.568	1.931	2.206
RESIDUAL	0.090	-0.268	0.139	-0.136
WEIGHT	6	5	6	6

****

EVENT NUMBER 57/10/34/10 REGION 280 BANDA SEA SUNDA ARC
LATITUDE -7.0590 LONGITUDE 123.7430 DEPTH 611. MAGNITUDE 5.2 ORIGIN TIME 10-45 58.10 SEC.
DISTANCE 87. B-BRNG 97. AZMTH 270. WT=6 DELAY= -0.065 ERROR= 0.030

STATION	19	30	27
MEASURED DELAY	2.820	2.120	2.700
CALCULATED DELAY	2.841	2.195	2.566
RESIDUAL	-0.021	-0.075	0.134
WEIGHT	6	5	5

****

EVENT NUMBER 45/12/34/10 REGION 171 SOUTH OF FIJI ISLANDS KERMADEC - TONGA - SAMOA A
LATITUDE -25.1360 LONGITUDE 179.6930 DEPTH 477. MAGNITUDE 5.8 ORIGIN TIME 12-27 30.10 SEC.
DISTANCE 136. B-BRNG 129. AZMTH 239. WT=2 DELAY= -2.007 ERROR= 0.007

STATION	30	27
MEASURED DELAY	0.280	0.620
CALCULATED DELAY	0.253	0.623
RESIDUAL	0.027	-0.003
WEIGHT	3	5

****

EVENT NUMBER 48/16/34/10 REGION 344 N.W. IRAN-USSR BORDER REGION WESTERN ASIA
LATITUDE 39.9330 LONGITUDE 48.4150 DEPTH 58. MAGNITUDE 5.2 ORIGIN TIME 16-40 40.60 SEC.
DISTANCE 42. B-BRNG 13. AZMTH 197. WT=3 DELAY= -0.054 ERROR= 0.103

STATION	30	29	27
MEASURED DELAY	1.950	2.330	2.230
CALCULATED DELAY	2.206	2.214	2.576
RESIDUAL	-0.256	0.116	-0.346
WEIGHT	4	5	3

****

EVENT NUMBER 6/20/35/10 REGION 278 BALI SEA SUNDA ARC
LATITUDE -6.9830 LONGITUDE 115.7470 DEPTH 413. MAGNITUDE 5.0 ORIGIN TIME 19-55 30.50 SEC.
DISTANCE 79. B-BRNG 97. AZMTH 270. WT=5 DELAY= -0.946 ERROR= 0.023

STATION	30	27
MEASURED DELAY	1.350	1.650
CALCULATED DELAY	1.315	1.685
RESIDUAL	0.035	-0.035
WEIGHT	6	6

****

EVENT NUMBER 20/ 8/44/10 REGION 249 LUZON, PHILIPPINE ISLANDS PHILIPPINES
LATITUDE 15.6700 LONGITUDE 121.7030 DEPTH 47. MAGNITUDE 5.4 ORIGIN TIME 8- 7 32.60 SEC.
DISTANCE 85. B-BRNG 74. AZMTH 267. WT=6 DELAY= 0.906 ERROR= 0.048

STATION	30	28	27
MEASURED DELAY	3.280	3.400	3.350
CALCULATED DELAY	3.167	3.448	3.537
RESIDUAL	0.113	-0.048	-0.187
WEIGHT	6	6	5

****

EVENT NUMBER 46/10/44/10 REGION 250 MINDORO, PHILIPPINE ISLANDS PHILIPPINES
LATITUDE 13.9160 LONGITUDE 120.1230 DEPTH 29. MAGNITUDE 5.6 ORIGIN TIME 10-33 42.70 SEC.
DISTANCE 84. B-BRNG 76. AZMTH 267. WT=5 DELAY= 0.906 ERROR= 0.031

STATION	30	29	28	27
MEASURED DELAY	3.140	3.110	3.370	3.630
CALCULATED DELAY	3.166	3.174	3.448	3.537
RESIDUAL	-0.026	-0.064	-0.078	0.093
WEIGHT	4	5	4	5

****

EVENT NUMBER 7/ 2/46/10 REGION 248 PHILIPPINE ISLANDS REGION PHILIPPINES
LATITUDE 13.0000 LONGITUDE 125.7800 DEPTH 33. MAGNITUDE 6.1 ORIGIN TIME 1-54 23.10 SEC.
DISTANCE 89. B-BRNG 77. AZMTH 269. WT=3 DELAY= -0.871 ERROR= 0.037

STATION	30	29	27
MEASURED DELAY	1.470	1.350	1.690
CALCULATED DELAY	1.390	1.398	1.760
RESIDUAL	0.080	-0.048	-0.070
WEIGHT	4	4	3

****

EVENT NUMBER 57/ 7/53/10 REGION 706 NORTHERN SUMATRA ANDAMAN ISLANDS TO SUMA
LATITUDE 3.1660 LONGITUDE 99.0150 DEPTH 180. MAGNITUDE 5.6 ORIGIN TIME 7-47 59.50 SEC.
DISTANCE 62. B-BRNG 86. AZMTH 267. WT=5 DELAY= -0.008 ERROR= 0.018

STATION	30	29	27
MEASURED DELAY	2.270	2.280	2.560
CALCULATED DELAY	2.252	2.260	2.622
RESIDUAL	0.018	0.020	-0.062
WEIGHT	4	6	5

****

EVENT NUMBER 15/ 9/54/10 REGION 244 TAIWAN TAIWAN
LATITUDE 23.0190 LONGITUDE 121.6870 DEPTH 33. MAGNITUDE 5.5 ORIGIN TIME 9- 2 31.60 SEC.
DISTANCE 86. B-BRNG 67. AZMTH 267. WT=4 DELAY= 0.176 ERROR= 0.020

STATION	30	29	27
MEASURED DELAY	2.390	2.370	2.830
CALCULATED DELAY	2.436	2.444	2.807
RESIDUAL	-0.046	-0.074	0.023
WEIGHT	5	4	6

****

EVENT NUMBER 39/14/55/10 REGION 280 BANDA SEA SUNDA ARC
LATITUDE -7.2570 LONGITUDE 129.1610 DEPTH 124. MAGNITUDE 5.3 ORIGIN TIME 14-26 45.40 SEC.
DISTANCE 92. B-BRNG 97. AZMTH 268. WT=4 DELAY= 0.427 ERROR= 0.050

STATION	30	29	27
MEASURED DELAY	2.720	2.560	3.160
CALCULATED DELAY	2.687	2.695	3.058
RESIDUAL	0.033	-0.135	0.102
WEIGHT	4	4	4

****

EVENT NUMBER 2/23/63/10 REGION 286 FLORES ISLAND REGION SUNDA ARC
LATITUDE -8.2320 LONGITUDE 121.4380 DEPTH 30. MAGNITUDE 6.0 ORIGIN TIME 22-50 10.00 SEC.
DISTANCE 85. B-BRNG 98. AZMTH 270. WT=6 DELAY= -0.014 ERROR= 0.023

STATION	30	29
MEASURED DELAY	2.290	2.210
CALCULATED DELAY	2.246	2.254
RESIDUAL	0.044	-0.044
WEIGHT	6	6

****

EVENT NUMBER 8/ 3/64/10 REGION 186 NEW HEBRIDES ISLANDS NEW HEBRIDES ISLANDS
LATITUDE -14.7440 LONGITUDE 167.1040 DEPTH 90. MAGNITUDE 6.4 ORIGIN TIME 2-50 0.50 SEC.
DISTANCE 128. B-BRNG 110. AZMTH 256. WT=4 DELAY= -1.022 ERROR= 0.021

STATION	30	29	27
MEASURED DELAY	1.270	1.240	1.520
CALCULATED DELAY	1.239	1.247	1.609
RESIDUAL	0.031	-0.007	-0.089
WEIGHT	5	5	4

****

EVENT NUMBER 19/11/66/10 REGION 265 NORTHERN SULAWESI BORNEO - CELEBES
LATITUDE 0.8380 LONGITUDE 122.6000 DEPTH 51. MAGNITUDE 5.5 ORIGIN TIME 11- 7 14.30 SEC.
DISTANCE 86. B-BRNG 89. AZMTH 269. WT=3 DELAY= -0.410 ERROR= 0.037

STATION	25	27	18	29
MEASURED DELAY	2.150	2.280	2.640	1.760
CALCULATED DELAY	2.190	2.221	2.799	1.859
RESIDUAL	-0.040	0.059	-0.159	-0.099
WEIGHT	4	5	3	4

****

EVENT NUMBER 35/ 7/76/10 REGION 353 SOUTHERN IRAN WESTERN ASIA
LATITUDE 27.3120 LONGITUDE 55.0630 DEPTH 33. MAGNITUDE 5.4 ORIGIN TIME 7-28 57.60 SEC.
DISTANCE 33. B-BRNG 30. AZMTH 215. WT=5 DELAY= 0.431 ERROR= 0.030

STATION	25	27	29	28	18
MEASURED DELAY	3.050	2.970	2.780	2.930	3.520
CALCULATED DELAY	3.031	3.062	2.700	2.974	3.640
RESIDUAL	0.019	-0.092	0.080	-0.044	-0.120
WEIGHT	6	6	6	4	2

****

EVENT NUMBER 34/14/77/10 REGION 41 SOUTHERN NEVADA CALIFORNIA - NEVADA RE(
LATITUDE 37.2560 LONGITUDE -116.3120 DEPTH 0. MAGNITUDE 6.1 ORIGIN TIME 14-15 0.10 SEC.
DISTANCE 136. B-BRNG 328. AZMTH 41. WT=2 DELAY= -1.271 ERROR= 0.104

STATION	27	29	28
MEASURED DELAY	1.190	1.250	1.190
CALCULATED DELAY	1.360	0.998	1.272
RESIDUAL	-0.170	0.252	-0.082
WEIGHT	4	4	4

****

EVENT NUMBER 12/13/79/10 REGION 718 HINDU KUSH REGION HINDU KUSH AND PAMIR
LATITUDE 36.6070 LONGITUDE 67.7850 DEPTH 33. MAGNITUDE 5.6 ORIGIN TIME 13- 3 38.40 SEC.
DISTANCE 47. B-BRNG 34. AZMTH 224. WT=5 DELAY= -0.191 ERROR= 0.035

STATION	28	27	25	18	29
MEASURED DELAY	2.150	2.480	2.330	3.040	2.140
CALCULATED DELAY	2.352	2.440	2.409	3.018	2.078
RESIDUAL	-0.202	0.040	-0.079	0.022	0.062
WEIGHT	5	5	5	6	6

****

EVENT NUMBER 19/ 1/80/10 REGION 244 TAIWAN TAIWAN
LATITUDE 24.2840 LONGITUDE 121.8000 DEPTH 40. MAGNITUDE 5.5 ORIGIN TIME 1- 6 58.70 SEC.
DISTANCE 86. B-BRNG 66. AZMTH 267. WT=3 DELAY= 0.032 ERROR= 0.039

STATION	29	28	27	25
MEASURED DELAY	2.260	2.580	2.860	2.600
CALCULATED DELAY	2.300	2.574	2.662	2.631
RESIDUAL	-0.040	0.006	0.198	-0.031
WEIGHT	6	5	5	[illegible]

****

EVENT NUMBER 5/ 5/84/10 REGION 178 KERMADEC ISLANDS KERMADEC - TONGA - SAM(
LATITUDE -29.8870 LONGITUDE -177.8730 DEPTH 33. MAGNITUDE 6.4 ORIGIN TIME 4-46 4.40 SEC.
DISTANCE 135. B-BRNG 136. AZMTH 233. WT=2 DELAY= 1.785 ERROR= 0.014

STATION	29	28	27	25
MEASURED DELAY	4.010	4.360	4.410	4.400
CALCULATED DELAY	4.053	4.327	4.416	4.384
RESIDUAL	-0.043	0.033	-0.006	0.016
WEIGHT	4	4	4	4

****

EVENT NUMBER 57/ 9/84/10 REGION 153 SOUTH SANDWICH ISLANDS REGION SOUTHERN ANTILLES
LATITUDE -56.1480 LONGITUDE -27.4270 DEPTH 33. MAGNITUDE 5.9 ORIGIN TIME 4-45 43.00 SEC.
DISTANCE 75. B-BRNG 211. AZMTH 69. WT=5 DELAY= 2.197 ERROR= 0.035

STATION	25	29	28	27
MEASURED DELAY	4.690	4.570	4.890	4.770
CALCULATED DELAY	4.796	4.465	4.739	4.828
RESIDUAL	-0.106	0.105	0.151	-0.058
WEIGHT	3	4	4	5

****

EVENT NUMBER 26/ 8/85/10 REGION 704 NICOBAR ISLANDS REGION ANDAMAN ISLANDS TO SUM(
LATITUDE 7.4770 LONGITUDE 94.5930 DEPTH 33. MAGNITUDE 5.3 ORIGIN TIME 8-16 30.30 SEC.
DISTANCE 58. B-BRNG 80. AZMTH 264. WT=5 DELAY= 1.409 ERROR= 0.064

STATION	25	29	28	27
MEASURED DELAY	4.190	3.700	3.690	4.100
CALCULATED DELAY	4.009	3.678	3.952	4.040
RESIDUAL	0.181	0.022	-0.262	0.060
WEIGHT	5	6	5	4

****

EVENT NUMBER 25/ 6/87/10 REGION 429 MID-INDIAN RISE INDIAN OCEAN
LATITUDE -38.6750 LONGITUDE 78.2595 DEPTH 33. MAGNITUDE 5.0 ORIGIN TIME 6-14 32.80 SEC.
DISTANCE 53. B-BRNG 140. AZMTH 304. WT=3 DELAY= 0.073 ERROR= 0.073

STATION	25	29	28
MEASURED DELAY	2.940	2.280	2.530
CALCULATED DELAY	2.672	2.341	2.615
RESIDUAL	0.268	-0.061	-0.085
WEIGHT	2	3	3

****

EVENT NUMBER 58/ 8/87/10 REGION 429 MID-INDIAN RISE INDIAN OCEAN
LATITUDE -38.7950 LONGITUDE 78.3280 DEPTH 33. MAGNITUDE 5.6 ORIGIN TIME 8-49 32.00 SEC.
DISTANCE 53. B-BRNG 140. AZMTH 304. WT=3 DELAY= -0.535 ERROR= 0.061

STATION	25	29	28	27
MEASURED DELAY	2.240	2.000	1.910	2.070
CALCULATED DELAY	2.064	1.734	2.007	2.096
RESIDUAL	0.176	0.266	-0.097	-0.026
WEIGHT	4	4	5	5

****

EVENT NUMBER 1/20/87/10 REGION 178 KERMADEC ISLANDS KERMADEC - TONGA - SAMOA
LATITUDE -30.5770 LONGITUDE -178.1980 DEPTH 59. MAGNITUDE 5.8 ORIGIN TIME 19-42 0.80 SEC.
DISTANCE 134. B-BRNG 137. AZMTH 233. WT=4 DELAY= -0.866 ERROR= 0.015

STATION	25	29	28	27
MEASURED DELAY	1.680	1.350	1.710	1.760
CALCULATED DELAY	1.733	1.402	1.676	1.765
RESIDUAL	-0.053	-0.052	0.034	-0.005
WEIGHT	4	4	5	5

****

EVENT NUMBER 31/20/88/10 REGION 403 NORTH ATLANTIC RIDGE ATLANTIC OCEAN
LATITUDE 33.7790 LONGITUDE -38.6290 DEPTH 33. MAGNITUDE 5.5 ORIGIN TIME 20-19 45.60 SEC.
DISTANCE 79. B-BRNG 305. AZMTH 99. WT=3 DELAY= -1.352 ERROR= 0.177

STATION	29	28	27	25
MEASURED DELAY	1.400	1.180	0.980	0.680
CALCULATED DELAY	0.917	1.190	1.279	1.248
RESIDUAL	0.483	-0.010	-0.299	-0.568
WEIGHT	3	3	2	2

****

EVENT NUMBER 58/ 5/89/10 REGION 76 OFF COAST OF CENTRAL AMERICA CENTRAL AMERICA
LATITUDE 3.9290 LONGITUDE -85.8800 DEPTH 33. MAGNITUDE 5.9 ORIGIN TIME 5-39 35.50 SEC.
DISTANCE 123. B-BRNG 274. AZMTH 89. WT=2 DELAY= -0.663 ERROR= 0.098

STATION	25	29	28	27
MEASURED DELAY	1.760	1.870	2.000	1.760
CALCULATED DELAY	1.937	1.606	1.880	1.968
RESIDUAL	-0.177	0.264	0.120	-0.208
WEIGHT	3	3	3	3

****

EVENT NUMBER 6/17/96/10 REGION 658 NORTHEASTERN CHINA EASTERN ASIA
LATITUDE 40.2170 LONGITUDE 112.2190 DEPTH 27. MAGNITUDE 5.3 ORIGIN TIME 16-54 40.10 SEC.
DISTANCE 80. B-BRNG 49. AZMTH 260. WT=5 DELAY= 0.856 ERROR= 0.030

STATION	28	27	25
MEASURED DELAY	3.330	3.600	3.410
CALCULATED DELAY	3.398	3.487	3.455
RESIDUAL	-0.068	0.113	-0.045
WEIGHT	4	4	4

****

EVENT NUMBER 10/ 3/97/10 REGION 429 MID-INDIAN RISE INDIAN OCEAN
LATITUDE -40.9300 LONGITUDE 78.7530 DEPTH 33. MAGNITUDE 5.4 ORIGIN TIME 3- 0 44.00 SEC.
DISTANCE 55. B-BRNG 142. AZMTH 305. WT=3 DELAY= 0.694 ERROR= 0.024

STATION	28	27
MEASURED DELAY	3.200	3.360
CALCULATED DELAY	3.236	3.324
RESIDUAL	-0.036	0.036
WEIGHT	4	4

****

EVENT NUMBER 49/ 2/[illegible]/10 REGION 339 UZBEK SSR WESTERN ASIA
LATITUDE 40.3310 LONGITUDE 63.7730 DEPTH 33. MAGNITUDE 6.5 ORIGIN TIME 2-40 27.00 SEC.
DISTANCE 48. B-BRNG 28. AZMTH 217. WT=4 DELAY= 0.673 ERROR= 0.028

STATION	25	28	27
MEASURED DELAY	3.220	3.280	3.290
CALCULATED DELAY	3.272	3.215	3.303
RESIDUAL	-0.052	0.065	-0.013
WEIGHT	6	6	6

****

EVENT NUMBER 7/ 3/99/10 REGION 339 UZBEK SSR WESTERN ASIA
LATITUDE 40.1670 LONGITUDE 63.8060 DEPTH 33. MAGNITUDE 6.2 ORIGIN TIME 2-59 5.50 SEC.
DISTANCE 48. B-BRNG 28. AZMTH 218. WT=4 DELAY= 1.188 ERROR= 0.024

STATION	25	28	27
MEASURED DELAY	3.700	3.770	3.810
CALCULATED DELAY	3.788	3.730	3.819
RESIDUAL	-0.088	0.040	-0.009
WEIGHT	5	6	6

****

EVENT NUMBER 53/10/99/10 REGION 275 JAVA SEA SUNDA ARC
LATITUDE -5.6080 LONGITUDE 111.5230 DEPTH 503. MAGNITUDE 5.2 ORIGIN TIME 10-42 53.00 SEC.
DISTANCE 75. B-BRNG 95. AZMTH 270. WT=5 DELAY= -0.355 ERROR= 0.008

STATION	27	25
MEASURED DELAY	2.290	2.230
CALCULATED DELAY	2.276	2.244
RESIDUAL	0.014	-0.014
WEIGHT	5	5

****

EVENT NUMBER 27/ 7/ 0/11 REGION 105 NEAR COAST OF ECUADOR ANDEAN SOUTH AME
LATITUDE 0.7820 LONGITUDE -79.8040 DEPTH 9. MAGNITUDE 6.1 ORIGIN TIME 7- 8 47.00 SEC.
DISTANCE 117. B-BRNG 270. AZMTH 91. WT=3 DELAY= -0.531 ERROR= 0.034

STATION	25	28	27
MEASURED DELAY	1.990	2.090	2.100
CALCULATED DELAY	2.069	2.011	2.100
RESIDUAL	-0.079	0.079	-0.000
WEIGHT	3	3	3

****

EVENT NUMBER 47/11/ 0/11 REGION 265 NORTHERN SULAWESI BORNEO - CELEBES
LATITUDE 0.9050 LONGITUDE 122.3750 DEPTH 105. MAGNITUDE 5.5 ORIGIN TIME 11-35 34.00 SEC.
DISTANCE 86. B-BRNG 89. AZMTH 269. WT=5 DELAY= -0.100 ERROR= 0.023

STATION	25	28	27
MEASURED DELAY	2.450	2.410	2.580
CALCULATED DELAY	2.499	2.442	2.531
RESIDUAL	-0.049	-0.032	0.049
WEIGHT	5	6	6

****

EVENT NUMBER 30/17/ 1/11 REGION 181 FIJI ISLANDS REGION FIJI ISLANDS ARE
LATITUDE -17.6500 LONGITUDE -178.5010 DEPTH 560. MAGNITUDE 5.7 ORIGIN TIME 17-12 9.20 SEC.
DISTANCE 140. B-BRNG 120. AZMTH 245. WT=1 DELAY= -0.717 ERROR= 0.047

STATION	25	28	27
MEASURED DELAY	1.890	1.920	1.810
CALCULATED DELAY	1.882	1.825	1.913
RESIDUAL	0.008	0.095	-0.103
WEIGHT	4	4	4

****

EVENT NUMBER 15/13/ 2/11 REGION 657 E. USSR-N.E. CHINA BORDER REGION EASTERN ASIA
LATITUDE 42.8290 LONGITUDE 130.8710 DEPTH 529. MAGNITUDE 5.0 ORIGIN TIME 13- 3 35.70 SEC.
DISTANCE 94. B-BRNG 47. AZMTH 272. WT=4 DELAY= -1.497 ERROR= 0.041

STATION	28	26	25
MEASURED DELAY	0.950	1.140	1.210
CALCULATED DELAY	1.046	1.152	1.103
RESIDUAL	-0.096	-0.012	0.107
WEIGHT	4	4	4

****

EVENT NUMBER 15/13/ 2/11 REGION 657 E. USSR-N.E. CHINA BORDER REGION EASTERN ASIA
LATITUDE 42.8290 LONGITUDE 130.8710 DEPTH 529. MAGNITUDE 5.0 ORIGIN TIME 13- 3 35.70 SEC.
DISTANCE 94. B-BRNG 47. AZMTH 272. WT=4 DELAY= -1.497 ERROR= 0.041

STATION	28	26	25
MEASURED DELAY	0.950	1.140	1.210
CALCULATED DELAY	1.046	1.152	1.103
RESIDUAL	-0.096	-0.012	0.107
WEIGHT	4	4	4

****

EVENT NUMBER 1/17/ 7/11 REGION 704 NICOBAR ISLANDS REGION ANDAMAN ISLANDS TO SUMA
LATITUDE 7.4940 LONGITUDE 94.3980 DEPTH 69. MAGNITUDE 5.2 ORIGIN TIME 5-53 56.10 SEC.
DISTANCE 86. B-BRNG 99. AZMTH 269. WT=6 DELAY= 0.251 ERROR= 0.053

STATION	25	27	26
MEASURED DELAY	2.920	2.750	3.080
CALCULATED DELAY	2.851	2.882	2.900
RESIDUAL	0.069	-0.132	0.180
WEIGHT	0	0	5

****

EVENT NUMBER 30/ 0/ 9/11 REGION 430 SOUTH OF AFRICA INDIAN OCEAN
LATITUDE -53.1630 LONGITUDE 25.3160 DEPTH 33. MAGNITUDE 5.4 ORIGIN TIME 0-21 24.50 SEC.
DISTANCE 52. B-BRNG 188. AZMTH 14. WT=5 DELAY= 0.867 ERROR= 0.052

STATION	25	27	26
MEASURED DELAY	3.530	3.570	3.380
CALCULATED DELAY	3.466	3.498	3.516
RESIDUAL	0.064	0.072	-0.136
WEIGHT	6	6	6

****

EVENT NUMBER 18/19/10/11 REGION 262 CELEBES SEA BORNEO - CELEBES
LATITUDE 4.1320 LONGITUDE 124.8060 DEPTH 303. MAGNITUDE 5.5 ORIGIN TIME 19- 6 11.20 SEC.
DISTANCE 88. B-BRNG 85. AZMTH 268. WT=6 DELAY= -0.776 ERROR= 0.023

STATION	27	26	25
MEASURED DELAY	1.920	1.860	1.770
CALCULATED DELAY	1.855	1.872	1.823
RESIDUAL	0.065	-0.012	-0.053
WEIGHT	6	6	6

****

EVENT NUMBER 9/17/13/11 REGION 353 SOUTHERN IRAN WESTERN ASIA
LATITUDE 28.7140 LONGITUDE 52.1280 DEPTH 24. MAGNITUDE 6.0 ORIGIN TIME 17- 3 7.90 SEC.
DISTANCE 33. B-BRNG 24. AZMTH 207. WT=4 DELAY= -0.190 ERROR= 0.019

STATION	25	27	26
MEASURED DELAY	2.440	2.360	2.450
CALCULATED DELAY	2.409	2.441	2.458
RESIDUAL	0.031	-0.081	-0.008
WEIGHT	5	4	5

****

EVENT NUMBER 52/ 6/20/11 REGION 177 KERMADEC ISLANDS REGION KERMADEC - TONGA - SAM
LATITUDE -28.1970 LONGITUDE -176.8870 DEPTH 62. MAGNITUDE 5.3 ORIGIN TIME 6-32 49.00 SEC.
DISTANCE 137. B-BRNG 135. AZMTH 234. WT=6 DELAY= 0.532 ERROR= 0.020

STATION	28	27	26	25
MEASURED DELAY	3.200	3.150	3.060	3.130
CALCULATED DELAY	3.074	3.162	3.180	3.131
RESIDUAL	0.126	-0.012	-0.120	-0.001
WEIGHT	4	3	4	3

****

EVENT NUMBER 11/ 5/26/11 REGION 178 KERMADEC ISLANDS KERMADEC - TONGA - SAM
LATITUDE -29.9340 LONGITUDE -177.8370 DEPTH 35. MAGNITUDE 6.2 ORIGIN TIME 4-52 51.00 SEC.
DISTANCE 136. B-BRNG 136. AZMTH 233. WT=5 DELAY= -1.228 ERROR= 0.058

STATION	25	28	26
MEASURED DELAY	1.510	1.450	1.220
CALCULATED DELAY	1.371	1.314	1.420
RESIDUAL	0.139	0.136	-0.200
WEIGHT	3	4	4

****

EVENT NUMBER 9/20/27/11 REGION 546 AUSTRIA NORTHWESTERN EUROPE
LATITUDE 46.3560 LONGITUDE 13.2750 DEPTH 9. MAGNITUDE 6.0 ORIGIN TIME 10- 0 11.60 SEC.
DISTANCE 52. B-BRNG 339. AZMTH 149. WT=5 DELAY= -0.344 ERROR= 0.099

STATION	25	28	26
MEASURED DELAY	2.380	2.370	2.090
CALCULATED DELAY	2.256	2.199	2.305
RESIDUAL	0.124	0.171	-0.215
WEIGHT	5	6	6

EVENT NUMBER 4/16/32/11 REGION 437 SOUTH OF AUSTRALIA INDIAN OCEAN
LATITUDE -51.6030 LONGITUDE 139.6830 DEPTH 33. MAGNITUDE 5.8 ORIGIN TIME 15-50 41.60 SEC.
DISTANCE 96. B-BRNG 142. AZMTH 259. WT=2 DELAY= 0.981 ERROR= 0.026

STATION	25	26
MEASURED DELAY	3.620	3.590
CALCULATED DELAY	3.580	3.630
RESIDUAL	0.040	-0.040
WEIGHT	2	2

EVENT NUMBER 7/17/32/11 REGION 399 IONIAN SEA WESTERN MEDITERRANEAN AI
LATITUDE 37.5600 LONGITUDE 20.3520 DEPTH 33. MAGNITUDE 5.8 ORIGIN TIME 16-59 48.20 SEC.
DISTANCE 42. B-BRNG 339. AZMTH 154. WT=2 DELAY= -0.872 ERROR= 0.070

STATION	25	28	26
MEASURED DELAY	1.860	1.650	1.650
CALCULATED DELAY	1.728	1.671	1.777
RESIDUAL	0.132	-0.021	-0.127
WEIGHT	5	4	5

EVENT NUMBER 7/ 3/38/11 REGION 339 UZBEK SSR WESTERN ASIA
LATITUDE 40.3810 LONGITUDE 63.6720 DEPTH 10. MAGNITUDE 6.3 ORIGIN TIME 2-58 40.60 SEC.
DISTANCE 48. B-BRNG 27. AZMTH 217. WT=5 DELAY= -0.100 ERROR= 0.051

STATION	31	26	25	24	23
MEASURED DELAY	2.990	2.530	2.370	2.300	2.820
CALCULATED DELAY	2.869	2.548	2.499	2.424	2.670
RESIDUAL	0.121	-0.018	-0.129	-0.124	0.150
WEIGHT	6	6	6	6	6

EVENT NUMBER 23/ 4/42/11 REGION 263 TALAUD ISLANDS BORNEO - CELEBES
LATITUDE 3.6840 LONGITUDE 125.0770 DEPTH 173. MAGNITUDE 5.9 ORIGIN TIME 4-11 15.20 SEC.
DISTANCE 38. B-BRNG 86. AZMTH 269. WT=6 DELAY= -0.948 ERROR= 0.045

STATION	31	26	25	24	23
MEASURED DELAY	1.900	1.830	1.680	1.690	1.670
CALCULATED DELAY	2.021	1.700	1.651	1.576	1.822
RESIDUAL	-0.121	0.130	0.029	0.114	-0.152
WEIGHT	6	6	6	6	6

EVENT NUMBER 31/12/50/11 REGION 318 YUNAN PROVINCE, CHINA INDIA - TIBET - SZECHWAN
LATITUDE 24.5700 LONGITUDE 98.9530 DEPTH 8. MAGNITUDE 6.1 ORIGIN TIME 12-23 18.70 SEC.
DISTANCE 65. B-BRNG 62. AZMTH 256. WT=2 DELAY= -1.506 ERROR= 0.018

STATION	50	24	23	22	18	12
MEASURED DELAY	1.640	1.060	1.290	1.560	1.690	1.830
CALCULATED DELAY	1.663	1.019	1.264	1.511	1.702	1.911
RESIDUAL	-0.023	0.041	0.026	0.049	-0.013	-0.081
WEIGHT	5	5	5	5	5	5

EVENT NUMBER 10/14/50/11 REGION 297 BURMA-CHINA BORDER REGION BURMA AND SOUTHEAST ASIA
LATITUDE 24.5310 LONGITUDE 98.7100 DEPTH 10. MAGNITUDE 6.0 ORIGIN TIME 14- 0 18.50 SEC.
DISTANCE 65. B-BRNG 62. AZMTH 256. WT=3 DELAY= -1.858 ERROR= 0.022

STATION	50	23	22	18	12
MEASURED DELAY	1.340	1.010	1.160	1.260	1.620
CALCULATED DELAY	1.311	0.912	1.159	1.351	1.559
RESIDUAL	0.029	0.098	0.001	-0.091	0.061
WEIGHT	3	3	5		[illegible]

EVENT NUMBER 47/19/50/11 REGION 297 BURMA-CHINA BORDER REGION BURMA AND SOUTHEAST ASI
LATITUDE 24.5470 LONGITUDE 98.9340 DEPTH 32. MAGNITUDE 5.2 ORIGIN TIME 19-36 55.70 SEC.
DISTANCE 65. B-BRNG 62. AZMTH 256. WT=4 DELAY= -1.110 ERROR= 0.027

STATION	50	24	23	22	18	12
MEASURED DELAY	1.900	1.500	1.690	1.940	2.040	2.290
CALCULATED DELAY	2.059	1.415	1.660	1.907	2.099	2.307
RESIDUAL	-0.159	0.085	0.030	0.033	-0.059	-0.017
WEIGHT	4	4	4	5	4	4

EVENT NUMBER 9/ 3/51/11 REGION 267 HALMAHERA BORNEO - CELEBES
LATITUDE -1.0520 LONGITUDE 127.0360 DEPTH 33. MAGNITUDE 5.5 ORIGIN TIME 2-56 39.60 SEC.
DISTANCE 90. B-BRNG 91. AZMTH 269. WT=3 DELAY= -0.539 ERROR= 0.056

STATION	50	24	23	22	18	12
MEASURED DELAY	2.320	2.140	2.250	2.500	2.480	2.950
CALCULATED DELAY	2.629	1.986	2.231	2.478	2.670	2.878
RESIDUAL	-0.309	0.154	0.019	0.022	-0.190	0.072
WEIGHT	3	4	4	4	3	3

EVENT NUMBER 19/ 5/52/11 REGION 297 BURMA-CHINA BORDER REGION BURMA AND SOUTHEAST ASI
LATITUDE 24.3430 LONGITUDE 98.6420 DEPTH 14. MAGNITUDE 5.5 ORIGIN TIME 5- 8 28.50 SEC.
DISTANCE 65. B-BRNG 62. AZMTH 256. WT=5 DELAY= -0.170 ERROR= 0.014

STATION	50	24	23	22	18
MEASURED DELAY	2.940	2.370	2.640	2.860	3.040
CALCULATED DELAY	2.998	2.355	2.600	2.847	3.039
RESIDUAL	-0.058	0.015	0.040	0.013	0.001
WEIGHT	5	4	5	5	5

EVENT NUMBER 3/17/55/11 REGION 190 NEW IRELAND REGION BISMARCK AND SOLOMON IS
LATITUDE -5.2010 LONGITUDE 153.4420 DEPTH 88. MAGNITUDE 6.2 ORIGIN TIME 16-44 38.80 SEC.
DISTANCE 115. B-BRNG 96. AZMTH 266. WT=2 DELAY= 1.083 ERROR= 0.042

STATION	50	24	23	18	12
MEASURED DELAY	4.150	3.700	3.910	4.100	4.540
CALCULATED DELAY	4.251	3.608	3.853	4.292	4.500
RESIDUAL	-0.101	0.092	0.057	-0.192	0.040
WEIGHT	4	4	4	3	4

EVENT NUMBER 51/ 0/56/11 REGION 712 INDIA-PAKISTAN BORDER REGION BALUCHISTAN
LATITUDE 24.5750 LONGITUDE 68.4100 DEPTH 33. MAGNITUDE 5.2 ORIGIN TIME 0-43 43.40 SEC.
DISTANCE 40. B-BRNG 48. AZMTH 235. WT=5 DELAY= -0.674 ERROR= 0.097

STATION	50	24	23	18	12
MEASURED DELAY	2.980	1.460	1.910	2.540	2.830
CALCULATED DELAY	2.495	1.851	2.096	2.535	2.743
RESIDUAL	0.485	-0.391	-0.186	0.005	0.087
WEIGHT	4	4	4	4	4

EVENT NUMBER 39/ 8/57/11 REGION 193 SOLOMON ISLANDS BISMARCK AND SOLOMON ISI
LATITUDE -10.0860 LONGITUDE 161.0120 DEPTH 61. MAGNITUDE 6.2 ORIGIN TIME 8-20 7.20 SEC.
DISTANCE 123. B-BRNG 103. AZMTH 262. WT=4 DELAY= -1.472 ERROR= 0.029

STATION	23	18	12
MEASURED DELAY	1.360	1.660	1.960
CALCULATED DELAY	1.298	1.737	1.945
RESIDUAL	0.062	-0.077	0.015
WEIGHT	4	4	4

EVENT NUMBER 49/ 7/59/11 REGION 249 LUZON, PHILIPPINE ISLANDS PHILIPPINES
LATITUDE 14.0870 LONGITUDE 124.8290 DEPTH 33. MAGNITUDE 6.1 ORIGIN TIME 7-36 55.40 SEC.
DISTANCE 88. B-BRNG 76. AZMTH 268. WT=5 DELAY= 0.137 ERROR= 0.044

STATION	50	23	18	12
MEASURED DELAY	3.370	3.030	3.210	3.500
CALCULATED DELAY	3.305	2.906	3.346	3.553
RESIDUAL	0.065	0.124	-0.136	-0.053
WEIGHT	5	[illegible]	[illegible]	

EVENT NUMBER 45/142/ 1/11 REGION 59 GUERRERO, MEXICO MEXICO - GUATEMALA AREA
LATITUDE 17.4553 LONGITUDE -100.6850 DEPTH 45. MAGNITUDE 6.1 ORIGIN TIME 14-26 39.10 SEC.
DISTANCE 134. B-BRNG 294. AZMTH 73. WT=5 DELAY= 0.542 ERROR= 0.134

STATION	50	23	18	12
MEASURED DELAY	3.190	3.520	3.970	4.050
CALCULATED DELAY	3.710	3.311	3.751	3.958
RESIDUAL	-0.520	0.209	0.219	0.092
WEIGHT	5	5	5	5

****

EVENT NUMBER 31/ 0/61/11 REGION 297 BURMA-CHINA BORDER REGION BURMA AND SOUTHEAST ASI
LATITUDE 24.8940 LONGITUDE 98.7520 DEPTH 33. MAGNITUDE 5.7 ORIGIN TIME 0-20 39.50 SEC.
DISTANCE 65. B-BRNG 62. AZMTH 256. WT=4 DELAY= 0.082 ERROR= 0.018

STATION	50	23	11	18
MEASURED DELAY	3.260	2.910	3.460	3.250
CALCULATED DELAY	3.250	2.852	3.486	3.291
RESIDUAL	0.010	0.058	-0.026	-0.041
WEIGHT	5	5	5	5

****

EVENT NUMBER 7/ 1/64/11 REGION 399 IONIAN SEA WESTERN MEDITERRANEAN A
LATITUDE 37.5450 LONGITUDE 20.5510 DEPTH 8. MAGNITUDE 5.5 ORIGIN TIME 0-59 16.90 SEC.
DISTANCE 41. B-BRNG 340. AZMTH 155. WT=3 DELAY= -0.731 ERROR= 0.144

STATION	50	23	18	11
MEASURED DELAY	1.820	2.160	2.770	2.520
CALCULATED DELAY	2.437	2.039	2.478	2.673
RESIDUAL	-0.617	0.121	0.292	-0.153
WEIGHT	4	4	5	5

****

EVENT NUMBER 45/13/55/11 REGION 269 MOLUCCA SEA BORNEO - CELEBES
LATITUDE -0.1750 LONGITUDE 125.0360 DEPTH 33. MAGNITUDE 5.7 ORIGIN TIME 18-36 3.10 SEC.
DISTANCE 88. B-BRNG 90. AZMTH 269. WT=5 DELAY= 1.142 ERROR= 0.044

STATION	50	23	18	11
MEASURED DELAY	4.180	3.980	4.340	4.670
CALCULATED DELAY	4.311	3.912	4.351	4.547
RESIDUAL	-0.131	0.068	-0.011	0.123
WEIGHT	5	4	5	5

****

EVENT NUMBER 43/23/67/11 REGION 407 NORTH OF ASCENSION ISLAND ATLANTIC OCEAN
LATITUDE -1.4380 LONGITUDE -14.0690 DEPTH 33. MAGNITUDE 5.4 ORIGIN TIME 23-34 35.60 SEC.
DISTANCE 51. B-BRNG 270. AZMTH 90. WT=4 DELAY= -0.165 ERROR= 0.077

STATION	50	23	18	11
MEASURED DELAY	2.780	2.300	3.210	3.220
CALCULATED DELAY	3.003	2.605	3.044	3.239
RESIDUAL	-0.223	-0.305	0.166	-0.019
WEIGHT	4	4	5	5

****

EVENT NUMBER 7/15/71/11 REGION 427 MASCARENE ISLANDS REGION INDIAN OCEAN
LATITUDE -18.0200 LONGITUDE 65.4140 DEPTH 33. MAGNITUDE 5.6 ORIGIN TIME 15- 0 46.70 SEC.
DISTANCE 33. B-BRNG 122. AZMTH 297. WT=4 DELAY= -2.010 ERROR= 0.032

STATION	50	23	18	11
MEASURED DELAY	1.260	0.710	1.130	1.450
CALCULATED DELAY	1.159	0.760	1.199	1.395
RESIDUAL	0.101	-0.050	-0.069	0.055
WEIGHT	4	4	5	5

****

EVENT NUMBER 51/ 3/72/11 REGION 246 SOUTHWESTERN RYUKYU ISLANDS TAIWAN
LATITUDE 24.7620 LONGITUDE 125.0290 DEPTH 36. MAGNITUDE 5.8 ORIGIN TIME 4-38 8.00 SEC.
DISTANCE 90. B-BRNG 65. AZMTH 268. WT=4 DELAY= -0.982 ERROR= 0.066

STATION	50	23	18	11
MEASURED DELAY	2.270	1.830	1.950	2.100
CALCULATED DELAY	2.186	1.788	2.227	2.422
RESIDUAL	0.084	0.042	-0.277	-0.322
WEIGHT	5	5	3	4

****

EVENT NUMBER 3/21/72/11 REGION 706 NORTHERN SUMATRA ANDAMAN ISLANDS TO SUMA
LATITUDE 3.3970 LONGITUDE 96.3180 DEPTH 43. MAGNITUDE 6.3 ORIGIN TIME 20-53 13.40 SEC.
DISTANCE 60. B-BRNG 85. AZMTH 267. WT=4 DELAY= -0.793 ERROR= 0.092

STATION	50	23	18	11
MEASURED DELAY	2.680	1.780	2.300	2.620
CALCULATED DELAY	2.375	1.977	2.416	2.611
RESIDUAL	0.305	-0.197	-0.116	0.009
WEIGHT	5	5	5	5

****

EVENT NUMBER 27/ 7/73/11 REGION 706 NORTHERN SUMATRA ANDAMAN ISLANDS TO SUMA
LATITUDE 3.3960 LONGITUDE 96.4040 DEPTH 32. MAGNITUDE 5.8 ORIGIN TIME 7-17 34.80 SEC.
DISTANCE 60. B-BRNG 85. AZMTH 267. WT=5 DELAY= 0.160 ERROR= 0.086

STATION	50	23	18	11
MEASURED DELAY	3.620	2.740	3.200	3.630
CALCULATED DELAY	3.328	2.930	3.369	3.564
RESIDUAL	0.292	-0.190	-0.169	0.066
WEIGHT	5	5	5	5

****

EVENT NUMBER 34/ 2/74/11 REGION 706 NORTHERN SUMATRA ANDAMAN ISLANDS TO SUMA
LATITUDE 3.4360 LONGITUDE 96.3630 DEPTH 43. MAGNITUDE 5.3 ORIGIN TIME 2-24 9.90 SEC.
DISTANCE 60. B-BRNG 85. AZMTH 267. WT=3 DELAY= 0.316 ERROR= 0.082

STATION	50	23	18	11
MEASURED DELAY	3.830	2.940	3.370	3.850
CALCULATED DELAY	3.484	3.086	3.525	3.720
RESIDUAL	0.346	-0.146	-0.155	0.130
WEIGHT	2	4	3	4

****

EVENT NUMBER 54/20/75/11 REGION 153 SOUTH SANDWICH ISLANDS REGION SOUTHERN ANTILLES
LATITUDE -59.6610 LONGITUDE -26.4430 DEPTH 59. MAGNITUDE 5.8 ORIGIN TIME 20-43 13.10 SEC.
DISTANCE 76. B-BRNG 208. AZMTH 67. WT=3 DELAY= 3.178 ERROR= 0.022

STATION	50	23	22
MEASURED DELAY	6.300	5.940	6.250
CALCULATED DELAY	6.347	5.948	6.195
RESIDUAL	-0.047	-0.008	0.055
WEIGHT	3	3	3

****

EVENT NUMBER 44/10/78/11 REGION 263 TALAUD ISLANDS BORNEO - CELEBES
LATITUDE 3.6650 LONGITUDE 126.7500 DEPTH 33. MAGNITUDE 5.8 ORIGIN TIME 10-30 59.40 SEC.
DISTANCE 90. B-BRNG 86. AZMTH 269. WT=3 DELAY= 0.392 ERROR= 0.111

STATION	50	23	22
MEASURED DELAY	3.340	3.300	3.590
CALCULATED DELAY	3.560	3.162	3.408
RESIDUAL	-0.220	0.138	0.182
WEIGHT	5	4	5

****

EVENT NUMBER 49/18/81/11 REGION 179 SOUTH OF KERMADEC ISLANDS KERMADEC - TONGA - SAMO
LATITUDE -35.8160 LONGITUDE -177.8340 DEPTH 48. MAGNITUDE 6.1 ORIGIN TIME 18-30 9.10 SEC.
DISTANCE 133. B-BRNG 140. AZMTH 230. WT=5 DELAY= 0.096 ERROR= 0.048

STATION	50	23	22
MEASURED DELAY	3.100	2.780	3.220
CALCULATED DELAY	3.265	2.866	3.113
RESIDUAL	-0.165	-0.086	0.107
WEIGHT	3	5	5

****

EVENT NUMBER 54/10/82/11 REGION 274 SOUTHERN SUMATRA SUNDA ARC
LATITUDE -2.1130 LONGITUDE 101.9470 DEPTH 138. MAGNITUDE 5.5 ORIGIN TIME 14-44 51.10 SEC.
DISTANCE 65. B-BRNG 92. AZMTH 270. WT=5 DELAY= 0.583 ERROR= 0.092

STATION	50	23	22
MEASURED DELAY	4.130	3.360	3.460
CALCULATED DELAY	3.751	3.353	3.599
RESIDUAL	0.379	0.007	-0.139
WEIGHT	5	6	6

****

EVENT NUMBER 18/21/26/71. REGION 249 LUZON, PHILIPPINE ISLANDS PHILIPPINES
LATITUDE 18.9450 LONGITUDE 121.3030 DEPTH 57. MAGNITUDE 5.7 ORIGIN TIME 21- 5 31.00 SEC.
DISTANCE 85. B-BRNG 71. AZMTH 267. WT=3 DELAY= -1.713 ERROR= 0.016

STATION	9	10	12	11	13
MEASURED DELAY	1.909	2.130	1.780	1.650	1.970
CALCULATED DELAY	1.873	2.153	1.704	1.691	1.974
RESIDUAL	0.027	-0.023	0.076	-0.041	-0.004
WEIGHT	3	3	2	3	3

****

EVENT NUMBER 21/22/83/12 REGION 262 CELEBES SEA BORNEO - CELEBES
LATITUDE 4.3500 LONGITUDE 124.8340 DEPTH 35. MAGNITUDE 5.5 ORIGIN TIME 22- 8 44.40 SEC.
DISTANCE 88. B-BRNG 86. AZMTH 269. WT=3 DELAY= -0.679 ERROR= 0.029

STATION	13	12	11	10	9
MEASURED DELAY	2.970	2.650	2.800	3.240	2.920
CALCULATED DELAY	3.008	2.738	2.725	3.187	2.907
RESIDUAL	-0.038	-0.088	0.075	0.053	0.013
WEIGHT	3	4	4	3	3

****

EVENT NUMBER 21/ 7/ 7/13 REGION 429 MID-INDIAN RISE INDIAN OCEAN
LATITUDE -29.3490 LONGITUDE 77.6590 DEPTH 33. MAGNITUDE 5.8 ORIGIN TIME 7-13 15.70 SEC.
DISTANCE 48. B-BRNG 130. AZMTH 298. WT=5 DELAY= -0.238 ERROR= 0.064

STATION	9	13	10	11
MEASURED DELAY	3.520	3.360	3.710	3.000
CALCULATED DELAY	3.347	3.449	3.628	3.166
RESIDUAL	0.173	-0.089	0.082	-0.166
WEIGHT	6	6	6	6

****

EVENT NUMBER 15/18/11/13 REGION 307 SZECHWAN PROVINCE, CHINA INDIA - TIBET - SZECHWAN
LATITUDE 27.6050 LONGITUDE 101.0520 DEPTH 33. MAGNITUDE 5.8 ORIGIN TIME 18- 4 8.90 SEC.
DISTANCE 68. B-BRNG 60. AZMTH 256. WT=3 DELAY= -0.972 ERROR= 0.024

STATION	13	10	11	8	12
MEASURED DELAY	2.710	2.960	2.390	2.570	2.540
CALCULATED DELAY	2.715	2.894	2.432	2.632	2.444
RESIDUAL	-0.005	0.066	-0.042	-0.062	0.096
WEIGHT	5	5	4	5	3

****

EVENT NUMBER 8/ 4/12/13 REGION 348 IRAN WESTERN ASIA
LATITUDE 33.8020 LONGITUDE 59.1550 DEPTH 13. MAGNITUDE 5.6 ORIGIN TIME 4- 0 51.60 SEC.
DISTANCE 41. B-BRNG 29. AZMTH 216. WT=4 DELAY= 0.358 ERROR= 0.039

STATION	13	9	10	11	8	12
MEASURED DELAY	3.950	4.090	4.310	3.880	3.900	3.690
CALCULATED DELAY	4.046	3.944	4.225	3.763	3.963	3.775
RESIDUAL	-0.096	0.146	0.085	0.117	-0.063	-0.085
WEIGHT	5	4	4	5	5	4

****

EVENT NUMBER 22/17/12/13 REGION 259 MINDANAO, PHILIPPINE ISLANDS PHILIPPINES
LATITUDE 8.4750 LONGITUDE 126.3750 DEPTH 60. MAGNITUDE 6.0 ORIGIN TIME 17- 9 6.10 SEC.
DISTANCE 90. B-BRNG 82. AZMTH 269. WT=4 DELAY= -0.342 ERROR= 0.021

STATION	13	10	11	8	12
MEASURED DELAY	3.390	3.500	2.970	3.340	3.100
CALCULATED DELAY	3.346	3.525	3.063	3.263	3.075
RESIDUAL	0.044	-0.025	-0.093	0.077	0.025
WEIGHT	3	4	3	3	3

****

EVENT NUMBER 1/11/13/13 REGION 259 MINDANAO, PHILIPPINE ISLANDS PHILIPPINES
LATITUDE 8.5550 LONGITUDE 126.0320 DEPTH 142. MAGNITUDE 6.3 ORIGIN TIME 10-48 44.50 SEC.
DISTANCE 89. B-BRNG 81. AZMTH 269. WT=4 DELAY= -0.633 ERROR= 0.054

STATION	13	12	11	8
MEASURED DELAY	3.170	2.860	2.780	2.770
CALCULATED DELAY	3.054	2.734	2.771	2.971
RESIDUAL	0.116	0.126	0.009	-0.201
WEIGHT	4	4	4	4

****

EVENT NUMBER [illegible]/10/16/13 REGION 173 TONGA ISLANDS KERMADEC - TONGA - SA
LATITUDE -1[illegible] LONGITUDE -17[illegible] DEPTH [illegible]. MAGNITUDE 5.3 ORIGIN TIME 10-20 9.70 SEC.
DISTANCE 1[illegible]5. B-BRNG 1[illegible]6. AZMTH 23[illegible]. WT=3 DELAY= 0.580 ERROR= 0.179

STATION	13	12	11	9	8
MEASURED DELAY	3.810	3.5[illegible]0	3.730	4.650	4.600
CALCULATED DELAY	4.267	3.997	3.984	4.166	4.184
RESIDUAL	-0.457	-0.437	-0.254	0.484	0.416
WEIGHT	3	4	4	4	4

EVENT NUMBER 5/14/20/13 REGION 658 NORTHEASTERN CHINA EASTERN ASIA
LATITUDE [illegible].4440 LONGITUDE 117.6880 DEPTH 15. MAGNITUDE 6.0 ORIGIN TIME 13-53 0.60 SEC.
DISTANCE 84. B-BRNG 50. AZMTH 263. WT=4 DELAY= -0.476 ERROR= 0.041

STATION	13	9	10	8	12
MEASURED DELAY	3.090	3.220	3.390	3.240	2.870
CALCULATED DELAY	3.211	3.110	3.390	3.128	2.941
RESIDUAL	-0.121	0.110	-0.000	0.112	-0.071
WEIGHT	5	5	5	4	4

EVENT NUMBER 31/17/22/13 REGION 717 AFGHANISTAN-USSR BORDER REGION HINDU KUSH AND PAMIR
LATITUDE 36.4680 LONGITUDE 71.1720 DEPTH 233. MAGNITUDE 5.4 ORIGIN TIME 17-23 23.60 SEC.
DISTANCE 43. B-BRNG 37. AZMTH 229. WT=4 DELAY= 1.429 ERROR= 0.012

STATION	13	9	11	8	12	10
MEASURED DELAY	5.080	5.050	4.890	5.060	4.790	5.290
CALCULATED DELAY	5.116	5.015	4.833	5.033	4.846	5.295
RESIDUAL	-0.036	0.035	0.057	0.027	-0.056	-0.005
WEIGHT	4	3	4	2	3	5

EVENT NUMBER 15/ 2/23/13 REGION 173 TONGA ISLANDS KERMADEC - TONGA - SA
LATITUDE -19.1350 LONGITUDE -173.6170 DEPTH 38. MAGNITUDE 5.1 ORIGIN TIME 1-55 46.70 SEC.
DISTANCE 145. B-BRNG 125. AZMTH 240. WT=4 DELAY= 0.196 ERROR= 0.099

STATION	13	9	11	10	8	12
MEASURED DELAY	3.950	3.950	3.160	3.890	4.020	3.730
CALCULATED DELAY	3.883	3.782	3.600	4.062	3.800	3.613
RESIDUAL	0.067	0.168	-0.440	-0.172	0.220	0.117
WEIGHT	5	5	5	4	5	4

EVENT NUMBER 42/ 3/23/13 REGION 193 SOLOMON ISLANDS BISMARCK AND SOLOMON
LATITUDE -9.8150 LONGITUDE 156.9410 DEPTH 33. MAGNITUDE 6.1 ORIGIN TIME 3-24 0.20 SEC.
DISTANCE 120. B-BRNG 101. AZMTH 264. WT=0 DELAY= -0.780 ERROR= 0.061

STATION	13	12	11	10	9
MEASURED DELAY	2.950	2.440	2.600	3.250	2.830
CALCULATED DELAY	2.907	2.636	2.624	3.086	2.806
RESIDUAL	0.043	-0.196	-0.024	0.164	0.024
WEIGHT	3	3	3	3	2

EVENT NUMBER 57/ 5/23/13 REGION 196 WEST IRIAN REGION NEW GUINEA
LATITUDE -4.1700 LONGITUDE 135.1410 DEPTH 33. MAGNITUDE 5.8 ORIGIN TIME 5-43 41.30 SEC.
DISTANCE 98. B-BRNG 94. AZMTH 268. WT=1 DELAY= 0.033 ERROR= 0.063

STATION	13	12	11	10	8
MEASURED DELAY	3.720	3.200	3.410	4.080	3.820
CALCULATED DELAY	3.721	3.450	3.438	3.900	3.638
RESIDUAL	-0.001	-0.250	-0.028	0.180	0.182
WEIGHT	4	3	3	3	2

EVENT NUMBER 29/12/29/13 REGION 348 N.W. IRAN-USSR BORDER REGION WESTERN ASIA
LATITUDE 3[illegible].1210 LONGITUDE 44.0290 DEPTH 36. MAGNITUDE 6.1 ORIGIN TIME 12-22 18.80 SEC.
DISTANCE 41. B-BRNG 9. AZMTH 191. WT=5 DELAY= 0.103 ERROR= 0.068

STATION	13	11	8	12	10	9
MEASURED DELAY	3.940	3.710	3.570	3.570	3.930	3.400
CALCULATED DELAY	3.795	3.512	3.712	3.[illegible]	3.974	3.694
RESIDUAL	0.145	0.198	-0.142	0.0[illegible]	-0.044	-0.294
WEIGHT	6	6	5	6	6	6

EVENT NUMBER 10/21/42/13 REGION 717 AFGHANISTAN-USSR BORDER REGION HINDU KUSH AND PAMIR
LATITUDE 36.5[illegible] LONGITUDE 71.04[illegible] DEPTH 140. MAGNITUDE 6.1 ORIGIN TIME 21-42 12.20 SEC.
DISTANCE 49. B-BRNG 37. AZMTH [illegible]. WT=6 DELAY= 0.381 ERROR= 0.027

STATION	11	10	12	8	13	9
MEASURED DELAY	3.880	4.200	3.750	3.900	3.940	3.960
CALCULATED DELAY	3.785	4.147	3.797	3.985	4.068	3.967
RESIDUAL	0.095	0.053	-0.047	-0.085	-0.128	-0.007
WEIGHT	6	6	5	6	5	5

****

EVENT NUMBER 12/18/46/13 REGION 704 NICOBAR ISLANDS REGION ANDAMAN ISLANDS TO SUMA
LATITUDE 7.4940 LONGITUDE 93.8110 DEPTH 33. MAGNITUDE 5.6 ORIGIN TIME 18- 8 4.40 SEC.
DISTANCE 57. B-BRNG 80. AZMTH 264. WT=3 DELAY= 2.701 ERROR= 0.065

STATION	13	9	10		12	11
MEASURED DELAY	6.320	6.340	6.440	6.620	6.100	5.990
CALCULATED DELAY	6.389	6.287	6.567	6.305	6.118	6.105
RESIDUAL	-0.069	0.053	-0.127	0.315	-0.018	-0.115
WEIGHT	5	4	5	5	5	5

****

EVENT NUMBER 47/ 6/48/13 REGION 307 SZECHWAN PROVINCE, CHINA INDIA - TIBET - SZECHWA
LATITUDE 27.3950 LONGITUDE 101.0550 DEPTH 17. MAGNITUDE 5.4 ORIGIN TIME 6-36 58.30 SEC.
DISTANCE 68. B-BRNG 60. AZMTH 257. WT=4 DELAY= -0.425 ERROR= 0.019

STATION	13	10	8	12	11
MEASURED DELAY	3.310	3.390	3.260	2.940	2.970
CALCULATED DELAY	3.262	3.441	3.179	2.992	2.979
RESIDUAL	0.048	-0.051	0.081	-0.052	-0.009
WEIGHT	4	4	3	3	4

****

EVENT NUMBER 19/16/49/13 REGION 238 RYUKYU ISLANDS SOUTHWESTERN JAPAN AND
LATITUDE 24.2940 LONGITUDE 130.6980 DEPTH 41. MAGNITUDE 6.3 ORIGIN TIME 16- 6 44.40 SEC.
DISTANCE 94. B-BRNG 62. AZMTH 271. WT=4 DELAY= -1.015 ERROR= 0.041

STATION	11	10	8	12	13
MEASURED DELAY	2.510	2.800	2.720	2.590	2.600
CALCULATED DELAY	2.389	2.851	2.589	2.401	2.672
RESIDUAL	0.121	-0.051	0.131	0.189	-0.072
WEIGHT	4	5	4	4	5

****

EVENT NUMBER 52/20/55/13 REGION 25 VANCOUVER ISLAND REGION EASTERN ALASKA TO VANCO
LATITUDE 48.8020 LONGITUDE -129.2920 DEPTH 10. MAGNITUDE 5.9 ORIGIN TIME 20-33 7.80 SEC.
DISTANCE 93. B-BRNG 41. AZMTH 271. WT=1 DELAY= -1.522 ERROR= 0.179

STATION	11	10	12	9	13
MEASURED DELAY	2.250	2.100	2.450	1.910	1.640
CALCULATED DELAY	1.882	2.344	1.895	2.064	2.165
RESIDUAL	0.368	-0.244	0.555	-0.154	-0.525
WEIGHT	3	3	3	3	3

****

EVENT NUMBER 9/ 0/56/13 REGION 266 MOLUCCA PASSAGE BORNEO - CELEBES
LATITUDE 0.5[illegible]0 LONGITUDE 126.0740 DEPTH 33. MAGNITUDE 5.5 ORIGIN TIME 23-56 54.60 SEC.
DISTANCE 89. B-BRNG 89. AZMTH 269. WT=4 DELAY= 1.143 ERROR= 0.028

STATION	11	10	12	9	13
MEASURED DELAY	4.630	4.950	4.470	4.690	4.830
CALCULATED DELAY	4.548	5.010	4.560	4.729	4.831
RESIDUAL	0.082	-0.060	-0.090	-0.039	-0.001
WEIGHT	5	5	3	4	4

****

EVENT NUMBER 33/19/61/13 REGION 410 SOUTH ATLANTIC RIDGE ATLANTIC OCEAN
LATITUDE -40.5[illegible]0 LONGITUDE 16.7110 DEPTH 33. MAGNITUDE 5.8 ORIGIN TIME 19-33 55.90 SEC.
DISTANCE 62. B-BRNG 224. AZMTH 65. WT=4 DELAY= 0.664 ERROR= 0.141

STATION	8	9	10	11	12	13
MEASURED DELAY	3.600	3.910	4.090	4.030	4.080	4.700
CALCULATED DELAY	4.268	4.250	4.530	4.068	4.081	4.351
RESIDUAL	-0.668	-0.340	-0.440	-0.038	-0.001	0.349
WEIGHT	4	4	3	4	4	5

****

EVENT NUMBER [illegible]/10 REGION 277 JAVA SUNDA ARC
LATITUDE -8.[illegible] LONGITUDE 108.6070 DEPTH 53. MAGNITUDE 5.9 ORIGIN TIME 20-31 38.20 SEC.
DISTANCE 77. B-BRNG 58. AZMTH 271. WT=4 DELAY= 0.636 ERROR= 0.039

STATION	30	29	28	27
MEASURED DELAY	3.030	2.920	3.090	3.390
CALCULATED DELAY	2.896	2.904	3.178	3.266
RESIDUAL	0.134	0.016	-0.088	0.124
WEIGHT	4	5	5	4

****

EVENT NUMBER 6/10/61/20 REGION 259 MINDANAO, PHILIPPINE ISLANDS PHILIPPINES
LATITUDE 6.7720 LONGITUDE 123.7400 DEPTH 52. MAGNITUDE 6.1 ORIGIN TIME 9-53 23.20 SEC.
DISTANCE 87. B-BRNG 83. AZMTH 267. WT=6 DELAY= -0.077 ERROR= 0.018

STATION	18	17	16	15	14	11
MEASURED DELAY	3.200	3.270	3.610	3.430	3.740	3.280
CALCULATED DELAY	3.132	3.236	3.572	3.407	3.840	3.327
RESIDUAL	0.068	0.034	0.038	0.023	-0.100	-0.047
WEIGHT	5	5	5	4	5	5

****

EVENT NUMBER 30/19/63/20 REGION 358 RUMANIA MIDDLE EAST - CRIMEA
LATITUDE 45.7720 LONGITUDE 26.7610 DEPTH 94. MAGNITUDE 6.4 ORIGIN TIME 19-21 54.10 SEC.
DISTANCE 48. B-BRNG 350. AZMTH 166. WT=3 DELAY= -1.702 ERROR= 0.044

STATION	18	17	16	15	14	11
MEASURED DELAY	1.530	1.550	2.150	1.870	2.130	1.730
CALCULATED DELAY	1.507	1.611	1.947	1.782	2.215	1.702
RESIDUAL	0.023	-0.061	0.203	0.088	-0.085	0.028
WEIGHT	4		[illegible]		[illegible]	

****

EVENT NUMBER 40/14/68/20 REGION 659 NORTH KOREA EASTERN ASIA
LATITUDE 41.6060 LONGITUDE 130.8780 DEPTH 528. MAGNITUDE 5.9 ORIGIN TIME 14-27 53.60 SEC.
DISTANCE 94. B-BRNG 49. AZMTH 272. WT=4 DELAY= -1.877 ERROR= 0.034

STATION	18	16	15	14	11
MEASURED DELAY	1.640	1.690	1.620	2.100	1.620
CALCULATED DELAY	1.332	1.772	1.607	2.040	1.527
RESIDUAL	0.308	-0.082	0.013	0.060	0.093
WEIGHT	3	6	5	6	3

****

EVENT NUMBER 56/21/77/20 REGION 249 LUZON, PHILIPPINE ISLANDS PHILIPPINES
LATITUDE 15.7730 LONGITUDE 122.3270 DEPTH 37. MAGNITUDE 6.2 ORIGIN TIME 21-43 52.60 SEC.
DISTANCE 86. B-BRNG 73. AZMTH 268. WT=4 DELAY= -0.850 ERROR= 0.031

STATION	18	17	16	15	14	11
MEASURED DELAY	2.260	2.400	2.900	2.590	2.970	2.610
CALCULATED DELAY	2.359	2.463	2.799	2.634	3.068	2.554
RESIDUAL	-0.099	-0.063	0.101	-0.044	-0.098	0.056
WEIGHT	4	4	5	5	4	4

****

EVENT NUMBER [illegible]/20 REGION 173 TONGA ISLANDS KERMADEC - TONGA - S
LATITUDE -18.[illegible] LONGITUDE -174.1470 DEPTH 93. MAGNITUDE 5.6 ORIGIN TIME 8-19 18.50 SEC.
DISTANCE 14[illegible]. B-BRNG 124. AZMTH 240. WT=0 DELAY= 3.960 ERROR= 0.133

STATION	18	16	14	11
MEASURED DELAY	6.840	7.530	8.170	7.480
CALCULATED DELAY	7.169	7.609	7.877	7.364
RESIDUAL	-0.329	-0.079	0.293	0.116
WEIGHT	4	4	4	4

****

EVENT NUMBER [illegible] 7/92/20 REGION 173 TONGA ISLANDS KERMADEC - TONGA - S
LATITUDE -16.6950 LONGITUDE -17[illegible].0950 DEPTH 33. MAGNITUDE 6.8 ORIGIN TIME 8-19 18.50 SEC.
DISTANCE 145. B-BRNG 124. AZMTH 241. WT=5 DELAY= 0.336 ERROR= 0.018

STATION	18	16	14	11
MEASURED DELAY	3.430	3.950	4.300	3.740
CALCULATED DELAY	3.545	3.985	4.253	3.740
RESIDUAL	-0.115	-0.035	0.047	-0.000
WEIGHT	4	6	6	6

****

EVENT NUMBER [illegible] REGION 406 CENTRAL MID-ATLANTIC RIDGE ATLANTIC OCEAN
LATITUDE [illegible] LONGITUDE -34.8570 DEPTH [illegible]. MAGNITUDE 5.5 ORIGIN TIME 17-5[illegible] [illegible].70 SEC.
DISTANCE [illegible]. B-BRNG [illegible]78. AZMTH 94. WT=3 DELAY= 0.924 ERROR= 0.063

STATION	18	16	14	11
MEASURED DELAY	4.400	4.620	4.850	4.240
CALCULATED DELAY	4.133	4.573	4.842	4.329
RESIDUAL	0.267	0.047	0.008	-0.089
WEIGHT	4	4	3	[illegible]

****

EVENT NUMBER 43/13/96/20 REGION 348 IRAN WESTERN ASIA
LATITUDE 31.9830 LONGITUDE 50.6830 DEPTH 41. MAGNITUDE 5.5 ORIGIN TIME 13-36 37.10 SEC.
DISTANCE 35. B-BRNG 21. AZMTH 204. WT=2 DELAY= 1.935 ERROR= 0.054

STATION	18	16	14	11
MEASURED DELAY	4.940	5.590	5.800	5.480
CALCULATED DELAY	5.144	5.584	5.853	5.340
RESIDUAL	-0.204	0.006	-0.053	0.140
WEIGHT	3	4	4	4

****

APPENDIX 5

DETAILS OF ALGORITHM FOR FINDING r, THE RAY LENGTH WITHIN THE ANOMALOUS ZONE

Introduction

We wish to solve Equation 6.18, which we reproduce here:

$$f(r) = a_z + rU_z - z_o + \sum_{i=1}^{n} C_i / \{1+A_i(a_x-X_i+rU_x)^2+B_i(a_y-Y_i+rU_y)^2 +D_i(a_x-X_i+rU_x)(a_y-Y_i+rU_y)\} = 0 \qquad (A5.1)$$

The function $f(r)$ is in fact the difference in depth between the point along the ray characterised by the distance parameter r, and the upper interface. Figure A5.1 represents the vertical plane through the ray and illustrates the geometry, while Figure A5.2 shows qualitatively how $f(r)$ behaves.

$f(0)$ is greater than zero and $f(r)$ may be calculated readily from Equation A5.1. Thus the smallest positive root of Equation A5.1 may be obtained by a modified interval halving method. It is essential that the method used reliably converges on the smallest root, and desirable that the number evaluations of $f(r)$ be kept to a minimum.

Method

The method devised first finds two values of r, r_{min} and r_{max}, such that r_{min} lies in Range 1, that is the first positive range of $f(r)$, and r_{max} lies in Range 2, the first negative range of $f(r)$ (Figure A5.2).

The required value of r, then corresponds to the only zero crossing between r_{min} and r_{max} and can be found by a method of successive approximations.

The algorithm used for finding suitable values of r_{min} and r_{max}, is given in the form of a flow diagram in Figure A5.3. This procedure is very simple, the only difficulty being to find a suitable value of g. Small values of g require many evaluations of $f(r)$, while large values run the risk of putting r into higher positive ranges of $f(r)$ than Range 2. A safe upper limit of g can be calculated from f_{min}, providing a lower bound, f'_{min}, for df/dr and an upper bound, f''_{max}, for d^2f/dr^2 are known

Figure A5.4 illustrates the region near the first positive going zero crossing at $r = r_1$. The shading indicates the region where curves with maximum curvature f''_{max} and minimum gradient $f._{min}$ cannot lie. In the range $\{r: r_1 - g_p < r < r_1\}$, the lower boundary to this region is a parabola with curvature f''_{max}, tangential to the line $f=0$, at $r=r_1$. In the range $\{r: r < r_1 - g_p\}$, the lower boundary is a straight line with gradient f'_{min}. g_p is such that the gradients of the two lines are equal at $r=r_1-g_p$. Elementary formulae for parabolas give

FIGURE A5.1

VERTICAL SECTION THROUGH RAY PATH

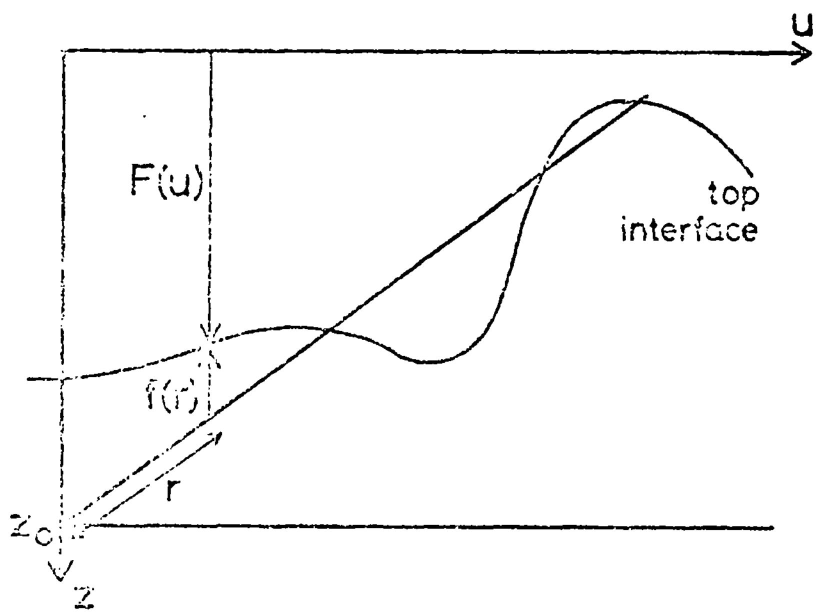

FIGURE A5.2

FORM OF f(r)

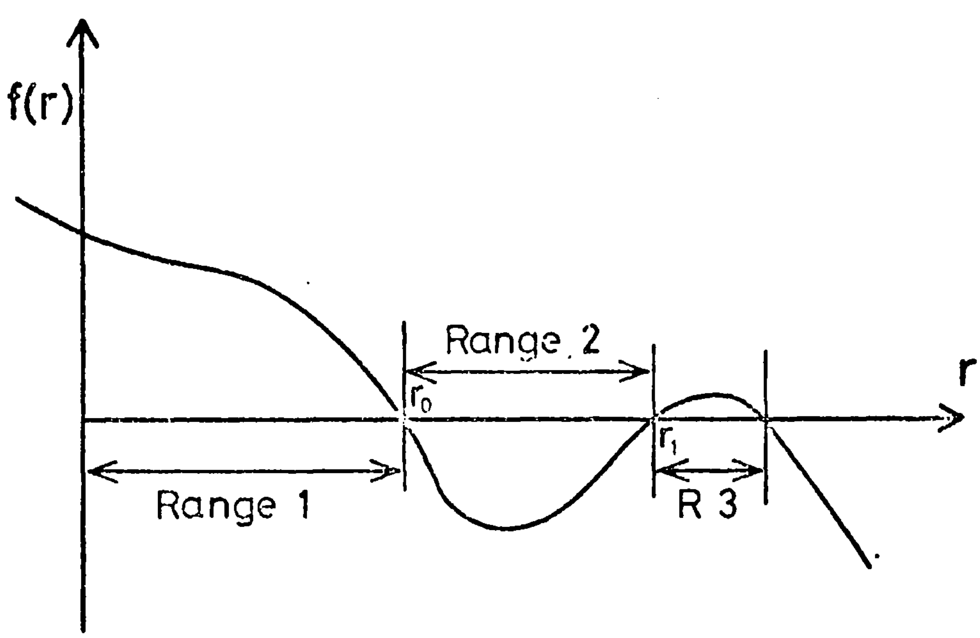

FIGURE A5.3

FLOWCHART FOR FINDING r_{min} AND r_{max}

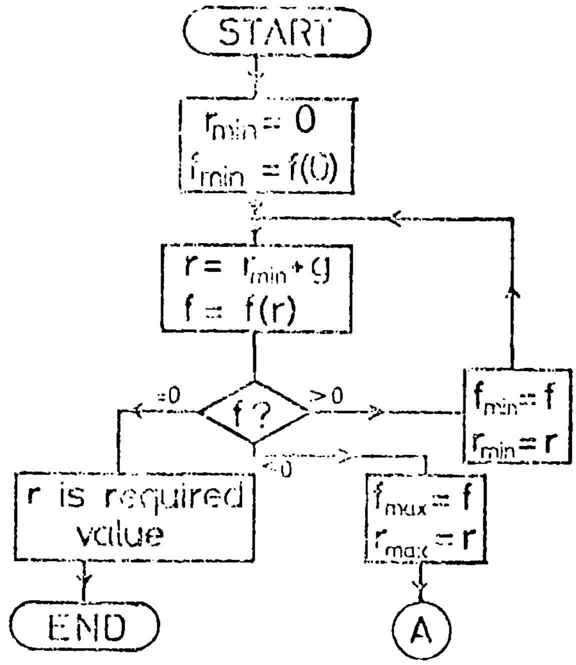

FIGURE A5.4

DIAGRAM ILLUSTRATING CALCULATION OF $g(f_{min})$

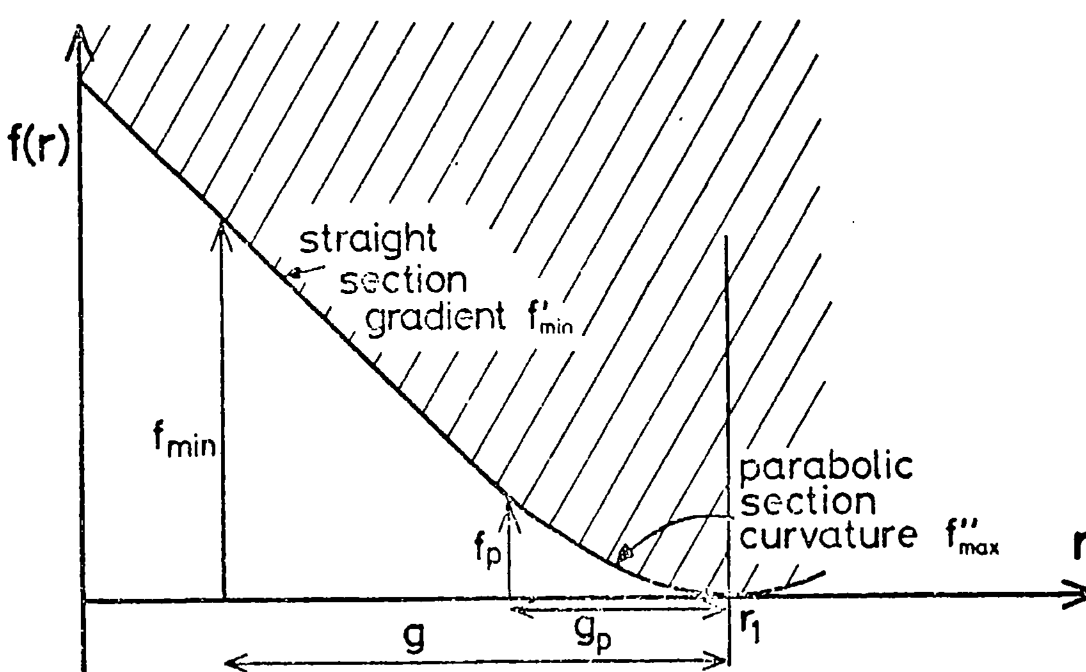

(A5

$$g_p = -f'_{min}/f''_{max}$$
$$f_p = f''_{max} g_p^2 \quad (A5.3)$$

Thus safe values of g may be calculated using

$$g(f_{min}) = (f_p - f_{min})/f'_{min} + g_p \quad , f_{min} \geqslant f_p$$
$$g(f_{min}) = (2f_{min}/f''_{max})^{1/2} \quad , f_{min} \leqslant f_p \quad (A5.4)$$

Values of f'_{min} and f''_{max} may be obtained from the height and X- and Y-dimensions of the humps. Consider an arbitrary vertical cross section through a single humped structure as illustrated in Figure A5.5, and with local coordinate axes as shown. The form of the upper interface is

$$z' = z_o - h/(1+kx'^2) \quad (A5.5)$$

Whence

$$dz'/dx' = 2hkx'/(1+kx'^2)^2 \quad (A5.6)$$
$$d^2z'/dx'^2 = 2hk(1-3kx'^2)/(1+kx'^2)^3 \quad (A5.7)$$
$$d^3z'/dx'^3 = 24hk^2x'(1-k.x'^2)/(1+kx'^2)^4 \quad (A5.8)$$

Putting the second and third derivatives equal to zero respectively gives

$$(dz'/dx')_{min} = -2hk \quad (A5.9)$$
$$(d^2z'/dx'^2)_{max} = (9/8)h(k/3)^{1/2} \quad (A5.10)$$

Extreme values for these quantities are obtained when h and k are as large as possible. This occurs for the section cut through the peak of the hump along the line of the minor axis. Then

$$h = C$$
$$k = MAX(1/L^2, 1/M^2) \quad (A5.11)$$

where C is the height and L and M are the X- and

FIGURE A5.5

DIAGRAM ILLUSTRATING THE CALCULATION OF THE BOUNDS OF THE FIRST AND SECOND DERIVATIVES OF f

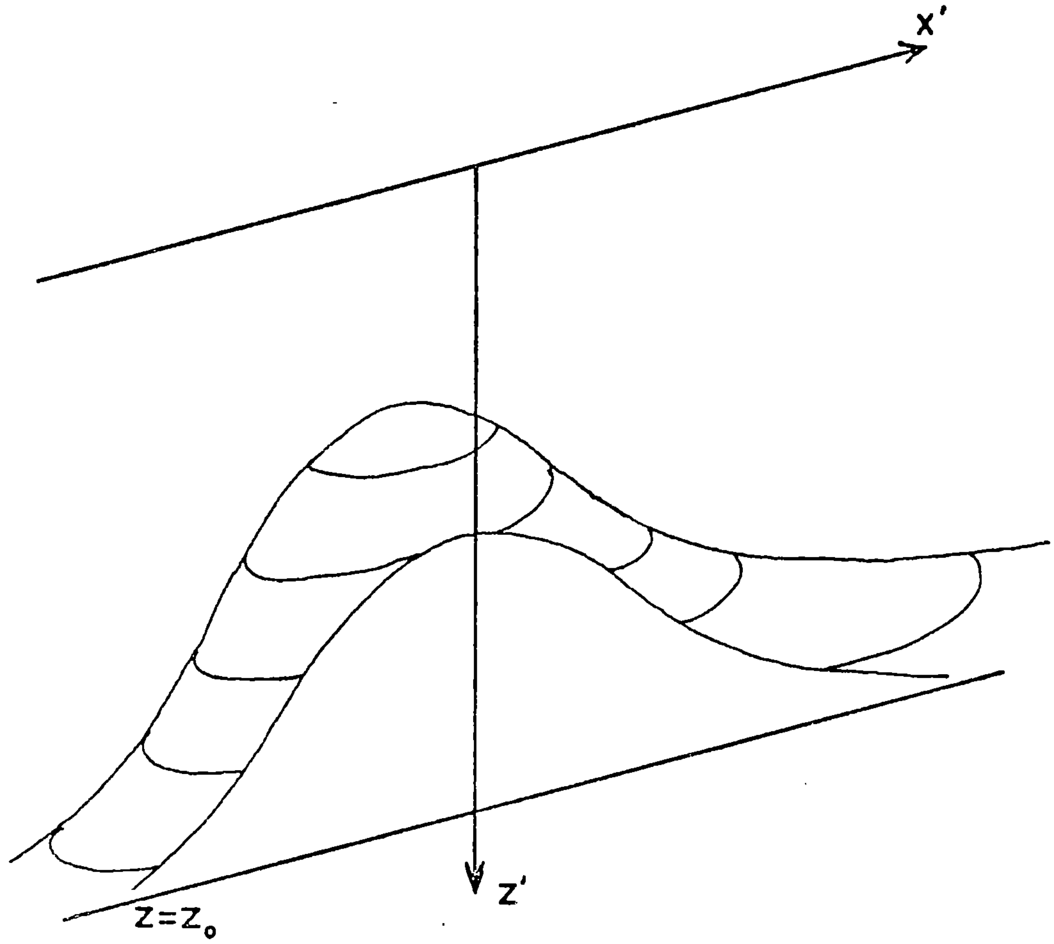

Y-dimensions of the hump. By adding the lower bounds on dz'/dx'^2 and the upper bounds on d^2z'/dx'^2 together for all the humps we obtain corresponding bounds on the curvature and gradient of the complete structure.

Referring once again to Figure A5.1, where the upper surface is represented as a function F(u) of the distance, u, corresponding to x', along the track of the ray on the x-y plane, it is clear that

$$f(u) = z_o + rUz - F(u) \qquad \text{(A5.15)}$$

and

$$d = r(U_x^2 + U_y^2)^{1/2} = r(1+U_z^2)^{1/2} \qquad \text{(A5.14)}$$

whence

$$f(r) = z_o + rU_z - F(r(1-U_z^2)^{1/2}) \qquad \text{(A5.15)}$$

thus

$$f'_{min} = U_z - (1-U_z^2)^{1/2}(dF/du)_{max} \qquad \text{(A5.16)}$$

and

$$f''_{max} = -(1-U_z^2)(d^2F/du^2)_{min} \qquad \text{(A5.17)}$$

$(dF/du)_{max}$ and $(d^2F/du^2)_{min}$ being the bounds on the gradient and curvature of the whole structure. Usually, three or four evaluations of f are required to find r_{max}.

Having obtained reliable values of r_{min} and r_{max}, together with corresponding values of f_{min} and f_{max}, the algorithm represented by the flow diagram of Figure A5.6, is used to "close down" on the value of r_o. During each iteration, a new estimate of r_o, r, is calculated by finding the point where the straight line between (r_{min} , $q_{min}f_{min}$) and (r_{max} , $q_{max}f_{max}$) intersects the r-axis. q_{min} and q_{max}

are relaxation factors whose values lie between zero and one. f(r) is then evaluated, and depending on whether it is positive or negative, r and f(r) become new values of either r_{min} and f_{min} or r_{max} and f_{max}. The variable relaxation factors operate in such a way that both r_{min} and r_{max} contract towards r_o. The algorithm converges more quickly than with $q_{min} = q_{max} = 1$, and has the advantages that the error margins are well controlled, and errors are equally likely to be positive or negative. Between five and eight iterations are usually required to give a fractional error in r of 1 part in 10^{-4}, or approximately 50 m absolute.

FIGURE A5·6

FLOW-DIAGRAM FOR FINDING r_0

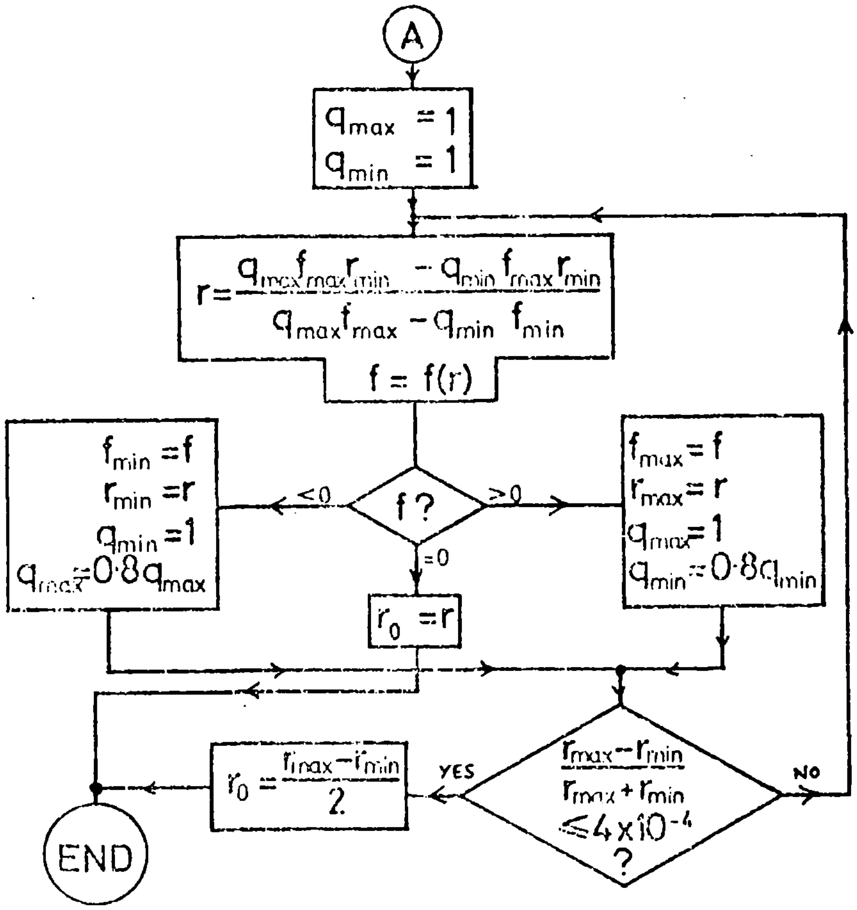

APPENDIX 6

SUBROUTINE MHUMP

Introduction

This subroutine calculates theoretical delay times for a number of events, at a number of stations, for a multi-humped, three dimensional velocity structure as described in Chapter 6. The theoretical delay times are compared with input measured delay times, and an objective function value, dependent on the closeness of fit between the relative theoretical delays and the relative measured delays, is calculated.

The subprogram is written to be used with MINUIT (James and Roos, 1969) a non-linear optimization package which adjusts the variable parameters representing the shape of the anomalous zone, to give the closest fit.

The main calculations are described in Chapter 6 and Appendix 5.

Calling

The subroutine is called thus:

```
CALL FCN(N,G,F,U,IND)
DIMENSION G(150),U(150)
```

```
N          :Number of adjustable parameters, set by MINUIT.
G          :Intended to return a vector gradient to MINUIT.
            Not used in this subprogram.
U          :Array of variable parameters, as follows:
U((I-1)*6+1)   :Latitude in degrees N (S negative) of centre
                of I^th hump.
```

U((I-1)*6+2) :Longitude in degrees E (W negative), of centre of I^{th} hump.
U((I-1)*6+3) :Height, in kilometers, of the I^{th} hump.
U((I-1)*6+4) :X-dimension of I^{th} hump, except for I=1. For I=1 a circular hump is assumed with radius U(4).
U((I-1)*6+5) :Y-Dimension of I^{th} hump, except for I=1.
U((I-1)*6+6) :Orientation of I^{th} hump, except for I=1.
U(5) :Seismic velocity in the anomalous zone.
U(6) :Depth of the base of the anomalous zone, in kilometers.
IND :This variable controls the action of the subprogram.
=1 Directs subprogram to input data. This value must be used on the first call.
=4 Performs ray tracing calculations and calculates objective function value, which is returned in F.
=3 Performs calculations as for IND=4, and proceeds to print comprehensive output.
=6 Allows internal constants and error tolerances to be reset. Used during debugging.
=7 Performs calculations as for IND=4, and procedes to plotting mode.

INPUT

UNIT 3 Unperturbed velocity structure, station data and raw delays:

(V(I),H(I),I=1,5) (5(F5.2,F10.2))

V(I) :Seismic velocity in km/sec in I^{th} layer, counting from the surface.
H(I) :Depth in kilometers to the base of I^{th} layer. Deepest layer flagged with H(I) greater than 9000.0.

Station coordinates one card per station:

KST,SLAT,SLON,SMT (I2,8X,3F10.5)

KST :Station number.
SLAT :Station latitude in degrees N (S negative).
SLON :Station longitude in degrees E (W negative).
SHT :Station height in meters above sea level.

End of station list flagged by card with KST=0

Onset weight values:

KWUS,(WLST(I),I=1,9)   (I5,9F5.2)

KWUS :Less than or equal to zero ⇒ weights used as input.
Greater than zero ⇒ weights set to 1.
WLST(I) :Weight assigned to onset weight code I.

Event data - one card per event:

KEV,ELAT,ELON,EDPT,EMG,IR,IH,IM,SC,DL,EBB,EAZ,IWE,EVEL

(I8,2F9.3,2F4.1,I4,2I3,F6.2,3F4.0,I2,F7.2)

KEV	:Event number.
ELAT	:Epicentral latitude in degrees N (Snegative).
ELON	:Epicentral latitude in degrees E (W negative).
EDPT	:Focal depth in kilometers.
EMG	:Magnitude.
IR	:Geographic area number.
IH	:Hours part of onset time.
IM	:Minutes part of onset time.
SC	:Seconds part of onset time.
DL	:Approximate epicentral distance in degrees.
EBB	:Epicentral back-bearing in degrees.
EAZ	:Azimuth of station network from epicentres.
IWE	:Event weight code.
EVEL	:Theoretical apparent surface velocity at a representative station.

End of event list is flagged with KEV=0.

Delay cards. One event per card with up to seven delays.

Use as many cards as required for each event:

KR,(ISR(J),DR(J),IWR(J),J=1,7)

(I8,2X,7(I3,F5.2,I2))

KR	:Event number.
ISR(J)	:Station number for the J^{th} delay.
DR(J)	:J^{th} delay.
IWR(J)	:Onset weight code for J^{th} delay.

"$ENDFILE" flags end of input.

UNIT 5 This unit is used by MINUIT to input its own command sequence as described in the MINUIT manual. MHUMP also uses command cards input on Unit 5, but only in the plotting mode. These are outwardly similar to the MINUIT commands. Each command is input thus:

```
CWD,(COM(I),I=1,7)    (A10,7F10.0)
```

CWD :command word.
COM :Array of general purpose input variables.

Plotting mode is entered with the MINUIT command:

CALL FCN 7.0

MHUMP recognises 3 commands, PLOT, MAP, and STOP.

PLOT :Draws a vertical section through the anomalous zone between any two points. The latitude and longitude of the first point are in COM(1) and COM(2) respectively, and the latitude and longitude of the second point are in COM(3)and COM(4). The section is drawn to a depth given in COM(5), in kilometers.

MAP: Draws a map between longitudes given in COM(1) and COM(2) and latitudes given in COM(3) and COM(4). If COM(5) is not negative, contours of the upper interface are drawn. The contour interval in kilometers is given in COM(5) (default value is 10 kilometers). If COM(6) is not zero, positions where rays enter and/or leave the anomalous zone are plotted. If |COM(6)| =2 or 3 then the entry position is marked with a "*".
If |COM(6)| =1 or 3 the exit position is marked with a "⊙".
If COM(6) is positive, the entry and exit points are joined.
If COM(6) is negative, the entry and exit points are not joined.

STOP :Halts the plotting mode and returns to the main MINUIT command sequence.

OUTPUT

UNIT 6 This unit outputs all printed matter.

UNIT 9 This unit outputs a standard plotfile.

EXTERNAL ROUTINES

The subroutine is designed to be called from MINUIT. A compiled version of this program is held in GPT9:MINUIT. The subroutine calls subroutines in the GHOST plotting library.

```
      SUBROUTINE FCN(N,G,F,U,IND)
C
C*** THIS SUBROUTINE CALCULATES AN OBJECTIVE FUNCTION, F
C    TO BE MINIMIZED BY MINUIT, A NON-LINEAR OPTIMIZING
C    PROGRAM AVAILABLE IN FILE TPT9:MINNEW.
C      THE OBJECTIVE FUNCTION IS THE WEIGHTED R.M.S. RESIDUALS,
C    THEORETICAL-MEASURED TELESEISMIC DELAYS AS OBSERVED
C    AT A NUMBER OF STATIONS. THEORETICAL DELAYS ARE
C    CALCULATED THROUGH A STRUCTURE WHOSE LOWER SURFACE
C    IS PLANE AND HORIZONTAL, AT DEPTH BASE, AND WHOSE
C    UPPER SURFACE IS DEFINED BY AN ANALYTIC FUNCTION.
C
C    THE MODEL OUTSIDE THE STRUCTURE IS DEFINE BY PLANE
C    HORIZONTAL LAYERS, EACH WITH A UNIFORM VELOCITY. UP
C    TO FIVE LAYERS CAN BE ACCOMODATED.
C
      COMMON /PAREXT/DUM(150),NAM(150),WERR(150),MAXEXT,NU
     % /CARD/CWD,CWRD2,CWRD3,WD7(7)
      REAL V(5),H(5),SLAT(40),SLON(40),SHT(40),SX(40),SY(40),EDWT(400),
     % EDSR(400),ELAT(400),ELON(400),EDIS(400),EBB(400),EAZ(400),
     % EDPT(400),EDEL(400),EMG(400),SC(400),DL(400),DEL(600),DSR(600),
     % EVEL(400),ECB(400),ESB(400),U(150),G(150),DR(7),WLST(9),WT(600),
     % XB(600),YB(600),ZB(600),ASTR(40),ANMST(40),ASTR2(40),AVDL(40),
     % HX(8),HY(8),A(8),B(8),C(8),D(8),DEN(8),XUNP(600),YUNP(600),
     % XBASE(600),YBASE(600),COM(8),ACT(3),X(80),Y(80),ROS(600),
     % P(80,80),CL(500)
      INTEGER KST(40),KEV(400),NMS(400),IR(400),IH(400),IM(400),
     % ISR(7),IWR(7),L(10),IWE(400),IEV(600),IST(600),NIT(600),IWT(600)
      DATA ACT/'PROF','MAP ','STOP'/
      EQUIVALENCE (COM(2),YS,XMIN),(COM(3),XS,XMAX),
     % (COM(4),YF,YMIN),(COM(5),XF,YMAX),
     % (COM(6),DPT,DINT)
      IF(IND.GT.1) GO TO 100
      WRITE(6,3)
    3 FORMAT('0  ***  MHUMP (NORMAL HUMPS) SUBROUTINE FCN  ***   ',
     % 'JOHN E.G. SAVAGE  (01AUG79).   BEGIN READING DATA.')
C
C*** SET CONSTANTS
C
      RTOD=45.0/ATAN(1.0)
      NCALL=0
      DTOR=1.0/RTOD
      DTOK=111.32
      RIT=0.93
      RITX=0.8
      RITN=0.8
      DER=.05
      ER=5.E-4
      NHMP=NU/6
      IF(NU-NHMP*6.EQ.0) GO TO 10
      NHMP=NHMP+1
      WRITE(6,9)NU,NHMP
    9 FORMAT('0 **WARNING**   ONLY',I4,
     % ' PARAMETERS DECLARED.  HUMP NO.',I3,
     % ' IS INCOMPLETELY DEFINED, AND WILL BE IGNORED.')
      NHMP=NHMP-1
C
C*** THIS SECTION READS IN DATA, STARTING WITH VELOCITY STRUCTURE.
C
   10 READ(3,11)(V(I),H(I),I=1,5)
```

```
   11 FORMAT(5(F5.2,F10.2))
      DO 12 I=1,5
      IF(H(I).LT.900.0) GO TO 12
      NLR=I
      GO TO 14
   12 CONTINUE
C
C*** READ IN STATION COORDINATES.
C
   14 NST=0
   13 NST=NST+1
      READ(3,15) KST(NST),SLAT(NST),SLON(NST),SHT(NST)
   15 FORMAT(I2,8X,3F10.5)
      IF(KST(NST).GT.0)GO TO 13
C
C*** CALCULATE INTERNAL COORDINATE ORIGIN AND INT. STN. COORDS.
C
      IF(SLAT(NST).GT.90.0) GO TO 5
      CLAT=SLAT(NST)
      CLON=SLON(NST)
      NST=NST-1
      GO TO 6
    5 NST=NST-1
      CLAT=0.0
      CLON=0.0
      DO 7 I=1,NST
      CLAT=CLAT+SLAT(I)
    7 CLON=CLON+SLON(I)
      CLAT=CLAT/NST
      CLON=CLON/NST
    6 DO 8 I=1,NST
      SX(I)=(SLON(I)-CLON)*DTOK
    8 SY(I)=(SLAT(I)-CLAT)*DTOK
C
C***   READ IN LIST OF WEIGHTS.
C
      READ(3,17)KWUS,(WLST(I),I=1,9)
   17 FORMAT(I5,9F5.2)
      IF(KWUS)20,20,18
   18 DO 19 I=1,9
   19 WLST(I)=1.0
C
C*** READ IN EVENT DATA
C
   20 NEV=0
   21 NEV=NEV+1
      READ(3,23) KEV(NEV),ELAT(NEV),ELON(NEV),EDPT(NEV),EMG(NEV),
     % IR(NEV),IH(NEV),IM(NEV),SC(NEV),DL(NEV),EBB(NEV),EAZ(NEV),
     % IWE(NEV),EVEL(NEV)
   23 FORMAT(I8,2F9.3,2F4.1,I4,2I3,F6.2,3F4.0,I2,F7.2)
      ECB(NEV)=COS(EBB(NEV)*DTOR)
      ESB(NEV)=SIN(EBB(NEV)*DTOR)
      IF(KEV(NEV).GT.0)GO TO 21
      NEV=NEV-1
C
C*** READ IN DELAYS
C
      NDEL=0
   40 READ(3,41,END=75)KR,(ISR(J),DR(J),IWR(J),J=1,7)
   41 FORMAT(I8,2X,7(I3,F5.2,I2))
```

```
   48 DO 50 I=1,NEV
      IF(KEV(I).NE.KR)GO TO 50
      II=I
      GO TO 55
   50 CONTINUE
      WRITE(6,53)KR,(ISR(J),DR(J),IWR(J),J=1,7)
   53 FORMAT(' **WARNING** DELAY CARD NOT MATCHED WITH EVENT:',
     % I8,2X,7(I3,F5.2,I2))
      GO TO 40
   55 DO 70 J=1,7
      IF(ISR(J).EQ.0)GO TO 70
   60 DO 58 K=1,NST
      IF(ISR(J).NE.KST(K))GO TO 58
      NDEL=NDEL+1
      IST(NDEL)=K
      GO TO 64
   58 CONTINUE
      WRITE(6,59)ISR(J),DR(J),IWR(J),KR
   59 FORMAT(' **WARNING** UNKNOWN STATION:',I3,' DELAY:',F6.2,
     % ' WEIGHT:',I2,' EV. NO.',I9)
      GO TO 70
   64 IEV(NDEL)=II
      IWT(NDEL)=IWR(J)
      WT(NDEL)=WLST(IWR(J))
      DEL(NDEL)=DR(J)
   70 CONTINUE
      GO TO 40
   75 RETURN
C
C***  THIS SECTION CALCULATES THE OBJECTIVE FUNCTION
C
C
C*** ALL CALCLATIONS ARE MADE IN A LOCAL COORDINATE SYSTEM,
C   CENTRED ON CLAT,CLON.
C
  100 IF(IND.EQ.6) GO TO 600
      NORY1=0
      NORY5=0
      NORYU=0
      ITRT=0
      ISTEP=0
      IHLF=0
      NCALL=NCALL+1
      IF(IND.NE.3) WRITE(6,105)NCALL,(U(I),I=1,NU)
  105 FORMAT(1X,I4,6G16.7/(5X,6G16.7,2X))
      DO 604 I=1,NHMP
      HX(I)=(U(I*6-4)-CLON)*DTOK
      HY(I)=(U(I*6-5)-CLAT)*DTOK
      C(I)=U(I*6-3)
      CTH=COS(U(I*6)*DTOR)
      STH=SIN(U(I*6)*DTOR)
      DX=1.0/U(I*6-2)**2
      DY=1.0/U(I*6-1)**2
      A(I)=CTH*CTH*DX+STH*STH*DY
      B(I)=STH*STH*DX+CTH*CTH*DY
  604 D(I)=2.0*CTH*STH*(DY-DX)
      A(1)=1.0/U(4)**2
      B(1)=A(1)
      D(1)=0.0
      VB=U(5)
```

```
      BASE=U(6)
      GMAX=1.125*C(1)*SQRT(A(1)/3.0)
      CMAX=2.0*C(1)*A(1)
      CSUM=C(1)
      IF(NHMP.LT.2) GO TO 608
      DO 607 I=2,NHMP
      TJ=AMIN1(U(I*6-2),U(I*6-1))
      CSUM=CSUM+C(I)
      GMAX=GMAX+0.6495191*C(I)/TJ
  607 CMAX=CMAX+2.0*C(I)/(TJ*TJ)
  608 DO 610 I=1,NEV
      EDEL(I)=0.0
      EDSR(I)=0.0
      EDWT(I)=0.0
  610 NMS(I)=0
      DO 102 I=1,NLR
      IF(H(I).LT.BASE)GO TO 102
      NBS=I
      GO TO 103
  102 CONTINUE
C
C***  FOR EACH MEASURED DELAY TIME CALCULATE A THEORETICAL DELAY.
C    THE METHOD FOR DETERMINING THE RAY PATH IS AN ITERITIVE ONE.
C    FIRST UNPERTERBED RAY TO BASE OF STRUCTURE. THEN TRACE RAY
C    BACK THROUGH STRUCTURE TO SURFACE. THIS WILL EMERGE
C    AT A POINT DISPLACED AWAY FROM THE STATION. DISPLACE THE
C    POINT AT THE BASE OF THE STRUCTURE BY AN AMOUNT PROPORTIONAL
C    TO RIT IN THE OPPOSITE DIRECTION, AND RETRACE THE RAY THROUGH THE
C    STRUCTURE FROM NEW INITIAL POINT TO SURFACE. IT SHOULD ARRIVE NEARER
C    THE STATION THAN BEFORE. THIS IS REPEATED UNTIL THE RAY ARRIVES
C    WITHIN SQRT(DER) OF THE STATION.
C
  103 VBS=V(NBS)
      DVBS=(VB/VBS)**2
      DO 350 I=1,NDEL
      RITR=1.0
      IS=IST(I)
      XST=SX(IS)
      YST=SY(IS)
      IV=IEV(I)
      CBB=ECB(IV)
      SBB=ESB(IV)
      VS=EVEL(IV)
C
C***  CALCULATE WHERE UNPERTERBED RAY INTERSECTS PLANE OF STRUCTURE BASE
C    AND TRAVEL TIME FOR THIS RAY
C
      TU=0.0
      IF(NBS.GT.1) GO TO 112
      SI=V(1)/VS
      CI=SQRT(1.0-SI*SI)
      DBS=SI*BASE/CI
      TU=BASE/(V(1)*CI)
      GO TO 122
  112 DO 120 J=1,NBS
      IF(J.EQ.NBS) GO TO 116
      IF(J.GT.1) GO TO 114
      SI=V(1)/VS
      CI=SQRT(1.0-SI*SI)
      DBS=H(1)*SI/CI
```

```
          TU=H(1)/(V(1)*CI)
          GO TO 120
      114 SI=V(J)/VS
          CI=SQRT(1.0-SI*SI)
          DBS=DBS+(H(J)-H(J-1))*SI/CI
          TU=TU+(H(J)-H(J-1))/(V(J)*CI)
          GO TO 120
      116 SI=V(J)/VS
          CI=SQRT(1.0-SI*SI)
          DBS=DBS+(BASE-H(J-1))*SI/CI
          TU=TU+(BASE-H(J-1))/(V(J)*CI)
      120 CONTINUE
      122 CZ=-CI
          YBS=YST+DBS*CBB
          XBS=XST+DBS*SBB
          XSRT=XBS
          YSRT=YBS
          XUNP(I)=XBS
          YUNP(I)=YBS
          CX=-SBB*SI
          CY=-CBB*SI
C
C*** CALCULATE RAY DIRECTION IN STRUCTURE
C
          SI2=1.0-CZ*CZ
          SR2=SI2*DVBS
          IF(SR2.GT.1.0) GO TO 9022
          TMP1=SQRT(SR2/SI2)
          FZ=-SQRT(1.0-SR2)
          FX=TMP1*CX
          FY=TMP1*CY
          DO=0.0
          ITER=0
          ITIR=0
C
C*** RAY STARTS AT BASE OF STRUCTURE.
C
      130 ITER=ITER+1
          ITRT=ITRT+1
          XBASE(I)=XSRT
          YBASE(I)=YSRT
C
C***  CALCULATE THE POINT (XO,YO,ZO) WHERE A LINE FROM (XSRT,YSRT,BASE)
C    WITH DIRECTION COSINES (FX,FY,FZ) INTERSECTS THE "NHMP" HUMPED
C    SURFACE DEFINED BY THE PARAMETERS HX,HY,A,B,C,AND D. THE BASE
C    OF THE STRUCTURE IS AT DEPTH "BASE". THE I.TH HUMP IS CENTRED
C    ON (HX(I),HY(I)), AND HAS THE FORM :-
C     HT(X,Y)=C/(1+A*(X-HX)**2+D(X-HX)*(Y-HY)+B*(Y-HY)**2)
C    WHERE HT IS THE HEIGHT ABOVE BASE. THE SURFACE IS THE SUM OF
C    THE HEIGHTS OF ALL THE HUMPS.
C     THE DIRECTION COSINES (BX,BY,BZ) OF THE NORMAL AT (XO,YO,ZO)
C    ALSO CALCULATED.
C
          S=BASE
          DO 1310 IQ=1,NHMP
     1310 S=S-C(IQ)/(1.0+A(IQ)*(XSRT-HX(IQ))**2+D(IQ)*(XSRT-HX(IQ))*
         % (YSRT-HY(IQ))+B(IQ)*(YSRT-HY(IQ))**2)
          FMIN=BASE-S
          IF(FMIN.GT.0.0) GO TO 1315
          R=-1.0
```

```
      GO TO 1380
 1315 T=SQRT(FX**2+FY**2)
      IF(T.EQ.0.0) GO TO 1360
      RMIN=0.0
      GLN=FZ/T
      IF(-GLN.GT.GMAX)GO TO 1370
      GR=(GMAX-GLN)/SQRT(1.0+GLN**2)
      CR=CMAX/(1.0+GLN**2)
      UP=GR/CR
      FP=GR*GR/(2.0*CR)
 1318 IF(FMIN.LT.FP) GO TO 1320
      RMAX=RMIN+UP+(FMIN-FP)/GR
      GO TO 1325
 1320 IF(FMIN.GT.0.0) GO TO 1322
      R=RMIN
      XO=XSRT+R*FX
      YO=YSRT+R*FY
      ZO=BASE+R*FZ
      GO TO 1350
 1322 RMAX=RMIN+SQRT(2.0*FMIN/CR)
 1325 XO=XSRT+RMAX*FZ
      YO=YSRT+RMAX*FY
      ZO=BASE+RMAX*FZ
      S=BASE
      ISTEP=ISTEP+1
      DO 1328 IQ=1,NHMP
 1328 S=S-C(IQ)/(1.0+A(IQ)*(XO-HX(IQ))**2+D(IQ)*(XO-HX(IQ))*
     % (YO-HY(IQ))+B(IQ)*(YO-HY(IQ))**2)
      FMAX=ZO-S
      IF(FMAX.LT.0.0) GO TO 1330
      RMIN=RMAX
      FMIN=FMAX
      GO TO 1318
C
C*** RMIN AND RMAX NOW LIE EITHER SIDE OF INTERSECTION POINT.
C    USE INTERVAL HALVING TO CLOSE DOWN ON THIS POINT.
C
 1330 QMAX=1.0
      QMIN=1.0
 1333 R=(QMAX*FMAX*RMIN-QMIN*FMIN*RMAX)/(QMAX*FMAX-QMIN*FMIN)
      IHLF=IHLF+1
      XO=XSRT+R*FX
      YO=YSRT+R*FY
      ZO=BASE+R*FZ
      S=BASE
      DO 1335 IQ=1,NHMP
      DEN(IQ)=1.0/(1.0+A(IQ)*(XO-HX(IQ))**2+D(IQ)*(XO-HX(IQ))
     % *(YO-HY(IQ))+B(IQ)*(YO-HY(IQ))**2)
 1335 S=S-C(IQ)*DEN(IQ)
      F=ZO-S
      IF(F) 1340,1350,1345
 1340 FMAX=F
      RMAX=R
      QMAX=1.0
      QMIN=QMIN*RITN
      GO TO 1347
 1345 FMIN=F
      RMIN=R
      QMIN=1.0
      QMAX=QMAX*RITX
```

```
 1347 R=RMAX+RMIN
      IF(RMAX-RMIN-ER*R)1348,1348,1333
 1348 R=R/2
C
C***  CALCULATE NORMAL.
C
 1350 BX=0.0
      BY=0.0
      DO 1355 IQ=1,NHMP
      GR=(DEN(IQ))**2
      BX=BX-C(IQ)*(2.0*A(IQ)*(XO-HX(IQ))+D(IQ)*(YO-HY(IQ)))*GR
 1355 BY=BY-C(IQ)*(2.0*B(IQ)*(YO-HY(IQ))+D(IQ)*(XO-HX(IQ)))*GR
      GR=SQRT(1.0+BX*BX+BY*BY)
      BX=BX/GR
      BY=BY/GR
      BZ=1.0/GR
      GO TO 1380
 1360 S=BASE
      DO 1365 IQ=1,NHMP
      DEN(IQ)=1.0/(1.0+A(IQ)*(XSRT-HX(IQ))**2+D(IQ)*(XSRT-HX(IQ))*
     % (YSRT-HY(IQ))+B(IQ)*(YSRT-HY(IQ))**2)
 1365 S=S-C(I)*DEN(I)
      R=BASE-S
      XO=XSRT
      YO=YSRT
      ZO=S
      GO TO 1350
 1370 RMAX=CSUM*SQRT(1.0+(1.0/GLN)**2)
      GO TO 1330
 1380 XB(I)=XO
      YB(I)=YO
      ZB(I)=ZO
      IF(R.LT.0.0) GO TO 9024
      IF(ZO)132,132,136
  132 ZO=0.0
      R=-BASE/FZ
      XO=R*FX
      YO=R*FY
      TT=R/VB
      GO TO 300
  136 TT=R/VB
      NP=2
      L(1)=0
C
C*** FIND WHICH LAYER RAY EMERGES INTO.
C
      DO 156 J=1,NBS
      IF(H(J).LE.ZO) GO TO 156
      NL=J
      GO TO 158
  156 CONTINUE
      STOP 1
  158 VO=V(NL)
      IP=1
C
C***  CALCULATE DIRECTION COSINES, CX,CY,CZ, OF REFRACTED
C     RAY, DUE TO INCIDENT RAY WITH DIRECTION COSINES FX,FY,FZ,
C     WHEN INTERFACE HASE NORMAL TO SURFACE WITH DIRECTION
C     COSINES BX,BY,BZ, AND VELOCITIES VB AND VO.
C
```

```
      AA=FX*BX+FY*BY+FZ*BZ
      AA2=AA*AA
      IF(AA2-1.0) 1510,1550,1540
 1510 BB2=1.0-VO*VO*(1.0-AA2)/(VB*VB)
      IF(BB2)9020,1520,1520
 1520 BB=SQRT(BB2)
      IF(AA.LE.0.0)BB=-BB
      CC=AA*BB+SQRT((1.0-AA2)*(1.0-BB2))
      Q=(CC-BB*AA)/(1.0-AA2)
      R=(BB-CC*AA)/(1.0-AA2)
      CX=Q*FX+R*BX
      CY=Q*FY+R*BY
      CZ=Q*FZ+R*BZ
      GO TO 160
 1540 Q=SQRT(FX*FX+FY*FY+FZ*FZ)
      CX=FX/Q
      CY=FY/Q
      CZ=FZ/Q
      GO TO 160
 1550 CX=FX
      CY=FY
      CZ=FZ
      GO TO 160
C
C***  TRACE RAY THROUGH LAYER.
C
  160 L(NP)=NL
      NP=NP+1
      IF(NL.GT.1) GO TO 163
      ZL=0.0
      GO TO 164
  163 ZL=H(NL-1)
  164 RN=(ZL-ZO)/CZ
  170 TT=TT+RN/VO
      XO=XO+RN*CX
      YO=YO+RN*CY
      ZO=ZL
      IF(NL.LE.1) GO TO 300
      IP=0
      NL=NL-1
      VN=VO
      VO=V(NL)
      DX=CX
      DY=CY
      DZ=CZ
C
C*** CALCULATE RAY DIRECTION IN NEW LAYER
C
      SI2=1.0-DZ*DZ
      SR2=SI2*(VO/VN)**2
      IF(SR2.GT.1.0) GO TO 9026
      TMP1=SQRT(SR2/SI2)
      CZ=-SQRT(1.0-SR2)
      CX=TMP1*DX
      CY=TMP1*DY
      GO TO 160
C
C***  RAY TRACED TO SURFACE. CALCULATE DELAY TIME, COMPARE
C     SURFACE POINT WITH STN. COORDS., AND IF SUFFICIENTLY
C     CLOSE STOP ITERATION.
```

```
      C
        300 TCRN=((XBS-XSRT)*SBB+(YBS-YSRT)*CBB)/VS
            DN=TT-TU+TCRN
            XDIF=XST-XO
            YDIF=YST-YO
            IF(XDIF*XDIF+YDIF*YDIF-DER)320,320,302
        302 IF(ITER.GT.10) GO TO 9028
      C
      C*** NOT YET CONVERGED. GET NEW XSRT & YSRT, AND ITERATE.
      C
            XSRT=XSRT+XDIF*RITR
            YSRT=YSRT+YDIF*RITR
            RITR=RITR*RIT
            DO=DN
            GO TO 130
      C
      C*** CONVERGED.
      C
        320 DSR(I)=DN
            NP=NP-1
            EDEL(IV)=EDEL(IV)+WT(I)*DEL(I)
            EDSR(IV)=EDSR(IV)+WT(I)*DSR(I)
            EDWT(IV)=EDWT(IV)+WT(I)
            NMS(IV)=NMS(IV)+1
            GO TO 348
       9028 DSR(I)=-15.0
            NORY5=NORY5+1
            GO TO 348
       9026 DSR(I)=-14.0
            NORYU=NORYU+1
            GO TO 348
       9024 DSR(I)=-13.0
            NORYU=NORYU+1
            GO TO 348
       9022 DSR(I)=-12.0
            NORYU=NORYU+1
            GO TO 348
       9020 ITIR=ITIR+1
            IF(ITIR.GT.5) GO TO 9021
            TJ=1.0+FLOAT(ITIR)/3.0
            XSRT=XST+TJ*(XBS-XST)
            YSRT=YST+TJ*(YBS-YST)
            GO TO 130
       9021 DSR(I)=-11.0
            NORY1=NORY1+1
        348 NIT(I)=ITER
        350 CONTINUE
            SHFT=0.0
            DO 380 I=1,NEV
            IF(NMS(I).EQ.0) GO TO 380
            EDSR(I)=EDSR(I)/EDWT(I)
            EDEL(I)=EDEL(I)/EDWT(I)
            SHFT=SHFT+EDSR(I)-EDEL(I)
        380 CONTINUE
            F=0.0
            SWT=0.0
            UN=0.0
            DO 390 I=1,NDEL
            J=IEV(I)
            IF(DSR(I).LT.-10.0) GO TO 390
```

```
      RES=DEL(I)-DSR(I)-EDEL(J)+EDSR(J)
      F=F+RES*RES*WT(I)
      SWT=SWT+WT(I)
      UN=UN+1.0
  390 CONTINUE
      F=SQRT(F/SWT)
      FL=ABS(SHFT)/FLOAT(NDEL)
      NUN=IFIX(UN+0.1)
      CX=FLOAT(ISTEP)/FLOAT(ITRT)
      CY=FLOAT(IHLF)/FLOAT(ITRT)
      WRITE(6,393)NUN,ITRT,CX,CY,F,FL
  393 FORMAT('  DLS. USED=',I5,'  RAYS TRACED=',I6,
     % ' STEPS/RAY=',F6.2,'  HALVINGS/RAY=',F7.2,
     % ' FN.VALUE=',F9.5,'  BASE SHIFT',F7.3)
      IF(IND.NE.3) GO TO 7000
      DO 403 I=1,NST
      AVDL(I)=0.0
      ASTR2(I)=0.0
      ASTR(I)=0.0
      ANMST(I)=0.0
  403 CONTINUE
  404 DX=1000.0*SQRT(DER)
      WRITE(6,405) F,NDEL,NUN,DX,CLAT,CLON,DTOK,VB,BASE,(U(I),I=1,4),
     % HX(1),HY(1),A(1),B(1),D(1)
  405 FORMAT('1   ***  MHUMP (NORMAL HUMPS) SUBROUTINE FCN ***    ',
     % ' JOHN E.G. SAVAGE      (01AUG79)'/
     % '0  OBJECTIVE FUNCTION VALUE (R.M.S. OF RESIDUALS)=',F8.5,
     % ' SECONDS.'/'0  TOTAL NUMBER OF DELAYS=',I5,'.  NUMBER USED=',I5,
     % '.  RAYS TRACED TO WITHIN',F7.1,' METERS OF STATIONS.'/
     % '0  ORIGIN OF INTERNAL COORDINATES IS AT',F8.3,
     % ' DEG. LATITUDE,',F9.3,' DEG. LONGITUDE.',
     % '  SCALING FACTOR USED IS',F8.3,' KM/DEG.'//
     % '0  BODY PARAMETERS:    SEISMIC VELOCITY=',F7.4,
     % ' KM/SEC.   DEPTH OF BASE=',F6.1,' KM.'/
     % '0  HUMP  LATITUDE  LONGITUDE      HEIGHT X-DIMENSION',
     % ' Y-DIMENSION    ANGLE',8X,'INTERNAL COORDINATES AND CONSTANTS'/
     % '   NO.      (DEG.)      (DEG.)',
     % '      (KM.)       (KM.)       (KM.)    (DEG.)',
     % '   HX(KM)  HY(KM)   "A"(KM**-2)   "B"(KM**-2)   "D"(KM**-2)'/
     % 5X,'1',3F11.3,F12.3,'(RADIUS OF THIS HUMP)',F9.1,F8.1,3E13.4)
      IF(NHMP.LT.2) GO TO 415
      WRITE(6,413)(I,(U(6*(I-1)+J),J=1,6),HX(I),HY(I),A(I),B(I),D(I),
     % I=2,NHMP)
  413 FORMAT(1X,I5,3F11.3,2F12.3,F9.1,F9.1,F8.1,3E13.4)
      WRITE(6,417)(H(I),I=1,NLR)
  417 FORMAT('0  NORMAL VELOCITY STRUCTURE:'/
     % '0  DEPTH TO BASE OF LAYER  (KM.)=',5F8.1)
      WRITE(6,419)(V(I),I=1,NLR)
  419 FORMAT('          LAYER VELOCITY (KM/SEC.)=',5F8.2)
  415 IF(KWUS)406,406,408
  406 WRITE(6,407)(I,I=1,9),(WLST(J),J=1,9)
  407 FORMAT('0 ONSET WEIGHT CODE:',9I7/
     % '     ASSIGNED WEIGHT:  ',9F7.2/'0',120('*'))
      GO TO 410
  408 WRITE(6,409)
  409 FORMAT('0'/'      *** ALL ONSET WEIGHTS SET TO UNITY. ***'/
     % '0',120('*'))
  410 DO 490 I=1,NEV
      WRITE(6,411)KEV(I),ELAT(I),ELON(I),EDPT(I),EMG(I),IR(I),
     % IH(I),IM(I),SC(I),DL(I),EBB(I),EAZ(I),IWE(I),EVEL(I),
```

```
     % EDEL(I),EDSR(I)
 411 FORMAT('  EVENT',I9,'  LAT.',F7.3,' LON.',F8.3,' DEPTH',
     % F5.0,'  MAG.',F4.1,'  REGION',I4,'  OR. TIME',I3,':',I2,
     % ':',F5.2/'  DIST.',F5.0,'  BACK-BRNG.',F5.0,
     % '  AZIM.',F5.0,'  WEIGHT',I2/
     % '  APP. VEL.',F6.2,'  MEAN OF MEAS. DLYS.=',F7.3,
     % ' SEC.,  MEAN OF TH. DLYS.=',F7.3,' SEC.'/
     % '0  STN MEAS.DLY. WT.    RES. TH.DLY.    RES.',
     % 3X,'XBDY     YBDY     ZBDY    XBASE  YBASE     XUNP    YUNP   ',
     % 'RESIDUAL')
      DO 450 J=1,NDEL
      IF(IEV(J).NE.I) GO TO 450
      RES1=DEL(J)-EDEL(I)
      IF(DSR(J).LT.-10.0) GO TO 440
      AVDL(IST(J))=AVDL(IST(J))+DSR(J)
      RES2=DSR(J)-EDSR(I)
      RES=RES1-RES2
      ROS(J)=RES
      ASTR(IST(J))=ASTR(IST(J))+RES
      ASTR2(IST(J))=ASTR2(IST(J))+RES*RES
      ANMST(IST(J))=ANMST(IST(J))+1.0
      WRITE(6,431) KST(IST(J)),DEL(J),IWT(J),RES1,DSR(J),
     % RES2,XB(J),YB(J),ZB(J),XBASE(J),YBASE(J),XUNP(J),YUNP(J),RES
 431 FORMAT(3X,I3,F9.3,I4,3F8.3,3F8.1,2(F8.1,F7.1),F9.3)
      GO TO 450
 440 KK=IFIX(-10.1-DSR(J))
      ROS(J)=DSR(J)
      WRITE(6,441)KST(IST(J)),DEL(J),IWT(J),KK
 441 FORMAT(3X,I3,F9.3,I5,3('     *** RAY NOT TRACED *** '),
     % ' CODE=',I2)
 450 CONTINUE
      WRITE(6,491)
 490 CONTINUE
 491 FORMAT(1X,120('*'))
      WRITE(6,501)
 501 FORMAT('1 *** STATION INFORMATION ***'/
     % '0 STN  LATITUDE LONGITUDE   HEIGHT  ',
     % 'X-COORD  Y-COORD  MEAN RES.  NO. MEAS.  STD. DEVN.',
     % '  DELAY')
      DO 507 I=1,NST
      J=IFIX(ANMST(I)+0.1)
      IF(J.EQ.0) ANMST(I)=1.0
      RES=ASTR(I)/ANMST(I)
      RES2=AVDL(I)/ANMST(I)
      RES1=SQRT(ASTR2(I)/ANMST(I)-RES*RES)
      WRITE(6,505)KST(I),SLAT(I),SLON(I),SHT(I),
     % SX(I),SY(I),RES,J,RES1,RES2
 505 FORMAT(1X,I4,2F10.3,F9.0,2F9.2,F10.4,I11,F12.5,F8.3)
 507 CONTINUE
      WRITE(6,509)
 509 FORMAT('0',120('*'))
      IF(NORY1.NE.0) WRITE(6,511) NORY1
 511 FORMAT('0 **WARNING**',I6,' RAY(S) NOT TRACED DUE TO',
     % ' TOTAL INTERNAL REFLECTION.')
      IF(NORY5.NE.0) WRITE(6,521) NORY5
 521 FORMAT('0 **WARNING**',I6,' RAY(S) NOT TRACED DUE TO',
     % ' ITERATIONS NOT CONVERGING.')
      IF(NORYU.NE.0) WRITE(6,523) NORYU
 523 FORMAT('0 **WARNING**',I6,' RAY(S) NOT TRACED DUE TO',
     % ' UNSPECIFIED PROBLEM(S).')
```

```
      IF(NORY1.NE.0.OR.NORY5.NE.0.OR.NORYU.NE.0) WRITE(6,509)
      RETURN
C
C***  THIS SECTION ALLOWS REDEFINITION OF CERTAIN CONSTANTS IN
C    THIS SUBROUTINE, AFFECTING ERROR MARGINS AND THE STABILITY
C    OF ITERATIVE PROCEEDURES.
C
  600 IF(WD7(2).GT.1.E-6.AND.WD7(2).LT.1.E-2) ER=WD7(2)
      IF(WD7(3).GT.1.E-6.AND.WD7(3).LT.50.0) DER=WD7(3)
      IF(WD7(4).GT.0.1.AND.WD7(4).LT.0.999) RIT=WD7(4)
      IF(WD7(5).GT.0.1.AND.WD7(5).LT.0.999) RITX=WD7(5)
      IF(WD7(6).GT.0.1.AND.WD7(6).LT.0.999) RITN=WD7(6)
      WRITE(6,605) ER,DER,RIT,RITX,RITN
  605 FORMAT('0 *** INTERNAL ERROR LIMITS AND ITERATION STABILITY',
     % ' FACTORS CHANGED.  NEW VALUES ARE: ER=',E12.3,',   DER=',G10.5,
     % ',   RIT=',F6.3,',   RITX=',F6.3,',   RITN=',F6.3,'.')
      RETURN
 7000 IF(IND.NE.7) RETURN
C
C***  THIS SECTION DRAWS PROFILES AND DEPTH CONTOURS OF MULTIHUMPED
C    VELOCITY STRUCTURES.
C
C
C***  READ COMMAND CARD AND GO TO RELEVANT SECTION
C
      WRITE(6,7011)
 7011 FORMAT('0**  PLOTTING BEGINS **')
      CALL PAPER(1)
      CALL CSPACE(0.2,0.6,0.1,0.95)
      CALL CTRMAG(27)
      CALL PLACE(1,1)
      CALL TYPECS('HUMP PARAMETERS',15)
      XMX=0.6
      DO 7029 I=1,NHMP
      IF(I.NE.5) GO TO 7028
      CALL CSPACE(0.6,1.0,0.1,0.95)
      CALL PLACE(0,2)
      XMX=1.0
 7028 CALL CRLNFD
      CALL CTRMAG(20)
      CALL TYPECS('  HUMP NUMBER',14)
      CALL TYPENI(I)
      CALL CRLNFD
      CALL CTRMAG(14)
      CALL TYPECS('   LATITUDE= ',13)
      CALL TYPENF(U(I*6-5),3)
      CALL CRLNFD
      CALL TYPECS('  LONGITUDE= ',13)
      CALL TYPENF(U(I*6-4),3)
      CALL CRLNFD
      CALL TYPECS('     HEIGHT= ',13)
      CALL TYPENF(C(I),1)
      CALL CRLNFD
      IF(I.EQ.1) CALL TYPECS('     RADIUS= ',13)
      IF(I.NE.1) CALL TYPECS('X-DIMENSION= ',13)
      CALL TYPENF(U(I*6-2),1)
      CALL CRLNFD
      IF(I.EQ.1) GO TO 7029
      CALL TYPECS('Y-DIMENSION= ',13)
      CALL TYPENF(U(I*6-1),1)
```

```
      CALL CRLNFD
      CALL TYPECS('      ANGLE= ',13)
      CALL TYPENF(U(I*6),2)
 7029 CALL CRLNFD
      CALL CRLNFD
      CALL TYPECS('   VELOCITY= ',13)
      CALL TYPENF(VB,3)
      CALL CRLNFD
      CALL TYPECS('       BASE= ',13)
      CALL TYPENF(BASE,2)
      CALL CRLNFD
      CALL TYPECS('OBJ.FN.VAL.= ',13)
      CALL TYPENF(F,4)
      CALL CRLNFD
      CALL TYPECS('(NORMAL HUMPS)',14)
      CALL PSPACE(0.15,XMX,0.1,0.95)
      CALL MAP(0.0,1.0,0.0,1.0)
      CALL BORDER
 7030 READ(5,7033,END=900) COM
 7033 FORMAT(A4,6X,7F10.4)
      WRITE(6,7035)COM
 7035 FORMAT('0',A4,6X,7G10.3)
      DO 7037 I=1,3
      IF(COM(1).NE.ACT(I)) GO TO 7037
      GO TO (7100,7200,7900), I
 7037 CONTINUE
      WRITE(6,7043)
 7043 FORMAT('0**  WARNING  ***  UNDECODEABLE COMMAND:-',
     $ '  RETURN TO MAIN PROGRAM.')
      GO TO 7900
C
C
C***  THIS SECTION DRAWS A PROFILE OF THE VELOCITY STRUCTURE FROM
C   (XS,YS) TO (XF,YF), DOWN TO DEPTH DPT.
C
 7100 DMX=SQRT((XF-XS)**2+(YF-YS)**2)
      NP=50
      SIZ=DPT/20.0
      CALL FRAME
      CALL PSPACE(0.1,0.765*DTOK*DMX/DPT+0.27,0.1,0.95)
      CALL CSPACE(0.0,0.5+0.9*DTOK*DMX/DPT,0.0,1.0)
      CALL MAP(-DPT/9.0,DTOK*DMX+DPT/9.0,DPT,-DPT/9.0)
      CALL CTRSIZ(DPT/50.0)
      CALL PLOTCS(-DPT/12.0,-DPT/15.0,' LATITUDE=',10)
      CALL TYPENF(YS,3)
      CALL PLOTCS(-DPT/12.0,-DPT/30.0,'LONGITUDE=',10)
      CALL TYPENF(XS,3)
      CALL PLOTCS(DMX*DTOK-DPT/6.0,-DPT/15.0,' LATITUDE=',10)
      CALL TYPENF(YF,3)
      CALL PLOTCS(DMX*DTOK-DPT/6.0,-DPT/30.0,'LONGITUDE=',10)
      CALL TYPENF(XF,3)
      XINC=(XF-XS)/FLOAT(NP-1)
      YINC=(YF-YS)/FLOAT(NP-1)
      DINC=DTOK*SQRT(XINC**2+YINC**2)
      DO 7120 I=1,NP
      XP=(XS+(I-1)*XINC-CLON)*DTOK
      YP=(YS+(I-1)*YINC-CLAT)*DTOK
      X(I)=(I-1)*DINC
      Y(I)=BASE
      DO 7116 J=1,NHMP
```

```
         DO 7116 J=1,NHMP
    7116 Y(I)=Y(I)-C(J)/(1.0+A(J)*(XP-HX(J))**2+
        % D(J)*(XP-HX(J))*(YP-HY(J))+B(J)*(YP-HY(J))**2)
    7120 CONTINUE
         CALL BORDER
         CALL SCALES
         CALL POSITN(X(1),0.0)
         CALL JOIN(X(NP),0.0)
         CALL POSITN(X(NP),BASE)
         CALL JOIN(X(1),BASE)
         DO 7140 I=3,NP
         IF(Y(I-2).LT.Y(I-1).OR.Y(I).LT.Y(I-1)) GO TO 7140
         CALL CTRSIZ(AMIN1((BASE-Y(I-1))/2.0,SIZ))
         CALL PLOTNF(X(I-2),Y(I-2)*0.25+BASE*0.75,VB,2)
    7140 CONTINUE
         DO 7160 I=1,NLR
         IF(I.LE.1) HT=0.0
         IF(I.GT.1) HT=H(I-1)
         IF(BASE.GT.HT.AND.BASE.LT.H(I)) HT=BASE
         IF(HT.GE.DPT) GO TO 7162
         HI=H(I)
         IF(HI.GT.DPT) HI=DPT*1.01
         IF(HI.LT.BASE) GO TO 7151
         XSL=0.0
         XFL=DMX*DTOK
         GO TO 7157
    7151 IX=0
    7152 IX=IX+1
         IF(IX.GT.NP) GO TO 7160
         IF(Y(IX).LT.HI) GO TO 7152
         IMN=IX
         HMN=Y(IX)-HI
         IF(IX.GT.1) GO TO 7154
         XSL=X(1)
         GO TO 7156
    7154 XSL=(X(IX)-X(IX-1))*(HI-Y(IX-1))/(Y(IX)-Y(IX-1))+X(IX-1)
    7156 IX=IX+1
         IF(IX.GT.NP) GO TO 7158
         IF(Y(IX)-HI.LT.HMN) GO TO 7153
         HMN=Y(IX)-HI
         IMN=IX
    7153 IF(Y(IX).GT.HI) GO TO 7156
         XFL=(X(IX)-X(IX-1))*(HI-Y(IX-1))/(Y(IX)-Y(IX-1))+X(IX-1)
    7157 CALL POSITN(XSL,HI)
         CALL JOIN(XFL,HI)
         CALL CTRSIZ(AMIN1((HI-HT)/2.0,SIZ))
         CALL PLOTNF(XSL*0.45+XFL*0.55,HI*0.75+HT*0.25,V(I),2)
         IF(I.GT.NLR-1) GO TO 7152
         IF(HI+HMN.GT.H(I+1)) GO TO 7152
         CALL CTRSIZ(AMIN1(HMN/2.0,SIZ))
         CALL PLOTNF(X(IMN),H(I)+0.75*HMN,V(I+1),2)
         GO TO 7152
    7158 XFL=X(NP)
         GO TO 7157
    7160 CONTINUE
    7162 CALL MASK(-DPT/9.0,DMX*DTOK+DPT/9.0,0.0,-DPT/9.0)
         CALL POSITN(X(1),Y(1))
         DO 7170 I=2,NP
    7170 CALL JOIN(X(I),Y(I))
         CALL UNMASK(0)
         GO TO 7030
```

```
C
C***  THIS SECTION DRAWS A MAP OF CONTOURS
C     OF THE UPPER SURFACE AND/OR RAYS THROUGH THE ANOMOLOUS
C     ZONE.
C
 7200 IRY=IFIX(COM(7))
      IF(DINT.GE.0.0.OR.IRY.NE.0) GO TO 7205
      WRITE(6,7201)
 7201 FORMAT('0 **  WARNING  ** NEITHER CONTOURS NOR RAYS',
     % ' REQUIRED. MAP NOT DRAWN.')
 7205 CALL FRAME
      NP=80
      CALL PSPACE(0.1,0.1+0.85*(XMAX-XMIN)/(YMAX-YMIN),0.1,0.95)
      CALL CSPACE(0.0,0.1+(XMAX-XMIN)/(YMAX-YMIN),0.0,1.0)
      CALL MAP(XMIN,XMAX,YMIN,YMAX)
      CALL BORDER
      CALL SCALES
      XMN=(XMIN-CLON)*DTOK
      XMX=(XMAX-CLON)*DTOK
      YMN=(YMIN-CLAT)*DTOK
      YMX=(YMAX-CLAT)*DTOK
      CALL MAP(XMN,XMX,YMN,YMX)
      IF(DINT.LT.0.0) GO TO 7240
      XINC=(XMX-XMN)/FLOAT(NP-1)
      YINC=(YMX-YMN)/FLOAT(NP-1)
      PMIN=BASE
      PMAX=0.0
      DO 7220 J=1,NP
      DO 7220 I=1,NP
      XP=XMN+XINC*(I-1)
      YP=YMN+YINC*(J-1)
      P(I,J)=BASE
      DO 7215 K=1,NHMP
      P(I,J)=P(I,J)-C(K)/(1.0+A(K)*(XP-HX(K))**2+
     % D(K)*(XP-HX(K))*(YP-HY(K))+B(K)*(YP-HY(K))**2)
 7215 CONTINUE
      IF(P(I,J).LT.0.0) P(I,J)=0.0
      IF(P(I,J).GT.PMAX) PMAX=P(I,J)
      IF(P(I,J).LT.PMIN) PMIN=P(I,J)
 7220 CONTINUE
      K=IFIX(DINT)
      IF(K.EQ.0) K=10
      ICS=1
      DO 7230 I=1,500
      J=K*(I/K)
      CL(I)=-10.0
      IF(J.EQ.I) CL(I)=FLOAT(I)
      IF(PMIN.GT.FLOAT(I))ICS=I
      IF(PMAX.GT.FLOAT(I))ICF=I
 7230 CONTINUE
      IF(ICF.LT.500)ICF=ICF+1
      CALL CONTRL(P,1,NP,80,1,NP,80,CL,ICS,ICF)
 7240 IF(IRY.EQ.0) GO TO 7030
      IF(IRY.LT.-3.5.OR.IRY.GT.3.5) GO TO 7250
      CALL CTRMAG(30)
      CALL CTRSET(4)
      DO 7245 I=1,NDEL
      IF(DSR(I).LT.-10.0) GO TO 7245
      CALL POSITN(XBASE(I),YBASE(I))
      IF(IRY.GE.2.OR.IRY.LE.-2) CALL TYPENC(59)
```

```
      IF(IRY.LT.0) GO TO 7243
      CALL JOIN(XB(I),YB(I))
      GO TO 7244
 7243 CALL POSITN(XB(I),YB(I))
 7244 IF(IRY.EQ.1.OR.IRY.EQ.3.OR.IRY.EQ.-1.OR.IRY.EQ.-3)
     % CALL TYPENC(54)
 7245 CONTINUE
      CALL CTRSET(1)
      GO TO 7030
 7250 CALL CTRSET(4)
      DO 7260 I=1,NDEL
      IF(ROS(I).LT.-10.0) GO TO 7260
      KK=IFIX(ABS(200.0*ROS(I)))
      IF(KK.GT.255) KK=255
      CALL POSITN(XB(I),YB(I))
      IF(ROS(I).LT.-0.070) CALL TYPENC(61)
      IF(ROS(I).GT. 0.070) CALL TYPENC(43)
 7260 CONTINUE
      CALL CTRSET(1)
      GO TO 7030
 7900 CALL GREND
      WRITE(6,7901)
 7901 FORMAT('0**  PLOTTING FINISHED. **')
      RETURN
  900 CALL GREND
      WRITE(6,903)
  903 FORMAT('0***  ERROR  ***  END OF FILE ON COMMAND SEQUENCE.')
      STOP
      END
```

APPENDIX 7

HYPERSPACE PLOTS

PLOT 1

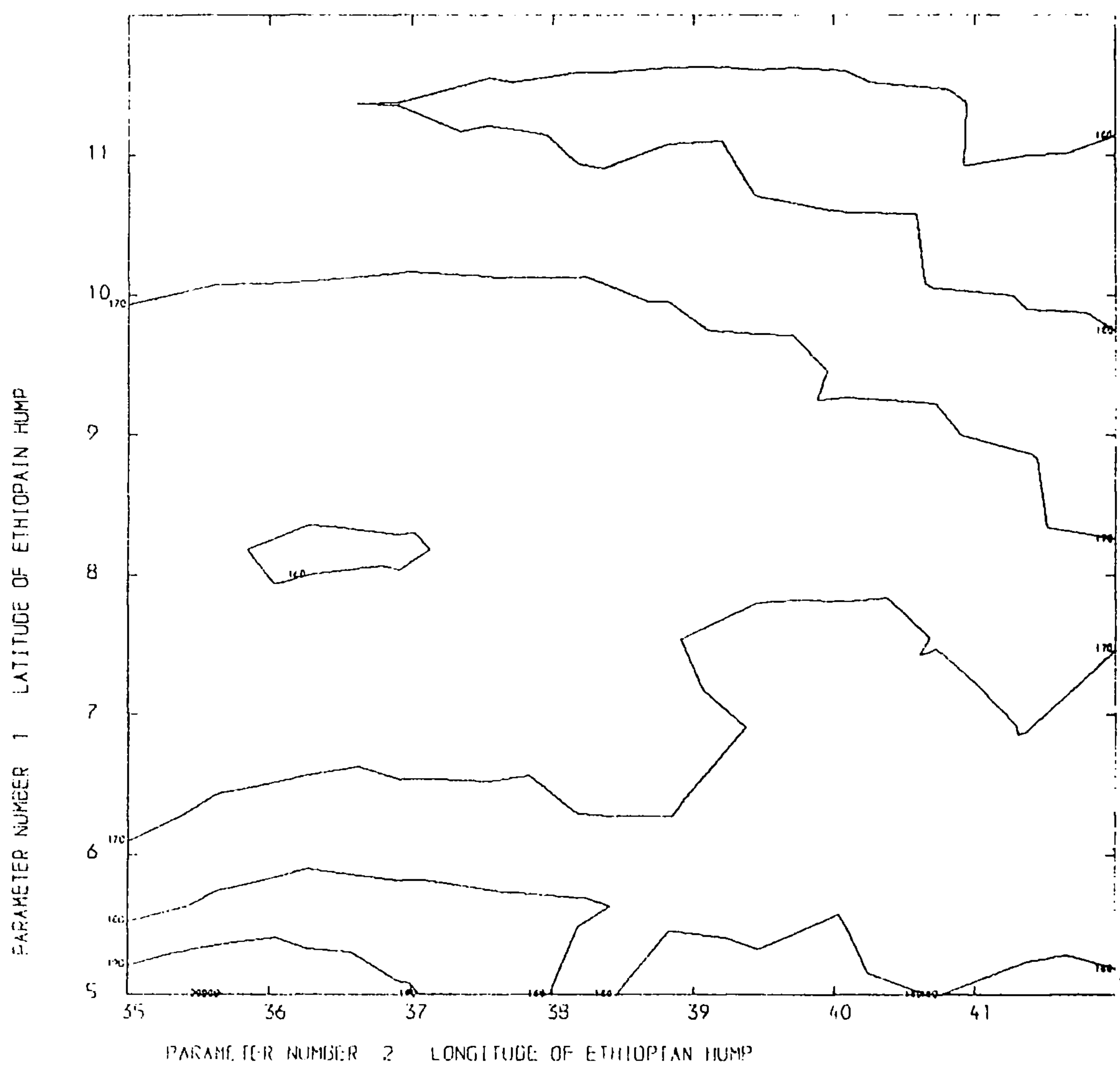

PLOT 2

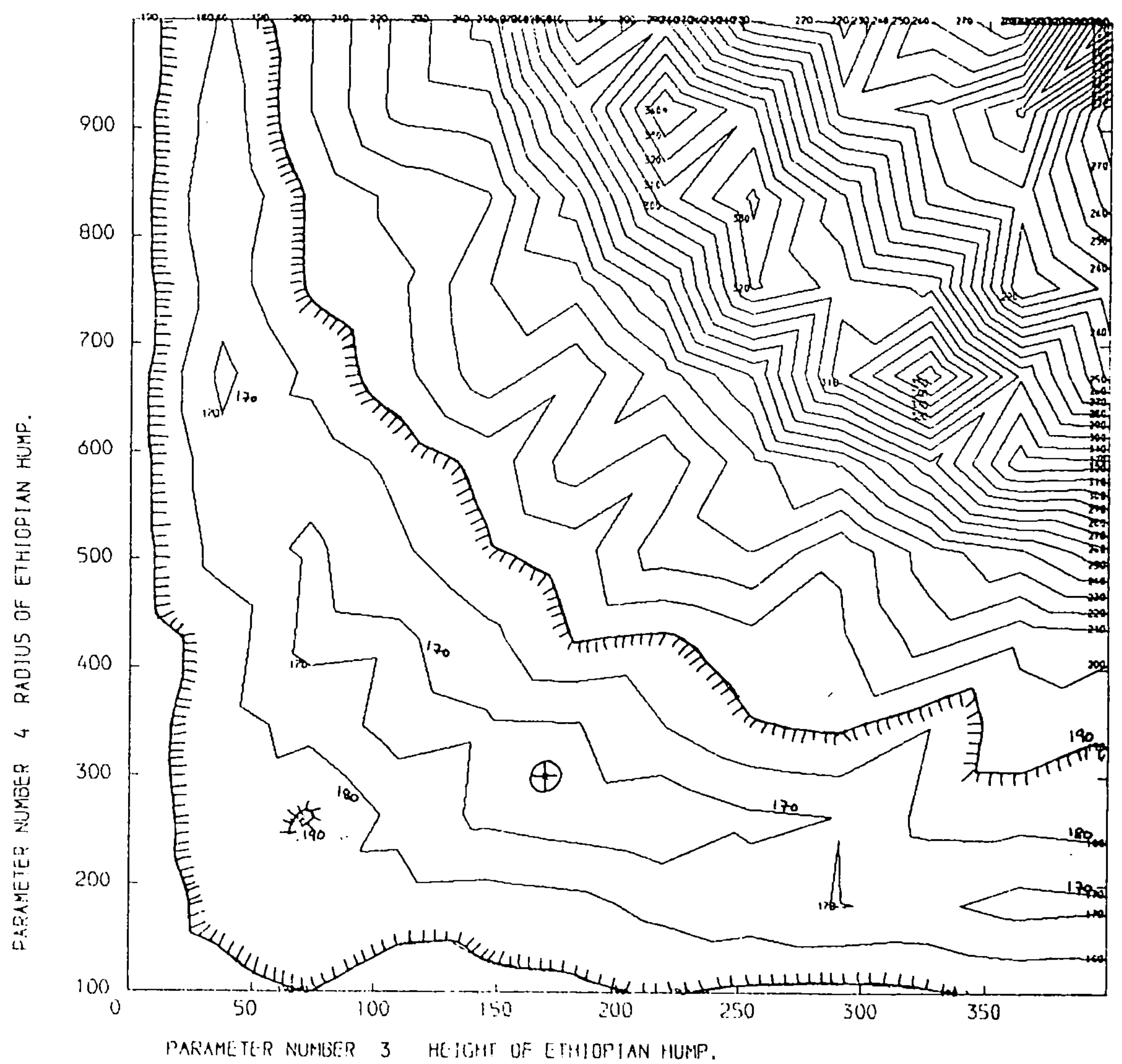
900
800
700
600
500
400
300
200
100
0
50
100
150
200
250
300
350
170
180
190
PARAMETER NUMBER 4 RADIUS OF ETHIOPIAN HUMP.
PARAMETER NUMBER 3 HEIGHT OF ETHIOPIAN HUMP.

HYPERSPACE PLOTS

PLOT 3

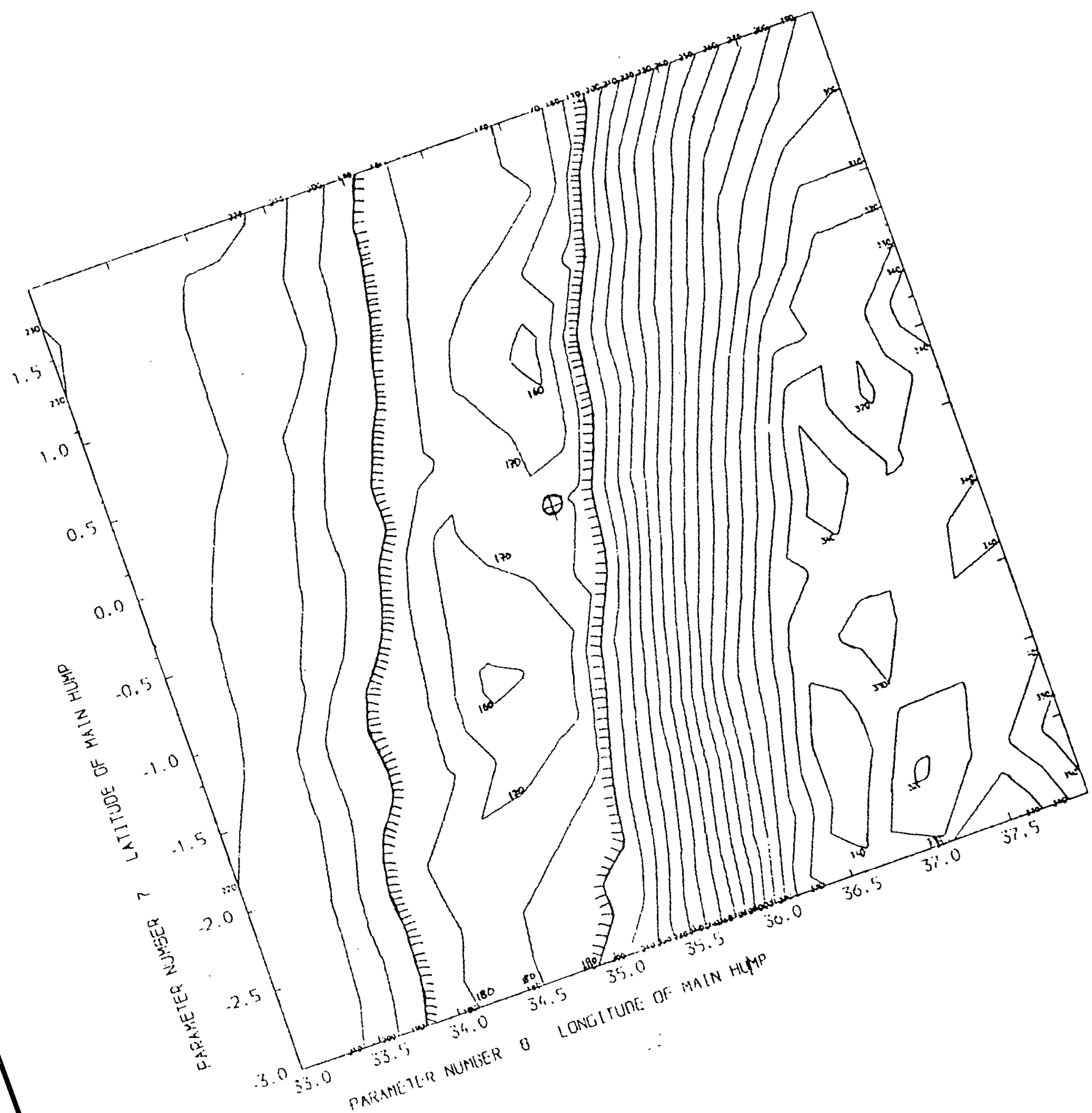

PLOT 4

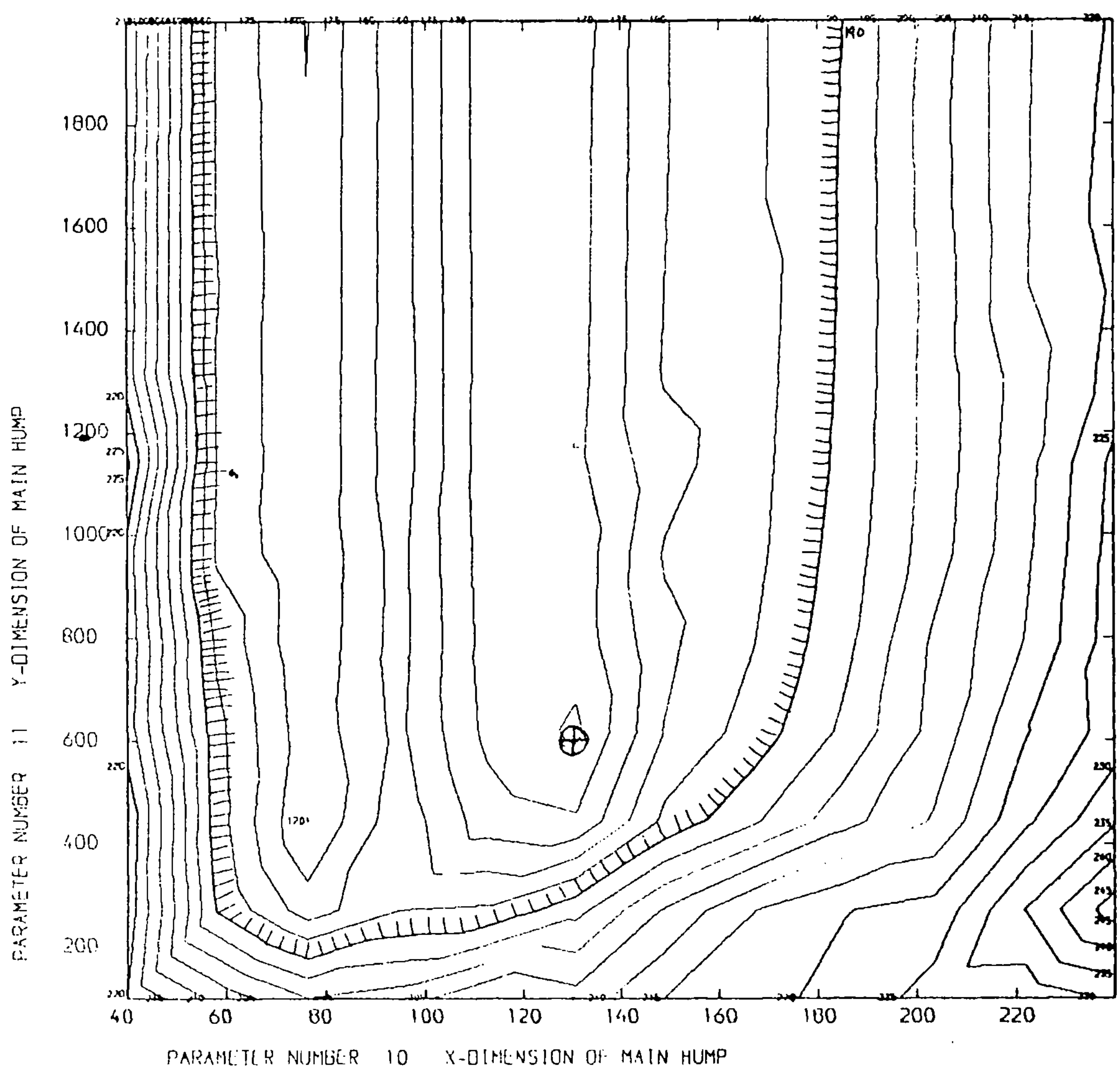
1800
1600
1400
1200
1000
800
600
400
200
40
60
80
100
120
140
160
180
200
220
PARAMETER NUMBER 11 Y-DIMENSION OF MAIN HUMP
PARAMETER NUMBER 10 X-DIMENSION OF MAIN HUMP

PLOT 5

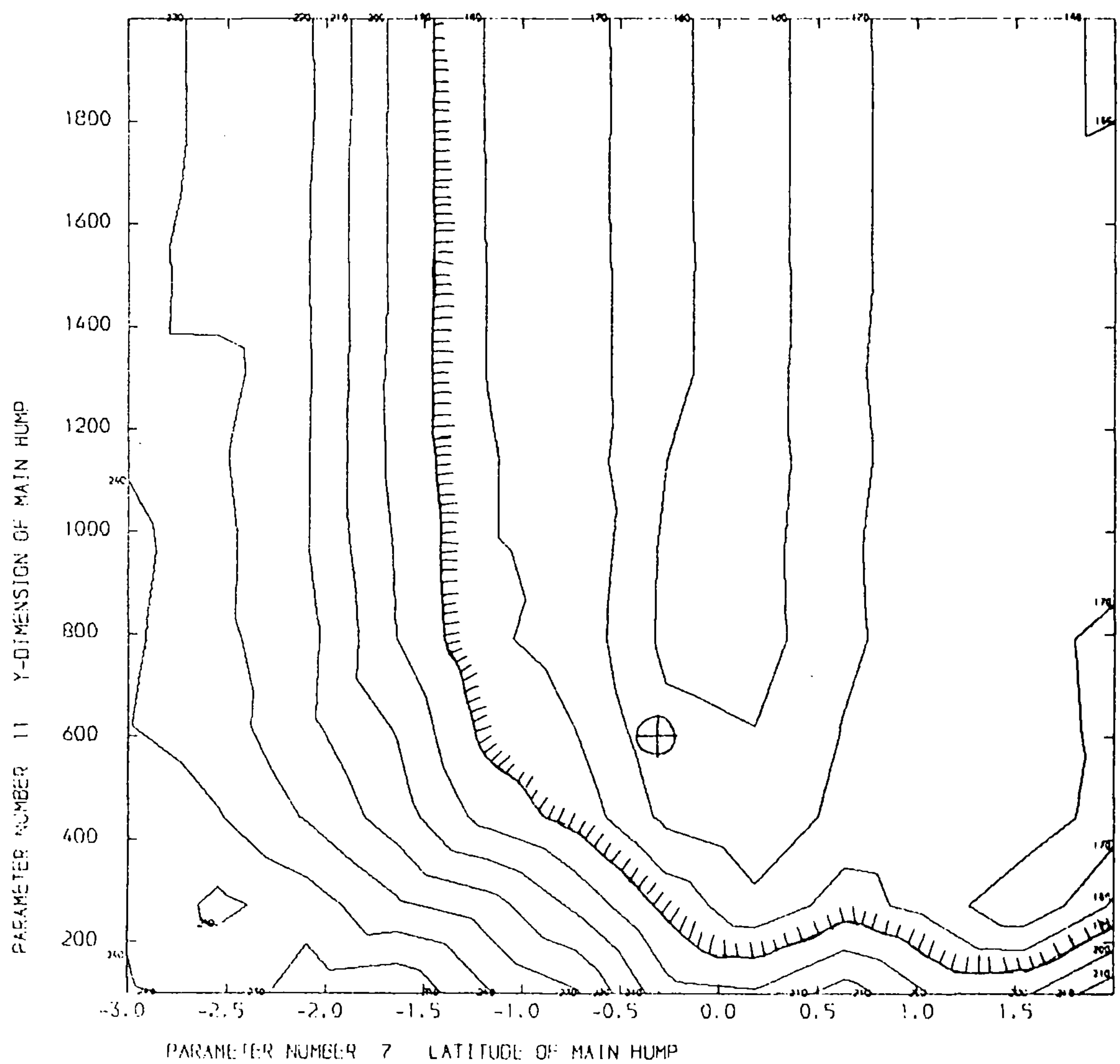
1800
1600
1400
1200
1000
800
600
400
200
PARAMETER NUMBER 11 Y-DIMENSION OF MAIN HUMP
-3.0
-2.5
-2.0
-1.5
-1.0
-0.5
0.0
0.5
1.0
1.5
PARAMETER NUMBER 7 LATITUDE OF MAIN HUMP

PLOT 6

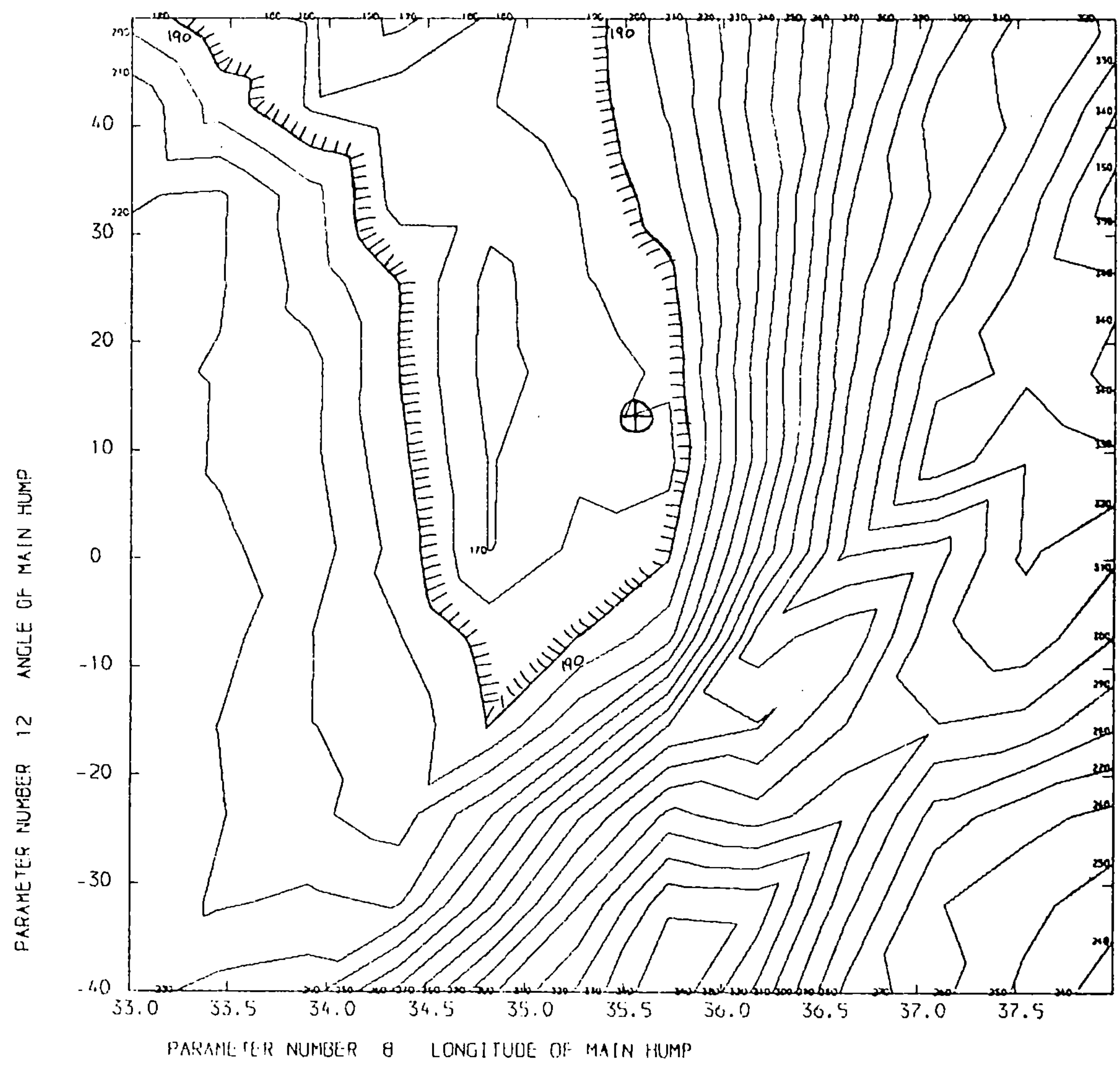
PARAMETER NUMBER 12 ANGLE OF MAIN HUMP
PARAMETER NUMBER 8 LONGITUDE OF MAIN HUMP
40
30
20
10
0
-10
-20
-30
-40
33.0
33.5
34.0
34.5
35.0
35.5
36.0
36.5
37.0
37.5
190
170

PLOT 7

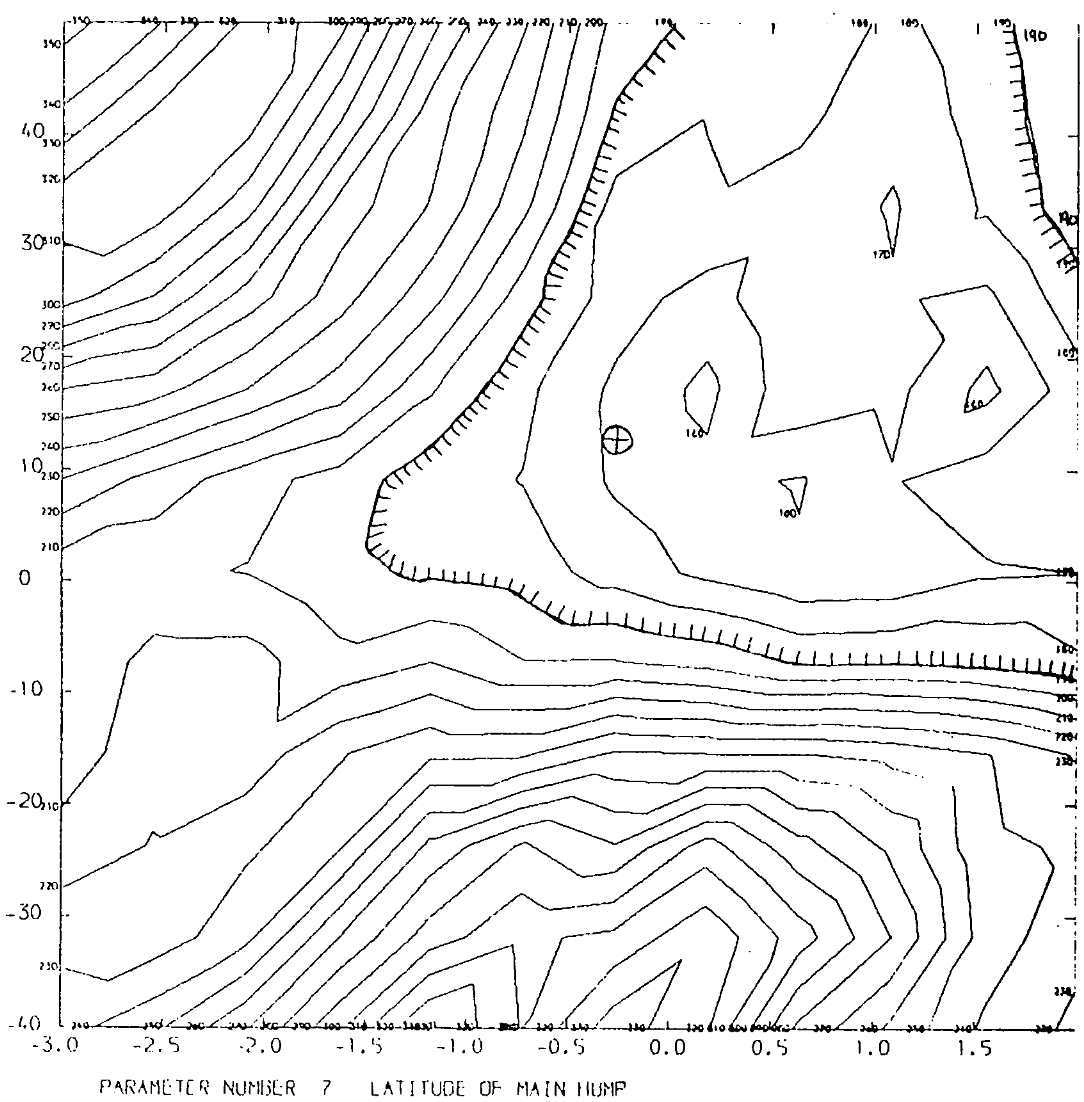
PARAMETER NUMBER 12 ANGLE OF MAIN HUMP
40
30
20
10
0
-10
-20
-30
-40
-3.0
-2.5
-2.0
-1.5
-1.0
-0.5
0.0
0.5
1.0
1.5
PARAMETER NUMBER 7 LATITUDE OF MAIN HUMP

PLOT 8

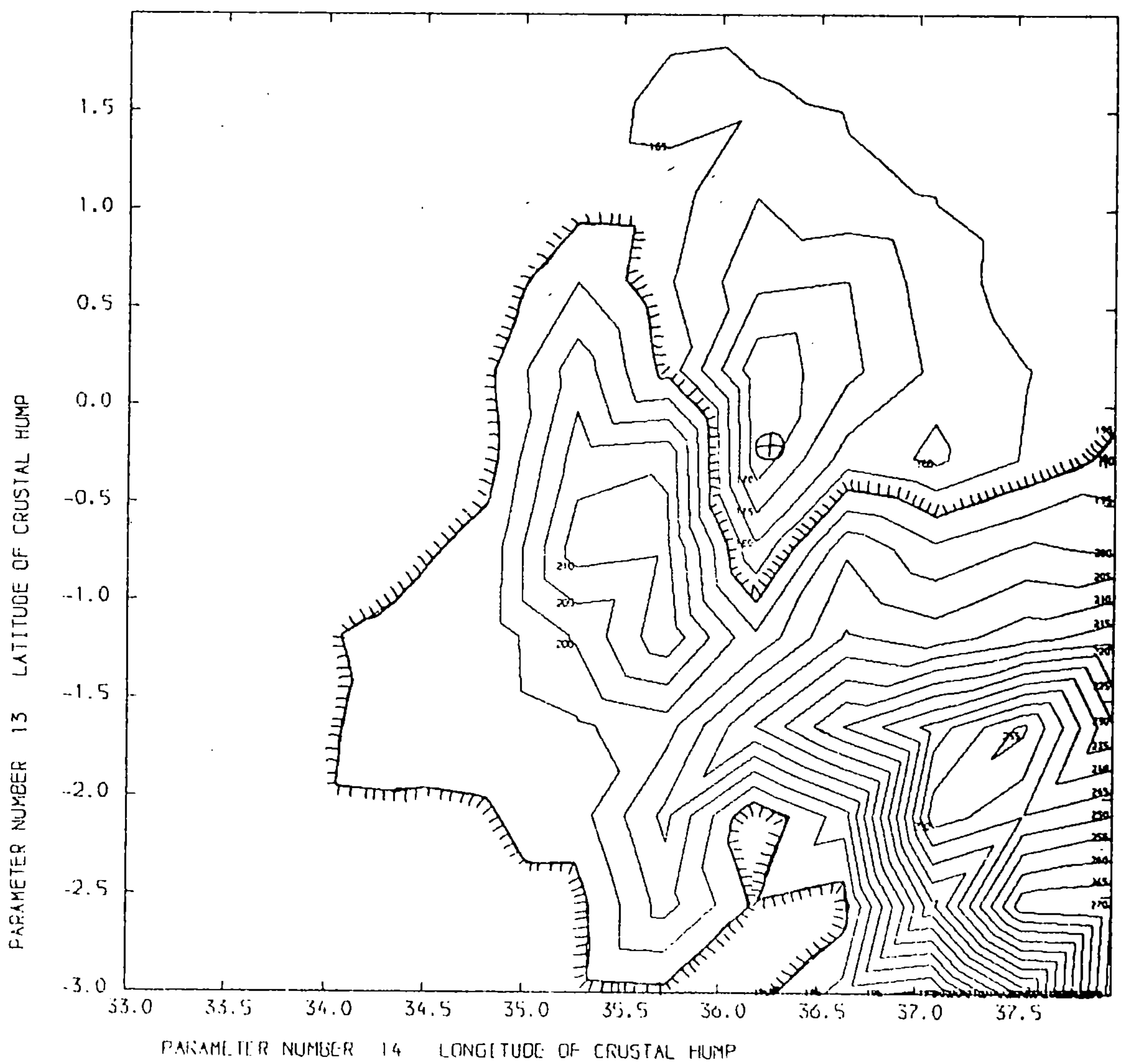

1.5
1.0
0.5
0.0
-0.5
-1.0
-1.5
-2.0
-2.5
-3.0
33.0
33.5
34.0
34.5
35.0
35.5
36.0
36.5
37.0
37.5
PARAMETER NUMBER 13 LATITUDE OF CRUSTAL HUMP
PARAMETER NUMBER 14 LONGITUDE OF CRUSTAL HUMP

PLOT 9

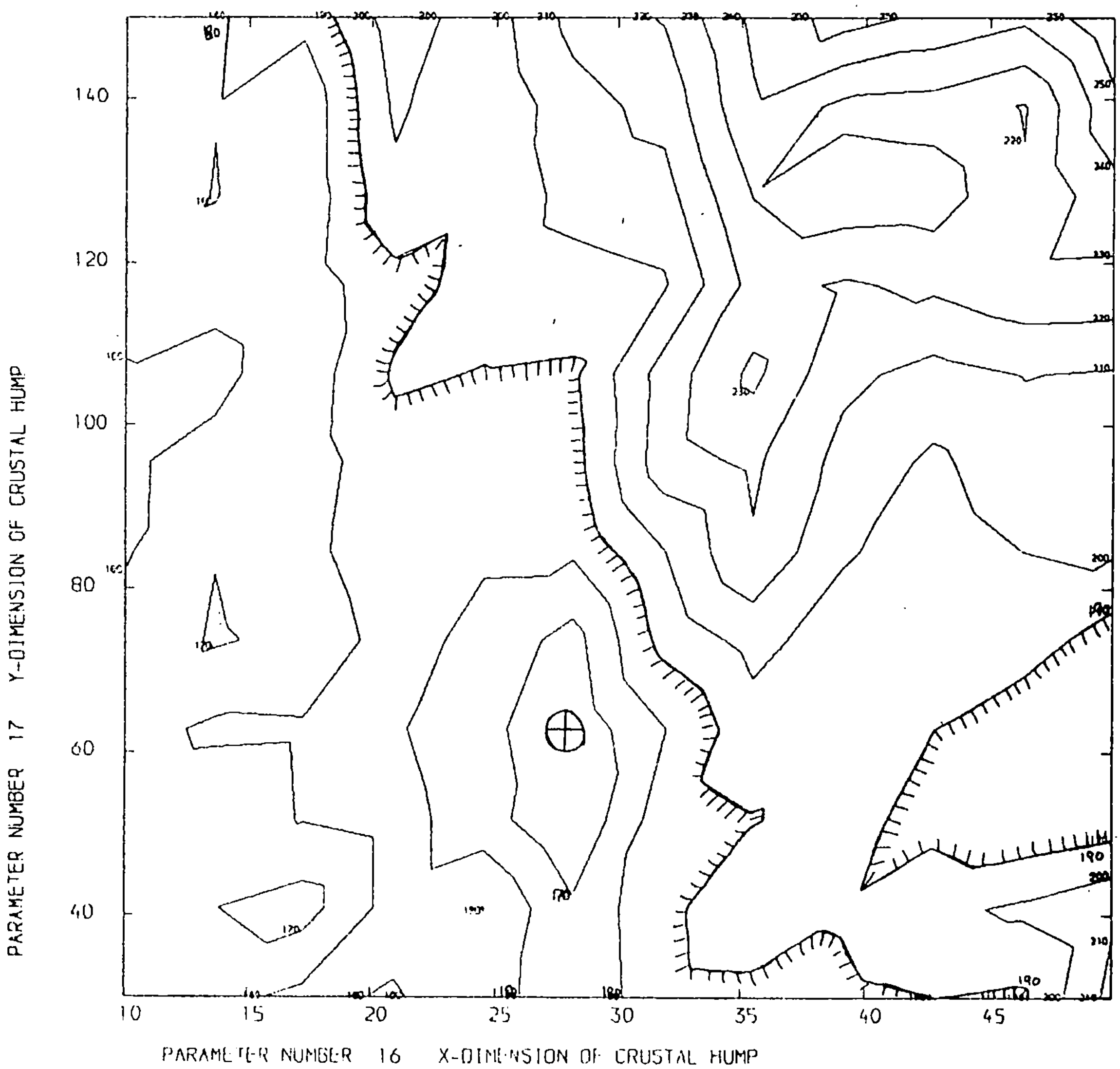
PARAMETER NUMBER 17 Y-DIMENSION OF CRUSTAL HUMP
140
120
100
80
60
40
10
15
20
25
30
35
40
45
PARAMETER NUMBER 16 X-DIMENSION OF CRUSTAL HUMP

PLOT 10

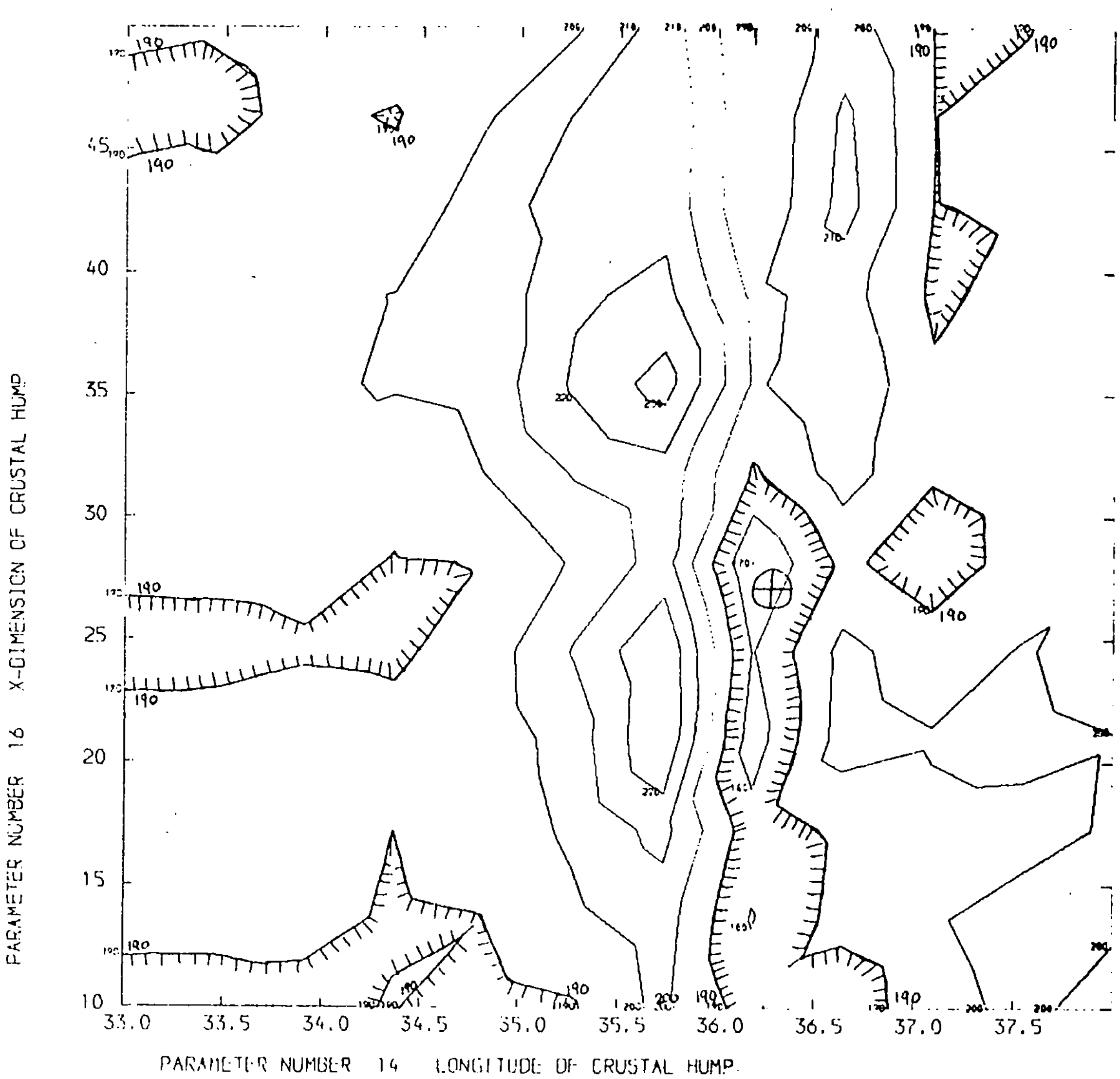
PARAMETER NUMBER 16 X-DIMENSION OF CRUSTAL HUMP
PARAMETER NUMBER 14 LONGITUDE OF CRUSTAL HUMP
10
15
20
25
30
35
40
45
33.0
33.5
34.0
34.5
35.0
35.5
36.0
36.5
37.0
37.5
190

PLOT 11

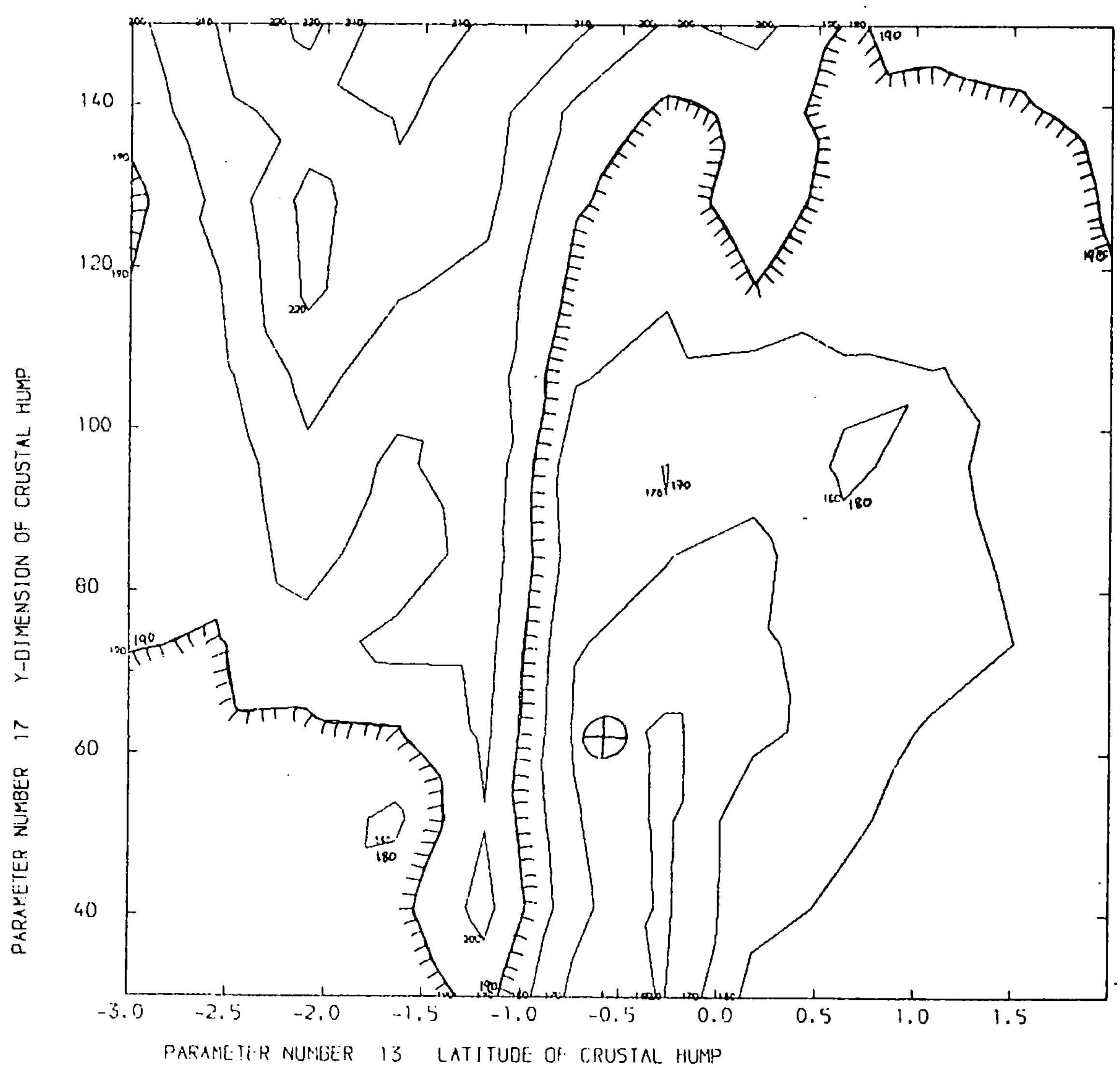

140
120
100
80
60
40
-3.0
-2.5
-2.0
-1.5
-1.0
-0.5
0.0
0.5
1.0
1.5
PARAMETER NUMBER 17 Y-DIMENSION OF CRUSTAL HUMP
PARAMETER NUMBER 13 LATITUDE OF CRUSTAL HUMP

PLOT 12

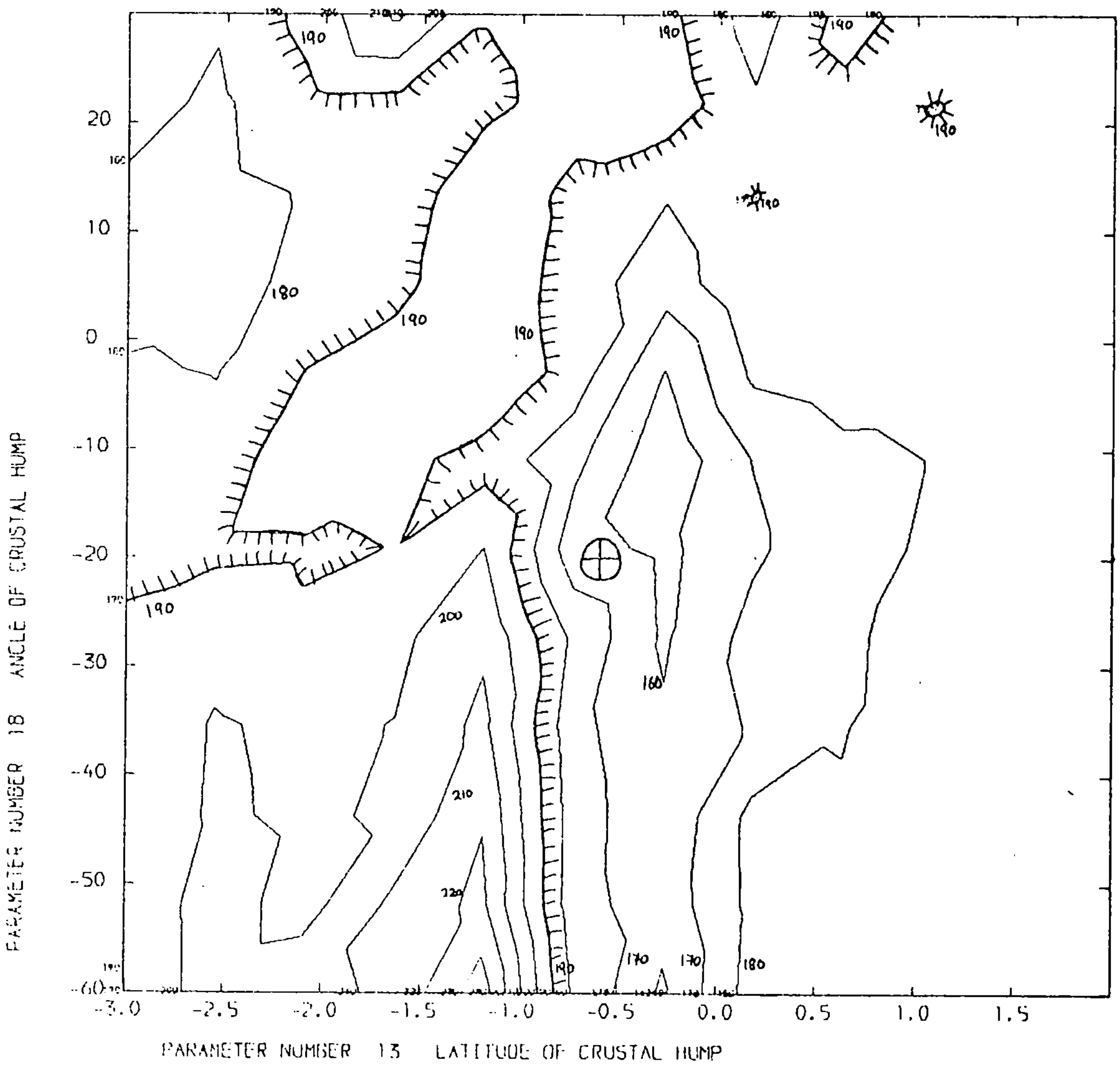
20
10
0
-10
-20
-30
-40
-50
-60
-3.0
-2.5
-2.0
-1.5
-1.0
-0.5
0.0
0.5
1.0
1.5
190
180
200
210
220
160
170
PARAMETER NUMBER 18 ANGLE OF CRUSTAL HUMP
PARAMETER NUMBER 13 LATITUDE OF CRUSTAL HUMP

PLOT 13

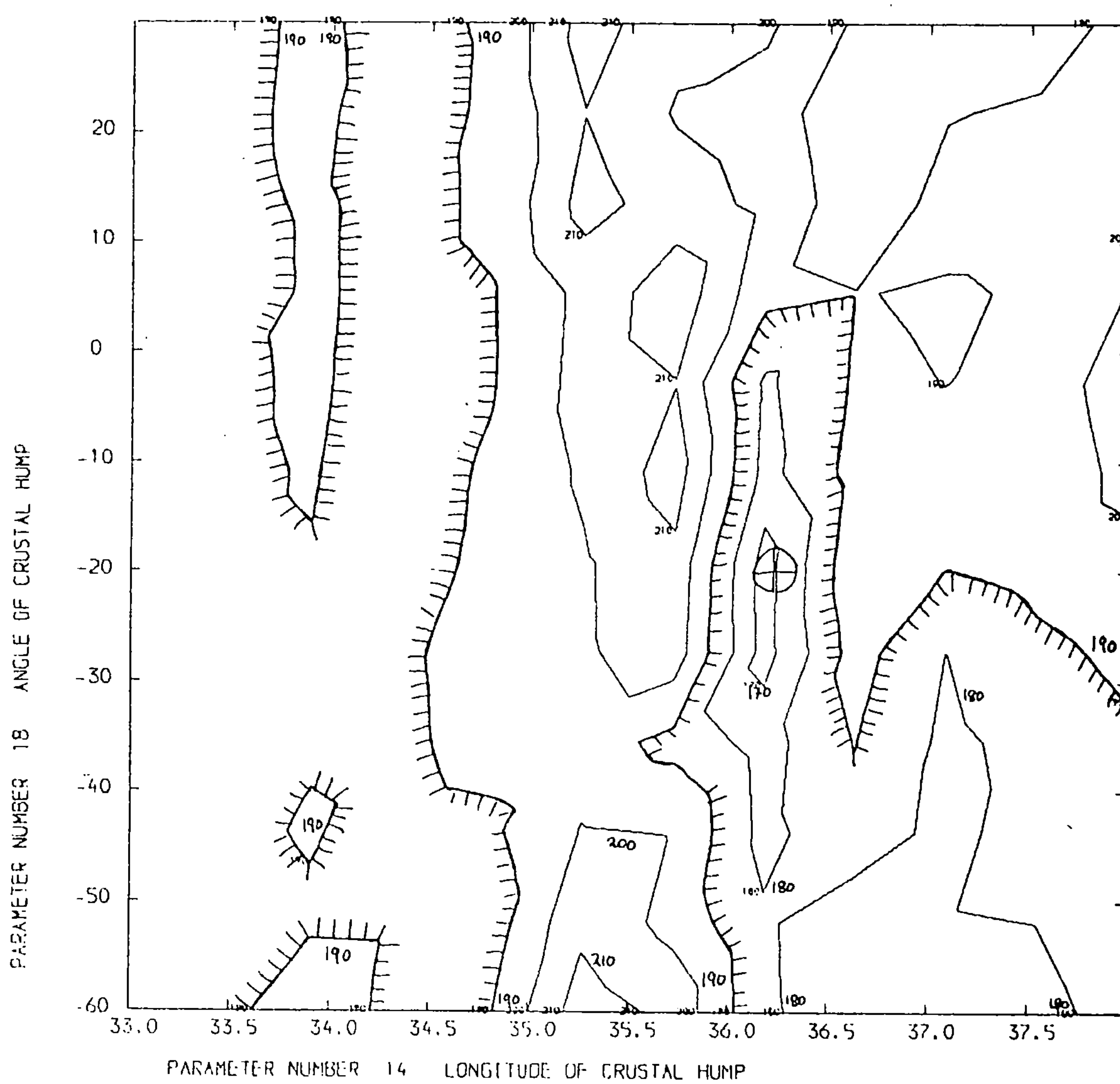
PARAMETER NUMBER 18 ANGLE OF CRUSTAL HUMP
PARAMETER NUMBER 14 LONGITUDE OF CRUSTAL HUMP
20
10
0
-10
-20
-30
-40
-50
-60
33.0
33.5
34.0
34.5
35.0
35.5
36.0
36.5
37.0
37.5
190
200
210
180
170

PLOT 14

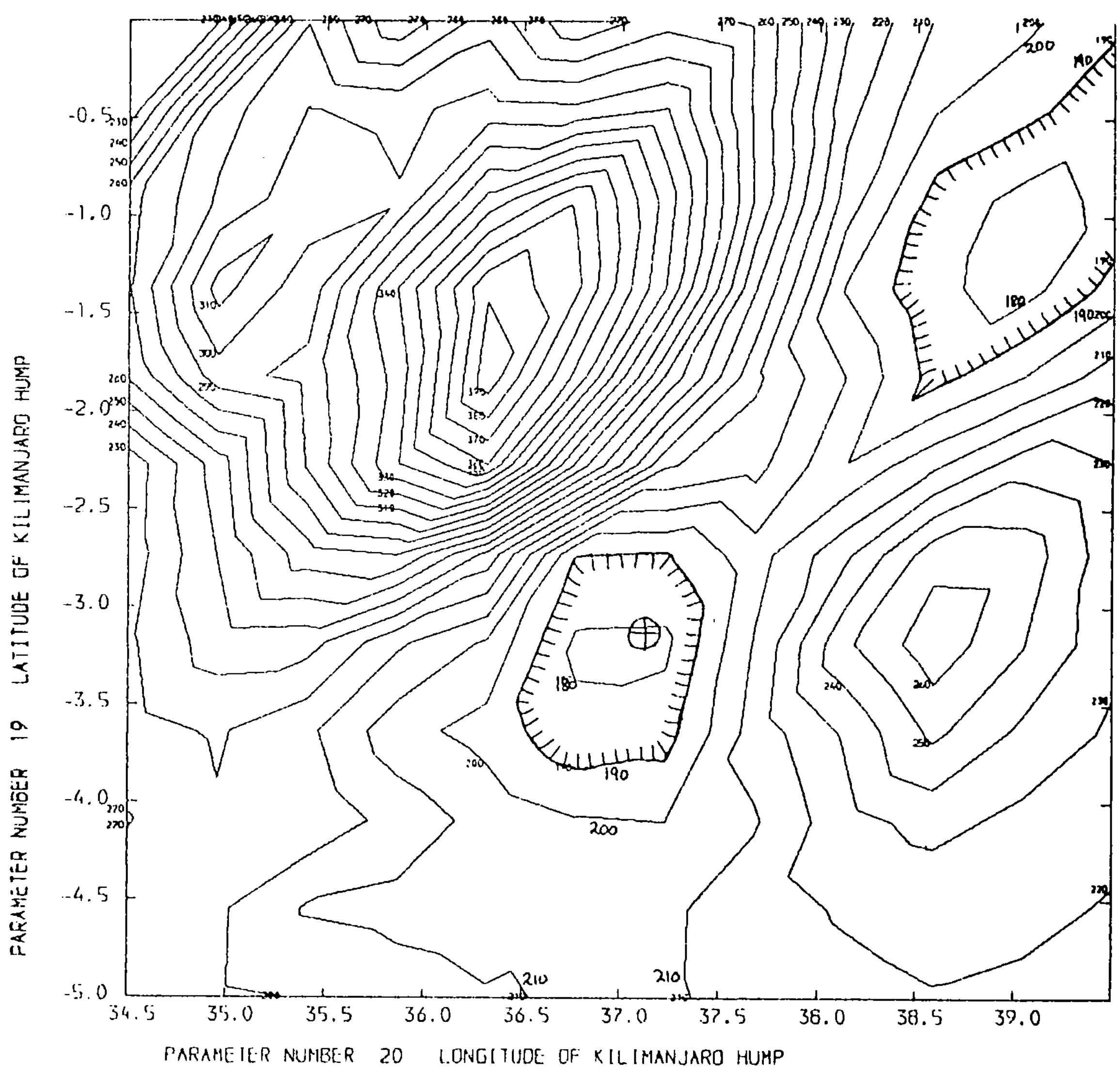
PARAMETER NUMBER 19 LATITUDE OF KILIMANJARO HUMP
PARAMETER NUMBER 20 LONGITUDE OF KILIMANJARO HUMP
-0.5
-1.0
-1.5
-2.0
-2.5
-3.0
-3.5
-4.0
-4.5
-5.0
34.5
35.0
35.5
36.0
36.5
37.0
37.5
38.0
38.5
39.0
200
190
180
210

PLOT 15

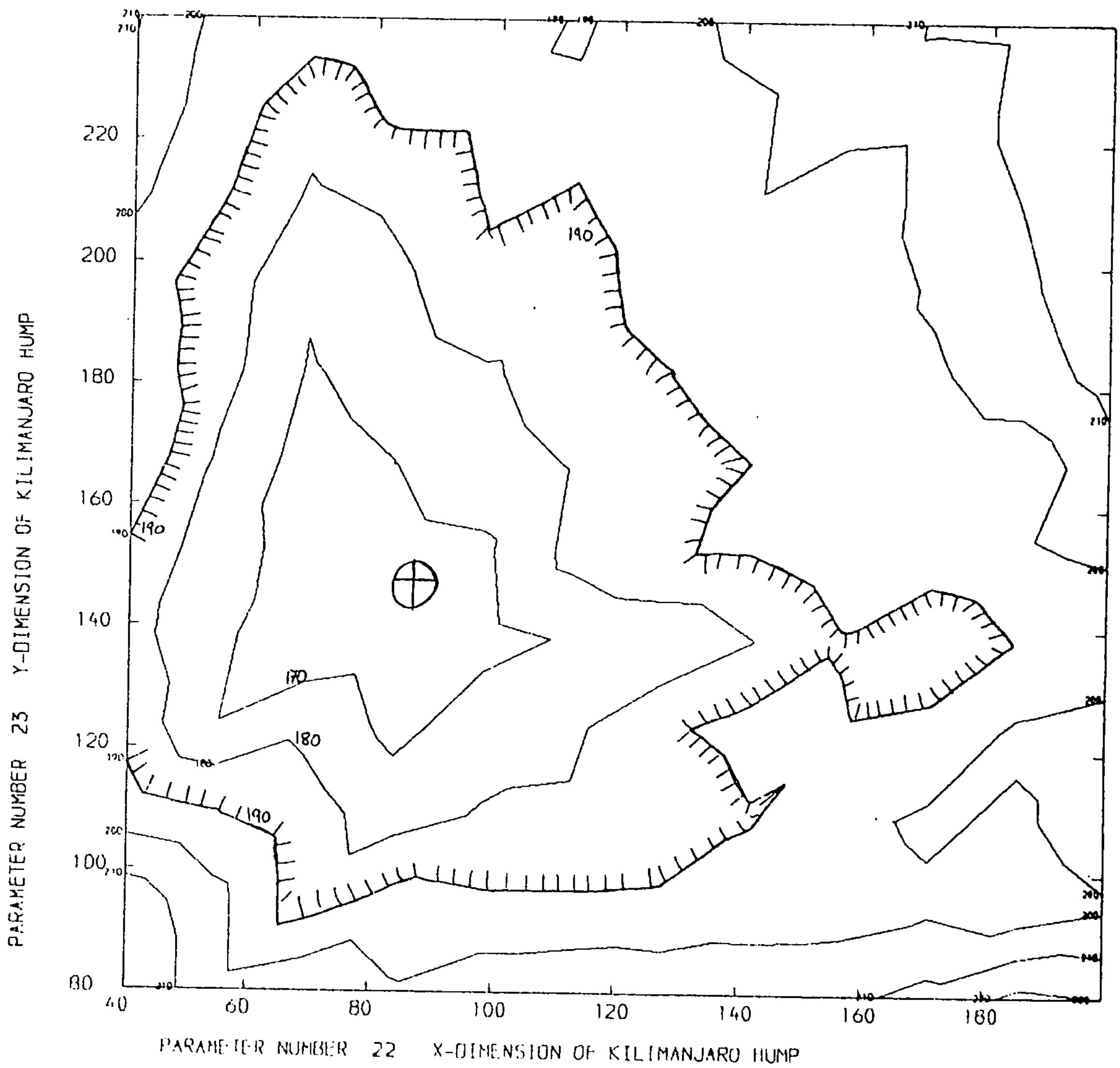
PARAMETER NUMBER 23 Y-DIMENSION OF KILIMANJARO HUMP
PARAMETER NUMBER 22 X-DIMENSION OF KILIMANJARO HUMP
220
200
180
160
140
120
100
80
40
60
80
100
120
140
160
180
190
170
180

PLOT 16

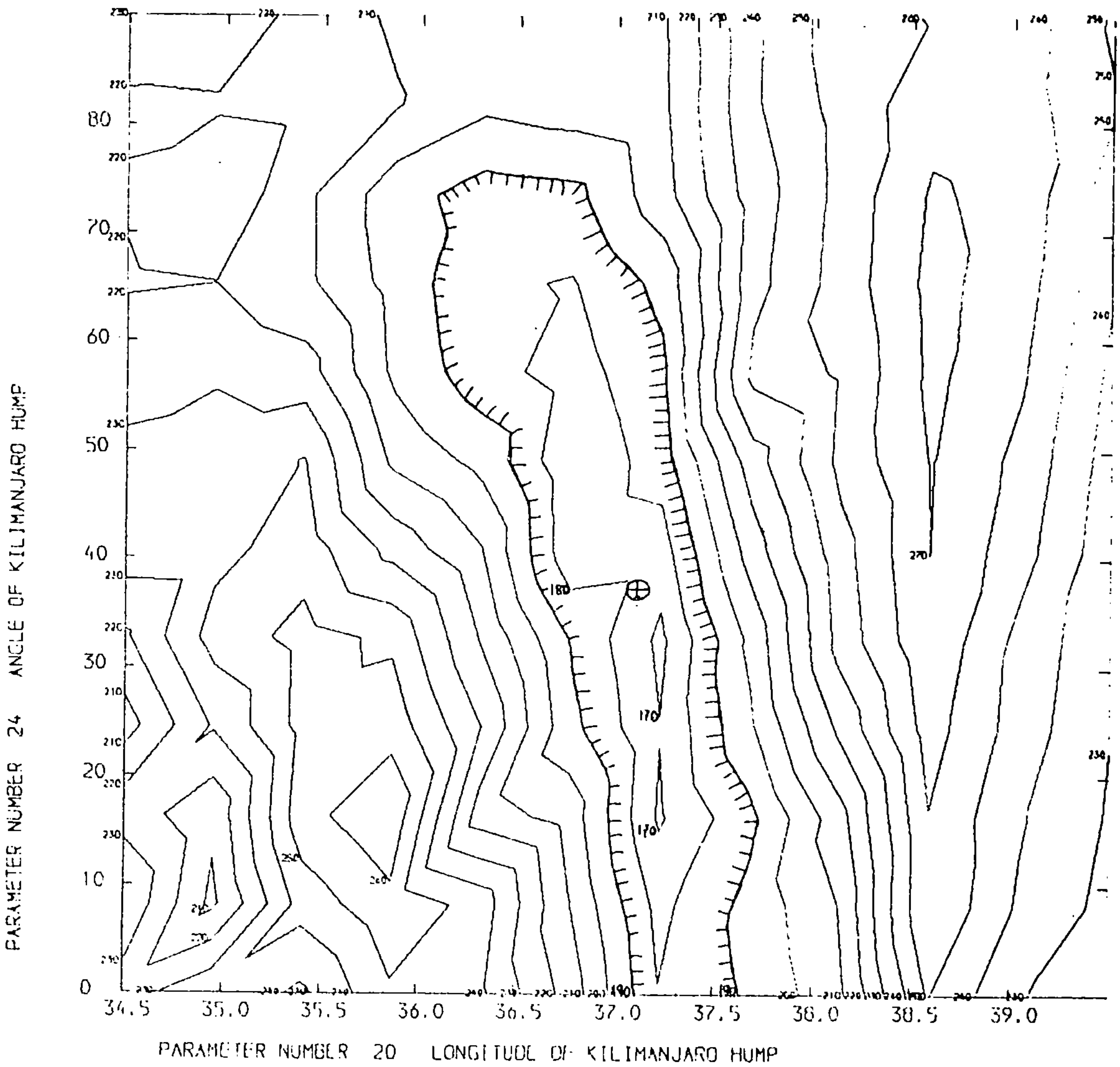

PARAMETER NUMBER 24 ANGLE OF KILIMANJARO HUMP
PARAMETER NUMBER 20 LONGITUDE OF KILIMANJARO HUMP
0
10
20
30
40
50
60
70
80
34.5
35.0
35.5
36.0
36.5
37.0
37.5
38.0
38.5
39.0
180
170
270

PLOT 17

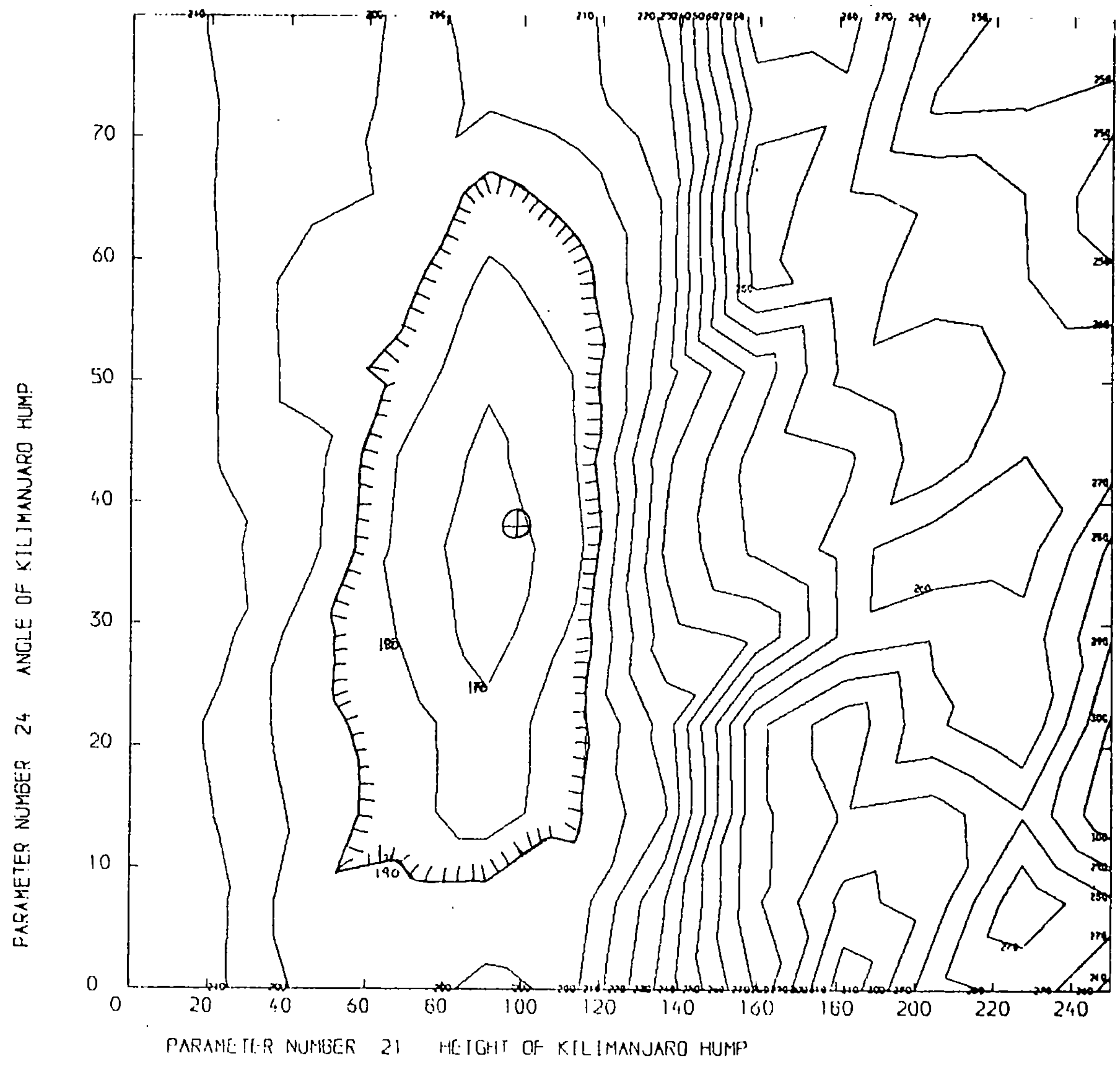
PARAMETER NUMBER 24 ANGLE OF KILIMANJARO HUMP
PARAMETER NUMBER 21 HEIGHT OF KILIMANJARO HUMP
0 20 40 60 80 100 120 140 160 180 200 220 240
0 10 20 30 40 50 60 70
180
170
190

PLOT 18

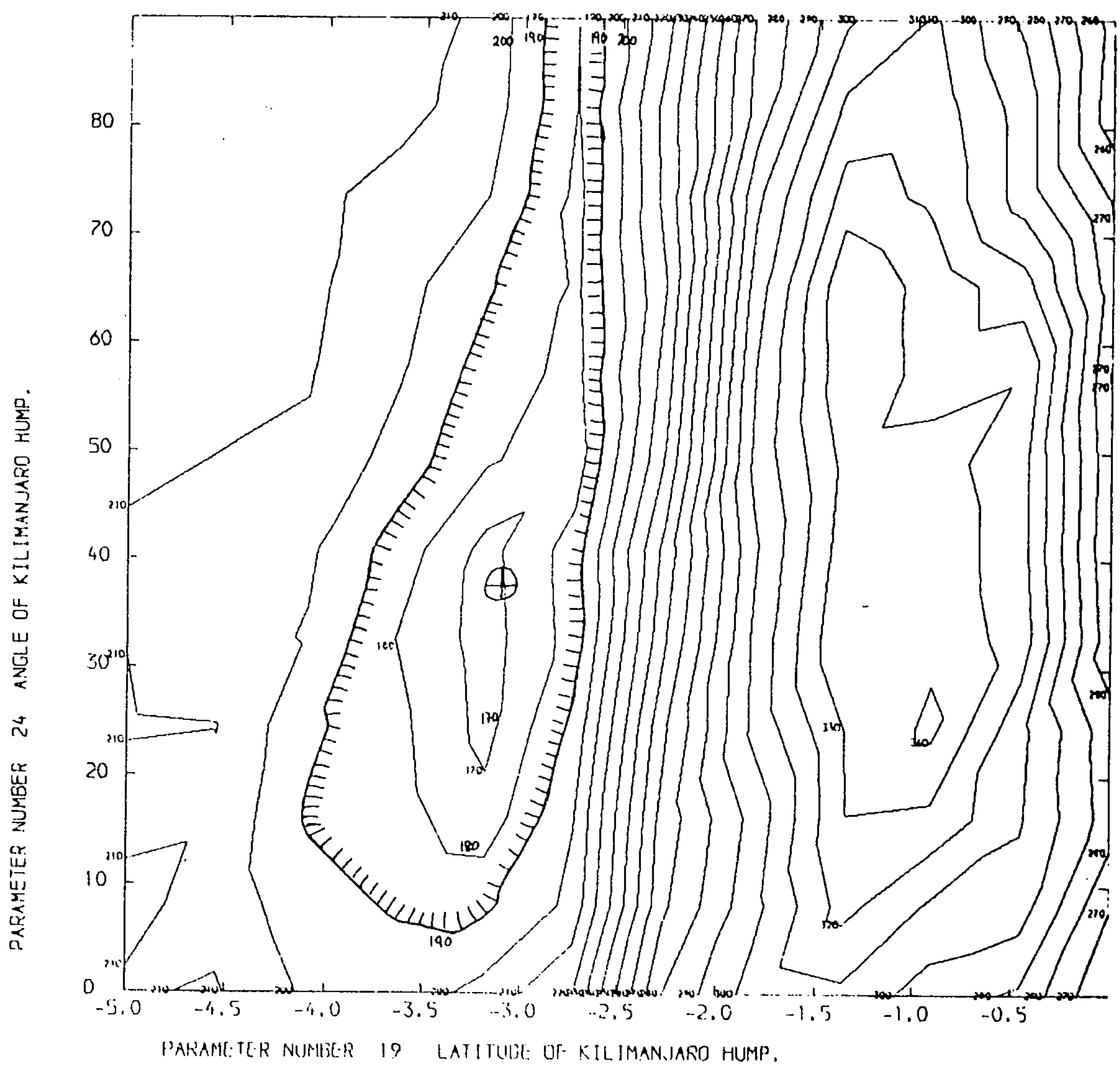
PARAMETER NUMBER 24 ANGLE OF KILIMANJARO HUMP.
0
10
20
30
40
50
60
70
80
-5.0
-4.5
-4.0
-3.5
-3.0
-2.5
-2.0
-1.5
-1.0
-0.5
PARAMETER NUMBER 19 LATITUDE OF KILIMANJARO HUMP.

PLOT 19

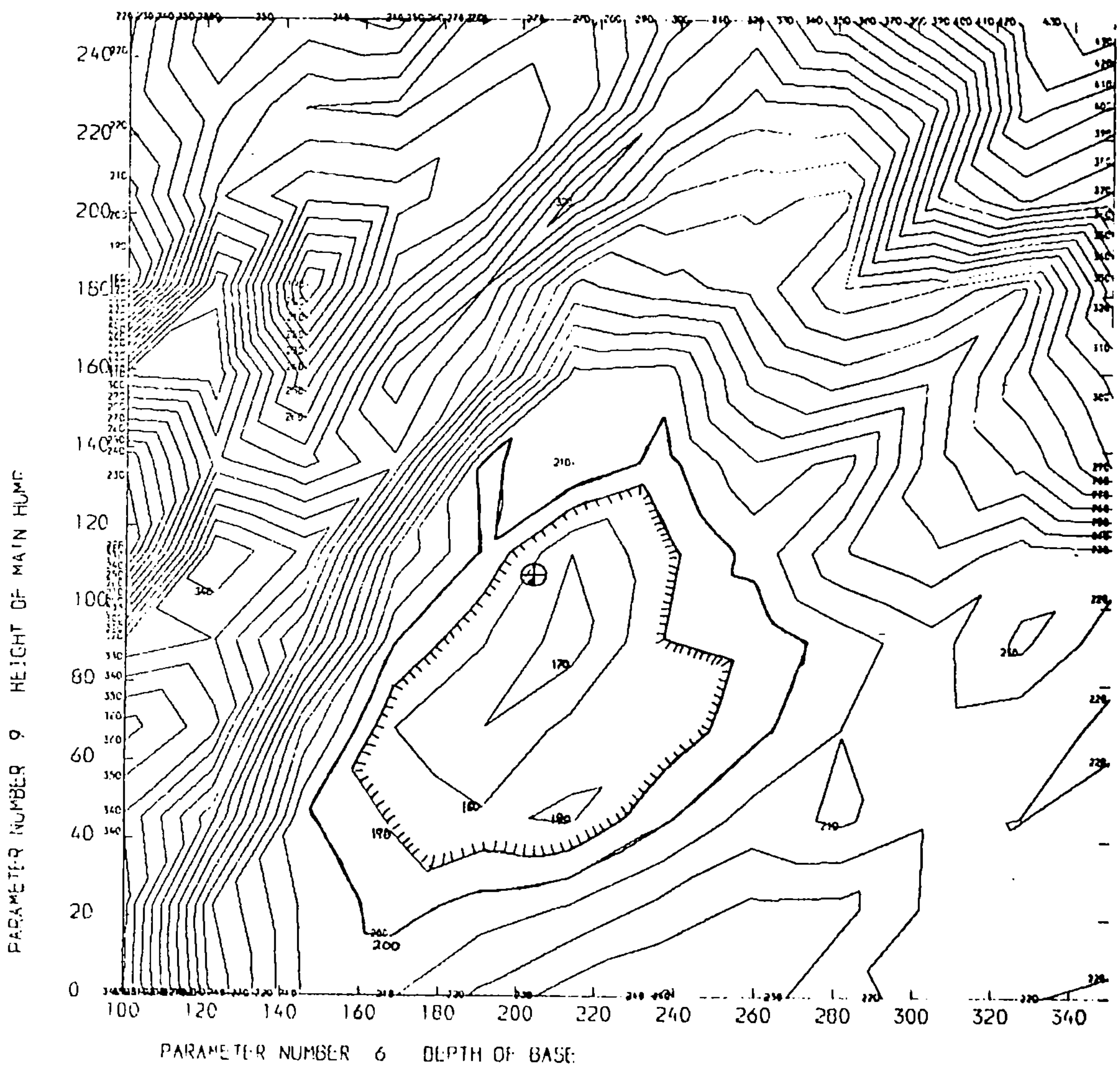
PARAMETER NUMBER 9 HEIGHT OF MAIN HUMP
PARAMETER NUMBER 6 DEPTH OF BASE
100 120 140 160 180 200 220 240 260 280 300 320 340
0 20 40 60 80 100 120 140 160 180 200 220 240

PLOT 20

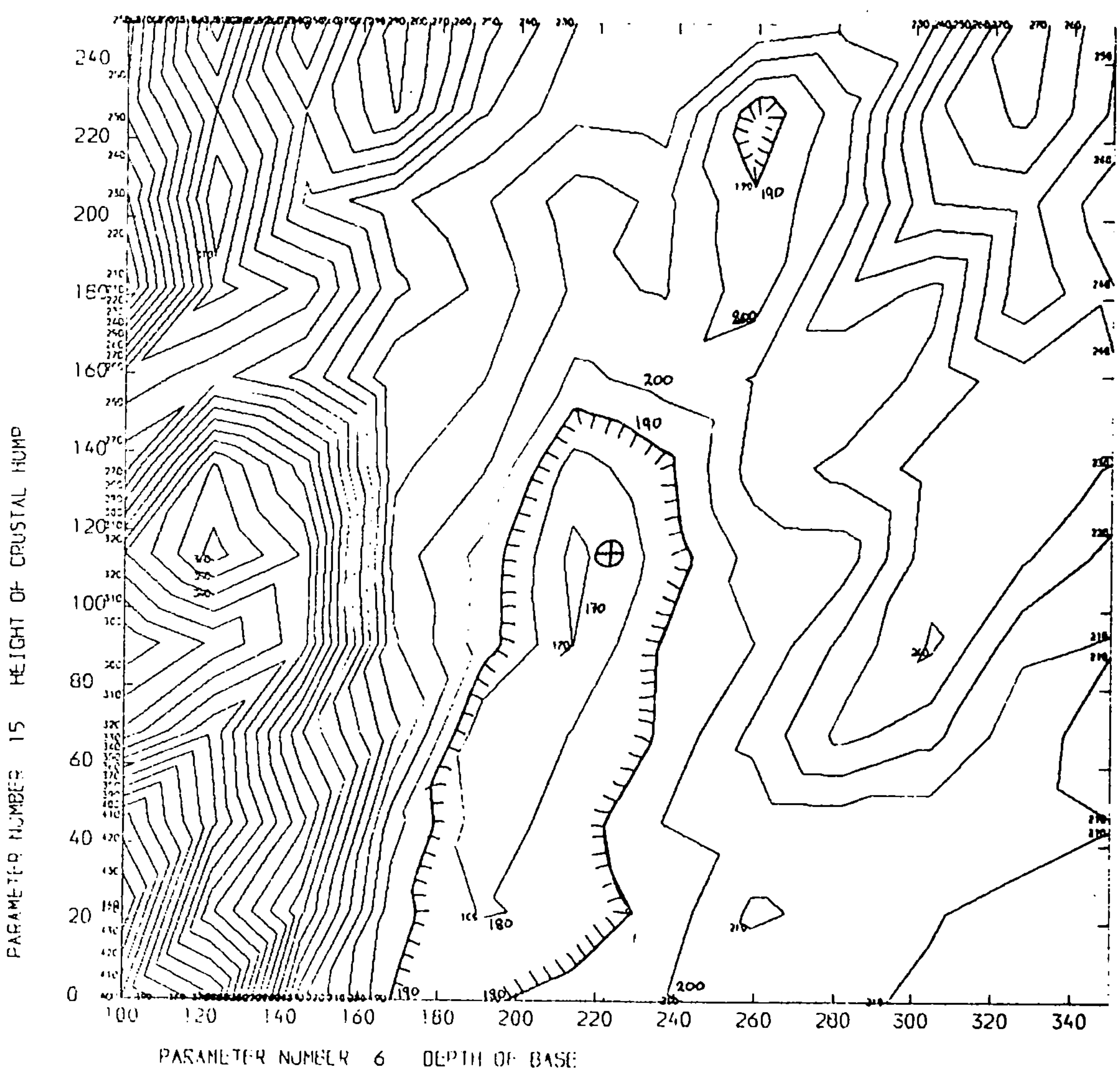
PARAMETER NUMBER 15 HEIGHT OF CRUSTAL HUMP
0
20
40
60
80
100
120
140
160
180
200
220
240
100 120 140 160 180 200 220 240 260 280 300 320 340
PARAMETER NUMBER 6 DEPTH OF BASE

PLOT 21

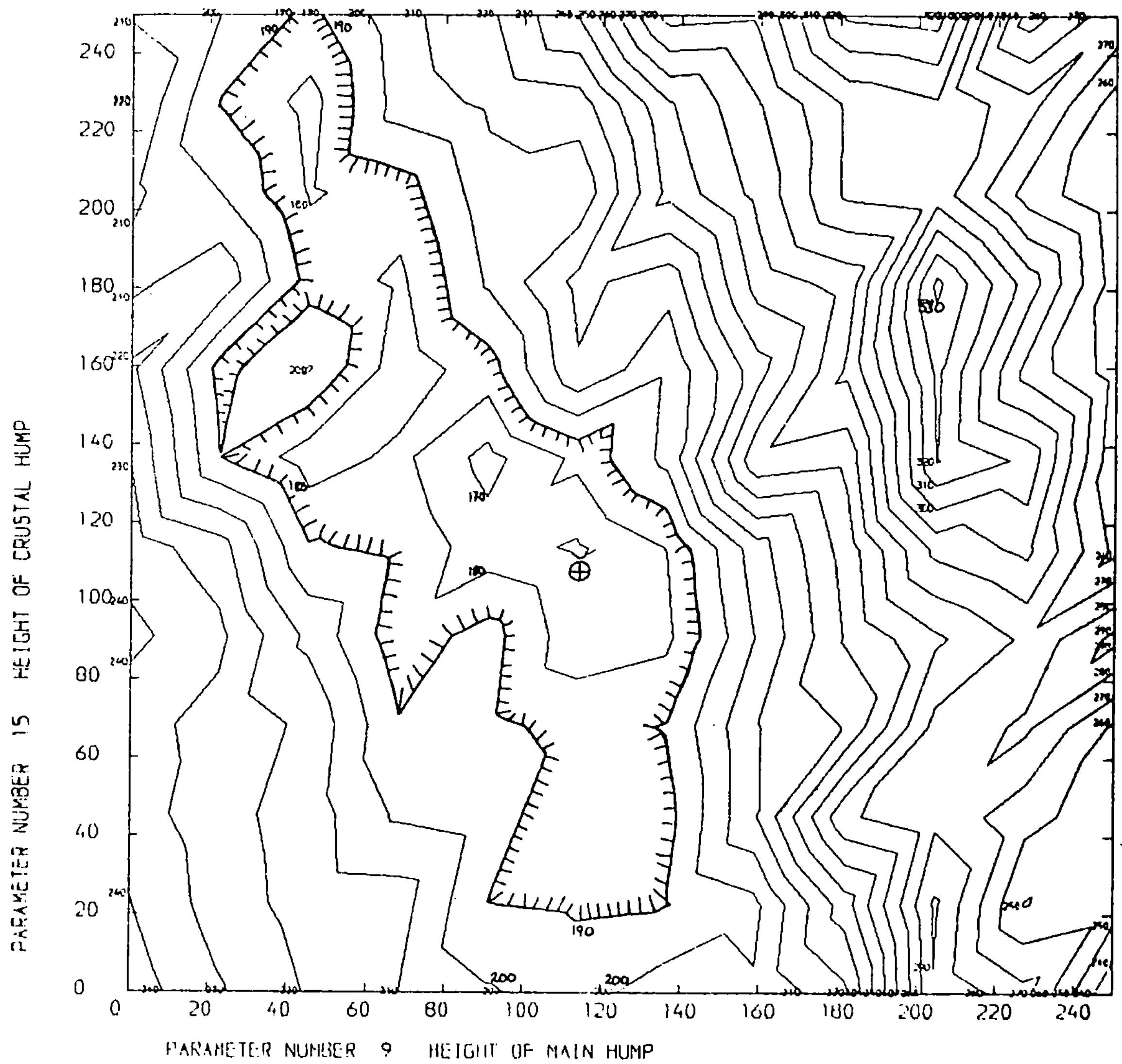

240
220
200
180
160
140
120
100
80
60
40
20
0
0 20 40 60 80 100 120 140 160 180 200 220 240
PARAMETER NUMBER 15 HEIGHT OF CRUSTAL HUMP
PARAMETER NUMBER 9 HEIGHT OF MAIN HUMP
190
170
180
200

BIBLIOGRAPHY

ABRAMOWITZ, M. & STEGAN, I.A. 1964. Handbook of Mathamatical Functions, Washington National Bureau of Standards.

AL-CHALABI, M. 1971. Interpretation of gravity anomalies by non-linear optimization, Geophysics. 20, 1-16.

AL-CHALABI, M. 1971. Reliability of the rotation pole in continental fitting, Earth and Planetary Sciences Letters. 11, 257-262.

ANDERSON, D.L. 1967. Latest information from seismic observations, In The Earth's mantle, 355-420, Ed. Gaskell, T.F., Academic Press

BACKHOUSE, R.W. 1972. Upper mantle structure using P-wave data from an East African array station, Ph.D. thesis, University of Durham.

BAKER, B.M. 1954. Geology of the southern Machakos district, Geological Survey of Kenya, Report No. 27.

BAKER, B.M., WILLIAMS, L.A.J., MILLAR, J.A. & FITCH, F.J. 1971. Sequence and geochronology of the Kenya rift volcanics, Tectonophysics 11, 191-215.

BAKER, B.M. & WOHLENBERG, J. 1971. Structure and evolution of the Kenya rift valley, Nature, Lond. 229, 538-542.

BAKER, B.M., MOHR, P.A. & WILLIAMS, L.A.T. 1972. Geology of the eastern rift system of Africa, Geol.Soc.Am., Special Paper No. 136.

BANKS, R.J. & OTTEY, P. 1974. Geomagnetic deep sounding in and around the Kenya rift valley, Geophys.J.R.Astr.Soc. 36, 321-335.

BATH, M. 1960. Crustal structure of Iceland, J.geophys.Res. 65, 1793-1807.

BERRY, M.J. & WEST, G.F. 1966. A time-term interpretation of the first arrival data of the 1963 Lake Superior experiment, In _The Earth beneath the continents_, 166-180, Eds. Steinhart, J.S. & Smith, T.J., American Geophysical Union,

BIRCH, F. 1961. The velocity of compressional waves in rocks to 10 kbar. Part 2, _J.geophys.Res._ _66_, 2199-2224.

BLOCK, S. & HALES, A.L. 1968. New techniques for the determination of surface wave phase velocities, _Bull.seism.Soc.Am._ _58_, 1021-1034.

BLOCK, S., HALES, A.L. & LANDISMAN, M. 1969. Velocities in the crust and upper mantle of southern Africa from multi-mode surface wave dispersion, _Bull.seism.Soc.Am._ _59_, 1599-1629.

BONJER, K.P., FUCHS, K. & WOHLENBERG, J. 1970. Crustal structure of the east African rift system from spectral response ratios of long period body waves, _Zeitschrift Geophys._ _36_, 287.

BOTT, M.H.P. 1965. Formation of oceanic ridges, _Nature, Lond._ _207_, 840-843.

BOTT, M.H.P. 1969. Orogeny in relation to the crust and upper mantle, In _Time and Place in Orogeny_, Eds. Kent, P.E., Salterthwaite, G.E. & Spencer, A.M., Special publication No.3 Geological Soc. of London.

BOTT, M.H.P. 1970. _The Interior of the Earth_, Published by Edward Arnold, London.

BROOKS, J.A. 1962. Seismic wave velocities in the New Guinea-Solomon Islands region, In _The Crust of the Pacific basin_, 2-10 Ed. MacDonald, G.A. & Kuno, H., Geophys. Monogr. No.6. American Geophysical Union, Washington D.C.

BRUNE, J.N., NAFE, J.E. & OLIVER, J.E. 1960. A simplified method for the analysis and synthesis of dispersed wave trains, _J.geophys.Res._ _65_, 287-304.

BRUNE, J. & DORMAN, J. 1963. Seismic waves and earth structures in the Canadian sheild, Bull.seism.Soc.Am. 53, 167-210.

BULLARD, E.C. 1936. Gravity measurements in East Africa., Phil.Trans.R.Soc. 235, 445-531.

BULLEN, K.E. 1937. The ellipticity correction to travel-time tables of P and S earthquake waves, Mon.Not.R.Astr.Soc., Geophys.Suppl. No.4, 143-156.

BULLEN, K.E. 1963. An introduction to the theory of seismology, 3rd edition, Cambridge University Press

CAPON, J. 1974. Characterisation of crust and upper mantle structure under LASA as a random medium, Bull.seism.Soc.Am. 64, 235-266.

CARDER, D.S., GORDON, D.W. & JORDAN, J.N. 1966. Analysis of surface foci travel times, Bull.seism.Soc.Am. 56, 815-840.

CHAPMAN, D.S. & POLLACK, H.N. 1975. Heat flow and incipient rifting in the central African plateau, Nature, Lond. 256, 28-30.

CHAPMAN, D.S. & POLLACK, H.N. 1977. Heat flow and production in Zambia: evidence for lithospheric thinning in Central Africa, Tectonophysics 41, 79-100.

CLAERBOUT, J. F. & MUIR, F. 1973. Robust modelling with erratic data, Geophysics. 38, 826-844.

CLEARY, J. & HALES, A.J. 1966. An analysis of the travel times of P-waves to North American stations in the distance range 32°-100°, Bull.seism.Soc.Am. 56, 497-489.

CLOOS, H. 1939. Hebung - Spathung - Vulkanismus, Geol. Rundsch. 30, 405-527.

CORBISHLEY, D.J. 1969. Measurements of the derivative of the P-wave travel time curve by means of an array network, Ph.D. thesis, University of Durham.

DARRACOTTE,B.W., FAIRHEAD, J.D. & GIRDLER, R.W. 1972. Gravity and magnetic surveys in northern Tanzania and southern Kenya., Tectonophysics 15, 131-141.

DAVIDON, W.C. 1967. Basis of MIGRAD minimisation, Comput.J. 10, 406.

DAVIES, D. & McKENZIE, D.P. 1969. Seismic travel-time residuals and plates, Geophys.J.R.Astr.Soc. 18, 51-63.

DER,Z., MASSE, R. & LANDISMAN, M. 1970. Effects of observational errors on the resolution of surface waves at intermediate disances, J.geophys.Res. 75, 3399-3409.

DOBRIN, M. B. 1974. Introduction to Geophysical prospecting, Third edition, Published by McGraw - Hill Inc.

DZIEWONSKI, A. M. & GILBERT, E. 1976. The effect of small, aspherical perturbations on travel times and a reexamination of the corrections for ellipticity, Geophys.J.R.Astr.Soc. 44, 7-17.

ELDER, J.W. 1966. Penetrative convection, its role in volcanism, Bull. Vulc. 29, 327-343.

ELDER, J.W. 1970. Quantitative laboratory structures of dynamic models of igneous intrusions, In Mechanisms of igneous intrusion, Eds. G.Newall & N.Rast Geol.J.Sp. No.2

ENGDAHL, E.R. & GUNST,R.H 1966. Use of a high speed computer for the preliminary determination of earthquake hypocentres, Bull.seism.Soc.Am. 56, 325-336.

ESPINOSA, A.F., SUTTON, G.H. & MILLAR, H.T. 1962. A transient technique for seismograph calibration, Bull.seism.Soc.Am. 52, 767-779.

FAIRHEAD, J.D. & GIRDLER, R.W. 1972. The seismicity of the East African rift system., Tectonophysics 15, 115-122.

FAIRHEAD, J.D. & HENDERSON, N.B. 1977. The seismicity of Southern Africa and incipient rifting, Tectonophysics 41, T19-T26.

FORTH, P.A. 1975. The structure of the upper mantle beneath east Africa., Ph.D. thesis, University of Durham.

GANE, P.G., ATKINS, A.R., SELLSCHOP, J.P.F. & SUIGMAN, P. 1956. Crustal structure in the Transvaal, Bull.seism.Soc.Am. 46, 293-316.

GASS, I.G. 1970. The evolution of volcanism in the junction area of the Red Sea, Gulf of Aden, and Ethiopian rifts, Proc.R.Soc. series A. 267, 369-381.

GASS,I.G. 1972. The role of magnetic processes in continental rifting, and sea-floor spreading, Fourth Tomkeieff Memorial lecture, geology dept., University of Newcastle upon Tyne

GIRDLER, R.W. 1964. Geophysical studies of rift valleys, Philos.Trans.Roy.Soc.Lond. Series A, 5, 121-156.

GOLES, G.G. 1975. Depths of origin of Kenyan basalts and implications for the Gregory rift, Nature, Lond. 225, 391-393.

GREGORY, J.W. 1921. The rift valleys and geology of East Africa, Seeley and Service Co. Ltd., London.

GRIFFITHS, D.H., KING, R.F., KHAN, M.A. & BLUNDEL, D.J. 1971. Seismic refraction line in Gregory rift, Nature, Phys.Sci. 229, 69-71.

GRIFFITHS, D.H. 1972. Some comments on the results of a seismic refraction experiment in the Kenya rift, Tectonophysics 15, 151-156.

GRIGGS, D.T., TURNER, F.J. & HEARD, H.C. 1960. Deformation of rocks at 500o to 800oC, Mem. Geol. Soc. Am. 79 39-104

GUMPER, F. & POMEROY, P.W. 1970. Seismic wave velocities and earth structure for the African continent, Bull.seism.Soc.Am. 60, 651-668.

GUTENBERG, B. 1959. Physics of the Earth's interior, Academic Press

HALES, A.L. & SACKS, F.S. 1959. Evidence for an intermediate layer from crustal structure in the Eastern Transvaal, Geophys.J.R.Astr.Soc. 2, 15-33.

HEISKANEN, W.A. & VENING MEINESZ, F.A. 1958. The Earth and its gravity field, Published by McGraw-Hill

HERRIN, E 1968. Introduction to 1968 seismological tables for P phases, Bull.seism.Soc.Am. 58, 1193-1241.

HERRIN, E. & TAGGART, J. 1968. Regional variations in P travel times., Bull.seism.Soc.Am. 58, 1325-1337.

HILGER & WATTS 1964. Instruction manual for the Willmore seismometer MkII, Published by Hilger & Watts Ltd., 98, St. Pancras Way, London NW4.

IYER, H.M. & HEALY H. 1972. Teleseismic residuals at the LASA-USGS Extended array and their interpretation in terms of crust and upper mantle structure, J.geophys.Res. 77, 1503-1527.

JACKSON, D.D. 1976. Most squares inversion, J.geophys.Res. 81, 1027-1030.

JAMES, F. 1967. Monte Carlo for particle physicists, In Methods in subnuclear physics (Section 6.1) IV, part 3, Ed. Nikolic, M.

JAMES, F. & ROOS, M. 1971. MINUIT, A package of programs to minimise a funtion of n variables, compute the covariance matrix, and find true errors, Manual produced by CERN COMPUTER 7600 Program library.

JEFFRIES, H. & BULLEN, K.E. 1967. Seismological tables, London Office of the British Association, Smith and Ritchie Ltd., Edinburgh

JOHNS, L. 1977. A study of the earthquake activity around Oloitokitok, South Kenya, M.Sc. thesis, University of Durham.

KHAN, M.A. & MANSFIELD, J. 1971. Gravity measurements in the Gregory rift, Nature, Phys.Sci. 229, 72-75.

KING, B.C. 1978. Structural and volcanic evolution of the Gregory rift valley, In Geological background to fossil man, Ed. Bishop, W.W. Edinburgh: Scottish Academic Press.

KNOPOFF, L. & SCHLUE, J.W. 1972. Rayleigh wave phase velocities for the path Addis-Ababa-Nairobi, Tectonophysics 15, 157-163.

LEHMAN 1964. On the travel times of P as determined from nuclear explosions, Bull.seism.Soc.Am. 54, 123-139.

LILWALL, R.C. & DOUGLAS, A. 1970. Estimation of P-wave travel tiomes using the Joint Epicentre method, Geophys.J.R.Astr.Soc. 19, 165-181.

LOGATCHEV, N.A., BELOUSSOV, V.V. & MILANOVSKY, E.E. 1972. East African Rift development, Tectonophysics 15, 71-81.

LONG, R.E. & MITCHELL, M.G. 1970. Teleseismic P-wave delay time in Iceland, Geophys.J.R.Astr.Soc. 20, 41-48.

LONG, R.E. 1974. A compact portable seismic recorder, Geophys.J.R.Astr.Soc. 37, 91-98.

LONG, R.E. & BACKHOUSE, R.W. 1976. The structure of the western flank of Gregory rift, Geophys.J.R.Astr.Soc. 44, 677-688.

MACK, H. 1969. Nature of short-period P-wave signal variations at LASA, J.geophys.Res. 74, 3161-3170.

MAGUIRE, P.K.H. 1974. The crustal structure of East Africa through earthquake seismology, Ph.D. thesis, University of Durham.

MAGUIRE, P.K.H. & LONG, R.E. 1976. The structure on the western flank of the Gregory rift (Kenya) Part 1. The crust, Geophys.J.R.Astr.Soc. 44, 661-675.

McCALL, G.J.H. 1967. Geology of the Nakuru- Thompson's Falls- Lake Hannington area, Geological Survey of Kenya, Report No. 78.

MICENKO, M. 1977. The structure of the upper mantle beneath Turkana, East Africa, M.Sc. thesis, University of Durham.

MOLNAR, P. & OLIVER, J. 1969. Lateral variations of attenuation in the upper mantle and discontinuities in the lithosphere, J.geophys.Res. 74, 2648-2682.

MORGAN, W.J. 1971. Convection plumes in the lower mantle, Nature, Lond. 230, 42-43.

NELDER, J.A. & MEAD, R. 1964. Basis of simplex minimization., Comput.J. 7, 308.

NEUBAUER, M. 1978. Crustal doming and the mechanism of rifting. Part 1: Rift formation, Tectonophysics 45, 159-186.

OLIVER, J., DORMAN, J. & SUTTON, G. 1959. The second shear mode of continental Rayleigh waves, Bull.seism.Soc.Am. 49, 379-389.

OTSUKA, M. 1966. Azimuth and slowness anomalies of seismic waves measured on the central Californian seismograph array. Part 2. Interpretation, Bull.seism.Soc.Am. 56, 655-675.

OXBURGH, E.R. & TURCOTTE, D.L. 1974. Membrane tectonics and the East African rift, Earth and Planetary Sciences Letters. 22, 133-140.

OXBURGH, E.R. 1978. Rifting in East Africa and large-scale tectonic processes, In Geological background to fossil man. Ed. Bishop, W.W. Edinburgh: Scottish Academic Press

PARKINSON, J. 1945. Preliminary geological map of the Mtito Andei -Tsavo area, Mining and geological department, Kenya.

PRESS, F. & EWING, M. 1956. A mechanism for G-wave propagation, Trans.Am.geophys.Un. 37, 355-356.

PRESS, F., EWING, M. & OLIVER, J. 1956. Crustal structure and surface-wave Dispersion in Africa, Bull.seism.Soc.Am. 46, 97-103.

ROONEY, D. & HUTTON, V.R.S. 1977. A magnetotelluric and magnetovariational study of the Gregory rift valley, Kenya, Geophys.J.R.Astr.Soc. 51, 91-119.

ROSENBROCK, H.H. 1960. An automatic method of finding the greatest or least value of a function, Comput.J. 3, 175-84.

RYKOUNOV, L.N., SEDOV, V.V., SAVRINA, L.A. & BORMIN, V.J.U. 1972. Study of microearthquakes in the rift zones of East Africa, Tectonophysics 15, 123-130.

SAGGERSON, E.P. 1963. Geology of the Simba-Kibwezi area, Geological Survey of Kenya, Report No. 58.

SAGGERSON, E.P. & BAKER, B.M. 1965. Post-Jurassic erosion surfaces in Eastern Kenya and their deformation in relation to rift structure, Q.J.geol.Soc.Lond. 121, 51-72.

SATTLEGER, J. 1965. A method of computing time interval velocities from expanding spread data in the case of arbitrarily long spreads and arbitrarily dipping plane interfaces., Geophys.Prospect. 13, 306-318.

SEARLE, D.L. 1954. Geology of the Sultan Hamud area, Geological Survey of Kenya, Report No. 29.

SEARLE, R.C. 1970. Evidence for thinning of the lithosphere beneath the rift valley in Kenya, Geophys.J.R.Astr.Soc. 21, 13-31.

SHACKLETON, R.M. 1978. Structural development of the East African rift system, In Geological background to fossil man. Ed. Bishop, W.W. Edinburgh: Scottish Academic Press.

SHAH, P.M. 1973. Ray tracing in three dimensions, Geophysics. 38, 600-604.

SHUEY, R.T. 1974. Comments on interpretation of gravity anomalies by non-linear optimisation, Geophys.Prospect. 22, 181-182.

SORRELS, C.G., CROWLEY, J.R. & VEITH, K.F. 1971. Methods for computing ray paths in complex geological structures, Bull.seism.Soc.Am. 61, 27-53.

SOWERBUTTS, W.T.C. 1969. Crustal structure of the East African plateau and rift valleys from gravity measurements,
Nature, Lond. 223, 143-146.

STEEPLES, D.W. & IYER, H.M. 1976. Low-velocity zone under long valley as determined from teleseismic events,
J.geophys.Res. 81, 849-860.

A SUNDARALINGAM, K. 1971. A seismic investigation of the crust and upper mantle of East Africa,
Ph.D. thesis, University of Durham.

SWAIN, C.J., KHAN, M.A., WILTON, T.J., MAGUIRE, P.K.H., GRIFFITHS, D.H. & BROWN, M. 1975. Kenya rift seismic profiles. KRISP,
Unpublished report

SWAIN, C.J. & KHAN, A.M. 1978. Gravity measurements in Kenya,
Geophys.J.R.Astr.Soc. 53, 427-429.

SWAIN, C.J. 1979. Ph.D. thesis, University of Leicester.

TOKSOZ, M.N., CHINNERY, M.A. & ANDERSON, D.L. 1967. Inhomogeneities in the Earth's mantle.,
Geophys.J.R.Astr.Soc. 13, 31-59.

TRYGGVASEN, E. 1964. Arrival times of P and upper mantle structure,
Bull.seism.Soc.Am. 54, 727-736.

TURCOTTE, D.L., & OXBURGH, E.R. 1973. Mid-plate tectonics,
Nature, Lond. 244, 337-339.

WALSH, J. 1963. Geology of the Ikutha area,
Geological Survey of Kenya, Report No. 56.

WAYLAND, E.J. 1930. Rift valleys and Lake Victoria,
C.R. Int. Geol.Congr. 15, 323

WHITMARSH, R.W. 1975. Axial intrusion zone beneath the median valley of the Mid-Atlantic ridge at 37°N detected by explosion seismology,
Geophys.J.R.Astr.Soc. 42, 189-215.

WOHLENBERG, J. 1970. On the seismicity of the East African rift system, In Graben problems I.U.M.P. Report No.27, 289-295.

WHOLENBERG, J. & BHATT, N.V. 1972. Report on airmagnetic surveys of two areas in the Kenya rift valley, Tectonophysics 15, 143-149.

WILLIAMS, L.A.J. 1972. The Kenya rift volcanics: A note on volumes and chemical compositions, Tectonophysics 15, 83-96.

WILLIAMS, L.A.J. 1978. The volcanological development of the Kenya rift, In Petrology and chemistry of continental rifts, Eds. E.R. Newman & I.B. Ranberg, 101-121

WILLIAMS, L.A.J. 1978. Character of quaternary volcanism in the Gregory riftvalley, In Geological background to fossil man, Ed. W.W Bishop Edinburgh: Scottish Academic Press.

WILLMORE, P.L., HALES,A.L. & GANE, P.G. 1952. A seismic investigation of the crustal structure in the Western Transvaal, Bull.seism.Soc.Am. 42, 53-80.

WOOLARD, G.P. 1966. Regional isostatic relations in the United States, In The Earth beneath the continents, 557-594 Ed. Steinhart, J.S. & Smith, T.J., Geophys. monogra. No. 10. American Geophysical Union. Washington D.C.

YOUNG, J.B. GIBBS, P.G. 1968. A series of computer programs for deriving information at selected seismic recording sites, for signals for known hypocentres, AWRE Report No. 54/68 GEDESS

ZORIN, Y.A. & ROGOZHINA, V.A. 1978. Mechanism of rifting and some features of the deep-seated structure of the Baikal rift zone, Tectonophysics 45, 23-30.